THE UNIVERSITY *of* EDINBURGH

Fatigue Load Monitoring of Offshore Wind Turbine Support Structures

Gabriel Marsh

A thesis submitted in partial fulfilment of the requirements for the award of an Engineering Doctorate

University of Strathclyde

2016

IDCORE

This thesis is submitted in partial fulfilment of the requirements for the award of an Engineering Doctorate, jointly awarded by the University of Edinburgh, the University of Exeter and the University of Strathclyde. The work presented has been conducted under the industrial supervision of E.ON Technologies Limited as a project within the Industrial Doctoral Centre for Offshore Renewable Energy.

Abstract

The uptake of renewable energy sources has increased dramatically in recent decades, in response to the contribution to climate change attributed to CO_2 emissions from the burning of fossil fuels, the need for governments to maximise the use of domestic energy forms with depleting conventional sources, and to reduce exposure to fuel price volatility. Renewable energy targets set by the European Union have been supported by legislation and economic incentives, and have resulted in a sharp increase in installed wind power capacity in particular.

Wind power is seen as a particularly attractive source of renewable energy capacity in the UK due to favourable resources and a competitive cost of energy for onshore sites, with 8.8 GW of capacity currently installed [1]. Constraints from visual and environmental impacts, together with improved wind resources, have led to the acceptance of greater financial costs and the exploitation of offshore sites, with over 5 GW installed to date [1].

Both onshore and offshore, the wind industry now has significant operational experience, with some of the earliest wind farms approaching the end of their design life. Material fatigue is a design critical factor which dictates the safe operational life of wind turbines, but is subjected to numerous areas of uncertainty in the level of environmental loading and structural response, as well as material properties and manufacturing methods. Therefore, a conservative design must be ensured from the outset, which presents the potential for fatigue life extension of installed assets if improved knowledge of their operational experience can be obtained.

This thesis details the methodology for a fatigue load assessment of operational offshore wind turbine support structures using measured data, and attempts to quantify areas of loading which contribute to total fatigue damage. The methodologies developed build on existing recommendations for onshore wind turbines to incorporate the additional effects of the offshore environment. Results from measured loading suggest that design fatigue levels can be reduced if operational monitoring is included. Operational experience can allow design conservatism, which is necessary due to uncertainties in structural properties and in levels of stochastic loading, to be more accurately quantified.

Acknowledgements

I have been fortunate to have been able to benefit from a vast amount of knowledge, experience and expertise over the last four years, from a large number of people from both industry and academia. I have an enormous debt of gratitude owed to my industrial supervisor, Dr Colin Wignall, for the time and support invested, and for helping both to focus on the technical detail of my project and to step back and see the bigger picture. Also to Steve Hillier of E.ON Climate & Renewables, for the practical discussions and for providing what has turned out to be a hugely enjoyable research topic.

I would like to thank my academic supervisors, Professor Atilla Incecik, Professor Lars Johanning and Dr Vengatesan Venugopal, who have helped to steer the project on course, and for whose guidance I am incredibly grateful. I also wish to thank everyone who has been involved in the IDCORE program, in particular Dr Philipp Thies and Professor Nigel Barltrop for their advice and insight.

I also want to thank my fellow IDCORE Research Engineers; Rebecca, Raffaello, Ampea and Alberto, for mutual motivation during the taught component of the doctorate, and for the entertaining email threads and moral support while on placement with our respective companies.

Finally, I want thank Vivien, for providing the love and support that has helped me through this endeavour, and for giving me the most wonderful gift imaginable.

The following trademarked software are used within this thesis and are hereby acknowledged: Matlab (version R2014b) of Math Works, Inc.; ABAQUS (version 13.3) of Dassault Systémes; Bladed (version 4.6) of DNV-GL; and Microsoft Office (version 2010).

Funding from the Energy Technologies Institute (ETI) and the RCUK Energy Programme for the Industrial Doctoral Centre for Offshore Renewable Energy (Grant number EP/J500847/1) is gratefully acknowledged.

This thesis is dedicated to my parents.

Declaration

I declare that this thesis was composed by myself and that the material presented, except where clearly indicated, is my own work. I declare that the work has not been submitted for consideration as part of any other degree or professional qualification. Furthermore, the journal paper in the Appendix is also my own work.

Signed:

Contents

Abbreviations

BBT	Beam Bending Theory
mCD	Metres above Chart Datum
CM	Capture Matrix
CoG	Centre of Gravity
DEM	Damage Equivalent Moment
DES	Damage Equivalent Stress
DLC	Design Load Case
EF	Effective Fixity depth
FE	Finite Element
FFT	Fast Fourier Transform
FLS	Fatigue Limit State
IEC	International Electrotechnical Commission
IFFT	Inverse Fast Fourier Transform
JONSWAP	Joint North Sea Wave Project
LC	Load Case
LCOE	Levelised Cost of Energy
MLC	Measured Load Case
MM	Meteorological Mast
MP	Monopile
OEM	Original Equipment Manufacturer
OWF	Offshore Wind Farm
OWT	Offshore Wind Turbine
PV	Peak-Valley
RF	Rainflow
RMSE	Root Mean Squared Error
RNA	Rotor Nacelle Assembly
SCADA	Supervisory Control and Data Acquisition System
SNR	Signal to Noise Ratio
TF	Transfer Function
TP	Transition Piece
ULS	Ultimate Limit State

Symbols

Greek Symbols

Symbol	Description	Units
α	Wind shear power law exponent	-
β	Cosine function coefficients, Fatigue damage fraction tolerance	-
δ	Dimensionless wind turbulence	-
δFE	Difference between FE & BBT stresses	Pa
$\Delta\sigma$	Stress drift error	Pa
ε	Strain	-
$\varepsilon_{\bar{U}}$	Wind speed error due to rounding	m/s
ε_{σ_U}	Wind speed standard deviation error due to rounding	m/s
θ	Wind direction, Loading direction	°
θ_{res}	Resultant bending moment angle	°
μ	mean	-
ν	Poisson's ratio	-
ρ	Density	kg/m^3
σ	Stress, standard deviation	Pa
σ_{BBT}	Stress from beam bending theory	Pa
σ_{FE}	Stress from Finite Element	Pa
σ_{BM}	Stress component resulting from applied bending moment	Pa
σ_{Fv}	Stress component resulting from axial load	Pa
σ_U	Wind standard deviation (turbulence)	m/s
σ_{eff}	Effective turbulence	m/s
σ_{eff}*	Effective turbulence calculated from maximum values in a distribution	m/s
σ*	Standard deviation of rounded wind speeds	m/s
φ	Circumferential gauge location	°
ϕ	Phase shift	°
ω	Angular velocity	Hz

Roman Symbols

Symbol	Description	Units
1P	Wind turbine rotor frequency	Hz
3P	Wind turbine blade pass frequency (for a three blade rotor)	Hz
A	Amplitude	-
$\bar{a}$	S-N curve intercept	-
B	Bandwidth	Hz
c	Blade chord length	m
C	Weibull scale parameter	-
C_d	Drag coefficient	-
C_l	Lift coefficient	-
Cm	Inertia coefficient	-
Cp	Power coefficient	-
Ct	Thrust coefficient	-
CSA	Cross Sectional Area	m^2
CSA_{TP}	Cross sectional area of the TP	m^2
df	Frequency interval	Hz
D	Diameter, Fatigue damage fraction, Drag force	m, -, N
D_{10min}	Damage fraction from a ten minute period	-
D_p	Damage fraction from a full population of measurements	-
D_s	Damage fraction from a sample of measurements	-
D'	Reduced fatigue damage fraction due to digital sampling	-
E	Elastic Modulus	Pa
f	Frequency	Hz
f_n	Natural frequency	Hz
f_s	Sample frequency	Hz
f_p	Peak wave energy frequency	Hz
F	Force	N
F_v	Vertical force component	N
G	Material shear modulus	Pa
H_s	Significant wave height	m
$\widehat{H_s}$	Fitted significant wave height	m
I	Electrical current	A
I_A	Second moment of area	m^4
I_{TP}	Transition Piece second moment of area	m^4

I_P	Polar moment of inertia	kg.m^2
I_{ref}	IEC reference TI at 15 m/s	-
J	Polar moment of area	m^4
k	Weibull shape parameter, Y-axis offset, Number of stress range bins, Degrees of freedom	-
k_B	Boltzmann constant	J.K^{-1}
L	Lift force	N
L_k	Turbulence integral length scale	m
m	Wöhler fatigue damage exponent	-
M	Number of data points	-
M_{res}	Resultant bending moment	N.m
M_x	Bending moment x component	N.m
M_y	Bending moment y component	N.m
n	Number of operational stress cycles	-
n_θ	Number of wind direction bins	-
n_U	Number of wind speed bins	-
n_{LC}	Number of LC bins	-
N	Number of data points, Number of bins, Maximum number of stress cycles to failure	-
$Nref$	Reference number of fatigue cycles	-
N_{RMS}	Root mean squared value of signal noise	Pa
P	Anemometer correlation coefficient, Number of consecutive erroneous measurements	m/rev
P_d	Partial pressure of dry air	Pa
P_v	Partial pressure of water vapour	Pa
r_{inside}	Radius of the TP inside surface	m
$r_{outside}$	Radius of the TP outside surface	m
R	Electrical resistance	Ohm
R^2	Sum of squared residuals	-
R_d	Gas constant for dry air	J/kg.K
Rv	Gas constant for water vapour	J/kg.K
S	Power Spectral Density	m^2, m^2/s^2
S_{RMS}	Root mean squared value of a measured signal	Pa
t	Time	s
T	Time period, Temperature	s,
TI	Turbulence Intensity	-

TI_{eff}	Effective turbulence intensity	-
T_p	Peak wave energy period	s
U	Wind speed	m/s
U*	Rounded wind speed	m/s
$\overline{U}$	Mean wind speed	m/s
U_{hub}	Wind speed at turbine hub height	m/s
U_{rated}	Wind speed at turbine rated power	m/s
U_{ref}	IEC reference wind speed	m/s
$\vec{U}'$	Wind variability metric	m/s/ten min
v	Water velocity	m/s
V	Electrical voltage	V
y'	Reduced stress amplitude due to digital sampling	Pa
z	Height above sea level/ground level	m

List of Figures

List of Tables

1 Introduction

1.1 General Overview

UK government targets to obtain 15% of energy demand from renewable sources by 2020 are projected to rely heavily on onshore and offshore wind power to make up the majority of renewable capacity. With over 13.8 GW of capacity already installed, offshore wind is expected to contribute the bulk of additional capacity required to meet stated targets, provided that UK government support for the industry remains in place.

Further afield, the European offshore wind market continues to grow, with over 3,230 individual turbines and support structures currently installed [2], the large majority of which are based on a Monopile (MP) design. Worldwide markets are also opening up, with projects developing in China, Japan, and the United States.

Investment in a typical offshore wind farm is in the order of £3million/MW [3], with the cost of the support structure contributing in the region of 14% of the total Levelised Cost of Energy (LCOE) [4]. The design lifetime of wind farms is typically between 20 to 25 years, with the financial support mechanism set to run over the life of the asset. However, most wind farm operators are expected to seek opportunities for operational life extension due to the significant potential for financial return.

The support structure for an Offshore Wind Turbine (OWT) is a design critical component with little or no redundancy. For the majority of Offshore Wind Farms (OWF) the support structure design is often highly repeatable with up to several hundred turbines across a given site, with variations in dimensions to account for different water depths, soil properties, and corresponding structural stiffnesses. This leads to a design which must be highly optimised in order to be cost effective in an industry with very small financial margins.

This project aims to investigate the ability of measured load data to support OWT design loads and provide an assessment of operational fatigue loading. The work is based on an investigation of one OWF, but it is hoped that the approach may be applicable to the wider industry, both to verify and support design stage calculations, and to identify potential for the reduction of design conservatism.

1.2 Industrial Relevance

The fatigue design of OWT support structures contains areas of uncertainty in the level of environmental loading, which is essentially stochastic, and the level of the structural response, as well as material properties and manufacturing methods. In order to achieve an acceptable level of safety, significant conservatism is therefore inherent in OWT design in order to address this uncertainty in a probabilistic way. Operational experience has the potential to allow some areas of uncertainty to be identified, through the validation or updating of design calculations, or through record of the actual level of environmental loading. However, although guidance exists to allow fatigue loading to be assessed via operational experience [5], no specific, detailed methodology is available. This work therefore seeks to investigate the potential for operational data to inform an assessment of the fatigue loading for a specific operational OWF, shown in Figure 1-1. Potential areas that this work may benefit the wider industry are outlined in Sections 1.2.1 and 1.2.2 below.

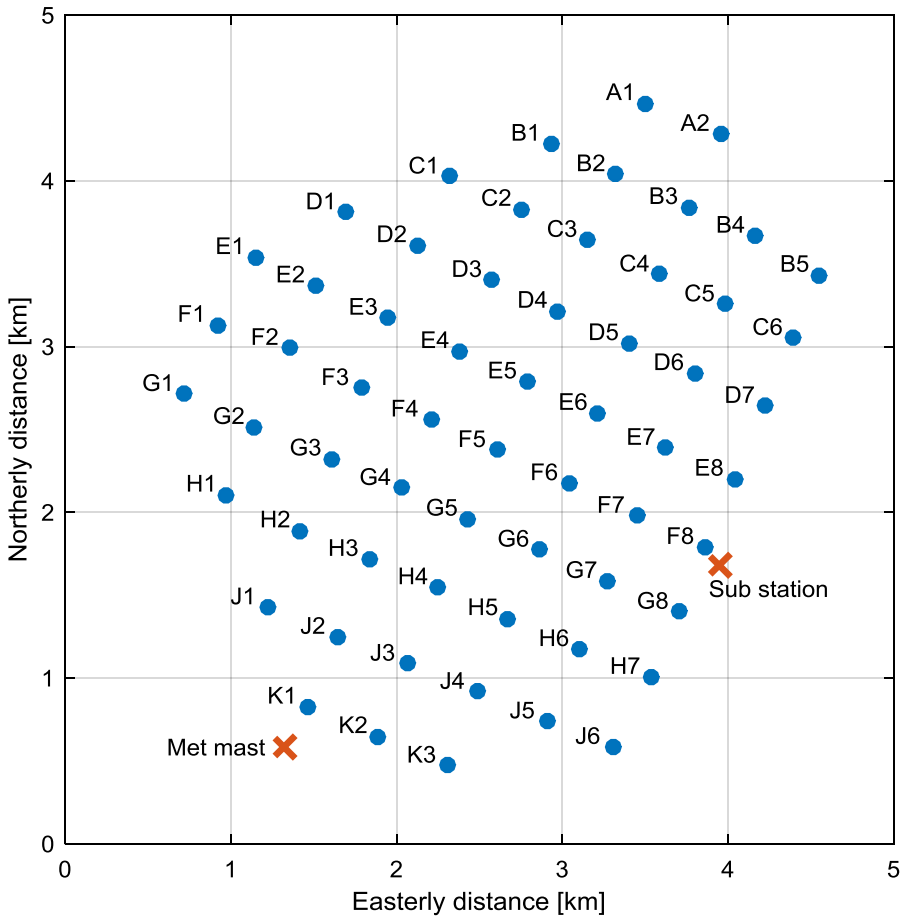

Figure 1-1. Layout of the Offshore Wind Farm. Turbine locations are shown with blue dots, which are scaled to the rotor diameter. The location of the sub-station and the pre-construction Meteorological Mast are also shown.

1.2.1 Grouted Connection Issues

A number of early offshore wind farms utilised a support structure with a grouted connection between a cylindrical MP foundation and Transition Piece (TP). The grouted connection design allowed verticality misalignment of the MP, which may be produced during pile driving, to be corrected, and was based on established and codified methods developed in the oil and gas industries [6]. However, industry experience identified in late 2009 that slippage of the TP had occurred systematically in many OWTs which were based on this design, resulting in settlement on the top of the MP of internal TP jacking brackets which were used to temporarily align the TP during curing of the grouted connection [6], [7]. Subsequently,

design standards have been modified to require the inclusion of shear keys with all grouted connection designs to ensure adequate axial capacity [8].

As a result of the grouted connection failure and the resulting changes to the load path across the TP and MP, the fatigue lives of the temporary TP jacking brackets were called into question and remedial modifications were instigated to ensure the long term integrity of the support structures. In order to provide information on the behaviour of the slipped connection, a number of OWF operators installed monitoring instrumentation in order to optimise the design of the remedial works. One such monitoring system has provided the data which forms part of the work presented in this thesis.

In conjunction with industry experience with grouted connections, the design of internal corrosion protection systems have also highlighted potential design issues in certain cases. Where corrosion protection systems had been found to under-perform, such as designs based on the assumption of the MP acting as an airtight compartment with subsequent identification of minor leaks at cable seals, or insufficient performance of cathodic protection systems, for example [9], the presence of corrosion has the potential to impact on fatigue lives where it has not been accounted for in the design. Whereas the installation of remedial corrosion protection systems may include significant costs, the potential to reduce design conservatism in the level of fatigue loading through operational load measurement may represent a cost effective alternative. It should be noted that where remedial corrosion protection systems are installed after a period of time in operation, certification bodies may still require any updated assessment of fatigue lives to be based on a free corrosion design, as the roughened surface can increase the likelihood of fatigue crack initiation. Therefore, the reduction of design conservatism through an assessment of operational loading may prove the only practicable means of demonstrating sufficient operational life, in some circumstances. More detail on fatigue design is provided in Section 2.2.

1.2.2 Design Life Extension

The financial case for the construction of an Offshore Wind Farm (OWF) is based on a typical operational life of 20 to 25 years. At the end of the design life the decision of whether to continue operation or to decommission the wind farm may be based on multiple factors [10], and assessing the financial implications of life extension must be based on the condition of the whole wind farm. The justification of a safety case for life extension of an OWT support structure may be based on inspections to assess integrity, but the inaccessibility of the offshore environment and the sheer volume of inspections that might be required means that costs may be prohibitively expensive. Therefore, the demonstration of

design conservatism through an assessment of operational loading provides an attractive option, with the potential to justify life extension without inspections at an acceptable level of risk.

The financial benefit of extending the operational life of an existing OWT asset by five years is shown in Figure 1-2, based on Equation (1-1), with variables defined in Table 1-1 below. Due to the discount rate assumed for Equation (1-1) it may appear more financially attractive to conduct a life extension assessment towards the end of the OWF operational life. However, an early assessment of the operational loading may present a more versatile and valuable approach as it provides the ability to benchmark loading and identify temporal changes in the level of fatigue damage, and to optimise the measurement campaign in subsequent years.

$$£(Y) = LF.H.(P - OM).\frac{1}{(1+DR)^{Y}} \tag{1-1}$$

Table 1-1. Definition of variables used with Equation (1-1)

Symbol	Description	Value	Unit	Reference
£(Y)	Annual electricity revenue as a function of financial year (Y)	(variable)	£/MWyear	-
LF	Load Factor, as a UK average (onshore & offshore)	27.82	%	[1]
H	Number of hours per year	8,760	Hours/year	-
P	Electricity price, taken as a current EU average (excluding subsidies, reflecting extended operation)	100	£/MWh	[11]
OM	Average Operation & Maintenance costs (upper bound, reflecting end of life costs)	45	£/MWh	[12]
DR	Discount rate	10	%	-
Y	Financial year (starting from 2015 = 0)	(variable)	-	-

Note: The Load Factor for an average UK offshore site is in the region of 40% [13].

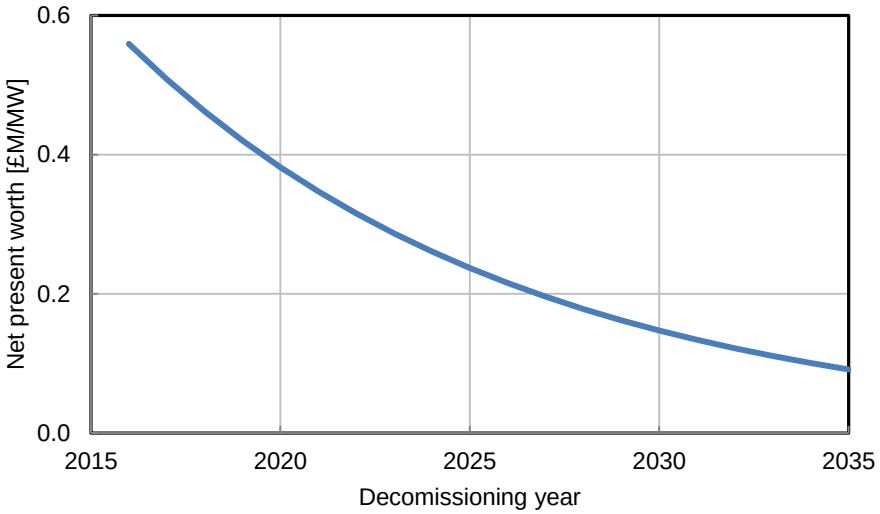

Figure 1-2. Net present worth of a 5 year life extension program versus initial decommissioning year (given in £M per MW capacity).

1.3 Aims and Objectives

The overarching aim of this thesis is to inform on the potential for fatigue life extension of an operational wind farm. The objectives of this work are:

- To develop a methodology to assess the level of fatigue loading of a wind turbine support structure using operational measurements,
- To investigate the operational states which contribute to fatigue damage, and to compare measured results with simulated loading,
- To determine the level of environmental loading across a wind farm site, and identify the location of most severe loading for fatigue,
- To conduct a sensitivity analysis to assess the potential impact of temporal changes to support structure dynamics on the measured fatigue loading.

1.4 Methodology Implemented

This thesis is made up of nine chapters, detailing a review of the background literature, the research methodology and results as outlined in Figure 1-3 below.

Chapter 2 presents the background to the existing wind turbine design standards, and the design methodologies used to define the fatigue loading expected to occur over the life of an

OWF. The design methodologies are summarised to provide an overview of the physical load and response processes that are undergone by an operational OWT, and to describe the tools which are available to analyse structural loads at the design stage. The stochastic nature of wind and waves lends to a probabilistic approach to quantify the level of environmental loading, and the necessary site analysis is briefly discussed. The methods used to process the design loads into a form which is compatible with fatigue damage calculations are reviewed, and potential shortcomings in the current best practice methodologies are highlighted. Finally, an overview of support structure load measurement is presented, which facilitates the comparison of design calculations with operational experience, which is the basis of the research contribution of the current work.

Chapter 3 presents the methodology for the research presented in this thesis. Data processing methods are presented to identify and account for quality issues in the environmental and structural loading data. As only two turbines were monitored and used to represent the fatigue critical location, the distribution of environmental loading across the site was analysed and, where the most severe loading was identified at other turbines within the wind farm, a methodology is presented to account for the discrepancy. A comparison between design and measured fatigue loading is described as framed by the Load Case methodology defined in existing standards, and areas of uncertainty are investigated in the application of the methodology where optimal information is not available. Part of the structural loading which is not normally included in the fatigue analysis is characterised and quantified, and strategies to account for the additional fatigue loading in the design approach are presented. Therefore, a complete operational fatigue histogram is derived from measured loading and used to demonstrate areas of conservatism in the design. The final part of the chapter describes a wind turbine structural model that was developed to represent the monitored structures and, noting the limited ability of the model to accurately represent the structural dynamics, investigate the potential impact on the measured loads of variations in environmental loading and structural stiffness that may occur over time and across the rest of the wind farm.

Chapter 4 presents the results of the quality processing of the measured data, and quantifies the effects of noise correction. Results of finite element analysis of the location of load measurement are presented, and a methodology is developed to allow results from unidirectional loading to be extrapolated to other directions, to allow a comparison between design and measured fatigue loading to be assessed.

Chapter 5 presents results of the environmental loading recorded during the measurement campaign, and finds good agreement with the design stage mean wind speed distribution and the assumption of correlated wind and wave directions. Turbulence levels measured by the turbine SCADA systems are compared with measurements from the Meteorological Mast and LIDAR system, and used to justify the use of SCADA data to characterise the operational turbulence loading across the wind farm and for use with model simulation results presented in Chapter 8.

Chapter 6 first compares results from the design and measured levels of fatigue loading under similar loading and turbine operational conditions, with investigation of the distribution of measured loading and the establishment of a conservative estimate for a representative measurement. Options are reviewed to allow incomplete measurement conditions to be accounted for in a conservative way, and it is demonstrated that design data can be reverted to, where incomplete measurements exist, in the construction of the complete load spectrum.

Chapter 7 presents results of the investigation of transition cycles and their impact on the total level of fatigue loading. The characterisation of a representative wind history used to quantify changes in wind speed and direction is investigated, utilising datasets from multiple sites and spanning multiple measurement years. Finally, methods to account for transition cycles at the design stage are reviewed, and it is demonstrated that transition cycles can constitute a significant proportion of the total fatigue loading.

Chapter 8 presents results of the wind turbine model simulations. It is found that the model definition does not provide an accurate representation of the structural dynamics and resulting levels of fatigue damage, compared to the design data produced by the turbine designer. However, a sensitivity analysis is presented which shows how sources of design conservatism can be investigated, and how fatigue loading measured at a certain location may vary with spatial and temporal differences in levels of environmental loading and the structural response frequencies.

Chapter 9 discusses the results presented in the previous chapters, and describes how the methodologies can be used to characterise operational fatigue and therefore to quantify levels of design conservatism using measured load and response data. Finally, the potential for operational measurement to inform decisions on levels of fatigue damage is discussed, together with the limitations of the work presented and potential areas for further work.

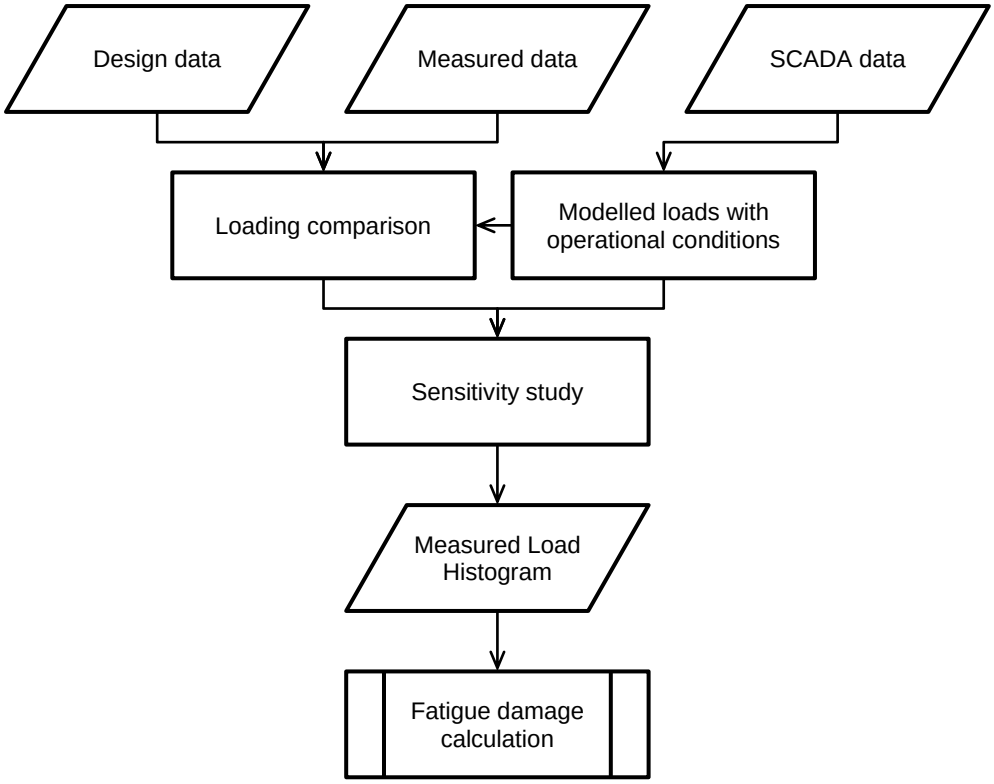

Figure 1-3. Overview of research methodology used to investigate the level of fatigue loading from measured data.

2 Background

2.1 Wind Turbine Support Structure Design

The support structure capital expenditure and installation costs of an OWT contributes one of the major components of increased LCOE compared to onshore wind farms, due to the additional distance to the sea bed, wave loading components, and logistical challenges associated with operating offshore [14]. Support structure costs are typically in the range of between 25% to 34% of the overall costs [15]. As wind turbines have increased in capacity over the years in pursuit of overall reductions in LCOE, so the supporting structures have developed to accommodate the associated larger forces and deeper waters. The first offshore wind farm was installed in Vindeby, Denmark, in 1991 and consists of eleven 450 kW turbines on gravity base foundations [16]. Fast forward 25 years, and 7 MW scale turbines are planned for commercial wind farms [17], mounted on lattice 'jacket' foundation structures in water depths of over 40 m, while demonstrator projects are planned to put similar scale turbines on floating foundations to enable deeper water depths to become available for development [18].

The most common form of substructure design remains the MP foundation, TP and tower, as shown in the schematic diagram in Figure 2-1. The MP foundation consists of a cylindrical steel tube typically of around 4 m to 7 m diameter which is driven into the sea bed by piling to a penetration depth which may be well over 20 m, depending on the loads and soil conditions at site, and transfers lateral loads into the soil via a pressure difference on either side of the pile [19]. For a typical design, the MP component extends from the sea bed to approximately the water level, and then connects to a TP which extends to above the wave loading zone and carries secondary steel details to facilitate access to the turbine tower, such as the boat landing, ladder and working platform. The rest of the support structure then consists of a tower connecting the TP to the wind turbine, and is similar to those used for onshore turbines.

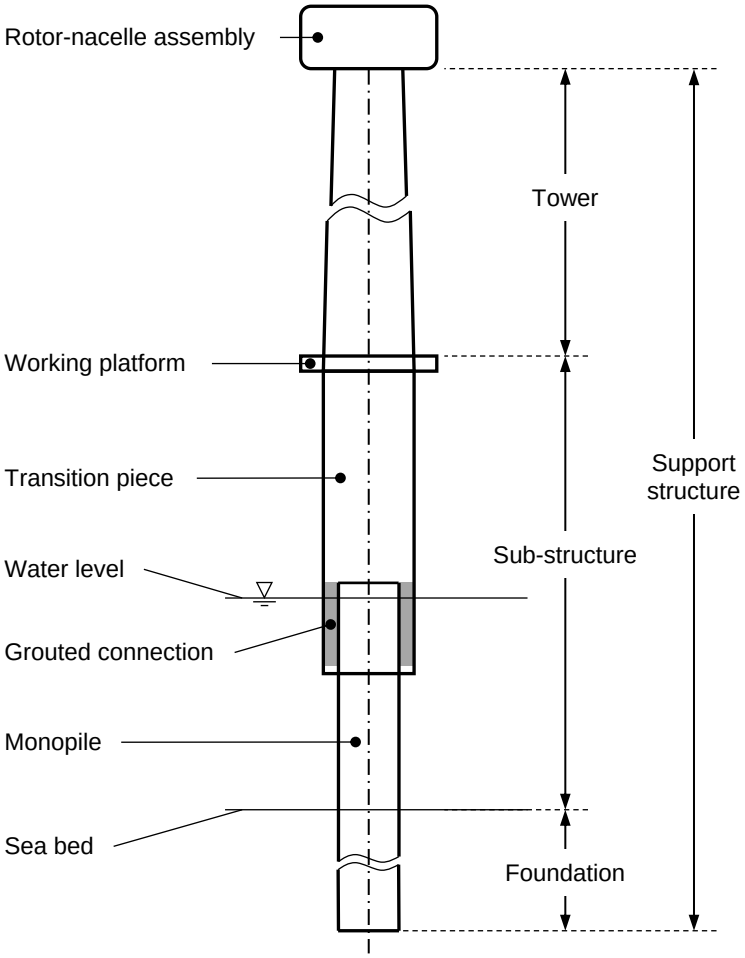

Figure 2-1. Schematic of an offshore wind turbine monopile support structure (turbine rotor not shown).

2.1.1 Design Standards

Industry standards establish best practice engineering design methods for the offshore wind industry, and support wind farm owners, insurers, and project financers in their assessment of risk. The International Elecrotechnical Commission (IEC) 61400 series standards [20] have evolved from initial application in the onshore wind industry, and form the basis of OWT design [21]. Due to the significantly different loading found offshore, standards have incorporated existing offshore engineering experience from the oil and gas industry, and marine certification bodies such as Det Norske Veritas and Germanischer Lloyd were the first to publish standards for OWTs [22], [23]. It increasingly became apparent that in order to achieve an optimised design it was necessary to approach the design of the entire wind turbine and support structure as an integrated system [24]. Following extensive industry participation and research work into the marinisation of wind turbines, such as the European

Union funded RECOFF project [25], the IEC-61400-3 standard for design of OWTs was published in 2009 [26]. The most recent publication follows the merger of Det Norske Veritas and Germanischer Lloyd in 2013 to form the certification body DNVGL, to provide the current DNVGL-ST-0126 standard for the design of support structures for OWTs [27].

2.1.1.1 Load Measurement

The International Energy Agency produced the first recommended practices for the assessment of onshore wind turbine loads in 1984, and released a second edition in 1990 [28], with the aim of defining an industry best practice procedure for classification of wind turbine performance through measurement. This formed the basis for the IEC 61400 series standards, and IEC-TS-61400-13 methodology for the measurement of loads in onshore turbines was published in 2001 as a Technical Specification [29] and later approved as an Industry Standard in 2015 [30]. In support of modern design methods, the latest version of the IEC-61400-13 standard outlines the methodology for the validation of wind turbine simulation models through full scale measurements. However, no standard currently exists for the measurement of operational loads on OWTs.

2.1.1.2 Life Extension

In support of operational assessment and life extension guidance, Germanischer Lloyd published in 2009 an industry guideline for the continued operation of wind turbines past their design life [31]. The guideline suggests two distinct routes to the certification of life extension suitability:

- Through analytical assessment of loading, via new calculations using updated structural models and environmental loading. This method may be supported by load measurement.
- Through practical inspection and assessment of load transferring and critical components. In practice, this method may be impractical for OWTs where fatigue critical welds may be below the sea bed level, and therefore inaccessible for inspection.

An updated version of the guideline has been released as an industry standard for the lifetime extension of wind turbines [5].

2.1.2 Dynamic Simulation

The design optimisation of large OWTs is typically an iterative process involving an initial structural definition from which stresses are calculated based on dynamic response to external loads. To simulate the structural dynamics the OWT definition is generally discretised via the finite element method, from which the equation of motion can be integrated in the time domain using finite difference methods. The equation of motion to be solved is, [32]

$$M\ddot{x} + C\dot{x} + Kx = f(t) \tag{2-1}$$

where M is the structural mass matrix, C is the damping matrix, K is the structural stiffness matrix, x is a matrix of nodal displacements (and the first and second time derivatives), and $f(t)$ is a matrix of time variable external forces (due to wind and wave loads) and internal forces (due to rotor velocities and actuation loads) [33]. Various strategies are used to solve the equations of motion, and an overview and comparison of existing design software is given in [34].

2.1.3 Structural Natural Frequency

Due to the large cost of OWT support structures, various design approaches are used to reduce the amount of structural steel required by minimising the operational stresses. Operational loads may be divided into:

1. Steady state loads arising from the rotor thrust and drag forces due to mean wind speed and water currents. The steady gravity load due to self-weight of the components may also be included here. The steady state loading is dominated by the rotor thrust force during operating conditions.
2. Dynamic loads arising from varying aerodynamic and hydrodynamic forces, as well as mass imbalances from moving parts.

The magnitude of the dynamic response is largely dictated by the resonant vibrational frequencies of the structure, see Figure 2-2 below. The forcing frequencies arise from wind and wave loading, which may for example be described by the Kaimal and JONSWAP spectrums, respectively [35], and the rotor and blade pass frequencies, commonly referred to as the 1P and 3P frequencies (for a three bladed turbine), respectively. Additionally, for turbines that operate at variable speed to maintain maximum energy capture at different wind speeds, the 1P and 3P frequencies are defined by a frequency range. Turbine and foundation designers need to avoid these frequency ranges with the natural frequencies of the structure

by a margin of greater than 10%, if a safe design is to be achieved [36]. The target frequency range for the first structural mode may be below 1P for onshore turbines due to the absence of wave loading, shown as the soft-soft frequency range in Figure 2-2, whereas the target for offshore turbines is typically between the 1P and 3P frequencies and is referred to as a soft-stiff design. Although the safest option may be to design the structure with the stiff-stiff approach, putting the first natural frequency above the 3P range, the increased material and installation costs make this option economically unattractive [15].

Therefore, the natural frequency of a wind turbine structure is a design critical factor which may be thought of as a corollary of both the maximum loading and the level of through-life fatigue loading, where a conservative design is dependent on the natural frequency being within acceptable limits. The natural frequency is a function of the actual and hydrodynamic mass, structural and soil stiffness, and the aerodynamic, hydrodynamic, structural and soil damping properties of the complete structure. Whereas the properties of the steel components and the fluid-structure interaction are well known at the design stage, one of the largest areas of uncertainty affecting the natural frequency are the properties of the soil. Full scale measurements suggest that existing design methods, which are based on empirical data from testing of relatively small diameter piles with large deflections, may under-predict soil stiffness for small displacements [37].

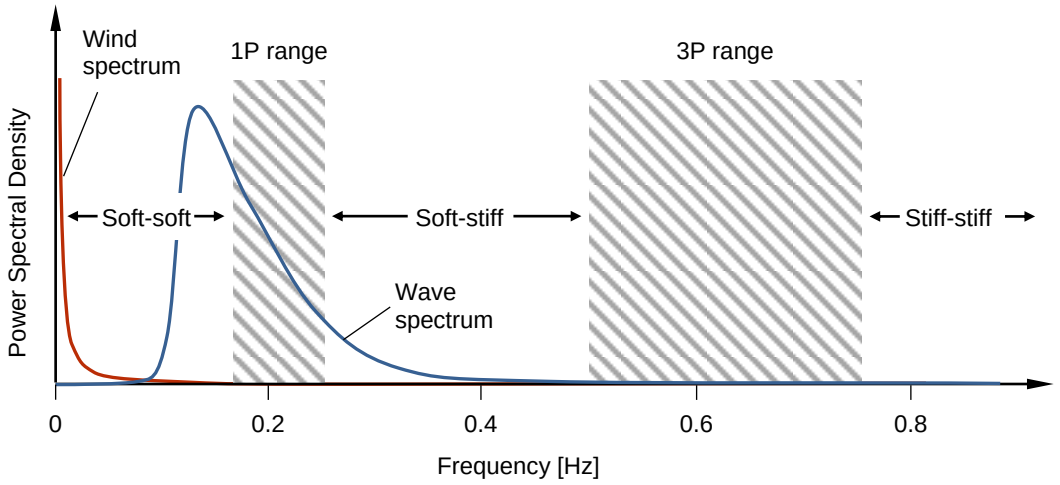

Figure 2-2. Example frequency spectrum showing the forcing frequency ranges for a three bladed OWT. The soft-soft, soft-stiff, and stiff-stiff ranges are targets for the first natural frequency of the wind turbine structure in order to minimise the dynamic response.

2.1.4 Load Case Design Methods

Wind turbines operate under a range of environmental and operational loading conditions during their design life. To account for this range of both stochastic and deterministic loading, design standards require the analysis to be broken into a series of short term operating states, known as Load Cases (LC). Design Load Cases (DLCs) defined in the IEC-61400 series standards [20] are divided into analysis for the Ultimate Limit State (ULS), defining the maximum design loads which may arise from a combination of extreme storm events or from fault conditions, and for the Fatigue Limit State (FLS), which is used to compile the through-life fatigue cycle spectrum. The LC is simulated in the time domain using the turbine designers' aero-hydro-servo-elastic software.

The FLS DLCs, as defined for offshore turbines, are outlined in Table 2-1 and describe all conditions expected to contribute a significant level of cycles to the support structure fatigue loading. For a given mean wind speed and direction bin, the LC is represented by a ten minute time domain simulation, a length of time over which the environmental loading is assumed to be statistically stationary [38]. Therefore, the load cycles which are produced in each LC are factored by the number of ten minute periods expected to occur over the life of the turbine, determined from the probability distribution of environmental loading for the steady state operating conditions, and from knowledge of the controller operation for the specific turbine model for the transient LCs.

In order to characterise a LC from measured data, the IEC 61400-13 standard [30] outlines the methodology recommended to define a Measured Load Case (MLC) to match the environmental and operational conditions that define the DLC. Due to the variation in results which are to be expected for operational data, a number of measurements are used in order to better capture the distribution of ULS and FLS loads which occur in practice.

Table 2-1. Overview of the Design Load Cases used for fatigue analysis, from IEC 61400-3 [26].

LC	Design Situation	Description	Number of occurrences
1.2	Power production	Normal steady state power production conditions, modelled under the range of mean wind speeds and wave conditions expected to occur between cut-in and cut-out wind speeds.	From wind and wave joint probability distribution
2.4	Power production plus occurrence of a fault	Transient event triggered by a fault condition during normal power production, which results in shut down of the turbine to protect components. Normal wind and wave conditions are included in the analysis	From wind probability distribution and turbine controller specifications
3.1	Start-up	Transient event modelling the turbine start-up sequence under normal wind and wave conditions	From wind probability distribution and turbine controller specifications
4.1	Normal shut-down	Transient event modelling the turbine shut-down sequence under normal wind and wave conditions	From wind probability distribution and turbine controller specifications
6.4	Parked/Idling	Steady state modelling of the Stationary turbine in parked conditions, under normal wind and wave loading at high and low wind speeds	From wind and wave joint probability distribution

2.1.5 Wind Loads

Wind loading acting on an OWT arises from a combination of aerodynamic lift and drag forces induced on the rotor blades, drag forces on the rest of the structure. Lift and drag forces, *L* and *D*, acting on an aerofoil blade element of length *dr* are given by, [33]

$$L = C_l \frac{1}{2} \rho U^2 c.\, dr$$
$$D = C_d \frac{1}{2} \rho U^2 c.\, dr \qquad (2\text{-}2)$$

where the half times air density times relative velocity squared term, $1/2\rho U^2$, is known as the dynamic pressure, C_l and C_d are the lift and drag coefficients for a given aerofoil and are a function of relative flow angle and Reynolds number, and $c.dr$ describes the plan area of the aerofoil element as the product of the chord and element length. Equations (2-2) provide a simplified representation of the aerodynamic forces acting on an OWT allowing efficient implementation of time marching numerical solutions for design analysis, as discussed briefly in Section 2.1.4.

Variations in the wind field due to turbulence and wind shear velocity profiles result in dynamic loads which are 'sampled' by the rotating blades, which in turn result in increased dynamic responses in the structure at the 1P and 3P frequencies, as discussed in Section 2.1.3. Therefore, knowledge of the wind characteristics at a given site is necessary to understand the level of loading likely to be experienced by the structure.

The standard wind turbine classes described in IEC-61400-1 [21] specify the maximum wind loading conditions to which a turbine is to be designed. These standard conditions are divided into three reference wind speeds which define the maximum ten minute average wind speed conditions for each turbine class. Additionally, three turbulence levels are defined within each reference wind speed class which define a reference level of Turbulence Intensity (see Equation (2-5) below). These wind turbine classes are shown in Table 2-2, below, together with a class 'S', for use when different wind conditions are specified by the turbine designer. An assessment of site conditions is therefore required to ensure that the projected loading will not surpass the structural capacity.

Table 2-2. IEC wind classes, where Roman numerals refer to a reference wind speed (U_{ref}), and the letters refer to a reference turbulence category (I_{ref}). From [21].

Wind Turbine Class		I	II	III	S
	U_{ref} [m/s]	50	42.5	37.5	Specified by the turbine designer
A	I_{ref} [-]	0.16	0.16	0.16	
B	I_{ref} [-]	0.14	0.14	0.14	Specified by the turbine designer
C	I_{ref} [-]	0.12	0.12	0.12	

2.1.5.1 Site Wind Assessment

Wind measurements are required to be recorded in order to accurately classify the wind resource in terms of the mean wind speed, direction, and turbulence expected at a given site over the life of the turbine. Probabilistic assessment of mean wind speeds are used for yield assessments as well as predicted loading. Wind speed measurements may be recorded via an anemometer mounted on a Meteorological Mast (MM) which usually consists of a lattice structure designed to present as little disturbance as possible to the ambient flow. Multiple anemometers are placed at various heights on the MM in order to assess the vertical wind speed profile due to the degree of wind shear, and should reach the turbine hub height as a minimum. The normal wind speed profile is given by the power law, [26]

$$U(z) = U_{hub}(z/z_{hub})^{\alpha} \tag{2-3}$$

where $U(z)$ is wind speed as a function of height z compared to the values at hub height (denoted by the subscript *hub*), and α is the power law exponent and is typically given as 0.14 for normal wind conditions [26].

Recent advances in the development of LIDAR technology have allowed wind speeds to be measured remotely over a range of heights without the need for a MM structure, although the assessment of turbulence may be reduced to 80% to 90% compared to conventional point measurement methods due to the volumetric averaging effect of LIDAR measurement [39], [40]. Therefore point measurement instruments such as cup or ultra-sonic anemometers are recommended for assessment of turbulence [41]. An example of cup and LIDAR anemometer instruments are shown in Figure 2-3.

Wind turbulence (σ_U), defined as the standard deviation of the lateral component of the wind vector, is typically measured over a ten minute period [35] due to the assumed level of statistical stationarity and ergodicity found over this time scale. In reality, wind time series seldom meet these statistical criteria as variations occur at virtually all scales, and therefore the ten minute period of measurement is a practical compromise [42]. Some analysts prefer to 'de-trend' the wind speed prior to calculation of σ_U in order to remove low frequency variations which may result in a deceptively high standard deviation, and this may be achieved by subtraction of a linear least-squares fit to the data . Alternatively, where wind speed measurements are stored as statistical data, de-trending may be achieved by combining standard deviations from one minute periods into a ten minute total, thus removing the influence of a varying mean,

$$\sigma_{U_{de-trended}} = \sqrt{\frac{1}{10}\sum_{i=1}^{10} {\sigma_{1min_i}}^2} \tag{2-4}$$

The turbulence values can be normalised by the mean wind speed ($\overline{U}$) to give the non-dimensional wind Turbulence Intensity (*TI*) over the ten minute period,

$$TI = \frac{\sigma_U}{\overline{U}} \tag{2-5}$$

The *TI* category from Table 2-2 is then selected to be greater than the 90th percentile of site specific *TI* measurements at each wind speed bin [21].

An effective *TI*, TI_{eff}, for each hub height wind speed may be used to approximate with an average value the distribution of *TI* occurring over the life of the turbine, [21]

$$TI_{eff}(U_{hub}) = \left\{ \int_0^{2\pi} P(\theta|U_{hub}) TI^m(\theta|U_{hub}) d\theta \right\}^{1/m} \quad (2\text{-}6)$$

where $P(\theta|U_{hub})$ is the wind direction probability distribution for each hub wind speed, $TI(\theta|U_{hub})$ is the turbulence intensity at each wind speed and direction, and *m* is the Wöhler exponent used for fatigue design of the structural detail, as discussed in Section 2.2.2. Equation (2-6), therefore, gives a weighted mean *TI* value, and is based on the assumption that structural response and the amplitude of the resulting fatigue cycles are directly proportional to the *TI*.

Figure 2-3. Wind speed measurement instruments. Left; cup anemometer (image from [43]). Right; LIDAR (image from [44]).

2.1.5.2 Wind Probability Distribution

Due to the stochastic nature of the wind, the wind climate at a given site is characterised by a distribution of mean wind speeds and directions. The direction distribution may follow features of the local geography, and is derived from empirical measurements. The ten minute mean wind speed distribution can typically be fitted to the two-parameter Weibull probability density function [45], given by,

$$P(x) = \frac{k}{C}\left(\frac{x}{C}\right)^{k-1} e^{-\left(\frac{x}{C}\right)^{k}} \tag{2-7}$$

where k is known as the shape parameter, C is the scale parameter, and x and P(x) are the measured quantity and probability of occurrence, respectively. In order to estimate the model parameters from measured data a suitable fitting technique must be used, such as the Maximum Likelihood Method [46], and an example of a fitted wind speed distribution is shown in Figure 2-4.

A typical pre-construction measurement campaign may last for only two years, due to time constraints for a wind farm project and the significant financial investment required to install and to maintain a MM in the offshore environment. Annual variations are commonly found in site specific wind distributions, and therefore it is desirable to derive a site characterisation from as long a dataset as possible. The measure-correlate-predict method is a pragmatic approach to this problem, as the relationship between short term site specific measurements and long term datasets from the nearest measuring station can be used to quantify the long term distribution of wind speed and direction [47].

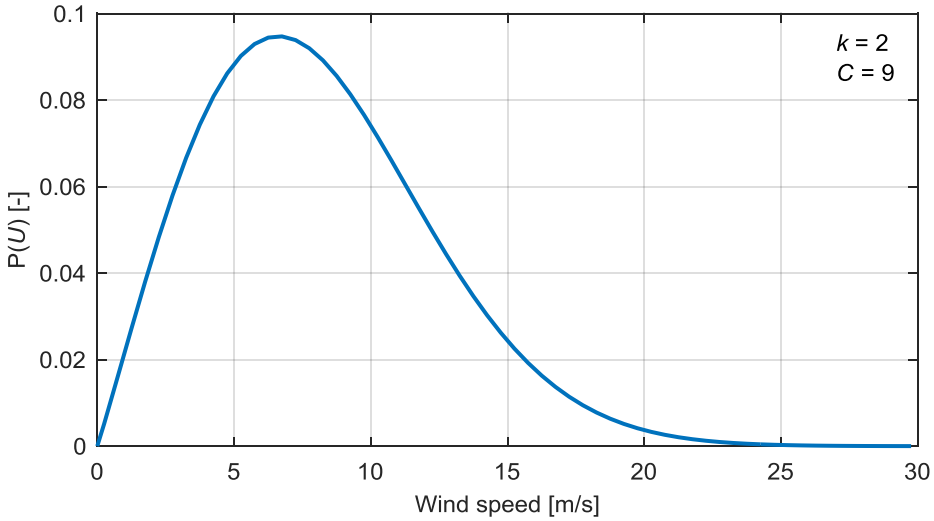

Figure 2-4. Example of the Weibull probability density function with shape parameter *k* = 2, scale parameter *C* = 9.

2.1.5.3 Turbulence spectrum

The design simulations used to model the wind turbine responses as outlined in Section 2.1.4 require the characteristics of the wind loading to be representative of reality. For the

purposes of design, three dimensional turbulent wind time series are generated to enable the aerodynamic loading on the wind turbine to be simulated. A suitable turbulence model is the Kaimal spectrum [48], which relates well to empirical measurements of atmospheric turbulence [49], and is defined by,

$$S(f) = {\sigma_U}^2 \frac{4\,L_k/U}{(1 + 6fL_k/U)^{5/3}} \tag{2-8}$$

Where $S(f)$ is the power spectral density, f is the frequency in Hertz, and L_k is the average length scale of the longitudinal component turbulent eddies (known as the integral length scale). This can produce the single-sided amplitude spectrum,

$$U(f) = \sqrt{2S(f)df}, \qquad f > 0 \tag{2-9}$$

where df is the frequency interval. An example of the Kaimal spectrum in shown in Figure 2-5.

The amplitude spectrum is converted to the time domain using Inverse Fast Fourier Transform (IFFT), and with the addition of the mean wind speed produces the synthetic single point wind time series,

$$U(t) = \overline{U} + \sum_{i=1}^{N} U(f_i)\cos(2\pi f_i t + \varphi_i) \tag{2-10}$$

where φ is a random phase shift, t is time, and N is the total number of frequency bins used.

In order to apply site specific levels of turbulence to the model, the simulated wind time series is defined in dimensionless form by, [33]

$$\delta = \frac{(U - \overline{U})}{TI.\overline{U}} \tag{2-11}$$

The dimensionless wind speed variations can then be used with a range of mean wind speeds and turbulence intensities using, [33]

$$U = \overline{U} + TI.\overline{U}\delta \tag{2-12}$$

Account can also be made for the effects of wind shear, tower shadow, and upwind wake effects on the time series.

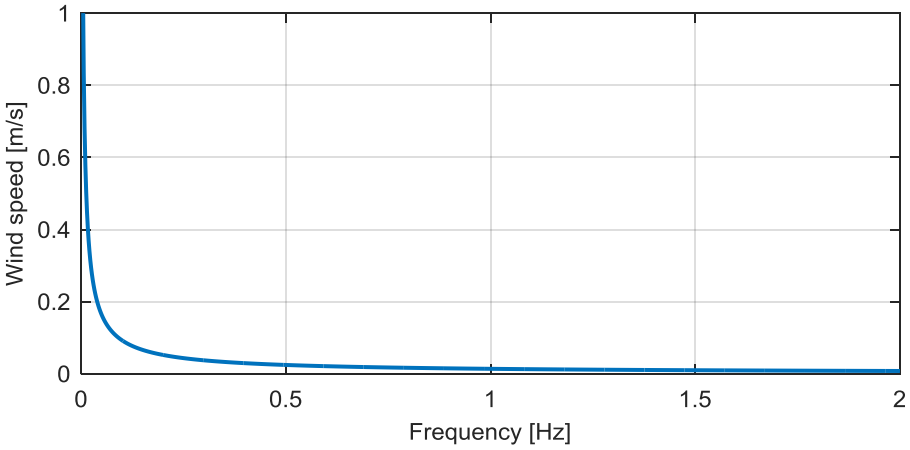

Figure 2-5. Example of the Kaimal wind speed amplitude spectrum.

2.1.6 Wave Loads

Similar to the definition of the wind turbulence, the wave loading distribution is described by a probability distribution in the frequency domain. The JONSWAP spectrum (Joint North Sea Wave Project) [50] gives a good representation of the characteristics of wind-driven seas [35], and is defined by, [51]

$$S(f) = \alpha {H_s}^2 T_p \left(\frac{f}{f_p}\right)^{-5} e^{\left\{-1.25\left(\frac{f}{f_p}\right)^{-4}\right\}} \gamma^{\beta}$$

$$\alpha = \frac{0.0624}{0.230 + 0.336\gamma - \frac{0.185}{1.9 + \gamma}} \tag{2-13}$$

$$\beta = e^{\left\{-0.5\left(\frac{\frac{f}{f_p}-1}{\sigma}\right)^2\right\}}, \quad \begin{cases} \sigma = 0.07 \text{ for } f \leq f_p \\ \sigma = 0.09 \text{ for } f > f_p \end{cases}$$

Where H_s is the significant wave height of the sea spectrum, T_p is the peak energy period, and f_p is the corresponding peak energy frequency. The average value for the peak shape parameter from experimental data is $\gamma = 3.3$, while the spectrum reduces to the Pierson-Moskowitz spectrum [52] where $\gamma = 1$ [35]. An example spectrum is shown in Figure 2-6 below. A time series of wave heights can then be generated from Equation (2-13) similar to the methodology in Section 2.1.5.3.

With the time series of random sea surface elevations defined with site specific values of H_s and T_p, the forces acting on the wind turbine support structure are calculated using the so-called Morison equation [53], which has been found to give a very accurate comparison to scale model test results [35]. The Morison equation is given by,

$$F = \rho C_m A\dot{v} + \frac{1}{2}\rho C_d D v|v| \tag{2-14}$$

where F is the force acting on the structure, ρ is the water density, v is the water velocity vector aligned with the force direction, A and D are the cross sectional area and diameter of the structure, respectively, and C_m and C_d are the inertia and drag coefficients, respectively. In order to integrate the force over the submerged length of the structure, a suitable wave theory is used to define the water particle kinematics. Suitable wave theories are given in [35], the selection of which is dependent upon the wave height, period, and water depths. As with the calculation of aerodynamic loads from Equation (2-2), Equation (2-14) provides a simplified representation of the hydrodynamic loading, allowing efficient implementation in design software.

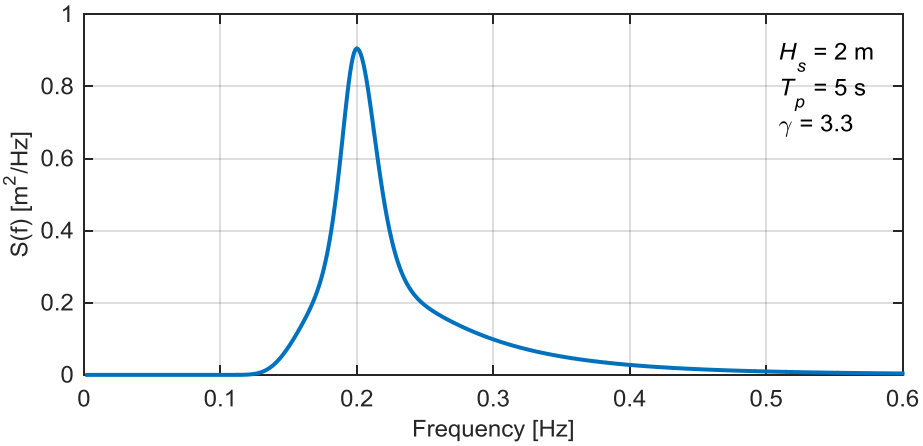

Figure 2-6. Example JONSWAP wave power spectral density plot.

2.2 Fatigue Life

2.2.1 Fatigue Loading in Offshore Wind Turbines

Most dynamically loaded structural components are subjected to variable amplitude cyclic stresses which can result in material damage which is typified by crack propagation in metallic materials. In the presence of a sea water environment, both corrosion and

mechanical fatigue can contribute to an increased rate of fatigue damage [54]. Due to the large number of stress cycles experienced by OWTs over their assumed 20 to 25 year operating life, they are considered to be fatigue critical structures in that the structural design and dimensions may be dictated by the fatigue life, rather than the maximum loading experienced in extreme conditions [55].

Early utility scale wind turbines were designed with little detailed understanding of the dynamic loading that their structures experience [56]. With significant research in testing and field measurement of operational turbines, and later with the development of time domain computer models, the spectrum of load cycles experienced by wind turbines can be tailored to the loading regime at a given site. However, due to the sensitivity of design methods used to quantify fatigue damage, as outlined below, large variations may be expected in calculated fatigue life [56].

2.2.2 Fatigue Design

The Palmgren-Miner linear damage hypothesis [57] [58] is among the most simplistic methods to quantify fatigue life under variable amplitude loading, and is based on the assumption that the fatigue damage in a component can be calculated as the sum of that identified at each stress level,

$$D = \sum_{i=1}^{k} \frac{n_i}{N_i} \tag{2-15}$$

where D is the fatigue damage fraction, k is the number of stress range bins used for the analysis, n_i is the number of cycles experienced by the component at each stress level, and N_i is the maximum number of cycles to failure at the corresponding stress range, as determined from material and component testing. Fatigue failure is assumed to occur at $D = 1$, and therefore damage values in the range of $0<D<1$ are required to ensure a safe design. Fatigue life can then be calculated by T/D, where T is the time period over which the fatigue damage is expected to occur.

Component testing produces S-N data (stress range compared to number of cycles to failure) which has been found to be well described by the Basquin relation, [55]

$$\log N = \log \bar{a} - \log \Delta\sigma^m \tag{2-16}$$

where $\Delta\sigma$ is the cyclic stress range, m is the Wöhler exponent which defines the gradient of the S-N curve, and $\log \bar{a}$ is the intercept of the curve on the $\log N$ axis. S-N curves for steel

components typically have a Wöhler exponent in the range of $m = 3$ to $m = 4$ [59], and example curves taken from [55] are shown in Figure 2-7 below, where the additional effects of corrosion fatigue on maximum number of cycles can be seen for the sea water environment. However, as empirical S-N data is difficult to obtain for fatigue in corrosive environments due to the time scales involved, fatigue endurance is typically taken as a factor of three reduction in the number of cycles derived from in-air testing, based on findings presented in [60].

Additionally, Figure 2-7 shows a double gradient for the 'in-air' and 'sea water with cathodic protection' environment curves, highlighting the lower contribution of lower amplitude stress cycles to total fatigue damage.

By combining Equations (2-15) and (2-16) for a single gradient curve, the fatigue damage can be written as,

$$D = \bar{a}^{-1} \sum_{i=1}^{k} n_i \Delta\sigma_i{}^m \tag{2-17}$$

Equation (2-17) can be used to relate the damage fraction produced by a spectrum of cycles to an equivalent value, termed the Damage Equivalent Stress (DES),

$$DES = \left[\frac{\sum_{i=1}^{k} n_i \Delta\sigma_i{}^m}{N_{ref}} \right]^{1/m} \tag{2-18}$$

where N_{ref} is a reference number of cycles, such as $N_{ref} = 10^7$, at which a stress range DES would produce the same damage fraction. As the S-N constant $\bar{a}$ cancels, Equation (2-18) is useful to compare the results of two different fatigue calculations, for instance results produced by the turbine and foundation designers, or between design and measured fatigue loads. However, it should be noted that Equation (2-18) essentially provides a linearised comparison of fatigue damage; i.e. the relationship between a comparison of damage fractions from Equation (2-17) and DES values from Equation (2-18) is given by,

$$\frac{D_A}{D_B} = \left(\frac{DES_A}{DES_B} \right)^m \tag{2-19}$$

where the subscripts *A* and *B* refer to two different cycle spectra.

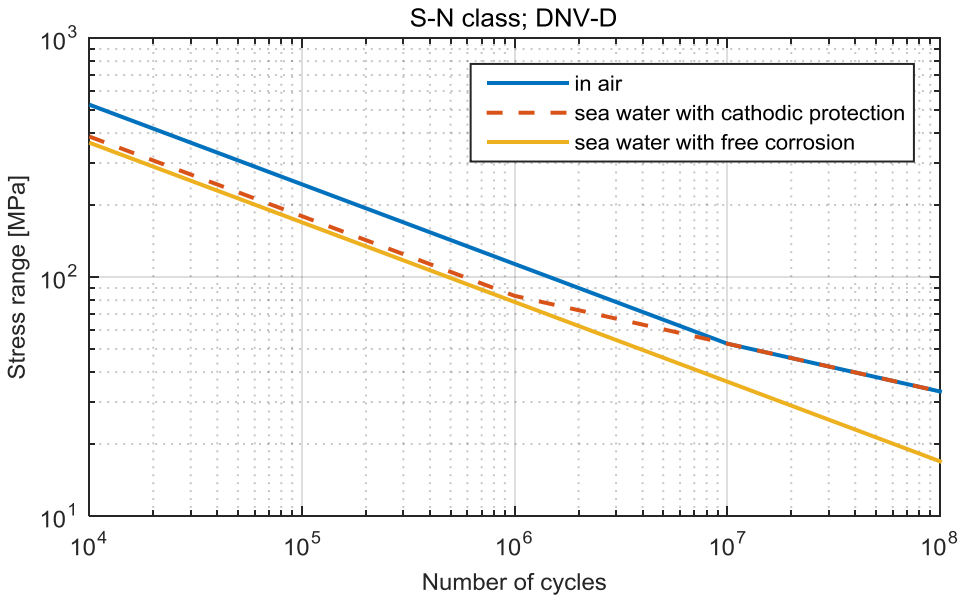

Figure 2-7. D-class S-N curves for transverse splice welds in air and sea water environments. The in-air and cathodic protection curves show a change of gradient from *m* = 3 to *m* = 5 at 10^6 and 10^7 cycles, respectively. From [55].

2.2.3 Rainflow Counting

The identification of individual fatigue loading cycles within a random stress amplitude time series is achieved through the use of a suitable cycle counting algorithm. Typical methods include level-crossing counting, range-pair counting, reservoir counting, and Rainflow counting. Variations of these algorithms are included in the ASTM cycle counting standard [61].

2.2.3.1 Background to the Rainflow Counting Algorithm

Rainflow (RF) counting has become the most widely accepted method for the processing of random signals for fatigue analysis, and testing has demonstrated good agreement with measured fatigue lives when compared to other counting algorithms [62]. The concept was first developed by Matsuishi and Endo [63], where the identification of cycles was likened to the path taken by rain running down a pagoda roof. In the paper, the authors defined a full RF cycle as a stress range formed by two points which are bounded within adjacent points of higher and lower magnitude; as the stress path returns past the first turning point it can be seen to form a cycle as described by a closed stress-strain hysteresis loop (Figure 2-8a). For the case where successive stress points are either converging or diverging, the hysteresis

curves do not form a closed loop (Figure 2-8b). For this case the authors assumed that fatigue damage could be attributed to each successive range as half-cycles.

The RF counting method was further developed by Okamura et al. [64] and Downing & Socie [65] as a vector based algorithm which identified full RF cycles and half-cycles based on a three-point criteria without the need to rearrange the data series, and enabled efficient utilisation in computer software. This greatly reduced the data storage requirements as the stress signal could be read into the algorithm in real-time and processed directly into RF cycle spectra. This definition of the algorithm has been refined and included in the ASTM cycle counting standard [61]. Amzallag et al. [66] conducted a wide ranging industry consultation and defined a standardised algorithm which identified RF cycles based on a four-point criterion. The three and four point versions of the algorithm were shown to identify the same cycles by McInnes & Meehan [67], who presented a series of fundamental properties of RF counting to demonstrate the equivalence of the two methods. Although various forms of the RF algorithm exist, the four-point algorithm presents the most unambiguous criterion for the identification of closed hysteresis loops, and is defined below.

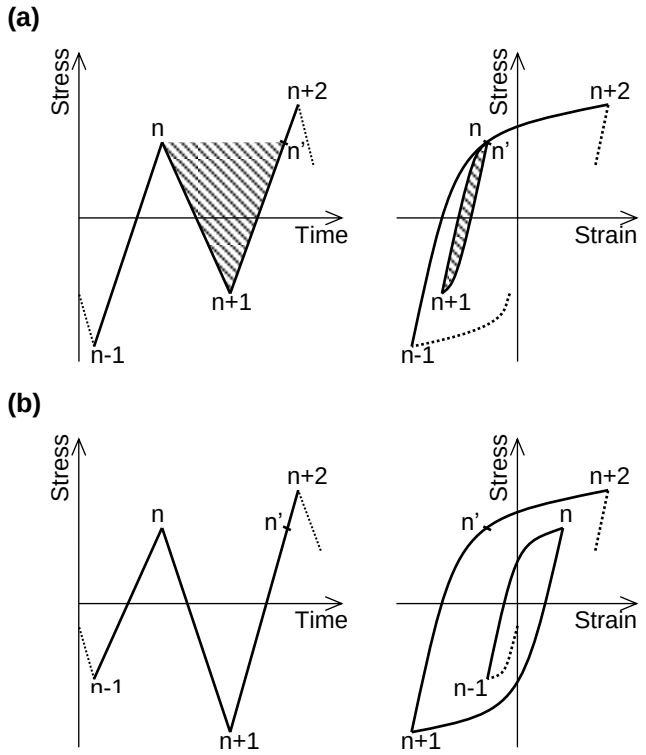

Figure 2-8. Example stress-strain hysteresis curves. (a) Stress time series of turning points and the corresponding closed stress-strain hysteresis loop formed by points n, n+1 and n'. (b) Diverging stress time series and the corresponding open stress-strain hysteresis curves.

2.2.3.2 Four-point Rainflow Counting Criterion

RF counting requires the time history to be first processed into a Peak-Valley (PV) series consisting of local maxima and minima which define the turning points, or load reversals, of a time series. Point x_m is identified as a local maxima or minima within a time series of length *M* if,

$$x_{m-1} < x_m > x_{m+1} \; or \; x_{m-1} > x_m < x_{m+1}$$
$$m = 2, 3, 4, \dots, M-1 \tag{2-20}$$

Once the data have been filtered according to the PV criteria, full RF cycles are identified in the range formed by points x_n to x_{n+1} if they meet the four-point criterion,

$$|x_{n-1} - x_n| \geq |x_n - x_{n+1}| \leq |x_{n+1} - x_{n+2}|$$
$$n = 2, 3, 4, \dots, N-2 \tag{2-21}$$

where *N* signifies the length of the PV filtered series. If the range formed by points x_n to x_{n+1} meets the four-point criterion then the points are recorded before deleting them from the PV series, thus enabling further ranges to be formed between the adjacent points x_{n-1} and x_{n+2}. The process is repeated until all ranges which meet the four-point criterion are recorded and deleted from the PV series.

Storage of the counted ranges is achieved with a two dimensional histogram to record the cycle stresses. The form of the histogram may be chosen to preserve detailed cycle hysteresis information which may be significant in further statistical analysis, for example with the min-max or max-min matrices where cycles are binned according to the loading sequence [68]. As a minimum, the histogram should record the cycle range and mean stress levels as inputs to final damage calculations.

2.2.3.3 Rainflow Residue

Once all full RF cycles which meet the four-point criterion have been identified and deleted from the PV series, a 'residue' of data points will typically remain. The residue consists of a series of diverging data points from the start to the maximum and minimum points, followed by a converging section of points to the end of the PV data series. Referring to Figure 2-9, no remaining closed hysteresis cycles can be identified within a diverging or converging series as no further ranges are bounded by adjacent points of higher and lower value. However, as the stress path formed by the residue constitutes some of the largest ranges in the original

series, they should be accounted for if a conservative estimate of fatigue damage is to be made. Two dominant methods exist in the literature to process the RF residue and are outlined in Sections 2.2.3.4.1 and 2.2.3.4.2.

Whenever a subset of a longer time history is RF counted, cycle ranges which are formed between points which span beyond the subset have the potential to be cropped. If there is a large variation in the mean stress level, which is not fully contained within the subset period, then some of the largest cycles will not be accounted for. These cycles are termed ‘transition cycles’ or ‘ground cycles’ [56], and a degree of artificiality will be introduced if the residue data points are processed as an isolated set, as closed hysteresis cycles cannot be formed. The only way to accurately identify all RF cycles within a data set according to the four-point criterion is to process the entire time history consecutively. However, the application of RF counting algorithms must always utilise a finite length of data, as chosen by the analyst and by limitations on computational capacity.

Glinka & Kam [69] presented an approach which allowed extended time periods to be read and processed incrementally, thus limiting the required computational capacity by minimising the amount of data required to be handled by the RF algorithm at any one time. A more versatile method is included in Amzallag et al. [66, pp. 292-293] which addresses the same issue by concatenating consecutive residue periods which remain after RF processing. However, although the method allows transition cycles to be accounted for accurately according the four-point criterion, it has not found widespread acknowledgement. An analytical proof was presented by Marsh et al. [70] demonstrating the equivalence of cycles which are identified from the residue concatenation methodology outlined in [66] with those which would be identified by RF processing a continuous series.

The three methods of processing the RF residue periods are presented in Section 2.2.3.4 below.

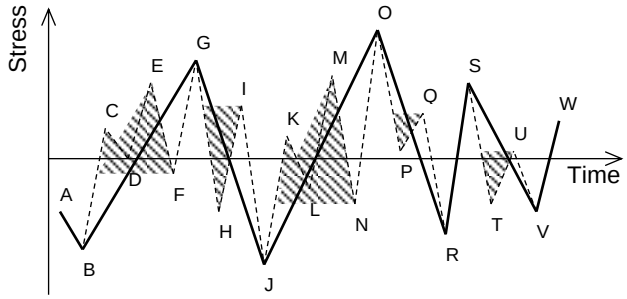

Figure 2-9. Residue remaining after application of the four-point criterion (points connected by solid line). Full RF cycles would be identified between points *C-D*, *E-F*, *H-I*, *K-L*, *M-N*, *P-Q*, *T-U*.

2.2.3.4 RF residue processing methodologies

The three distinct methods available for processing the residue data points are described below and presented in the process diagram in Figure 2-10.

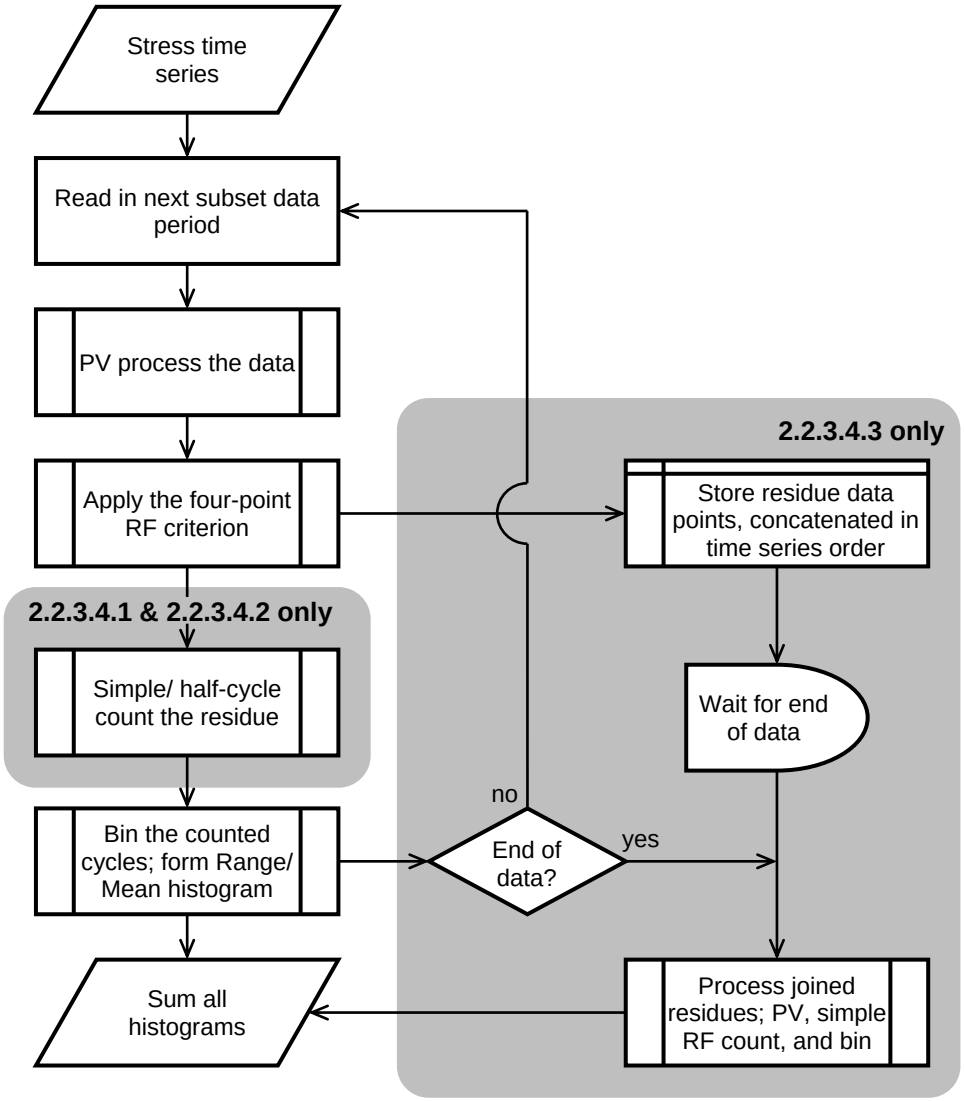

Figure 2-10. RF counting process diagram for long time periods (modified from [71]). Grey boxes identify steps which relate to the residue processing methods outlined in Sections 2.2.3.4.1, 2.2.3.4.2, 2.2.3.4.3 below.

2.2.3.4.1 Half-cycle Counting Methodology

This approach is identified in the original definition of RF counting given by Matsuishi & Endo [63], where the authors assumed that each successive range will attribute half a cycle of fatigue damage in the material. From Figure 2-9, subsequent half-cycle ranges are identified between points *A-B*, *B-G*, *G-J*, *J-O*, *O-R*, *R-S*, *S-V*, *V-W*. At least twice as many ranges will be identified from the residue data points as would be identified as fully closed cycles. Therefore, when the counted residue cycles are stored in the RF histogram the

number of cycles added to each bin is reduced by a factor of 0.5. The ASTM RF counting definition of the three-point algorithm [61, pp. 5-6] is capable of identifying half-cycles which occur up to the maximum data point in the series; after completion of the algorithm, the residue data points following the maximum still remain and must be accounted for as half cycles. Half-cycle counting may be applied directly to the residue which remains from application of the four-point RF criterion, and the resulting cycles can be shown to be identical to those produced by the three-point algorithm.

2.2.3.4.2 Simple Rainflow Counting Methodology

If the stress time history is representative of a repeated loading sequence then all residue data points will ultimately form fully closed cycles as they will fall between repeated extremes. With the four-point algorithm this can be achieved by joining two repeated residues and then reapplying the four-point criterion (Equation (2-21)). Closed cycles can then be identified between the repeated maximums, leaving the residue points outside of the maximums which can then be discarded. This is expressed as [*residue*] + [*residue*] → [*residue*] + {*cycles*} [66].

From Figure 2-9, the residue series is repeated to give a sequence *A-B-G-J-O-R-S-V-W-A-B-G-J-O-R-S-V-W*. Equation (2-20) is then reapplied and the repeated point *A* must be deleted to ensure that the PV sequence is maintained. Equation (2-21) is then reapplied to identify closed cycles from all points that fall between *J* and repeated point *O*; ranges are formed by points *V-W, R-S, B-G, J-O*. The remaining points account for the repeated residue, and are therefore discarded.

The simple RF counting methodology is implemented in the three-point algorithm by rearranging the stress time series to start and end with the maximum data point prior to PV processing and RF counting, and will identify identical cycles [67]. Therefore, the approaches implemented in [61, pp. 6-7], [65, p. 32], [66] and [67] are equivalent.

2.2.3.4.3 Residue Concatenation Methodology

The following steps apply the residue concatenation procedure outlined in [66, pp. 292-293] to the simple case of two PV periods, with reference to Figure 2-11:

1. Define two series of PV processed data points A_1, B_1, C_1,…, H_1 and A_2, B_2, C_2,…, H_2.
2. Apply the four-point criterion, Equation (2-21), to both series to identify all full RF cycles. Full cycles are identified between points D_1-E_1, and E_2-F_2 (Figure 2-11a).

3. Store the cycles and delete the identified data points D_1, E_1 and E_2, F_2 from the respective PV series (Figure 2-11b). No more full RF cycles can be identified according to Equation (2-21). The remaining points form the two RF residues.
4. Concatenate the two residues in their original chronological order. Apply the PV criteria to the concatenated points H_1 and A_2 to ensure the PV series is maintained; delete point H1 (Figure 2-11c).
5. Repeatedly apply the four-point criterion to the concatenated series until all fully closed RF cycles have been stored and removed from the concatenated series.
6. The remaining residue points must be processed by either half-cycle or simple RF counting. In practice, successive residue periods may be concatenated to allow additional closed hysteresis cycles to be unlocked.

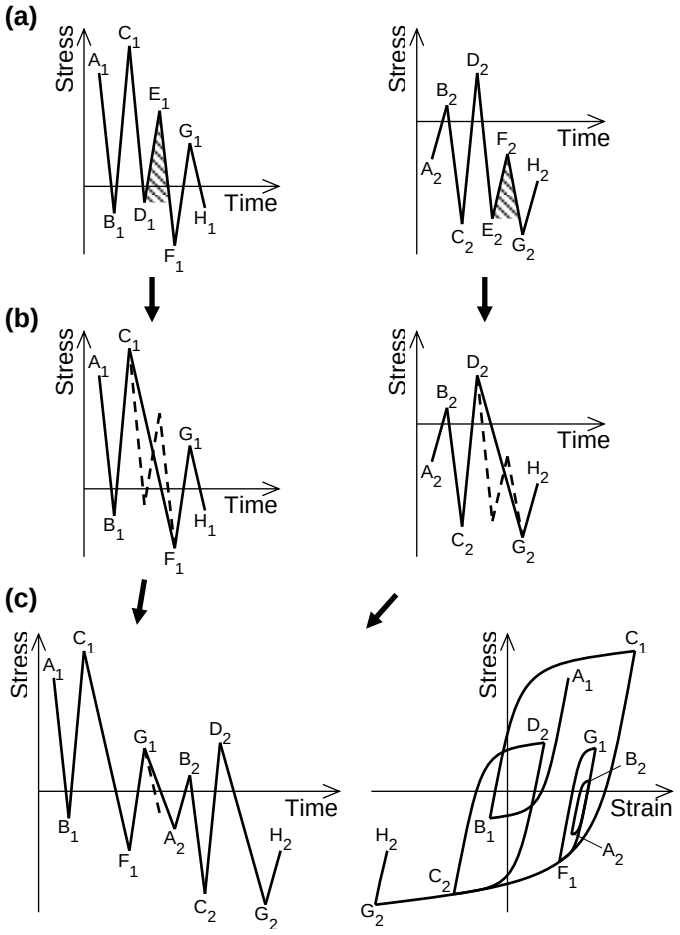

Figure 2-11. Concatenation of RF residues. (a) Two separate PV series. (b) The residue series from which no further fully closed RF cycles can be identified. (c) Concatenation of the two RF residue series in stress-time and stress-strain space.

2.2.3.5 Transition Cycles

The stress cycle histogram from a modelled or measured wind turbine typically come from individual ten minute periods of load data, the assumption being that the short time history is representative of mean loading conditions (wind speed and direction bins, operational state, etc.) which will occur repeatedly throughout the operational life. Typically, the short time periods used are RF counted independently of each other [56], using one of the processing methodologies outlined in Sections 2.2.3.4.1 and 2.2.3.4.2, and therefore the stress cycles which arise from transitions between each ten minute period are not accounted for. However, although industry design standards do not make specific mention of transition cycles, all cycles which contribute to fatigue are required to be taken into account [8], [20], [27].

Larsen and Thomsen [72] presented an approach to quantify the effect of transition cycles on the fatigue load spectrum of wind turbine blades. The approach made use of a one year time history of ten minute average values of wind speeds from which the transitions between operating conditions could be identified. Assuming that the wind history was representative of the wind variations that occur in other years, a synthetic stress history was constructed using the maximum and minimum stress of the LC relating to each ten minute wind speed value in chronological order. The synthetic stress history was then RF counted, presumably using one of the methods outlined in Sections 2.2.3.4.1 and 2.2.3.4.2 above. From a case study example on a 150 kW scale wind turbine blade, using simulated loads from an aeroelastic model, the authors found that the inclusion of transition cycles accounted for in this way contributed an additional 3% to 60% fatigue damage using Wöhler exponents of $m = 3$ and 12, respectively (the higher value relating to fibre glass composite blade material), to the fatigue damage produced by RF counting ten minute LCs as independent periods. However, the methodology presented by Larsen and Thomsen effectively double counts cycles which are accounted for as both half-cycles in independent LC periods and as data points within the synthetic one year stress history. Additionally, other cycles which span individual data periods are not accounted for correctly according to the four-point RF counting criterion [70].

Mouzakis and Morfiadakis [73] conducted a similar study using results of a load measurement campaign from a 500 kW stall regulated wind turbine, and unlike the study conducted by Larsen and Thomsen, the authors included analysis of loading on the wind turbine tower. The authors also used a one year synthetic stress series following the methodology outlined in [72], but conducted an additional study whereby the RF residue from each ten minute period was not included as an independent sequence, but was

concatenated in sequence to account for transitional cycles correctly. The two methods to assess the impact of transition cycles are similar, but the residue concatenation methodology does not produce the double counting of stress cycles which result from the method presented by Larsen and Thomsen. From measurments of the tower base bending moment, the authors found that transition cycles contributed an additional 3% to the fatigue damage value produced by RF counting the data in independent ten minute series, using a Wöhler exponent of $m = 4$. However, the authors used a wind speed time history of ten minute average values to construct the synthetic stress history, and therefore, as with the methodology employed by Larsen and Thomsen, did not account for the stress cycles which would arise in the tower due to changes in wind direction. Additionally, the authors investigated the effect of transition cycles directly from time history measurements of stresses, using datasets of six to seven days in length, and found that accounting for transition cycles in the correct manner reduced the calculated fatigue life for the tower bending moment by a factor of approximately 12%, using $m = 4$.

Sutherland [56] has written explicitly about the significance of transition cycles, and presents a review of research articles which address the issue for wind turbines. From a review of operational measurements and analytical studies on the significance of transition cycles, the author states that the contribution to fatigue damage is negligible for materials with low Wöhler exponents. The author notes that, as transition cycles do exist, they should be accounted for in the fatigue predictions if the analysis is practicable, but concludes that they may be ignored from the assessment in most applications.

However, Marsh et al. [70] presented a sensitivity analysis using data from a multi-megawatt offshore wind turbine support structure, and found that RF processing a one year time history of stresses in independent ten minute periods accounted for only 37% to 43% of the damage produced by RF processing the data as a continuous series using the methodology outlined in Section 2.2.3.4.3, using $m = 5$. The difference was insignificant using a lower Wöhler exponent of $m = 3$. The authors compared the results from the wind turbine support structure with a similar dataset from an offshore measurement buoy, and concluded that the impact of transition cycles is dependent upon the underlying load process, the length of data subsets used to process independent sequences, and the Wöhler exponent used.

2.3 Load Measurement

2.3.1 Measured Quantities

The operational behaviour of an OWT may be of interest to wind farm operators to enable design calculations to be verified or challenged. While periodic inspections and routine maintenance are useful to assess the condition of OWT structures, it is not practicable to inspect every weld on all turbines in a wind farm due to the logistical difficulty and sheer volumes that are typically involved.

While the turbines themselves will normally include a standard level of instrumentation to provide operators with information on quantities like particle counts in gearbox oil, bearing temperatures, and nacelle vibrations and accelerations [74], little additional information is typically collected on the response of the support structures themselves. In order to derive an understanding of the level of fatigue loading it is necessary to measure either displacements of the support structure, from which stresses can be derived from either beam bending theory or from finite element modelling, or measurement of local strains which can be converted into stresses using the elastic modulus of the base material.

2.3.2 Measurement Issues

2.3.2.1 Measurement Constraints

An ideal measurement system would provide knowledge of the load and response condition of the entire structure, enabling the analyst to determine stresses at any location. This is desirable as the fatigue critical location on the structure may be inaccessible for direct inspection, such as below the sea bed, and multiple locations on multiple turbines may be of interest. Additionally, inspection will not always enable the consumed fatigue life to be determined.

Accelerometers may provide the ability to extrapolate measurements in this way if they are installed at multiple heights on the structure. Displacements can be calculated from accelerometer measurements through double integration with time, however, a large range of uncertainty will result without accurate knowledge of the initial velocity and displacement of the entire structure. Photogrammetry offers the potential to obtain displacement measurements at all parts of the structure with a very high degree of accuracy [75] using high resolution cameras and image processing techniques, but may be most applicable to onshore turbines due to the necessity for multiple cameras to be mounted on stable locations within several hundred meters of the target. Additionally, due to the large amount of

information recorded and the necessary computer processing power, photogrammetry may not be a feasible method for long measurement campaigns.

Local strain gauge measurement gives the potential for the highest accuracy in the assessment of stresses, and if collected at multiple levels it is possible to derive the global response of the support structure. However, structural discontinuities such as flange connections or welded details result in stress raising effects which may cause uncertainties in the relationship between the local measurement and the global response. An optimum measurement system may therefore involve a combination of accelerometer and strain measurements at multiple locations in order to offset the uncertainties and constraints of both approaches [37], [76].

2.3.2.2 Data noise

No sensor can provide perfect data about the system of interest, and desired quantities, such as strain, must be derived indirectly from an understanding of the functional relationship with measureable quantities (such as strain gauge voltage output). Sensors and measurement systems are almost always noise corrupted to a certain extent [77].

Noise is an apparently random variation in a sensor's output which is unrelated to the measured quantity of interest. In order for measured data to provide useful information about a system the magnitude of the noise must be of an acceptable level when compared to the underlying signal. This leads to the definition of the signal-noise ratio (SNR),

$$SNR = \frac{S_{RMS}}{N_{RMS}} \tag{2-22}$$

where S_{RMS} and N_{RMS} are the root-mean-squared values of the underlying signal and noise, respectively. High quality data requires the SNR to be high so that the underlying signal is not buried in the noise. For instance, fatigue calculations from measured strain gauge data would be distorted by excess noise, as the amplitude of the underlying stress cycles would be extended, and an artificially high number of small amplitude stress cycles would be identified by the RF algorithm.

Noise in an electrical system can arise from the following sources, [77] [78]

- Thermal noise

  The temperature induced motion of charge carriers in resistors and semiconductors results in a random voltage known as Thermal, or Johnson, noise. The thermal noise r.m.s. voltage is given by,

$$V_{RMS} = \sqrt{4k_B TRB} \tag{2-23}$$

where k_B is the Boltzmann constant, T is temperature in Kelvin, R is electrical resistance in Ohms, and B is the bandwidth response in Hz. Thermal noise has the characteristics of white noise; i.e. it is random with a Gaussian distribution and uniform power over an infinite range of frequencies.

- Shot noise

  Also termed quantum noise, this noise source arises in transistors due to the quantum nature of charge carrier flow rates. The shot noise current r.m.s. is given by the relation,

$$I_{RMS} = \sqrt{2qI_{DC}B} \tag{2-24}$$

  where q is the electron charge, I_{DC} is the DC current across the instrument, and B is the bandwidth response in Hz. Due to the random nature of its origins, shot noise also has the characteristics of white noise.

- Flicker noise

  The origins of Flicker noise are material/component dependant, but the result is long term drift in all instruments. Flicker noise is also known as 1/f noise, or pink noise, because most of the power is towards the low frequency side of the spectrum. The inverse frequency dependency of Flicker noise means that it can be difficult to identify and remove from a data set.

- Interference noise

  Common sources are nearby AC power circuits which can produce inductive or capacitive coupling effects. AC fields typically induce noise at the same frequency and higher harmonics (e.g. 50 Hz and higher multiples).

Thermal and Shot noise sources have the characteristics of white noise, which is defined as being random (un-correlated in time), with uniform power over all frequencies and a Gaussian distribution. Therefore, as indicated by Equations (2-23) and (2-24), white noise can be reduced by limiting the system bandwidth using a low-pass filter. Suitable examples include the Butterworth filter [79] and the Bessel-Thomson filter [80].

Gauge drift correction may be more challenging, and can be dependent upon the cause of the drift. In the case of strain gauge instrumentation, gauge drift can arise from several possible sources.

- Temperature variations and subsequent effects on gauge circuit resistances can have a large impact on apparent strain [81]. Temperature compensation can be used to correct temperature induced strains with the use of additional thermocouple measurements, and therefore diurnal temperature variations which may typically arise due to solar heating and tide level may be accounted for. However, long term drift in the thermocouple calibration will therefore also result in drift in the corrected strain values.
- Power supply variations or faulty ground connections can cause electronics and balanced circuit resistances to drift. Periodic recalibration of the measurement system may be the best way to account for these effects.
- Stress relief of the installed gauges or curing/ageing of the gauge connection and protective coatings over time [82]. This may simply result in changes to the gauge datum offset level, or may be non-linear with the system gain. Again, periodic recalibration of the system may be used to account for these effects, along with assessment that the system continues to meet its' functional requirements. However, for remote structures such as OWTs, repeated site visits may prove impracticable.

3 Methodology

3.1 Measured Data

3.1.1 Site Characteristics

The wind farm on which the analyses is based may be considered to have typical structural design, distance to shore, and metocean conditions compared to other offshore wind farms of the same era. Turbine hub heights are approximately 80 m above Chart Datum (mCD), with sea bed depths in the range of approximately 0 mCD to -10 mCD, with a maximum tidal range of approximately 9 m. The wind turbine class, based on wind speed and turbulence levels, is IEC 1S (see Table 2-2). Wave conditions are reasonably low, with mean significant wave heights of less than 1 m.

3.1.2 Measured Load Data

Data was provided by third party sub-contractor who undertook design, installation, calibration, temperature correction, and provision of the data. This section describes the data analysis undertaken by the author.

3.1.2.1 Selection of Monitored Turbines

Turbine selection was initially based on the condition of the loaded stopper brackets above the grouted connection. Turbine K1 was selected as all six stopper brackets were in full contact with the top of the MP, and the turbine was located on the edge of the wind farm in the direction of the prevailing wind and wave loading. Turbine H4 was selected as the stopper brackets were only in contact with the top of the MP on the downwind side of the structure, while the location of the turbine within the wind farm meant that the structure was subjected to a combination of both turbulent wake and wave loading [83].

The strain measurements were essentially used as secondary data for investigation of the fatigue load response of the structures, as the primary purpose of the measurement system was to determine the behaviour of the grouted connection. In the ideal case, turbine selection would be based on specific analysis to identify the fatigue critical location across the wind farm [84]. It is reasonable to assume that the variables which drive fatigue loads are the wind and wave conditions; however, it is unlikely that the worst case turbulence and mean wave height would coincide at the same location. Therefore, a range of combined turbulence levels and wave heights across the site may be required to be investigated.

From metocean analysis conducted during the design stage in 2006 [85], Turbine K2 was determined as having the most severe wave climate. The analysis involved the propagation of wave spectral data from the UK Met Office Wave model across the wind farm site using wave transformation models for a range of projected worst case bathymetry scenarios. The analysis presented results at three discrete locations corresponding to Turbines E7, H2, and K1 (Figure 3-1 below), where K2 was identified as the location of most severe wave loading for fatigue.

Three discrete locations were used for the metocean analysis, and therefore the specific locations of Turbines H4 and K1 were included in the investigation. However, it is reasonable to assume that similar wave conditions would occur at Turbines K1 and K2 due to their close proximity (approximately 465 m separation). Additionally, Turbine K1 was found to have the deepest water depth across the wind farm, as identified in the 2009 bathymetry survey [86], and is the closest position in the wind farm aligned with the dominant wave direction from the South West [87]. Turbine K1 is therefore assumed to be representative of the maximum wave conditions in the wind farm.

It should also be noted that wave loading at Turbine H4, which is in close proximity to Turbines H2 and K2 (approximately 900 m and 970 m separation, respectively), was also of relatively high magnitude. Turbine location H4 was used to investigate the effect of increased turbulence loading resulting from the presence of trailing wakes, as described below.

Turbine H4 is located on the third row of turbines with respect to the prevailing wind direction, and should therefore be subjected to turbulent trailing wakes from each directional sector. Although from a design perspective it is not required to assess wake effects from wind turbines which are ‘hidden’ behind other turbines [21], the level of turbulence within the wind farm is expected to increase along the direction of prevailing wind as trailing wake structures generated by individual turbines break down into an additional level of ambient turbulence, ultimately converging at a maximum level. Also associated with the break-down of trailing wakes is the well-known wake deficit effect [88], whereby mean wind speeds diminish within a turbine array as energy is extracted by upwind turbines, and also converted into turbulence. Detail of the methodology used to investigate the distribution of turbulence throughout the wind farm using measured data is outlined in Section 3.1.3.1.1 below.

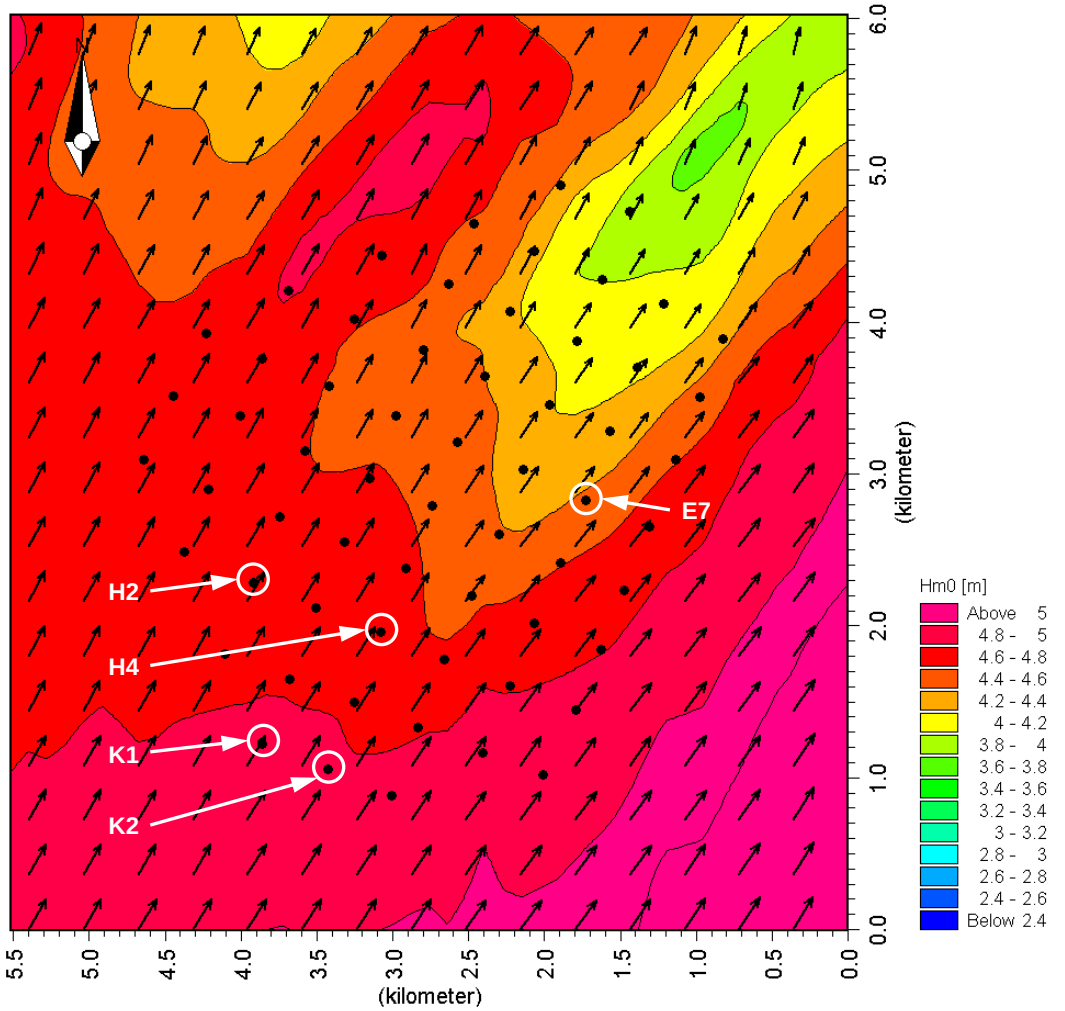

Figure 3-1. Graphic displaying the significant wave height and mean wave direction for a 1 in 50 year storm from 205° wind direction, for one bathymetry scenario produced by the design metocean study (reproduced from [85]). Turbine locations identified by black dots. Note that the dominant wave direction for fatigue was found to be from the 240° sector.

3.1.2.2 Instrumentation

The gauges used for this analysis were installed on the inside of the TP above the grouted connection and the loaded stopper brackets, with the general location shown in Figure 3-2 below. The data acquisition system, consisting of a PC, AC/DC converter, modem and power supply, was located separately on the upper working deck. Six gauges were used to measure the global axial strains on Turbine K1, labelled according to the position above the

stopper brackets (S1-SGAV to S6-SGAV). Only four global gauges were used on Turbine H4 (labelled S1-SGAV, S3-SGAV, S5_SGAV, S6-SGAV).

The global gauges were installed above the top of the existing stopper brackets to measure strains remote from the stress raising effects of the brackets and grouted connection, at 6.608 mCD. The global gauges consisted of spot-welded linear strain gauges, which were installed aligned in the vertical and horizontal directions to measure the nominal axial and hoop strains. Detail of the spot-welded strain gauges is shown in Figure 3-3. All strain gauge instrumentation was calibrated by the contractor post-installation using the shunt technique. Temperature compensation was also applied by the contractor to account for induced thermal strains using the thermocouple measurements prior to measurements being provided to the client.

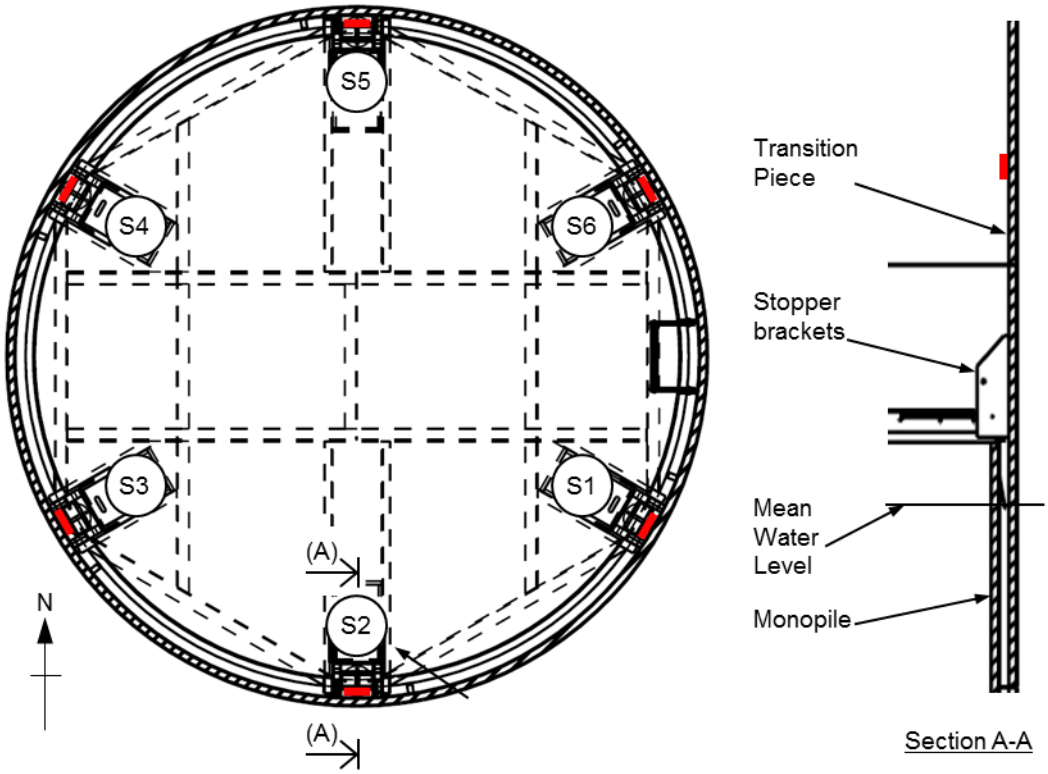

Figure 3-2. Schematic of Turbine K1 working platform, with layout of the global gauges (highlighted red) installed at 6.608 mCD on the inside of the TP. Stopper bracket numbering shown starting clockwise from South East. Turbine H4 global gauges were installed above stopper brackets S1, S3, S5, and S6 only. From [89].

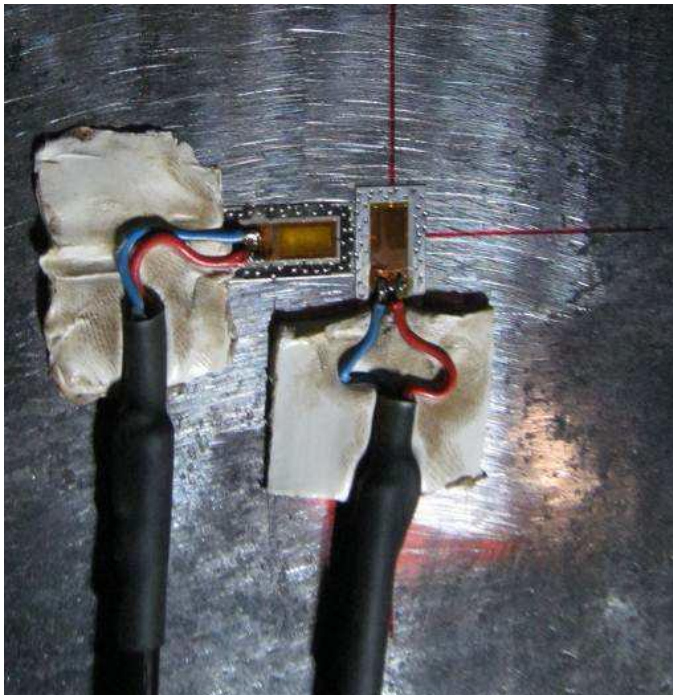

Figure 3-3. Global strain gauges installed at 1.058 m above the existing stopper brackets. From [90].

3.1.2.3 Gauge Positioning

The assumption that the position of the global gauges was far enough from the stress raising effects of the loaded stopper brackets and grouted connection was analysed using Abaqus finite element (FE) software [91]. The FE model used in this analysis was developed and provided by an external contractor, but the analysis was re-run to provide information about the stresses at the gauge locations over the full range of incremental loads which were expected to occur.

The FE model consisted of the TP primary steel with the connected stopper brackets, the grout connection, and the MP down to the level of the sea bed at -10.6 mCD, as shown in Figure 3-4. Half of the structure was modelled, with the cut plane specified with a fixed translational boundary condition in the normal direction. The bottom of the MP was fixed with a stationary boundary condition, and the MP/grout/TP interfaces were modelled with contact surfaces with a friction coefficient of 0.6 [92]. The TP and MP were modelled with shell elements, with four elements through the wall thickness. The stopper plates were modelled in contact with the top of the MP with a friction coefficient of 0.5. The turbine

tower was represented by a beam element connecting the top of the TP to the height of the nacelle, and the top node was used as the location of applied loads.

The loads were applied in two steps,

- Step 1: The vertical load representing the mass of the TP (primary and secondary steel), tower, and rotor nacelle assembly (RNA) was applied to the top node of the tower beam element in 25 increment steps to account for nonlinearities in the TP/grout/MP and stopper plate/MP interfaces.
- Step 2: Keeping the vertical load constant, the horizontal load representing the maximum bending moment from the design results was applied to the top node of the tower beam element in 25 load increments up to the maximum value. The maximum horizontal load applied at the top node was calculated to match the maximum design ULS sea bed bending moment, from [93]. The loads used are given in Table 3-1.

Outputs from the model were the stress components on the inside surface of the TP in a circumferential path at the height of the global gauges (6.608 mCD). As a half model was used for the FE analysis, it was only possible to apply loads parallel to the plane of symmetry. Therefore, the FE results could only provide information about the stress distribution at the location of the gauges with the structure under four applied horizontal loading directions (oriented at 0, 60, 120, and 180 degrees with respect to the gauge locations). However, in order to quantify the impact of any stress raising effects at the location of the gauges on calculated fatigue damage, a methodology was developed to enable the stress response to be interpolated to any loading direction, and is described in conjunction with the FE results in Section 4.1.2. This enabled the impact of the stress raising effects on the calculated fatigue damage to be analysed, and determined that by calculating the design stresses using simple Euler beam theory a conservative comparison would be made with the measured loading. Therefore, simple beam bending theory was used for the calculation of stresses from the simulated loads.

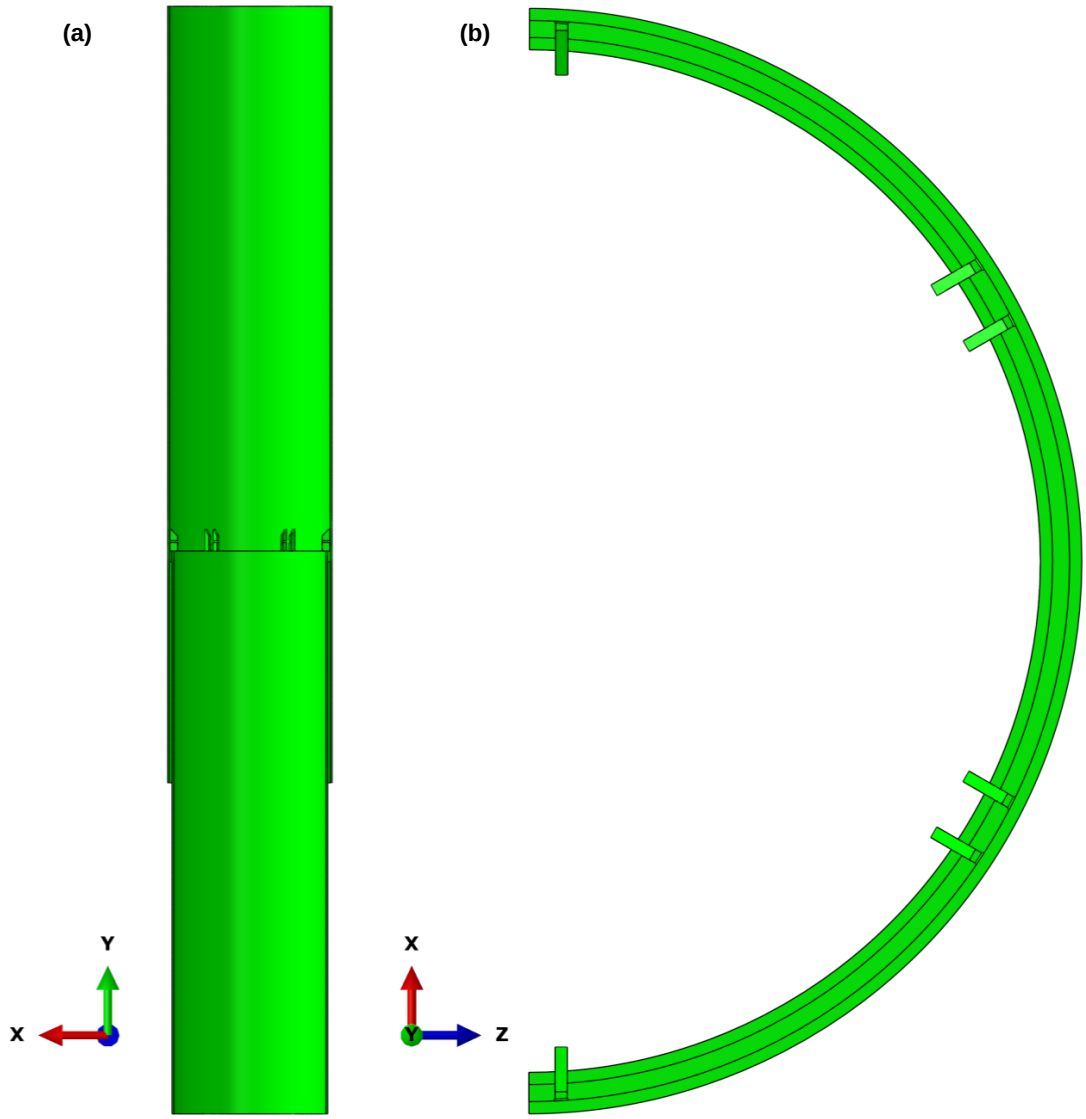

Figure 3-4. Outline of FE model used to analyse the stresses at the location of the global strain gauges. (a) Side view of the TP and MP modelled to the sea bed boundary condition (beam element representing the tower not shown). (b) Bottom view of the TP, grout connection and MP.

Table 3-1. Load values used with the FE model.

Maximum vertical load	Maximum horizontal load
-1,839.0 kN	502.7 kN

3.1.2.4 Data Description

The measurement systems on Turbines H4 and K1 were installed in August 2011 and data from the global gauges were collected over the period from 01/09/2011 to 31/03/2013, at a sample resolution of 20 Hz. The gauges were datum set to zero during an arbitrary period of low loading and with a stationary turbine rotor on 01/09/2011 at 06:30 [90], and therefore the data did not account for embedded strains due to structural self-weight and centre of gravity (CoG) offset of the RNA.

The data contained multiple periods of gaps and erroneous readings totalling approximately 13-15% of the coverage period. Erroneous readings were identified as either significant data spikes, flat-lining data periods, or missing values, and were deleted (Figure 3-5 below). Additionally, the strain data were found to contain periods of significant data noise which were identified and corrected as outlined in Sections 3.1.2.5 and 3.1.2.6 below. Prior to further processing, the strain measurements were converted to stress using,

$$\sigma = E\varepsilon \tag{3-1}$$

where E is the Elastic Modulus of the base material, equal to 210 GPa for S355 steel [94].

Figure 3-5. Ten minute average strain values, filtered to remove erroneous readings. (a) K1 global gauges S1-SGA to S6-SGA. (b) H4 global gauges S1-SGA, S3-SGA, S5-SGA, and S6-SGA.

3.1.2.5 White Noise Removal

The measurement systems installed on the turbines employed a low-pass filter to limit the measurement frequencies to 10 Hz [90]. However, noise was still found to be present in the measured data with significant increase after a period of 1-3 months from the date of commissioning. The level of noise was found to be constant with changes in the level of environmental loading, and had characteristics of white noise indicating that it was an artificial phenomenon and not a real, physical response of the structure.

Figure 3-6 shows a time series of noisy strain gauge data from a period of minimal environmental loading, together with a spectral representation of the signal produced by Fast Fourier Transform (FFT). A small amplitude response can be seen in the frequency domain at 0.33 Hz (close to the design 1st mode frequency) and at the far left of the spectrum, due to actual response of the structure to the minimal loading. A constant minimum level of energy of approximately 0.03 MPa is also present across all frequencies; this is indicative of white noise rather than real physical response of the structure. The noise is overlaid on top of the underlying signal, and therefore by subtracting the underlying signal (identified using low-pass filter) from the original data the remaining noise can be isolated. From the quantile plot in Figure 3-7, the isolated noise can be seen to closely follow a normal distribution, further evidence that it comes from a white noise source.

White noise can be partially removed from the measured signal by restricting the frequency pass band to retain only the frequencies of interest (from Equations (2-23) and (2-24)). To ensure that this was completed in a conservative way it was essential that the real physical response of the structure was preserved in the signal to avoid any information about the underlying fatigue cycles from being removed. The structural dynamics were found to be dominated by the first mode response in the region of 0.3-0.33 Hz, but slight response could also occasionally be found around the second mode frequency of 1.5 Hz (this estimate corresponds closely with the design calculation for a high sea bed at Turbine K1 [95]). Although the amplitude of the second mode response was minimal, and only rarely occurred in the measured data, it was decided to design a low pass filter to protect all frequencies below this level. A 6^{th} order Butterworth filter with a cut-off frequency of 2 Hz was found to perform well, and the pass band is shown in Figure 3-8 below.

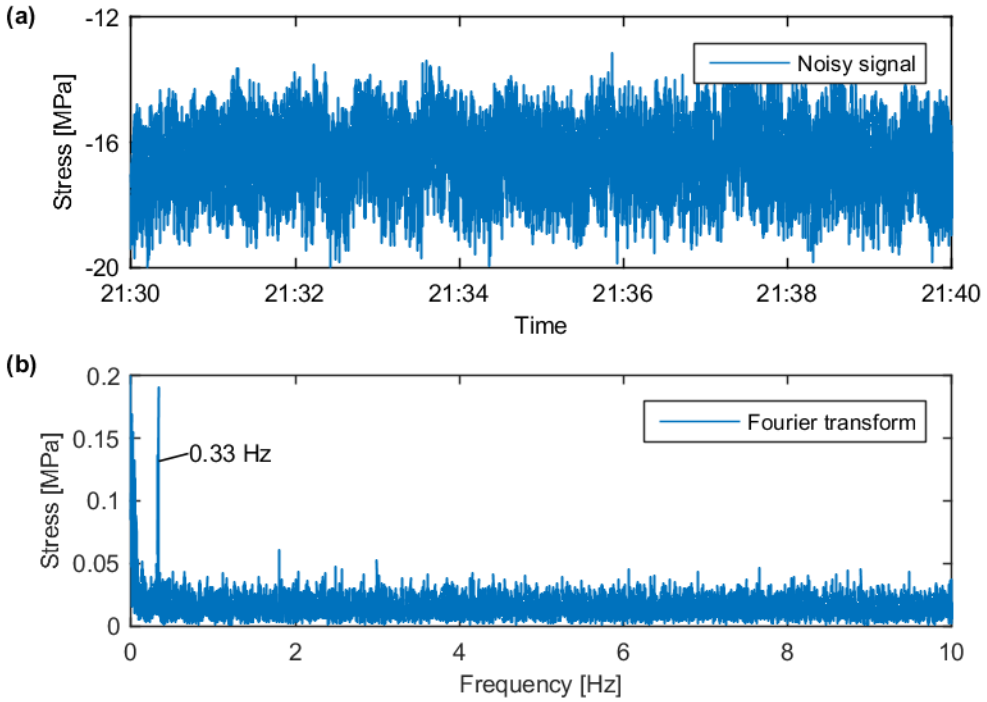

Figure 3-6. Measured stress data from gauge K1-S4-SGAV during minimal loading. a) Ten minute stress time series consisting of structural response and additional noise. b) Amplitude spectrum produced from FFT of the ten minute series, displaying slight structural response at 0.33 Hz, and constant level stress amplitude across all other frequencies.

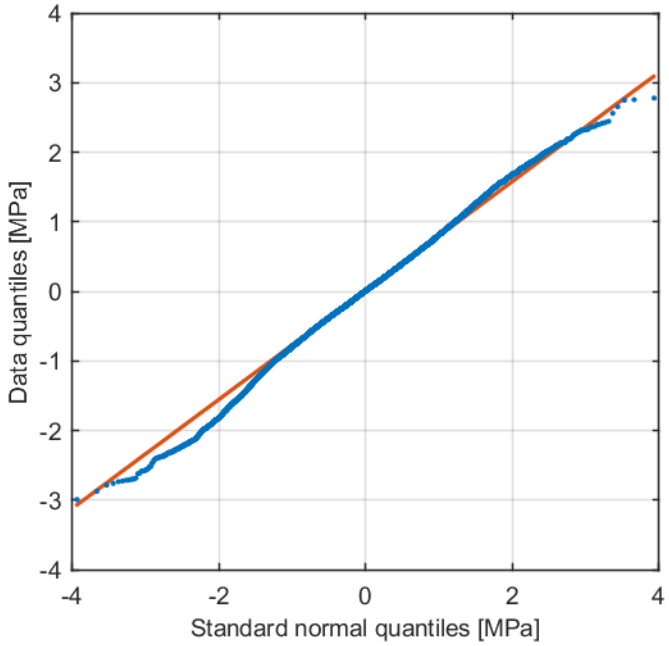

Figure 3-7. Quantile plot of isolated data noise versus normal distribution. Noise isolated from the signal using the low pass filter design shown in Figure 3-8 below (original signal minus filtered signal).

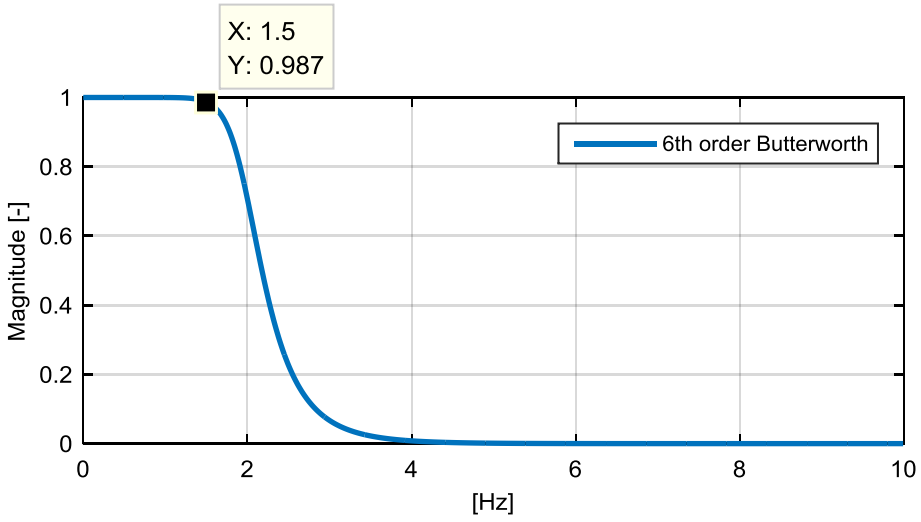

Figure 3-8. Pass band of a 6th order Butterworth filter using a 2 Hz cut off frequency.

3.1.2.6 Datum Drift Correction

As well as the need to account for the level of embedded strain from the self-weight of the structure, the presence of long term drift was identified in the measured data. Correction of

the datum levels is made difficult by the presence of large variations in the mean strain levels in the structure, which arise from changes in the direction and amplitude of the wind loading, and the corresponding rotor thrust vector. Therefore, a correlation with speed and direction was required to identify and correct the gauge datum level. The quasi-static bending moment at the height of the global gauges is dominated by a combination of wind loading on the rotor, nacelle, and tower. The CoG offset of the RNA, which varies with the yaw position of the nacelle, will also have a slight contribution to the tower bending moment, but during operation the yaw position will track the wind direction and therefore variation of the CoG was assumed to be described by the wind direction only.

To approximate the wind loading as accurately as possible, the results of the design simulations were used to calculate the average stresses around the TP circumference under the wind loading conditions described by the power production DLCs. The *x* and *y* bending moment components and the vertical force at the height of the gauges were interpolated from the design simulation output locations at 0 mCD and 20 mCD, and the average stresses were calculated from each simulation,

$$\overline{\sigma(\phi|\bar{U},\bar{\theta})} = \frac{1}{N}\sum_{i=1}^{N}\left[\cos\phi\,\frac{M_{x\,i}r_{inside}}{I_{TP}} + \sin\phi\,\frac{M_{y\,i}r_{inside}}{I_{TP}} - \frac{F_{V\,i}}{CSA_{TP}}\right] \tag{3-2}$$

Where N is the number of data points in the ten minute DLC simulation, ϕ is the circumferential stress location (in degrees, relating to compass direction), r_{inside} is the TP inside radius, I_{TP} is the TP second moment of area, F_V is vertical gravity load at the height of the global gauges, and CSA_{TP} is the TP cross sectional area. M_x and M_y are the *x* and *y* components of the resolved bending moment, and are a strong function of the mean wind speed and direction; i.e., Equation (3-2) provides a mean stress level which is a function of circumferential location, mean wind speed, and mean wind direction. Using the results from Equation (3-2), a transfer function was produced relating mean wind speed and direction to the mean stresses around the circumference of the TP. The deviation and drift of the strain gauge measurements over time from the correct datum level was then calculated using,

$$\Delta\sigma = TF(\bar{U},\bar{\theta},\phi) - \overline{\sigma_{GG}}_{\phi} \tag{3-3}$$

where $\Delta\sigma$ is the error of the ten minute mean stresses measured by the global gauges $\overline{\sigma_{GG}}_{\phi}$, and $TF(\bar{U},\bar{\theta},\phi)$ is the stress calculated using the design data transfer function accounting for wind speed, direction, and circumferential location on the structure. Cubic interpolation was used to enhance the transfer function resolution, and a 1,000 point moving average was then

used to calculate the mean drift over the period of measurement. In this way the initial embedded stress and the mean drift was corrected in each of the gauges, and the effect was quantified by calculating the root mean squared error (RMSE) between the measurements and the transfer function stresses. The effect of the drift correction is shown in Section 4.3.

3.1.2.7 Cosine Fitting

The variation of axial stress around the circumference of a simple cylinder under an applied bending moment is described by a sinusoid. Therefore, the stresses measured by the global gauges were fitted to a cosine function to allow the measurements to be interpolated to any circumferential location. An additional benefit is that function fitting would further reduce the level of white noise remaining from the low-pass filter.

The stress variation around the cylinder is described by the equation,

$$\sigma(\phi) = \sigma_{BM} \cos(\theta - \phi) + \sigma_{Fv} \tag{3-4}$$

where σ_{BM} is the maximum stress resulting from a bending moment applied in direction θ, ϕ is the circumferential location around the cylinder, and σ_{Fv} is the applied axial stress. The stress variation is shown in Figure 3-9.

In this form, the cosine function can be related by the following trigonometric identity,

$$\sigma_{BM} \cos(\theta - \phi) + \sigma_{Fv} = \beta_1 + \beta_2 \cos\phi + \beta_3 \sin\phi \tag{3-5}$$

where $\beta_{1\text{-}3}$ are a set of constants. The function can be fitted to a set of circumferential measurements by minimising the sum of the residuals, given by,

$$R^2 = \sum_{i=1}^{n} [y_i - (\beta_1 + \beta_2 \cos\phi_i + \beta_3 \sin\phi_i)]^2 \tag{3-6}$$

The least squares fit is found by taking the partial derivatives and setting to zero,

$$\frac{\partial R^2}{\partial \beta_1} = -2\sum_{i=1}^{n}[y_i - (\beta_1 + \beta_2 \cos\phi_i + \beta_3 \sin\phi_i)] = 0$$

$$\frac{\partial R^2}{\partial \beta_2} = -2\sum_{i=1}^{n}[y_i - (\beta_1 + \beta_2 \cos\phi_i + \beta_3 \sin\phi_i)]\cos\phi_i = 0 \quad (3\text{-}7)$$

$$\frac{\partial R^2}{\partial \beta_3} = -2\sum_{i=1}^{n}[y_i - (\beta_1 + \beta_2 \cos\phi_i + \beta_3 \sin\phi_i)]\sin\phi_i = 0$$

The three equations can be expressed in matrix form,

$$\begin{bmatrix} n & \sum_{i=1}^{n}\cos\phi_i & \sum_{i=1}^{n}\sin\phi_i \\ \sum_{i=1}^{n}\cos\phi_i & \sum_{i=1}^{n}\cos^2\phi_i & \sum_{i=1}^{n}\cos\phi_i\sin\phi_i \\ \sum_{i=1}^{n}\sin\phi_i & \sum_{i=1}^{n}\cos\phi_i\sin\phi_i & \sum_{i=1}^{n}\sin^2\phi_i \end{bmatrix} \begin{bmatrix}\beta_1 \\ \beta_2 \\ \beta_3\end{bmatrix} = \begin{bmatrix} \sum_{i=1}^{n} y_i \\ \sum_{i=1}^{n} y_i\cos\phi_i \\ \sum_{i=1}^{n} y_i\sin\phi_i \end{bmatrix} \quad (3\text{-}8)$$

As the axial load consists mainly of the constant gravity load, σ_{Fv} was assumed constant and was calculated from the design simulations as in Equation (3-2). This additional constraint meant that the fitting procedure was optimised to find the correct direction and amplitude of the sinusoidal stresses (which are ultimately the most important component for the fatigue calculations) rather than fitting vertical load cycles to the measured data. With σ_{Fv} kept constant, Equation (3-8) becomes,

$$\begin{bmatrix} \sum_{i=1}^{n}\cos^2\phi_i & \sum_{i=1}^{n}\cos\phi_i\sin\phi_i \\ \sum_{i=1}^{n}\cos\phi_i\sin\phi_i & \sum_{i=1}^{n}\sin^2\phi_i \end{bmatrix} \begin{bmatrix}\beta_1 \\ \beta_2\end{bmatrix} = \begin{bmatrix} \sum_{i=1}^{n} y_i\cos\phi_i + \sigma_{Fv}\cos\phi_i \\ \sum_{i=1}^{n} y_i\sin\phi_i + \sigma_{Fv}\sin\phi_i \end{bmatrix} \quad (3\text{-}9)$$

From which the unknown coefficients can be found,

$$\beta = \phi^{-1}Y \quad (3\text{-}10)$$

and the cosine coefficients from Equation (3-4) are given by,

$$\theta = \tan^{-1}\frac{\beta_2}{\beta_1}$$
$$\sigma_{BM} = \frac{\beta_1}{\cos\theta} \tag{3-11}$$

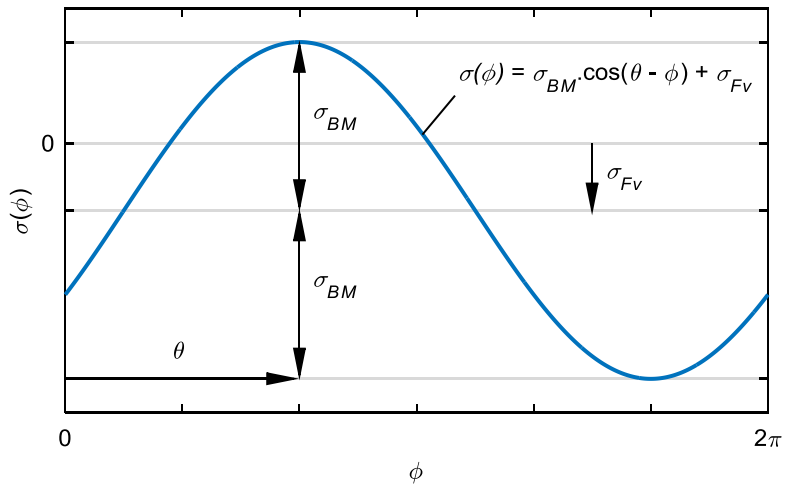

Figure 3-9. General cosine function representing stress variation around the circumference of a cylinder under combined bending and axial load.

3.1.2.8 Global Bending Moments

The fitted stress signal produced by Equation (3-4) was converted to bending moments at the height of the global gauges using,

$$M_x = \cos\theta\frac{\sigma_{BM}I_{TP}}{r_{inside}}$$
$$M_y = \sin\theta\frac{\sigma_{BM}I_{TP}}{r_{inside}} \tag{3-12}$$
$$F_v = \sigma_{Fv}CSA_{TP}$$

As the axial load was assumed to be constant, the measured bending moments could be converted back to stress at any circumferential location using,

$$\sigma(\phi) = \cos\phi\frac{M_x r_{inside}}{I_{TP}} + \sin\phi\frac{M_y r_{inside}}{I_{TP}} + \frac{F_v}{CSA_{TP}} \tag{3-13}$$

3.1.2.9 Sensitivity of Fatigue Calculations to Digital Sampling

During fatigue calculations, individual stress cycles are determined from the time series by first identifying the peak and valley stress values, before application of the RF algorithm. As the measured data time series was digitally sampled it is possible that some of the underlying peak values may be missed, and the underlying cycle ranges can therefore be underestimated [56]. In practice, the cycle peaks will only be missed by a significant amount if the sample rate is too low. Based on the assumption of a simple sine wave, the worst case reduced stress amplitude produced by digital sampling is found when the sampled data points lay either side of the underlying cycle peak, given by,

$$y' = \cos(\pi f_n / f_s) \tag{3-14}$$

where *y'* is the sampled peak expressed as a fraction of the underlying cycle peak, f_n is the frequency of the underlying signal, and f_s is the sample frequency, both in radians. The worst case digital sample is displayed in Figure 3-10a, whereas the best case condition is shown in Figure 3-10b, where the digital sample may fall on the true cycle peak. Assuming the offset of the data samples from the cycle peaks to be uniformly distributed, the average reduction in identified cycle amplitudes is therefore approximated by,

$$\bar{y'} = \frac{1}{\beta}\int_0^{\beta} \cos(x)\, dx$$
$$\beta = \pi\, f_n / f_s \tag{3-15}$$

and the corresponding reduced fatigue damage value is,

$$D' = \frac{1}{\beta}\int_0^{\beta} \cos(x)^m\, dx \tag{3-16}$$

where *m* is the fatigue damage exponent. It is assumed here that the sample rate should be at least greater than the Nyquist frequency, and therefore $f_s/f_n > 2$. The function given in Equation (3-16) is plotted in Figure 3-11 below against the normalised sample frequency (f_s/f_n) with example values highlighted. For the monitored OWT support structures with underlying first and second mode structural frequencies of approximately 0.33 Hz and 1.5 Hz respectively [95], normalised sample frequencies of 20/0.33 = 60 and 20/1.5 = 13.33 would correspond to an average reduced fatigue damage fraction of 99.9% and 97.3%,

respectively, using $m = 3$. Therefore, as the structural responses of the measured structures are dominated by the first mode (see example response spectrums in Figure 6-7 and Figure 6-8), the reduction in fatigue damage due to digital sampling can be expected to be negligible in most cases.

To confirm the estimated reduced fatigue damage values shown in Figure 3-11, a method presented in [56] was used to estimate the true cycle peaks from the measured data by fitting a quadratic curve to the three digitally sampled data points around each peak and valley. The estimated maxima or minima of the individual stress cycles could then be interpolated from the fitted curves, at the point $dy/dx = 0$. Cycle peaks and valleys were interpolated for individual ten minute periods of measured data, which were then RF counted and converted to a single damage calculation using Equation (2-17), and compared to the equivalent value calculated without the interpolated peaks. This was calculated for 10^4 individual ten minute periods of measured data, and the distribution of results is shown in Section 4.5.

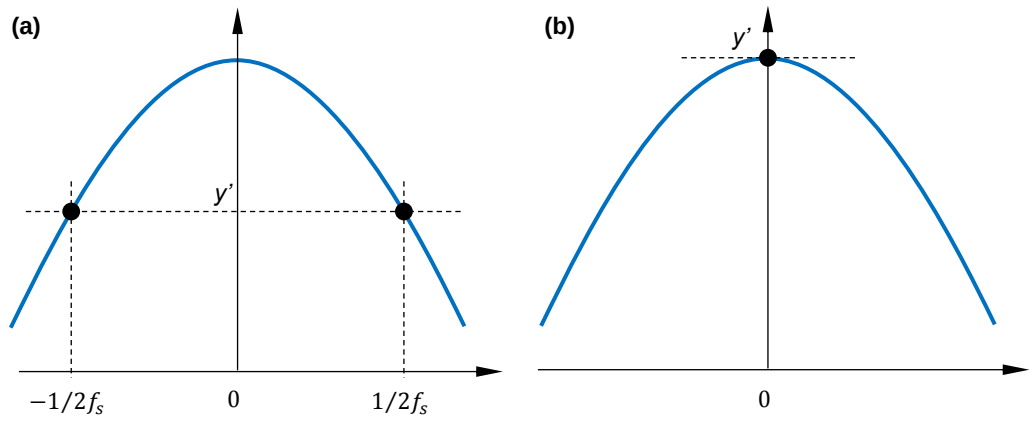

Figure 3-10. Digitally sampled cycle peaks. (a) Worst case, where the sampled data points fall either side of the cycle peak. (b) Best case, where the sampled data point falls on the cycle peak.

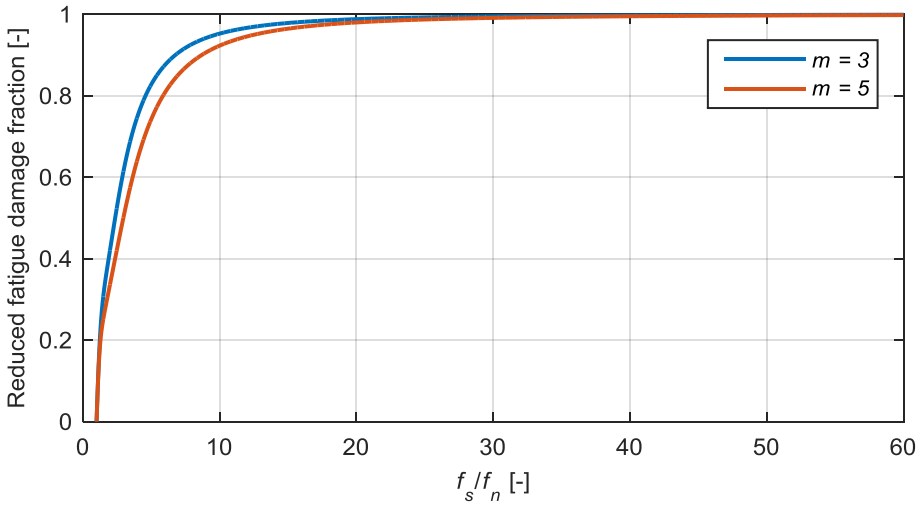

Figure 3-11. Average fatigue damage underestimation, as a function of sampling frequency (normalised by underlying frequency). From Equation (3-16).

3.1.3 Environmental and Operational Data

3.1.3.1 Wind Data

3.1.3.1.1 SCADA Data

Wind speed and direction data from the turbine Supervisory Control and Data Acquisition System (SCADA) were used to evaluate the operational wind conditions at the monitored turbines. Data were extracted from the database in 10 minute average values at Turbine K1 over a four year period from 2010 to 2013 inclusive. Data drop outs were identified, including erroneous values such as data spikes or flat lining data points, and were replaced with measurements from either Turbine K2 or K3. This resulted in a dataset which was 99.8% complete. The four year data period was fitted to the two-parameter Weibull probability density function and directional distribution, as given by Equation (2-7). A comparison was then made between the fatigue damage produced by factoring the DLC time series loads by both the design and measured wind distributions, based on a calculation of Damage Equivalent Moment (DEM), from Equation (2-18),

$$DEM = \left[\frac{\sum_{i=1}^{k} n_i M_{res}(\phi)_i{}^m}{N_{ref}}\right]^{1/m} \quad (3\text{-}17)$$

where $M(\phi)$ is the resultant bending moment at a given circumferential location, *n* is the corresponding number of bending moment cycles found using RF counting, and *m* is the Wöhler exponent. The results were expressed as a ratio, meaning that the reference number of cycles (N_{ref}) could be ignored, and are presented in Section 5.1.

Wind speed standard deviation data were extracted from the database to enable location-specific turbulence levels to be determined. The data were extracted in one minute intervals and combined into a ten minute standard deviation value using Equation (2-4) in order to de-trend long term variations in mean wind speed. Multiple turbine locations were analysed to identify the distribution of turbulence as the wind progressed through the wind farm. To account for the variation of turbulence with the distribution of wind speed and direction, an effective standard deviation (σ_{eff}) was calculated from two years' worth of measurements using, from Equation (2-6) and [96],

$$\sigma_{eff}(\overline{U},\bar{\theta}) = \left[\frac{1}{N}\sum_{i=1}^{N}\sigma(\overline{U},\bar{\theta})^{m}\right]^{1/m} \tag{3-18}$$

where *N* is the number of standard deviation measurements relating to each mean wind speed and direction bin $(\overline{U},\bar{\theta})$, and *m* is the Wöhler exponent.

3.1.3.1.2 Meteorological Mast Data

Wind data were available from the Meteorological Mast (MM) for the pre-construction period from 2004 to 2007. The MM position was in close proximity to the future location of Turbine K1, as shown in Figure 1-1. As the MM data was provided in ten minute values of mean direction, speed, and standard deviation it was not possible to de-trend the data using Equation (2-4). However, a level of distortion was found in the wind speed standard deviation values which were corrected using the following methodology.

The mean and standard deviation values calculated from a ten minute period may be distorted if significant rounding is used with the sampled data. Such rounding was commonly found with older measurement programs which employed cup anemometers and recorded their rotational velocity in integer rotations per second. With a wind speed sample resolution in multiples of the correlation coefficient *P* (used to convert anemometer rotational velocity to measured wind speed using $U = fP$, where *f* is angular frequency in Hz), the rounded value of sampled wind speed is given by,

$$U^* = P \times round\{U/P\} \tag{3-19}$$

The distorted mean and standard deviation are then defined by,

$$\overline{U^*} = \frac{1}{N}\sum_{i=1}^{N} U^*{}_i \tag{3-20}$$

$$\sigma_U{}^* = \sqrt{\frac{1}{N}\sum\nolimits_{i=1}^{N}(\overline{U^*} - U_i{}^*)^2} \tag{3-21}$$

where N is the number of sample points used in the ten minute period. The mean and standard deviation error resulting from rounding are defined by,

$$\varepsilon_{\overline{U}} = \overline{U^*} - \overline{U} \tag{3-22}$$

$$\varepsilon_{\sigma_U} = \sigma_U{}^* - \sigma_U \tag{3-23}$$

In order to estimate the distortion due to rounding, it may be observed that the range of possible mean wind speed errors is given by,

$$-\frac{P}{2} \le \varepsilon_{\overline{U}} \le \frac{P}{2} \tag{3-24}$$

The range of standard deviation error is more complex, but the minimum distorted value of $\sigma_U{}^*$ in the range of $0<\overline{U^*}<P$ is given by,

$$\sigma_U{}^*{}_{min}(\overline{U^*}) = \sqrt{\frac{1}{N}\left[\sum\nolimits_{i=1}^{n}(\overline{U^*} - P)^2 + \sum\nolimits_{i=1}^{N-n}(\overline{U^*} - 0)^2\right]}$$
$$\sigma_U{}^*{}_{min}(\overline{U^*}) = \sqrt{P\overline{U^*} - \overline{U^*}^2} \tag{3-25}$$

Equation (3-25) is also the maximum error due to rounding for the minimum value of $\sigma_U{}^*$. It should be noted that, although the number of sample points used for calculation of the actual MM data (N from Equations (3-20) and (3-21)) cannot be confirmed, the variable cancels in Equation (3-25) and does not affect the minimum σ^* function. For values of $\overline{U^*}$ greater than P, the minimum value of σ^* may be defined by,

$$\sigma_{U^*}{}_{min}(\overline{U^*}) = \sqrt{P(\overline{U^*} - P \times round\{\overline{U^*}/P\}) - (\overline{U^*} - P \times round\{\overline{U^*}/P\})^2} \quad (3\text{-}26)$$

The function is plotted in Figure 3-12 below.

For values of $\overline{U^*}$ and σ^* which lay outside of the function defined by Equation (3-26), the range of errors becomes more complicated, and although the likely values of $\varepsilon_{\overline{U}}$ and ε_{σ_U} can be shown to decrease with increasing $\sigma_U{}^*$, the errors cannot be determined analytically. Therefore, the distribution of possible errors was investigated using a Monte Carlo approach [97] with a large number of synthetic wind speed time series, simulated using a suitable turbulence model.

The Kaimal spectrum from Equation (2-8) was used to simulate 10^6 individual ten minute wind speed time series with 1 Hz sample rate (N = 600), to which rounding was applied using Equation (3-19). A large number of rounding errors, $\varepsilon_{\overline{U}}$ and ε_{σ_U}, were then calculated to give the empirical distributions which were used to correct the distorted values of $\overline{U^*}$ and $\sigma_U{}^*$ from the MM data using Equations (3-22) and (3-23).

The measured mean wind speeds were then extrapolated from the measurement height above mean sea level at the top of the MM (h = 54 m [98]) to the turbine hub height (h = 79.975 m [93]) using the wind shear profile in Equation (2-3). The wind speed standard deviation was not extrapolated to hub height, as anemometers at various heights on the MM were found to give consistent values. Furthermore, the IEC design standard [21] specifies that the longitudinal turbulence component should be assumed invariant with height.

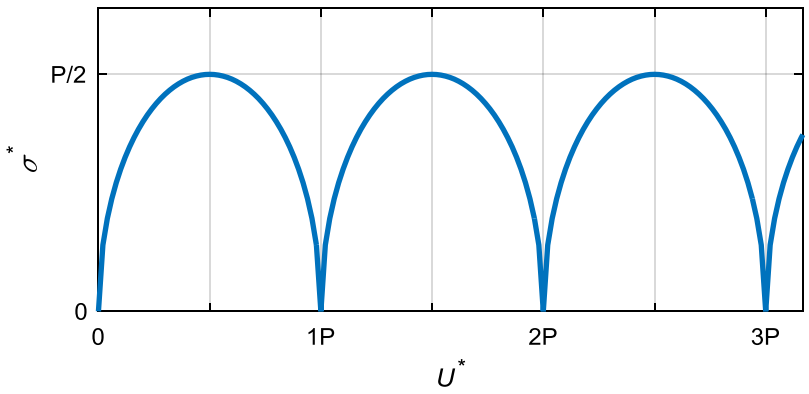

Figure 3-12. Minimum standard deviation with rounding, from Equation (3-26).

3.1.3.1.3 LIDAR Data

The LIDAR instrumentation was located on the offshore substation shown in Figure 1-1, and data was collected after the date of site commissioning, from 2010 onwards. LIDAR data was provided in ten minute values of mean wind direction, speed and standard deviation, and therefore it was not possible to de-trend the TI assessment using Equation (2-4).

3.1.3.2 Wave Data

The wave climate at the OWF site is dominated by local winds, as the shape and proximity of the coastline shelters the site from large swell. The dominant wave direction comes from the South West where the site is open to more exposed seas, and the fetch is limited in other directions. The effect is that the wave climate is dominated by wind driven seas and therefore wind and wave directions tend to be closely aligned.

The wave loading used for design was based on metocean reports, from which the site wave direction distribution was found to be well correlated with wind direction, with alignment expected almost 80% of the time [87].

During operation of the wind farm, sea surface elevation data was collected using a non-directional wave radar system, mounted on the substation located on the East side of the wind farm (see Figure 1-1), and stored as sea state statistics in ten minute periods. The bathymetry at the location of the substation was far shallower than the depths at the monitored turbines [86], and therefore the measured wave heights can be expected to be lower than at the South West of the wind farm. Acknowledging the limitations of the wave radar measurements, the correlation of significant wave heights with wind measurements at Turbine K1 was investigated by fitting a simple second order polynomial and calculating the adjusted R-squared value,

$$adjusted\ R_{squared} = 1 - \frac{(N-1)}{(N-k)} \frac{\sum_{i=1}^{N} \left(H_{s_i} - \widehat{H_s}(U,\theta)_i\right)^2}{\sum_{i=1}^{N} \left(H_{s_i} - \overline{H_s}\right)^2} \qquad (3\text{-}27)$$

where N is the total number of measurements used, k is the degrees of freedom of the fitted function (equal to 3 for a second order polynomial), $\widehat{H_s}(U,\theta)$ is the fitted data point (as a function of both wind speed and direction), and $\overline{H_s}$ is the mean of all the measurements.

3.1.3.3 Tide Data

Tide height measurements from a local measurement station were downloaded from the British Oceanographic Data Centre [99] for the period of load measurement at Turbines H4 and K1. The data were available in 15 minute sample periods, and were filtered to identify and remove erroneous values (identified as data spikes and flat-lining data points). Missing data points were interpolated using the tidal constituents fitted to the existing data points using a Matlab tool available from [100], and were added to a linear gradient to ensure a smooth transition into the existing data. Finally, the data were up-sampled to ten minute intervals using cubic interpolation.

3.1.3.4 Turbine Operation

SCADA signals which were used to identify ten minute environmental conditions and operational state at each turbine are outlined in Table 3-2 below. Data were also extracted in one minute intervals to enable transient operational states to be identified within each ten minute period.

Table 3-2. List of SCADA signals used with the analysis.

Name	Description	Units
Wind speed	Wind speed measurements from the nacelle mounted sonic anemometer.	m/s
Wind direction	Wind direction measurement from the nacelle mounted anemometer	Degrees
Rotor speed	Rotor angular velocity	Hz
Blade pitch angle	Recorded angle of the blade pitch mechanism	Degrees
Operational state	Operational state recorded by the turbine controller: 3: Normal operation 2: Pause 1: Stop 0: Emergency stop	[-]
Ambient temperature	Ambient air temperature measured at the nacelle	°C
Ambient pressure	Ambient air pressure measured at the nacelle	Mbar
Generator connection	Connection of the generator to the grid (either Star of Delta formation).	[-]

3.1.3.5 Average Air Density

The aerodynamic loads are dependent upon the air density. IEC 61400-3 [26] recommends the standard atmosphere characterised in [101] of 1.225 kg/m^3, while the turbine designer used a more conservative value of 1.235 kg/m^3 to take account of the distribution of site air temperature [93].

Air density was calculated from ambient temperature and pressure measurements recorded by Turbine K1 SCADA system, using,

$$\rho_{air} = \frac{P_d}{R_d T} + \frac{P_v}{R_v T} \tag{3-28}$$

where P and R are respectively the partial pressure and gas constants for dry air and water vapour, and T is the measured temperature. The water vapour partial pressure was calculated using the saturation pressure relationship developed by Herman Wobus [102], and an estimated average humidity of 80% relating to a nearby weather station [103].

3.2 Load Case Classification

3.2.1 Distribution of Measured Fatigue Damage

IEC-TS-61400-13 [29] outlines the minimum criteria required to construct a statistically representative LC histogram from measured data for onshore turbines. This requires a minimum number of ten minute measurement periods to be recorded so that the variations in environmental loading and the corresponding structural response that occur within each LC bin can be sufficiently accounted for. The wind vector (speed and direction) is the dominant variable influencing the level of fatigue loading for onshore turbines, and therefore LCs are binned according to wind speed and directional sectors, with maximum bin sizes specified in [29] .

For offshore locations the level of ambient turbulence is generally lower than onshore, but the addition of hydrodynamic loading means that the minimum criteria specified in [29] may not sufficiently quantify the statistical distribution of fatigue loads found in each wind speed and direction bin. Although local sea states are a strong function of wind speed and direction, swell seas generated from remote locations may result in wave loading at exposed sites which is uncorrelated with local wind conditions in terms of both magnitude and direction.

The influence of additional environmental loading factors can be roughly approximated by investigating whether significant correlations can be identified between a specific variable and the resulting level of fatigue loading. Correlations between DES and air density, turbulence intensity, tide level, and significant wave height were investigated by fitting a second order polynomial and quantifying the goodness of fit using the R-squared value (Equation (3-27)).

Although further refinement of the analysed LC bins according to wave distribution would reveal further detail, the variation in fatigue loading within each wind vector bin can be accounted for as long as the number of measurements is sufficiently large as to be representative of the full distribution. The full measurement period of approximately 18 months can be argued to be representative of the variation in environmental and operational variables that would occur over the life of the turbine. Therefore, the full measurement period should be an accurate description of the underlying population distribution of fatigue loading, and was used as a bench mark against which to assess shorter measurement periods.

A Bootstrap approach [104] was used to quantify the confidence limits that the full measurement period was sufficiently representative of the underlying distribution of fatigue damage. The full measurement period was first filtered to include only the ten minute periods where the turbine was operating in power production mode (using the methodology outlined in Section 3.2.2.1). The fatigue damage produced by each ten minute period was calculated using a simplified version of Equation (2-17),

$$D_{10min} = \sum_{i=1}^{k} n_i \Delta\sigma_i{}^m \tag{3-29}$$

where $\bar{a}$, the log$N$ offset from Equation (2-17), can be ignored as only the percentage spread of results are of interest, rather than the actual damage value which would result from a specific S-N curve. The damage value produced by the entire population of measurements, (D_P), consisting of N ten minute power production data periods, was then calculated using,

$$D_P = \sum_{i=1}^{N} D_{10min_i} \tag{3-30}$$

The power production data periods were then randomly resampled with replacement to identify a resample of size N, from which the resampled value of D_P was recalculated according to Equation (3-30). The resampled calculation of D_P was repeated B = 100,000

times, from which the empirical probability distribution P(D_P) was calculated. The spread of the resampled D_P values should follow a normal distribution, according to the central limit theorem [105]. Therefore, the relative standard deviation of the Bootstrap D_P values could then be used to quantify the confidence that the full measurement period was sufficiently representative of the underlying population.

Another resampling approach was then used to calculate the distribution of values that would be produced by selecting a small sample of measurements at each wind vector bin. From the power production periods identified as above, a random sample with replacement of size *n* ten minute periods were selected at each wind vector bin, from which the average fatigue damage value was calculated,

$$\overline{D_{10min}} = \frac{1}{n}\sum_{i=1}^{n} D_{10min_i} \tag{3-31}$$

The average fatigue damage for each bin was then factored by the number of occurrences of each wind vector bin over the entire measurement period, and the total was summed to produce the total fatigue damage calculated from the samples,

$$D_S = \sum_{i=1}^{n_U}\sum_{j=1}^{n_\theta} \overline{D_{10min}}_{i,j} \times N \times P(U_i, \theta_j) \tag{3-32}$$

Where n_U and n_θ are the number of wind speed and direction bins, respectively, and $N \times P(U_i, \theta_j)$ is the number of occurrences of each bin in the total dataset. The sampled fatigue damage calculation was repeated C = 60,000 times, from which the empirical probability distribution of sampled fatigue damage $P(D_S)$ was calculated. The above procedure was repeated for varying values of sample size *n*.

The probability that the total fatigue damage calculated from the samples is equal to the damage calculated from the total dataset, P(D_S = D_P), can be expected to be approximately 50%, but the probability that the sampled fatigue damage is greater than an acceptable percentage of the value given by the entire population is given by,

$$P(D_S > \beta D_P) = \int_{\beta D_P}^{\infty} P(D_S)\, dP(D_S) \tag{3-33}$$

where β is a fraction specifying an acceptable tolerance, and Equation (3-33) can be used to quantify the number of samples necessary for the measurement campaign.

3.2.2 Definition of Measured Load Cases

3.2.2.1 Steady State Load Cases

The steady state LCs constitute normal power production and idling operational modes. SCADA data covering wind speed, direction, and wind turbine power production were used to identify ten minute periods of measured strain gauge data which corresponded with the LCs. Ten minute average values of wind speed and direction were used to identify the wind vector bin, while the power output signal was used in one minute averages to ensure that constant operating conditions were identified. The SCADA signals and criteria used to identify each LC are shown in Table 3-3. The number of measurements available for each LC was then recorded, together with the range of turbulence intensity values included in the measurements.

Table 3-3. Criteria used for identification of the steady state MLCs from the SCADA data. Ten minute average wind speeds and direction values were used for each LC bin.

Design Conditions		Criteria Applied to the Measured Signals	
DLC	Wind Speed [m/s]	Wind Speed [m/s]	Power Output [kW]
1.1	4-24	$4 \leq \overline{U} \leq 24$	$P_{(1\ldots10)} > 0$
6.4	3	$\overline{U} = 3$	$P_{(1\ldots10)} < 0$
	26 - 34	$26 \leq \overline{U} \leq 34$	$P_{(1\ldots10)} < 0$

Note: The counter (i = 1,2,3,…,10) indicates the separate one minute intervals used to identify transient operating conditions within each ten minute period.

3.2.2.2 Transient Load Cases

The transient LCs include turbine normal start-up, shut-down, and emergency stop operations. The criteria used to identify the transient LCs from the SCADA data are outlined below, and summarized in Table 3-4.

Normal start-up events (LC 3.1) have been selected using the power output signal, with the transition from zero or negative power production to positive power production identified from one minute average values. A single start-up case has been identified where the criteria are met within a ten minute period, to conform to the ten minute time series simulations provided by the turbine designer. Three wind speed bins were used to identify start-up at cut-in, cut-out, and intermediate wind speeds, but a wider bin size was used than the design simulations to account for operational variability.

Normal shut-down events (LC 4.1) have also been selected from one minute average values from the power output signal, with the transition from positive power production to zero or negative power production identified within a single ten minute period. The same wind speed bins were used as the start-up criteria, to match the design simulations.

Emergency shutdown events (LC 5.1) were identified using the wind turbine controller Operational State signal, which recorded four possible turbine operating conditions as outlined in Table 3-2 above. A single emergency stop event was identified from one minute sampled values by the transition between operational states greater than zero, to a zero signal. Two wind speed bins were used to identify the initial operating conditions used by the turbine designer, as outlined in Table 3-4. Additionally, the rotor speed signal was used to distinguish between emergency stops which occurred during a moving and near-stationary rotor condition, using a threshold of 0.5 rpm. This additional criterion was used as it was assumed that an emergency stop event triggered with a stationary rotor would not cause additional loading to the support structure.

Table 3-4. Criteria used for identification of transient MLCs from the SCADA data. Ten minute average wind speeds and direction values were used for each LC bin. One minute values of power output, rotor speed, and operational state were used to identify transient conditions within each ten minute period.

Design Conditions		Criteria Applied to the Measured Signals			
DLC	Wind Speed	Wind Speed [m/s]	Power Output [kW]	Rotor Speed [rpm]	Operational State [-]
3.1	4	$\overline{U} < 6$	$P_{(i-1)} < 0,$ $P_{(i)} > 0$	-	-
	13	$6 \leq \overline{U} < 16$	$P_{(i-1)} < 0,$ $P_{(i)} > 0$	-	-
	20	$16 \leq \overline{U}$	$P_{(i-1)} < 0,$ $P_{(i)} > 0$	-	-
4.1	4	$\overline{U} < 6$	$P_{(i-1)} > 0,$ $P_{(i)} < 0$	-	-
	13	$6 \leq \overline{U} < 20$	$P_{(i-1)} > 0,$ $P_{(i)} < 0$	-	-
	25	$20 \leq \overline{U}$	$P_{(i-1)} > 0,$ $P_{(i)} < 0$	-	-
5.1	13	$\overline{U} < 18$	-	$\omega_{(1\ldots i)} > 0.5$	$OS_{(i-1)} > 0,$ $OS_{(i)} \leq 0$
	25	$18 \leq \overline{U}$	-	$\omega_{(1\ldots i)} > 0.5$	$OS_{(i-1)} > 0,$ $OS_{(i)} \leq 0$

Note: The counter (i = 1,2,3,…,10) indicates the separate one minute intervals used to identify transient operating conditions within each ten minute period.

3.2.3 Capture Matrix

The Capture Matrix (CM) defined in [29] was used to organise the measured time series to ensure that sufficient measurements have been recorded for each LC, wind vector bin, and range of turbulence values. Specifications of the minimum number of measurements required to classify the MLC used in this analysis are given in Table 3-5, where the criteria for the minimum number of measurements used for LCs 3.1 to 6.4 is greater than specified in [29].

The IEC-TS-61400-13 methodology specifies the minimum number of TI bins used to classify the power production MLCs, but does not specify what the distribution of those measurement bins should be. Guidance given in [35] suggests that the TI at a given wind speed may be represented by a lognormal distribution, but to ensure that the samples used to characterise the MLC at each wind vector bin are representative of the underlying TI

distribution would add significant complexity to the selection criteria. Therefore, to simplify the selection of sample periods, a flat turbulence distribution was used as it was assumed that this would result in a conservative assessment of the loading conditions. The selection methodology for the power production MLCs is outlined in Figure 3-13.

Table 3-5. Minimum number of measurements used for characterisation of MLCs from measured data.

MLC	No. of ten minute periods	Minimum number of TI bins
1.1	30	4
3.1	10	1
4.1	10	1
5.1	10	1
6.4	10	1

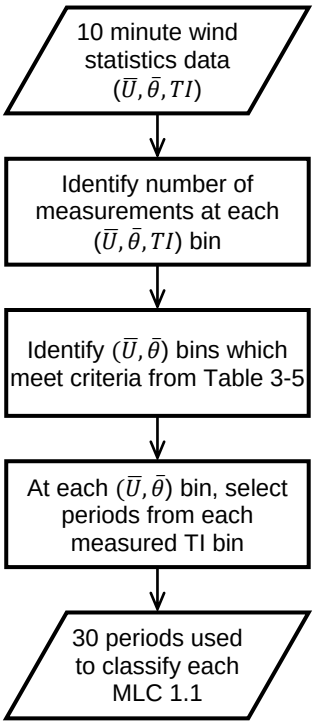

Figure 3-13. Methodology used to select measurement periods used to classify the power production MLCs.

3.2.3.1 Substitution of Measurement with Design Data

Where sufficient measurements did not exist to meet the criteria in Table 3-5, due to the infrequent occurrence of certain wind speed and direction combinations, the design data was reverted to in order to ensure that the full CM could be populated. This approach is assumed to be conservative based on a comparison of design conditions with measurements which did exist, as shown in the results presented in Section 6.3.

The fatigue damage produced by the measured and design data were compared using the DES calculated from Equation (2-18). The mean DES for each MLC was calculated from the measured values in each wind vector bin using,

$$\overline{DES} = \left[\frac{1}{N}\sum_{i=1}^{N} {DES_i}^m\right]^{1/m} \tag{3-34}$$

where N is the number of measurements in each bin. Confidence intervals for the MLCs were calculated using a Bootstrap approach, using the methodology outlined in Section 3.2.1. The variability of the Bootstrapped $\overline{DES}$ values could then be used to quantify the confidence in the MLC value.

Once the mean DES values for each bin had been identified for each LC from the DLCs or MLCs, the total combined DES for the 20 year design life was calculated using,

$$DES_{total} = \left[\sum_{i=1}^{n_{\bar{U}}}\sum_{j=1}^{n_{\bar{\theta}}}\sum_{k=1}^{n_{LC}} \overline{DES}_{i,j,k}^{m} \times N \times P\left(\bar{U}_i, \bar{\theta}_j, LC_k\right)\right]^{1/m} \tag{3-35}$$

where $\overline{DES}_{i,j,k}$ is the mean DES relating to the wind speed, wind direction, and LC operational state ($\bar{U}_i, \bar{\theta}_j, LC_k$, respectively).

3.2.3.2 Directional Extrapolation of Measured Data

An alternative approach to the substitution of missing MLCs with the DLC results is to extrapolate measurements to other directional bins. This approach means that wind speed and directional combinations which occur during the measurement period are used to represent directional sectors for which sufficient measurements don't exist.

Directional extrapolation requires that the level of environmental loading which produce the measured loads can be shown to be the same of more severe than for the directional sectors

which are to be replaced, in order to ensure a conservative assessment of the full loading. The least frequently occurring wind directions measured at the OWF are fetch-limited, and were shown by the metocean design assessments to result in the lowest level of wave loading [85]. Therefore, it was assumed that the wave loading could be conservatively represented by the loading measured from the most frequently occurring wind directions. The level of turbulence loading, however, is strongly influenced by the presence of trailing wake loads, and therefore the directional extrapolation approach was required to account for upwind turbines.

As the cylindrical support structure is rotationally symmetrical, the fatigue damage D_1 at a circumferential location ϕ_1 corresponding to mean wind speed bin $\overline{U}$ and mean wind direction bin $\bar{\theta}_1$ was extrapolated from measurements taken from different mean wind direction $\bar{\theta}_2$ using the directional transposition,

$$D_1(\overline{U}, \bar{\theta}_1, \phi_1) = D_2(\overline{U}, \bar{\theta}_2, \phi_1 + \bar{\theta}_2 - \bar{\theta}_1) \tag{3-36}$$

where the directional sector $\bar{\theta}_2$ was identified as having similar ambient turbulence and upwind wake characteristics, which were assumed to correspond to the distance and orientation of any upwind turbines in the 30° directional sector. The layout of the directional extrapolation methodology is shown in Figure 3-14.

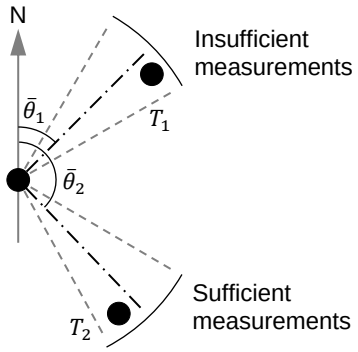

Figure 3-14. Coordinate system used for directional extrapolation of measurements. θ_1 and θ_2 are the direction of the centre of the sectors containing Turbines T_1 and T_2, respectively (identified by black dots).

3.3 Transition Cycles

3.3.1 Definition of Representative Wind History

Larsen & Thomsen [72] presented a method to account for transition cycles by relating the maximum and minimum stresses in each ten minute LC to a long term time history of ten minute average wind speed measurements. This allowed the stress cycles which arise from long term variations in the wind loading to be partially accounted for, and was based on the assumption that a single one year measurement period would be representative of the wind variation in other years. To investigate the accuracy of this assumption a series of long term wind measurement periods were taken from a number of sites and used to calculate time scales of wind speed variability. Rather than using peak structural stresses from each ten minute LC, which are largely influenced by the dynamic response of the specific wind turbine from which the measurements or modelled loads arise from, a normalised 'distance covered' by the wind time series was used, as given by the arc length mapped out by the wind vector. In parametric form this is given by,

$$arc\ length = \int_0^T \sqrt{\left(\frac{dx}{dt}\right)^2 + \left(\frac{dy}{dt}\right)^2}\, dt \tag{3-37}$$

where T is the total time length of the data series, and x and y are Cartesian coordinates as indicated in Figure 3-15. With a time series of ten minute average values, and averaging over a given period, the wind variability is given by,

$$\begin{aligned} \vec{U}' &= \frac{1}{N-1}\sum_{i=1}^{N-1}\sqrt{{\Delta x_i}^2 + {\Delta y_i}^2} \\ \Delta x_i &= \bar{U}_{i+1}\sin\bar{\theta}_{i+1} - \bar{U}_i \sin\bar{\theta}_i \\ \Delta y_i &= \bar{U}_{i+1}\cos\bar{\theta}_{i+1} - \bar{U}_i \cos\bar{\theta}_i \end{aligned} \tag{3-38}$$

where N is the total number of valid measurements in the dataset, and $\bar{U}$ and $\bar{\theta}$ are the ten minute average wind speed and direction measurements, respectively. In this form the wind variability metric $\vec{U}'$ has units of m/s per 10 minute period, analogous to an average rate of change of wind vector for a given site.

The wind variability metric was calculated for each calendar year in order to encompass seasonal variations, and to investigate the reference period used by Larsen & Thomsen [72]. Data sets were filtered to remove erroneous readings (identified as spikes, flat lining data

points, or missing values), and replace them with null values. This ensured that an artificial abrupt change in wind vector measurements, which could result if a period of erroneous readings were removed and the remaining data were concatenated together, would not distort the calculated value. Accounting for periods of null data to ensure that $\vec{U}'$ is normalised correctly, Equation (3-38) becomes,

$$\vec{U}' = \frac{1}{N-P-1}\sum_{i=1}^{N-1}\sqrt{{\Delta x_i}^2 + {\Delta y_i}^2} \tag{3-39}$$

where P is the number of consecutive periods of erroneous data identified in the measurement period. Equation (3-39) was then used to analyse the average wind variability at a given site over various years.

The datasets used for the analysis are described in Table 3-6 below, and come from a variety of sources. Buzzard Bay and Pulaski Shoals represent offshore locations off the coasts of Rhode Island and Florida, US, while the Panther Creek and Munnsville datasets come from onshore locations in Texas and New York state, US. The remaining datasets come from offshore locations in the North and Baltic seas. Therefore the wind datasets represent a range of geographical locations and would be expected to display a range of levels of variability. However, the ten minute mean wind speed measurements were recorded at different heights above ground or sea level (for instance, measurements from Buzzards Bay and Robin Rigg were recorded at 24.8 m and 90 m above mean sea level, respectively), and therefore a site specific wind shear profile such as Equation (2-3) would be necessary to provide measurements at equivalent elevations (a linear increase in $\overline{U}$ would be expected to result in an equivalent increase in $\vec{U}'$). Therefore, the coefficient of variation (standard deviation divided by the mean) of the yearly wind variability values was used to calculate the annual variability at each site, as a linear increase or decrease of wind speed with height would cancel with the σ/μ ratio.

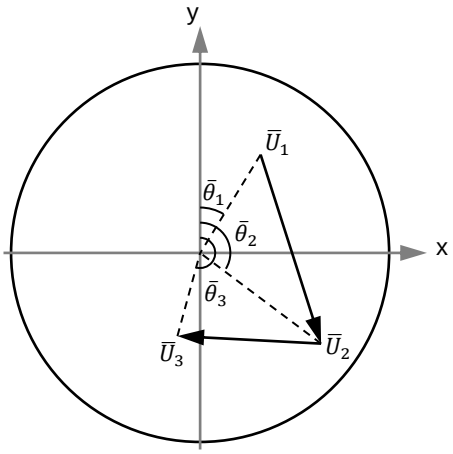

Figure 3-15. Wind vector transition distance between average wind speed and direction measurements.

Table 3-6. Sites and data periods used for analysis of wind variability.

Site Name	Location	Data Periods (inclusive)	Source
Buzzards Bay	41°23'48"N 71°02'00"W	1997-2014	[106]
Karehamn	56°59'02"N 17°01'20"E	2014-2015	E.ON
London Array	51°38'38"N 01°33'13"E	2014-2015	E.ON
Munnsville	42°55'09"N 75°32'04"W	2011-2015	E.ON
OWEZ	52°36'22"N 04°25'08"E	2006-2010	[107]
Panther Creek III	31°58'06"N 99°54'06"W	2012-2015	E.ON
Pulaski Shoals	24°41'36"N 82°46'23"W	2006-2010	[108]
Robin Rigg	54°45'00"N 03°43'00"W	2010-2014	E.ON
Rodsand II	54°33'36"N 11°33'00"E	2013-2015	E.ON
Scroby Sands	52°38'42"N 01°47'13"E	2011-2015	E.ON

3.3.2 Transition Cycles from Measured Data

To investigate the significance of transition cycles on the total level of fatigue damage on the support structure the RF counting methods outlined in Section 2.2.3.4 were applied to a one year period of stress data from the tower of Turbine K1. The conventional RF counting methods, entailing processing of the data in independent ten minute subsets, were compared to the result produced by effectively RF counting the entire data period as a consecutive sequence. Additionally, the method presented by Larsen and Thomsen [72] was investigated

by accounting for only the stress cycles linking the maximum and minimum values in each ten minute period. A description of the RF methodologies used is presented in Table 3-7.

To compare the fatigue damage produced by each RF processing method, a fatigue damage ratio was used, from Equation (2-17),

$$\frac{D_A}{D_B} = \frac{\sum_{i=1}^{k} n_{A_i} \Delta\sigma_i{}^m}{\sum_{i=1}^{k} n_{B_i} \Delta\sigma_i{}^m} \tag{3-40}$$

where n_A and n_B are the cycle spectra produced by different RF counting methods. It can be seen that, by taking the damage ratio, the $\log \bar{a}$ intercept term cancels and the impact of the different counting methods is affected only by the Wöhler exponent from the S-N curve. It can also be seen that a hypothetical linear increase in stress ranges such as may arise from a stress concentration factor, for example, would also cancel with the damage ratio, indicating that the difference between the RF counting methods would be affected by the underlying load process, but not by the stress magnitude. As a fatigue endurance limit could be exceeded by such a linear increase in stresses any results calculated in this analysis would be trivial; i.e. the use of a constant gradient S-N curve means that the form of Equation (3-40) enables the general case to be examined [70].

Table 3-7. Description of RF counting methods used to investigate the significance of transition cycles.

RF Method	Description of Methodology
Half-cycle counting	Process the one year dataset in independent ten minute periods, accounting for the residue as half cycles according to Section 2.2.3.4.1.
Simple RF counting	Process the one year dataset in independent ten minute periods, accounting for the residue from each period by rearranging the sequence to start and end with the maximum value to ensure that no unclosed hysteresis cycles remain (from Section 2.2.3.4.2).
Continuous	Process the one year dataset in independent ten minute periods, but concatenate the residues in their original time series order to effectively ensure that all RF cycles can be accounted for correctly (from Section 2.2.3.4.3). Account for the residue which remains from the entire dataset with Simple RF counting, based on the assumption that a one year stress history is representative of subsequent years.
Larsen and Thomsen	Process the one year dataset in independent ten minute periods, accounting for the residue as half cycles according to Section 2.2.3.4.1. Additionally, concatenate the maximum and minimum values from each ten minute period in their chronological order, and process the sequence using Simple RF counting.

3.3.3 Transition Cycles from Load Case Analysis

The significance of transition cycles on the standard design approach was investigated, by which a one year representative time history of ten minute LCs was defined. The time history was identified from Turbine K1 SCADA wind data as outlined in Section 3.1.3.1.1, from which the steady state LCs could be readily identified. The number of transient LCs was taken from the frequency of occurrence supplied by the turbine designer, with instances substituted into the time history randomly in appropriate locations which were identified based on the wind speed criteria presented in Table 3-4. This resulted in a four year time history of $4\,years \times 365.25\,days \times 24\ hr/day \times 6\ periods/hr = 210{,}384$ ten minute LC periods. The methodology used to construct the LC history is shown in Figure 3-16.

The LC time history was then related to the corresponding time series stresses. To investigate the impact of transition cycles on the full life fatigue loading, the load histograms were processed using the methodologies outlined in Table 3-8, which are also displayed in the process diagrams in Figure 3-17 and Figure 3-18.

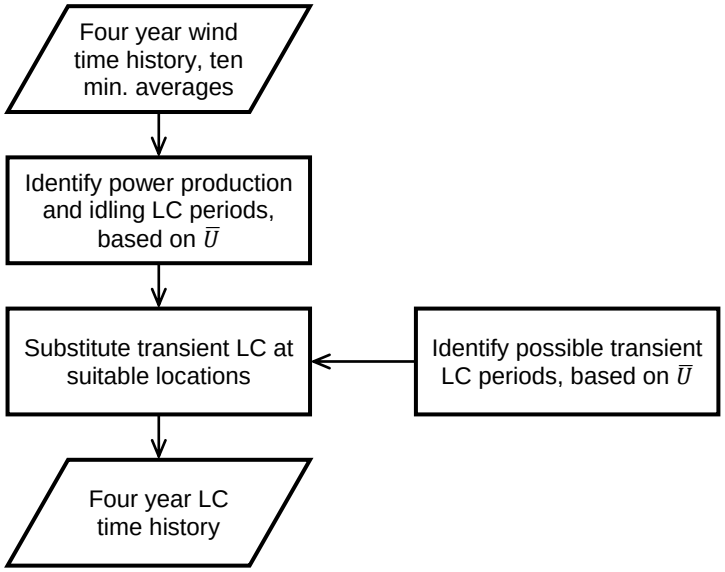

Figure 3-16. Process diagram showing methodology used to construct a representative LC history.

Table 3-8. Methodologies used to process the through-life fatigue load histograms. The methodologies were applied to the measured loading from Turbines H4 and K1, as well as the loading produced by the turbine designer.

Method	Description
Half-cycles	Each ten minute MLC/DLC was RF counted independently, with half-cycle counting of the RF residue, and then factored by the design frequency of occurrence. Using this methodology, the transition cycles, which link each LC period, are not accounted for.
Continuous	The ten minute MLC/DLC periods were RF counted independently without accounting for the residue, and then factored by the design frequency of occurrence. The four year representative LC sequence was then used to construct a synthetic stress history using the residue sequence from each MLC/DLC time series, concatenated in the time sequence order. The complete synthetic stress history was then processed using simple RF counting, so that no unclosed cycles remained, and the counted cycles were factored up to the twenty year design life. The methodology is shown in the process diagram in Figure 3-17.
Larsen & Thomsen	The four year representative LC sequence was used to construct a synthetic stress history following the methodology outlined by Larsen and Thomsen [72], which was then processed using simple RF counting and then factored by the twenty year design life. The identified transition cycles were then added to the cycles produced using the half-cycles methodology outlined above. The methodology is shown in the process diagram in Figure 3-18.

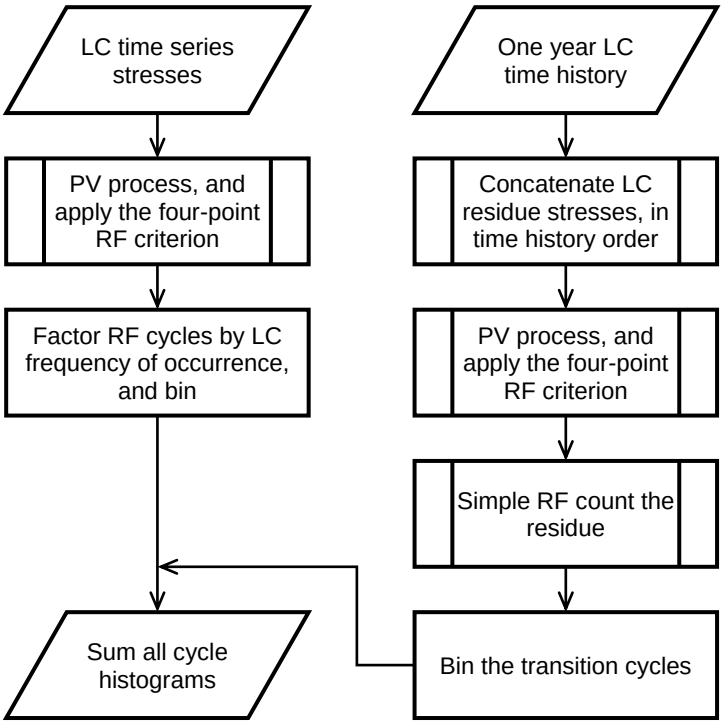

Figure 3-17. Process diagram showing method used to correctly identify transition cycles, without double counting of residue data points.

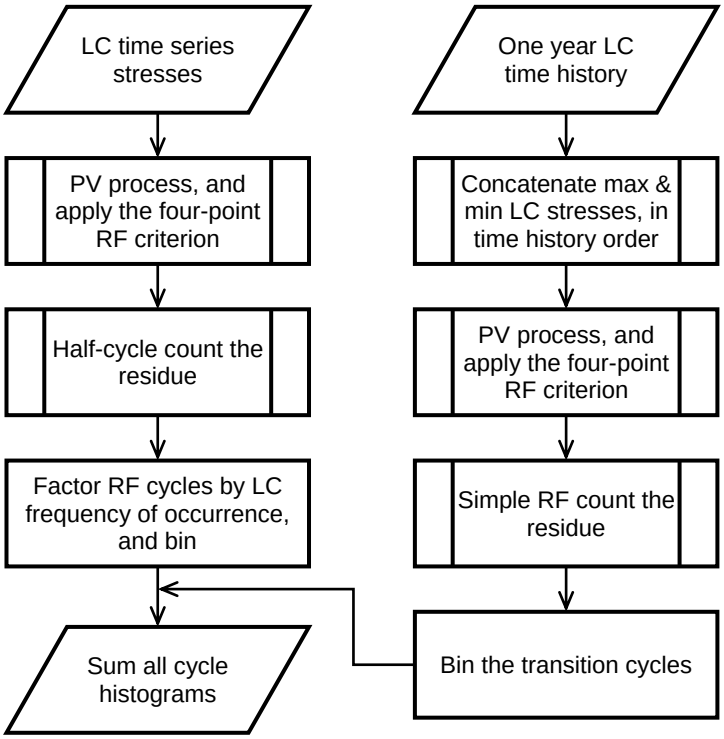

Figure 3-18. Process diagram showing method used by Larsen and Thomsen to identify transition cycles (methodology outlined in [72]).

3.4 Numerical Modelling

To understand the potential variation in the measured loading across the site, with changes in sea depth and with natural frequency of the structures, the turbines were modelled using DNV-GL Bladed software [109]. The following sections detail the model definition and variables that were investigated.

3.4.1 Model Definition

3.4.1.1 Support Structure

The turbine support structure was modelled on dimensions of Turbine K1, using geometry information from the turbine and substructure design reports [93], [94]. Bladed software requires inputs at various heights specifying the outside dimensions in order to calculate aerodynamic and hydrodynamic loads, and structural mass and stiffness properties to determine the structural responses. The structural properties and equations are shown in Table 3-9, with material properties shown in Table 3-10. For the MP/grout/TP connection

the structural properties were estimated as the simple sum of the properties from each section over the length of the overlap. Point masses were included to represent non-distributed loads such as working platforms or the mass damper. The calculated values at each station are shown in Figure 3-19.

It was not possible to model the foundation-soil interaction as a software license for the foundation module add-on was not available. Therefore, an Effective Fixity (EF) depth with a stationary bottom node below the sea bed level was used to approximate tower displacement and rotation at the sea bed, which could not be more accurately represented with soil springs. The height of the bottom node was adjusted to match the structural first mode frequency given by the foundation designer for a range of projected sea bed levels [87].

Damping values are required to be specified for each tower bending mode, given as a fraction of critical damping. The overall damping on the support structure arises from a combination of hydrodynamic damping (from wave radiation and viscous forces), material damping in the structural steel and grout connection, and soil damping, as well as aerodynamic damping arising from viscous forces and vortex shedding [23]. Recommendations available in the literature give a range of 0.8% - 1.2% of critical damping for the first structural mode [23], [110]. Based on these values a structural damping value of 1% was used for each structural mode.

Table 3-9. Calculation of structural properties for the support structure node stations.

Structural Property	Equation
Mass per unit length (m/l)	$\rho\pi({r_{outside}}^2 - {r_{inside}}^2)$
Bending Stiffness (EI_A)	$E\frac{\pi({r_{outside}}^4 - {r_{inside}}^4)}{4}$
Torsional stiffness (GJ)	$\frac{E}{2(1+\nu)}\frac{\pi({r_{outside}}^4 - {r_{inside}}^4)}{2}$
Polar moment of inertia per unit length (I_P/l)	$\frac{1}{2}\rho\pi({r_{outside}}^4 - {r_{inside}}^4)$

Note: ρ indicates density of the structural material, E is Young's Modulus, I_A is the section's second moment of area, G is the material shear modulus, J is the polar moment of area, ν is the material Poisson's ratio.

Table 3-10. Material properties used for the support structure.

	S355 Steel	Ducorit Grout
Young's Modulus *E* [GPa]	210 [94]	60 [92]
Density ρ [kg/m^3]	7,850	2,000 [94]
Poisson's Ratio *v* [-]	0.303	0.19 [92]

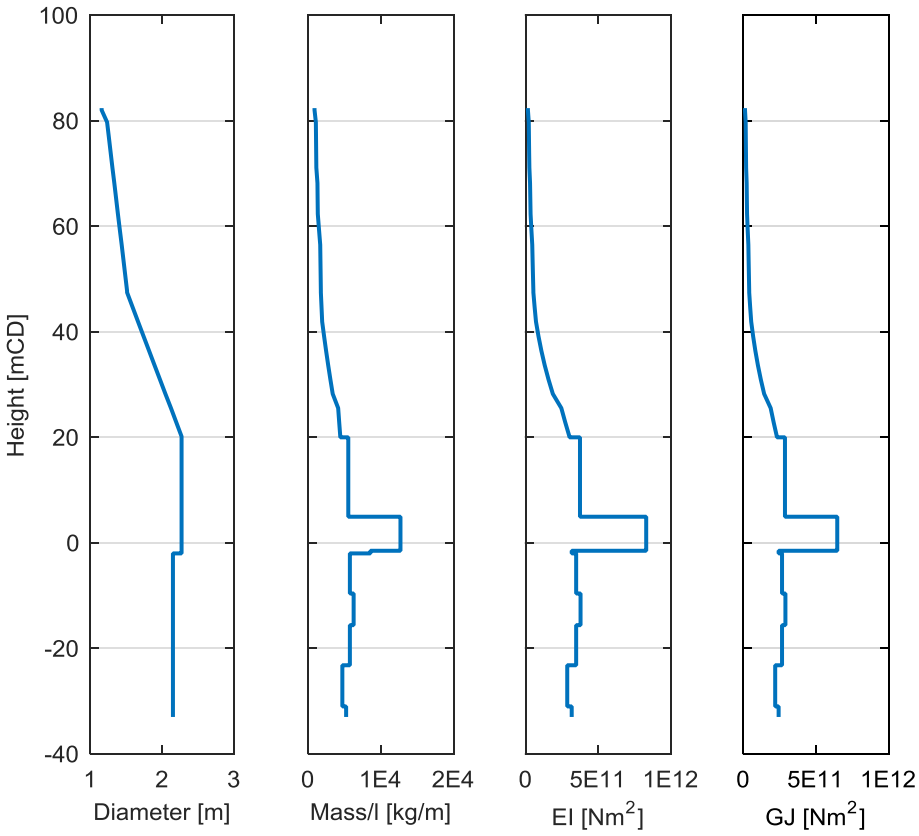

Figure 3-19. Properties used to define the support structure stations. Left to right; outside diameter, mass per unit length, bending stiffness, torsional stiffness.

3.4.1.2 Nacelle

The nacelle assembly specifications were taken from [93] and [111]. This included nacelle dimensions for calculation of drag loads, and mass distribution for the influence on structural dynamics. Values which could not be determined from the available information, such as drive train flexibility and generator inertia, were based on properties for a 5 MW reference turbine developed by NREL [112].

3.4.1.3 Rotor

The blade properties have an important influence on the aerodynamic loading and structural response of the turbine. As minimal detailed information for the turbine blades was available in the public domain, the model was based on the properties of the NREL 5 MW reference turbine [112]. The blade definition was scaled to a 3 MW equivalent based on the weight, dimensions, and operating conditions given in Table 3-11.

The blade station geometrical properties were scaled by the total blade radius and maximum chord length, while the mass and inertia properties were scaled by the total blade weight, using information provided in [111]. The blade bending and torsion stiffness properties were scaled to maintain the same deflection angle under the assumption of equal pressure load acting on the blade surface. As the blade station aerofoils were kept the same, the blade station twist angle was simply adjusted according to the tip speed ratio to maintain the same angle of attack. The conversion methodologies are shown in Table 3-12, and some of the converted properties are displayed in Figure 3-20.

Table 3-11. Rotor dimensions used to scale blade properties.

	NREL 5 MW [112]	3 MW [93], [111]
Rotor diameter [m]	126	90
Max chord length [m]	4.65	3.512
Rated speed [rpm]	12.1	16.07
Total mass [tonnes]	17.75	6.76

Table 3-12. Conversion methodologies used to scale blade properties from the NREL 5 MW turbine rotor.

Blade Property	Scaling Conversion
Blade station radius	$r_{2_i} = r_{1_i}\frac{R_2}{R_1}$
Chord length	$c_{2_i} = c_{1_i}\frac{C_2}{C_1}$
Aerodynamic twist	$\beta_{2_i} = \tan\left(\frac{\omega_{1_i} r_{1_i}}{\omega_{2_i} r_{2_i}} \tan^{-1}\beta_{1_i}\right)$
Mass per unit length	$m_{2_i} = m_{1_i}\frac{M_2}{M_1}\frac{R_1}{R_2}$
Polar inertia per unit length	$I_{2_i} = I_{1_i}\frac{M_2}{M_1}\frac{R_1}{R_2}\left(\frac{C_2}{C_1}\right)^2$
Bending stiffness	$EI_{2_i} = EI_{1_i}\frac{C_2}{C_1}\left(\frac{R_2}{R_1}\right)^2$
Torsional stiffness	$GJ_{2_i} = GJ_{1_i}\left(\frac{R_2}{R_1}\frac{C_2}{C_1}\right)^2$

Note: Subscripts 1 and 2 identify the 5 MW and 3 MW rotors, respectively, while *i* indicates the individual blade stations. *R*, *C*, and *M* are the total blade radius, maximum chord length, and total blade mass, respectively, where lower case symbols indicate individual blade station properties. ω is the rotor rotational velocity at rated wind speed, and β is the aerodynamic twist at each blade station.

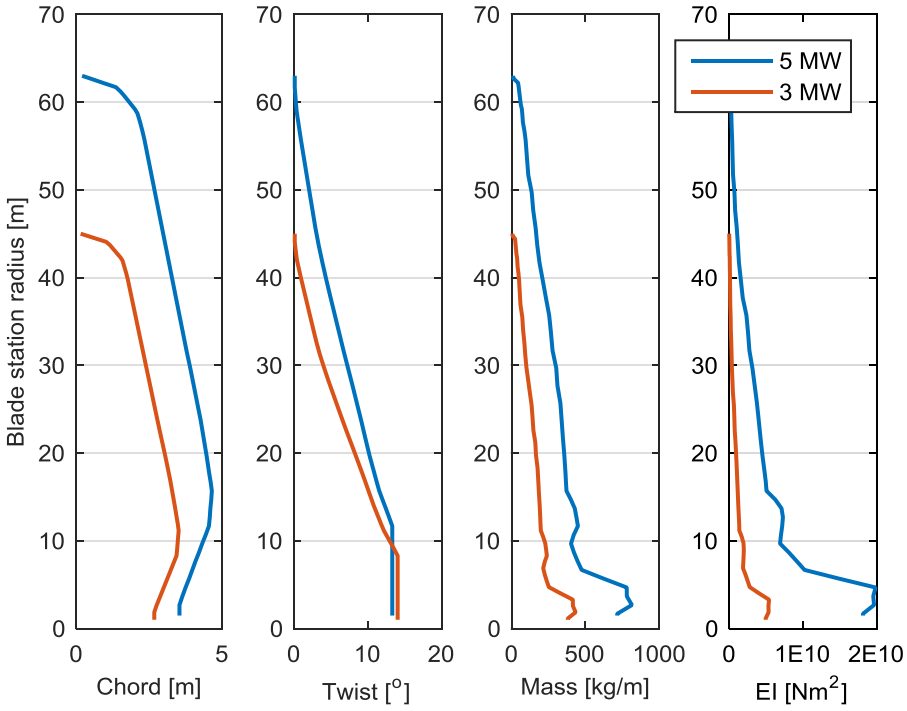

Figure 3-20. Blade station properties scaled from 5 MW to 3 MW. Left to right; chord length, aerodynamic twist angle, mass per unit length, bending stiffness.

3.4.1.4 Controller

The turbine controller defines the nacelle yaw, blade pitch, and generator torque responses to external wind loading conditions. For a variable speed, pitch regulated turbine the rotor speed varies with wind speed to keep the turbine operating at optimum tip speed ratio for wind conditions up to rated wind speed (U_{rated}). Above U_{rated} the rotor velocity is kept constant while the blade pitch angle varies in order to catch less wind and limit the generator power. The turbine varies the generator torque in both regimes to control the rotor speed via a closed loop system which is usually based on a PI controller (proportional and integral gains). However, the design of the controller is a specialist task as the gain can be varied with operating point in order to minimise actuations and potentially to reduce structural dynamics [113]. As limited information was available in the public domain to enable the specific turbine controller to be defined accurately, an automatic calculation of the controller gains was performed within Bladed. It is noted that the resulting controller is designed for steady operation loads and does not account for structural and actuator dynamics, or turbulent and non-uniform wind [113].

The steady state power and thrust coefficient curves resulting from the blade and controller definitions are compared to those of the actual turbine (from [111]) in Figure 3-21 below. It can be seen that the model has similar rotor characteristics to the turbine above rated wind speed (13 m/s), but with a different profile below rated wind speed.

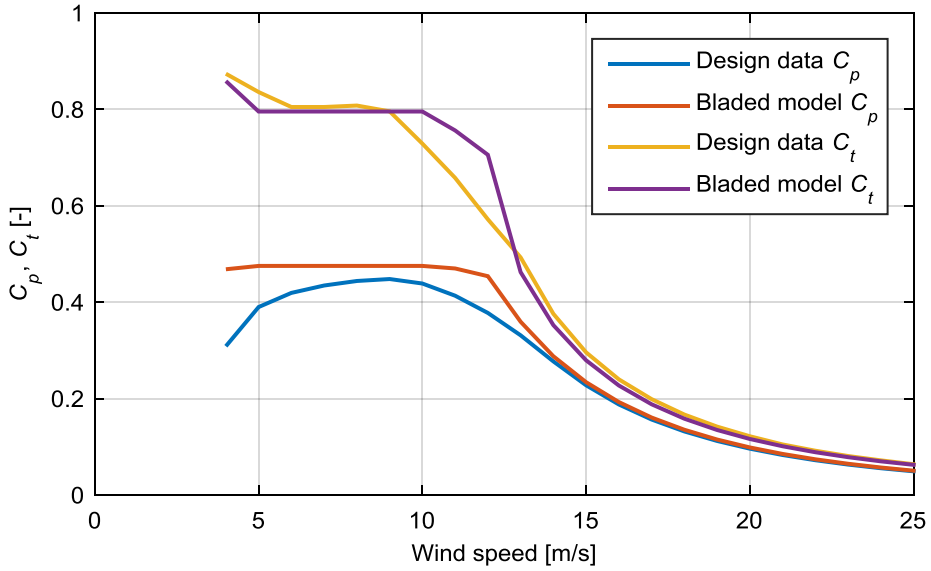

Figure 3-21. Comparison of thrust (C_t) and power (C_p) coefficient curves from the Bladed model and actual turbine design data (from [111]).

3.4.2 Wind Regime

The wind loading used for the model simulations was generated within Bladed, based on specifications given in [21]. A three dimensional turbulence time history was generated using a Mann spectrum [114] with parameters recommended in [113]. An exponential wind shear profile was included, with the same exponent used for design [93]. The simulated loads produced by the turbine designer used wind turbine class 'S' for the turbulence characteristics, whereby the TI values used differ from the IEC normal turbulence model [21]. The TI values used by the turbine designer were not available, but it was possible to calculate the standard deviation of the hub height wind speeds which were included with the model outputs for each LC bin, and to compare these values with the IEC normal turbulence model standard wind turbine classes A, B, and C. As reasonably close approximations are produced by the normal turbulence models with class B and C turbulence levels, these were used to model the wind loading to compare the model output with results provided by the turbine designer.

Additionally, the TI_{eff} values calculated using operational SCADA measurements from Turbine K1, as described in Section 3.1.3.1.1, were used to investigate the effect of operational turbulence levels on the model results. The measured values should be representative of the mean level of fatigue loading experienced by the operational turbines.

3.4.3 Wave Regime

Wave loading was included in the simulations, modelled with a JONSWAP spectrum with a peakedness parameter of $\gamma = 3.3$ [115]. Significant wave height H_s and peak spectral period T_p were varied with wind speed and direction LC according to the design distribution [87]. As limited information was available regarding the distribution of wave loading at the site, and the wave height measurements recorded at the offshore substation were assumed not to be representative of the wave conditions at Turbines H4 and K1, the design wave conditions were used for all sea bed depths used in the analysis.

As outlined in Section 3.4.1.1, an EF value was used to model the foundation stiffness for a range of sea bed depths. To ensure that wave loading was applied to the correct level of the support structure, the sea bed depth was varied according to the design values provided in [95].

3.4.4 Load Cases Investigated

Only the power production LCs were simulated as they were identified from the design documentation as having the dominant contribution to total fatigue damage [87].

Additionally, the transient LCs (start-up, shut-down, and emergency stop) require additional detailed controller information in order to accurately model actuation rates and resulting load effects.

Results of the model simulations were transformed to stresses at the location of the measured gauges and RF counted. RF cycles were then factored by the design frequency of occurrence to produce the through life fatigue histogram.

4 Discussion of Results: Measured Load Data Processing

4.1 Gauge Positioning; Finite Element Modelling

4.1.1 Comparison of Finite Element and Beam Bending Theory Stresses

The results from the FE analysis of the global gauge location are shown below. Figure 4-1 shows the stresses and displacements of the model under the maximum applied vertical and horizontal load, where the stopper brackets transfer a large portion of the load to the top of the MP on the compressive side of the structure, but are seen to lift away from the MP in tension (note that the stresses shown in Figure 4-1 are based on an arbitrary, hypothetical maximum load). Figure 4-2 shows a vertical stress path on the inside surface of the TP in two circumferential locations, also under maximum applied horizontal load, and shows close agreement between FE results and stresses calculated from simple beam bending theory (BBT) using Equation (3-13) down to the location of the global gauges. Below the global gauges the FE and BBT stress results start to diverge due to the stress raising effects of the stopper brackets and grout connection; towards the bottom of the grout most of the axial load has been transferred into the MP.

Figure 4-3 shows a circumferential stress path on the inside of the TP surface at the height of the global gauges under four horizontal load values. With zero horizontal loading there is a slightly more compressive stress with the FE result above the loaded stopper brackets as a result of the proportion of load transferred through the brackets to the top of the MP; under an applied horizontal load the effects of the stopper brackets are small except for the most compressive stopper bracket, where stresses are lower by approximately 6 MPa, or 7% of the maximum compressive stress. As the axial load is transferred through the TP into the MP, the load path is focussed through the stopper brackets, meaning that the stresses calculated in between the circumferential locations of the stopper brackets are proportionally lower. Although the difference between FE stresses and simple beam bending theory is small, it was considered important to quantify the influence that the difference would have on calculated fatigue damage, and this is detailed in Section 4.1.2 below.

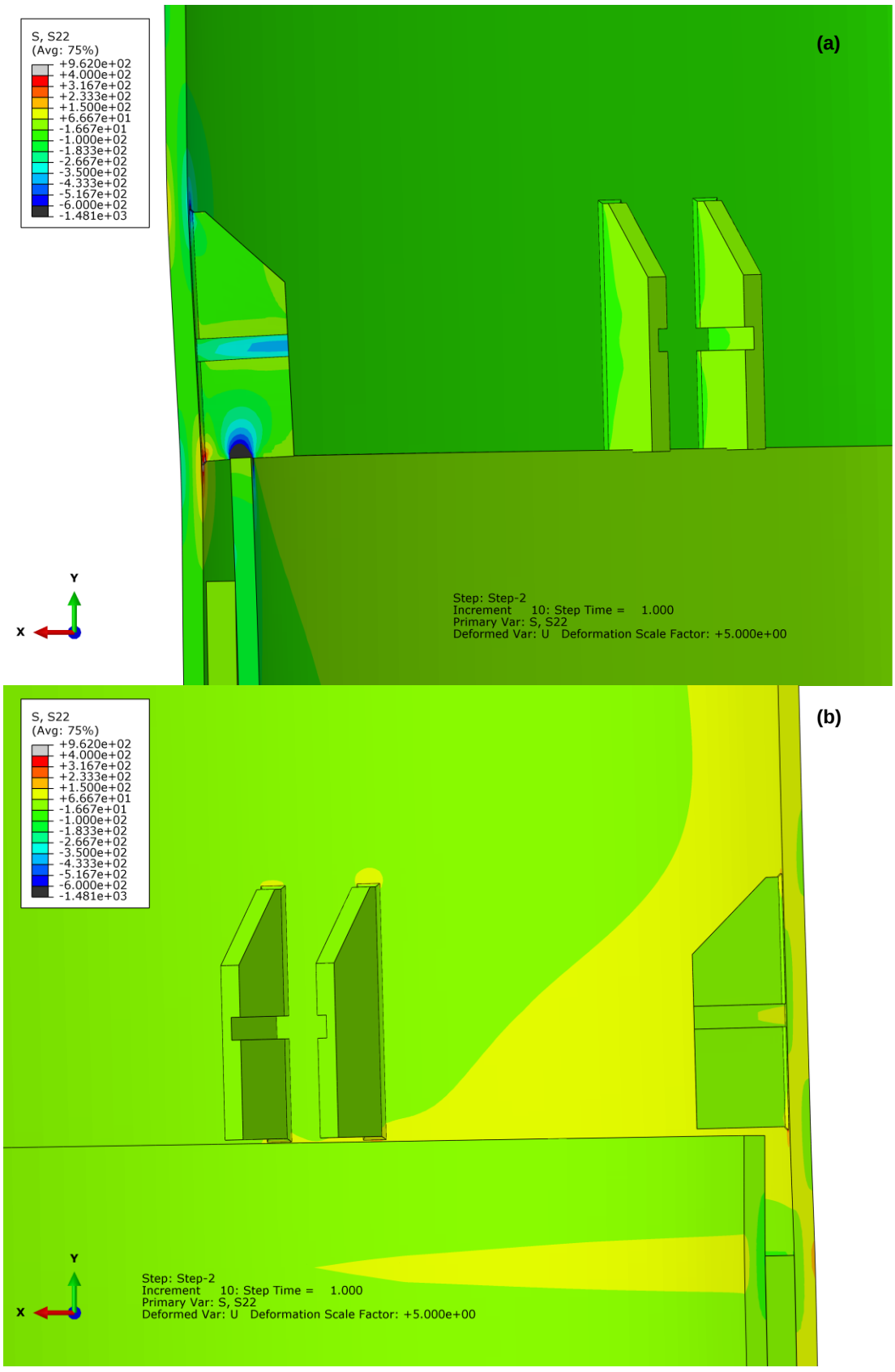

Figure 4-1. FE results showing the stress distribution and scaled displacements for the stopper brackets on the compressive side (a) and tensile side (b) of the structure.

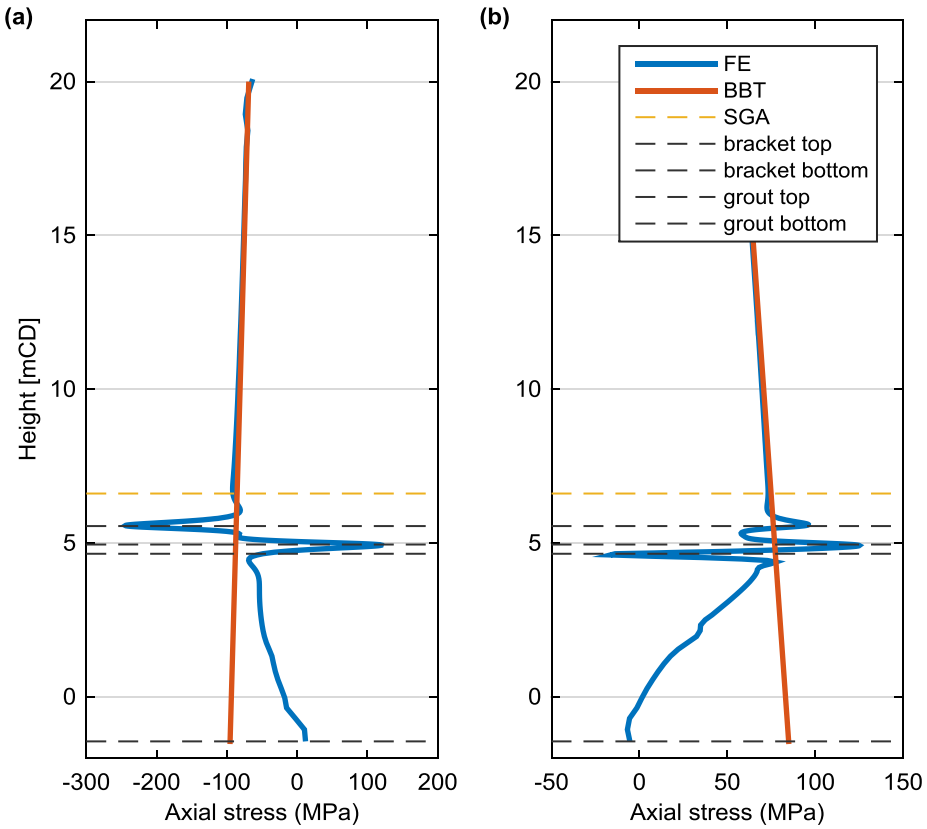

Figure 4-2. Surface stress on the inside face of the TP under maximum horizontal load. (a) Vertical path through the stopper bracket on the compressive side of the structure. (b) Vertical path through the tensile side. Blue line shows results from FE, red line shows results calculated from BBT using Equation (3-13). The yellow dashed line shows the height of the global gauges, while the grey dashed lines show other notable features of the brackets and grouted connection.

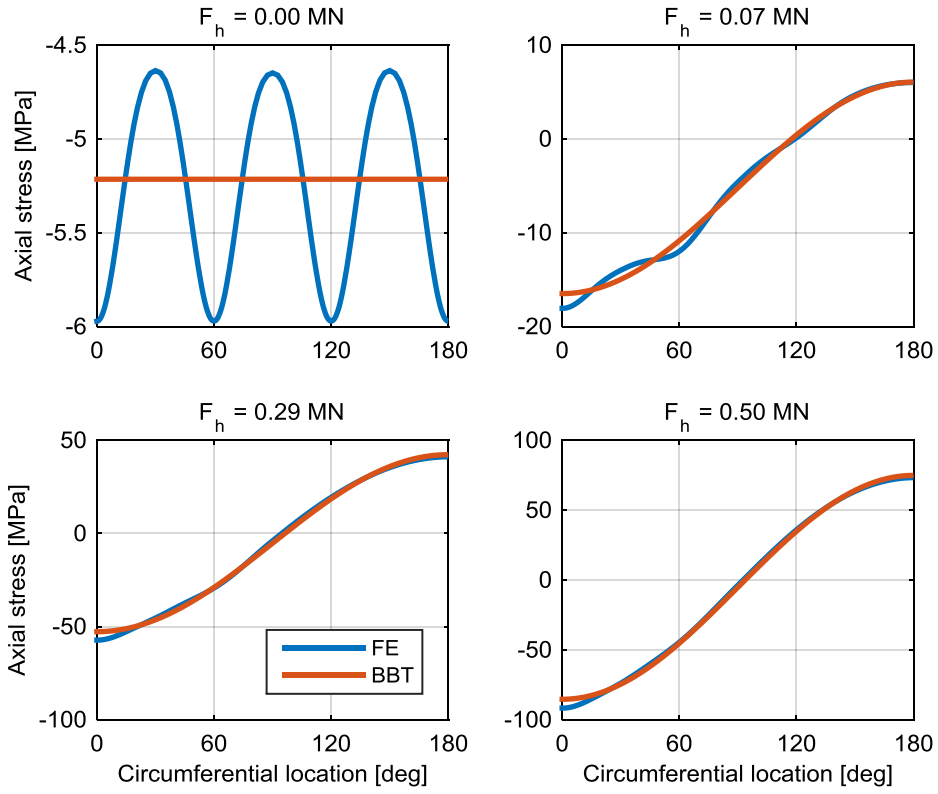

Figure 4-3. Surface stress on the inside face of the TP; circumferential path at the height of the global gauges (6.608 mCD). Blue line shows results from FE, red line shows results calculated from BBT using Equation (3-13).

4.1.2 Influence of Stress Raising Effects on Calculated Fatigue Damage

The FE results show very close agreement with stresses found from simple BBT at the location of the measured gauges, indicating that the gauges were installed far enough from the stress raising influence of the loaded brackets to assess the global loading of the structure. Therefore, a comparison between measured data and design stresses calculated from BBT should give reasonable results. However, it was decided to investigate the impact of the slight stress raising effects shown in Figure 4-3 on calculated fatigue damage to ensure that the use of measured data would give a conservative comparison with the design loading.

To enable the FE results at the location of the strain gauges to be used for different loading directions to those which are able to be directly interpreted (i.e. at 0, 60, 120, 180 degrees offset between the gauge location and horizontal load vector), a directional transfer function

was calculated. The differences between FE and BBT stresses were calculated from the results at the circumferential location of the stopper brackets,

$$\delta FE(\varphi) = \sigma_{FE}(\varphi) - \sigma_{BBT}(\varphi), \;\; \varphi = 0^0, 60^0, 120^0, 180^0 \tag{4-1}$$

where φ is the circumferential location of the stopper brackets/global gauges in degrees, and σ_{FE} and σ_{BBT} are the stresses calculated from FE and BBT, respectively. As the results from Equation (4-1) were derived from a half cylinder FE model, the results could be converted to the other circumferential gauge locations using $\delta FE(240^0) = \delta FE(120^0)$ and $\delta FE(300^0) = \delta FE(60^0)$. The results from Equation (4-1) were then used to linearly interpolate a stress correction value to account for any directional misalignment between gauge location and resultant bending moment,

$$\delta FE(\varphi, \theta_{res}) = interpolate\{\delta FE(\varphi)\}, \;\; 0 \leq \theta_{res} < 360 \tag{4-2}$$

where the resultant bending moment angle (θ_{res}) is given by,

$$\theta_{res} = \tan^{-1}\frac{M_y}{-M_x}, \;\; \theta_{res} = \begin{cases} \theta_{res} + \pi, M_x > 0 \\ \theta_{res} + 2\pi, M_y < 0 > M_x \end{cases} \tag{4-3}$$

The stress correction could then be applied to the BBT stress to account for the elevated stresses at the gauges under any direction of applied loading using,

$$\sigma_{FE}(\varphi, \theta_{res}) = \sigma_{BBT}(\varphi) + \delta FE(\varphi, \theta_{res}) \tag{4-4}$$

An example of the stress correction is shown in Figure 4-4, and a stress time series produced using design loads is shown in Figure 4-5.

Finally, the DES values produced from the DLC load results were calculated using both BBT and the FE correction from Equation (4-4), and then factored by the full life frequency of occurrence to give the total DES using each method of stress calculation. The ratio of DES values is shown in Figure 4-6, and indicate that by accounting for the stress raising influence of the stopper brackets at the location of the measured gauges an increased level of fatigue damage would be calculated, by an approximate factor of $0.95^{-3} = 17\%$ using $m = 3$, or $0.95^{-5} = 30\%$ using $m = 5$ (from Equation (2-19)). This indicated that, although the effects of the stress raisers are small, a conservative fatigue damage comparison would result from stresses calculated from the measured data and stresses calculated from the design simulation results using simple BBT. This result is important as the exact height tolerance of each stopper bracket is not known, and therefore cannot be used to determine the specific stress

raising effects accurately. Therefore, the FE results have been used to demonstrate that, although the measured data is slightly affected by the presence of the stopper brackets, the comparison with design stresses calculated with simple BBT is conservative.

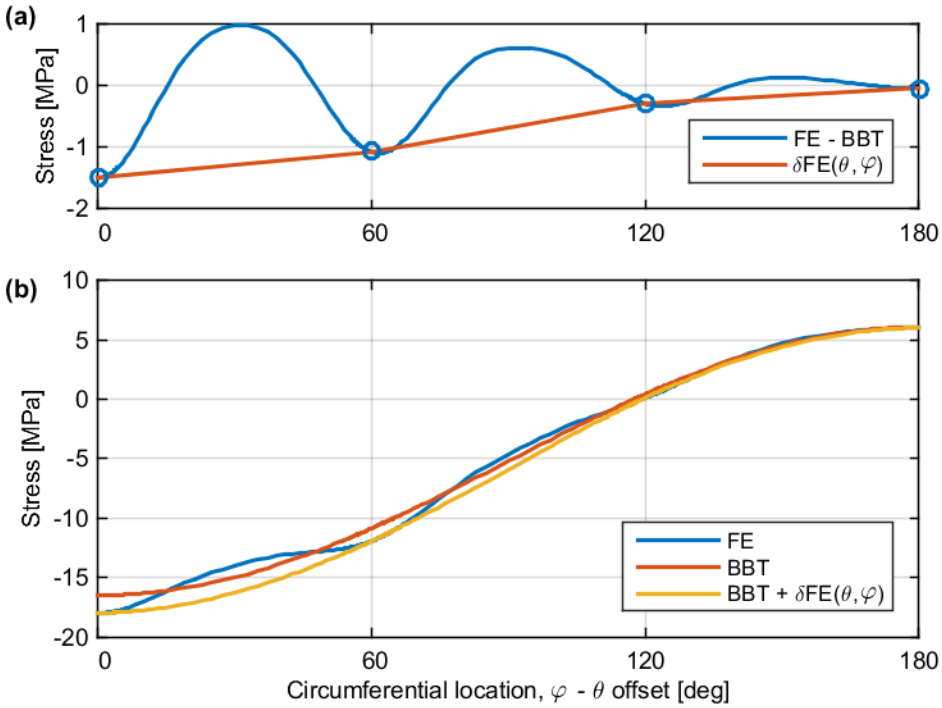

Figure 4-4. Correction used to apply FE results to multidirectional loading, with an applied horizontal load of F_h = 0.07 MN. (a) Blue line shows stress from FE results minus BBT stress from Equation (4-1); red line shows linearly interpolated values between gauge locations from the FE model using Equation (4-2). (b) Stress from FE and BBT (blue and red lines, respectively) vs circumferential location. Yellow line shows stress vs directional misalignment between gauge location and resultant bending moment, from Equation (4-4).

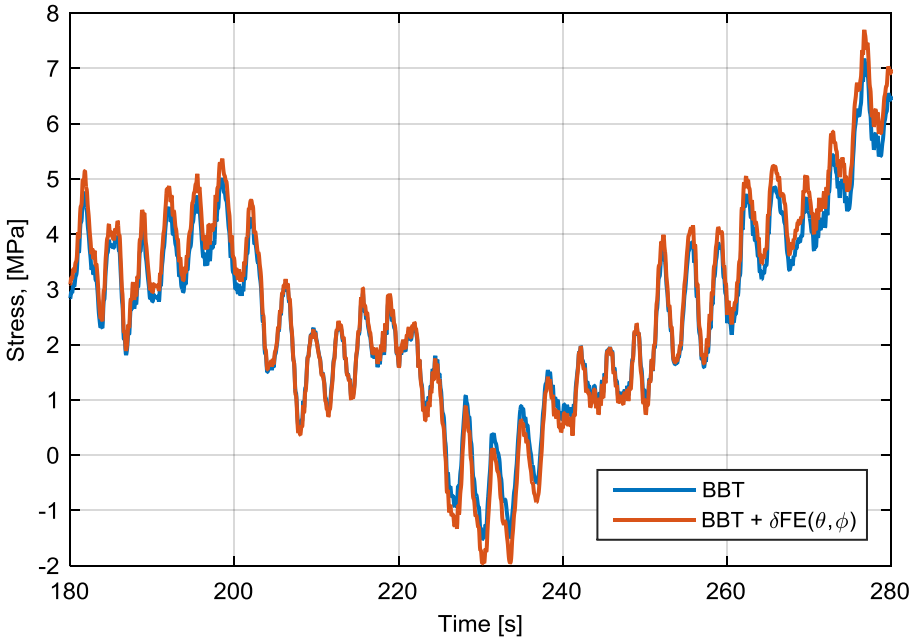

Figure 4-5. Example stress time series accounting for stress raising effects, calculated from the design simulation results. Blue line shows gauge location stresses calculated from simple BBT; Red line shows BBT stress plus FE correction value from Equation (4-4).

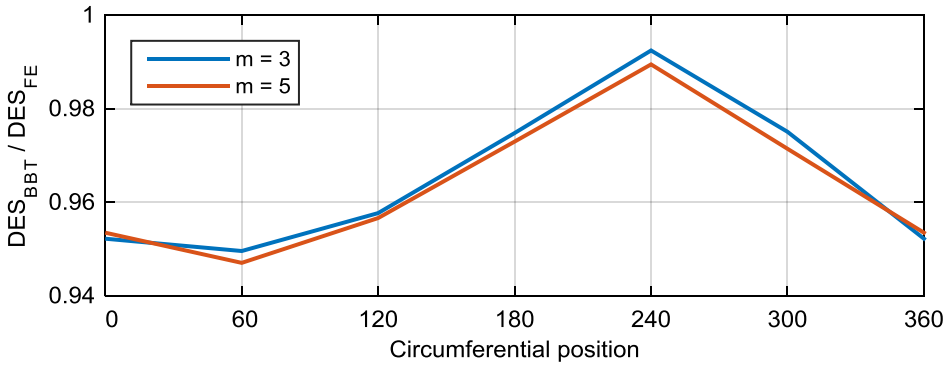

Figure 4-6. Ratio of Damage Equivalent Stresses calculated using BBT and FE, for the full life fatigue loading (from design loads).

4.2 White Noise Reduction

The effect of the low pass filter is shown below in Figure 4-7 and Figure 4-8, with two sets of data from gauge K1-S4-SGA with similar environmental and operational loading

conditions. The first time period in the below figures includes minimal noise, while the later period includes a significant level of additional white noise overlaid on the stress signal. The structural response at the second mode of approximately 1.5 Hz is apparent in Figure 4-8a, and is retained after application of the low pass filter (cut-off frequency = 2 Hz). However, it should be noted that that the second mode response is rarely observed in the full 18 month data period, and is of low amplitude compared to the response at lower frequencies.

Figure 4-9 below shows the impact of the low-pass filter on the DES calculated from Equation (2-18) for each of the global gauges from Turbine K1. Some of the gauges display 'spikes' in the calculated DES at a number of occasions in October and at the beginning of December; these periods represent erroneous readings which were identified and later removed during data quality checks. The unfiltered signals display a significant increase in DES values after a period of one to two months of operation, particularly for gauges S4-SGAV and S6-SGAV (Figure 4-9d & f). Although S6-SGAV only displays a DES increase by a factor of approximately three, Equation (2-19) shows that the relative increase in calculated fatigue damage would be in the order of 3^3, or approximately 27 times higher than at the beginning of the measurement period, and hence the variation of the DES value with changes in the environmental loading can be seen to be effectively swamped. The filtered signal for gauge S6-SGAV, however, can be seen to retain a minimum level of increased DES compared to the values at the beginning of the measurement period, which results from the noise level which is retained below the 2 Hz cut-off frequency. Although an optimal measurement system would contain only the underlying signal, it would be difficult to justify lowering the filter cut-off to further eliminate the additional noise at lower frequencies, as the loss of information of the real physical response at these frequencies could reduce the level of calculated fatigue damage. Therefore the low pass filter design as described in Section 3.1.2.5 was used to reduce the level of noise in the measured data, as it has been demonstrated to be conservative.

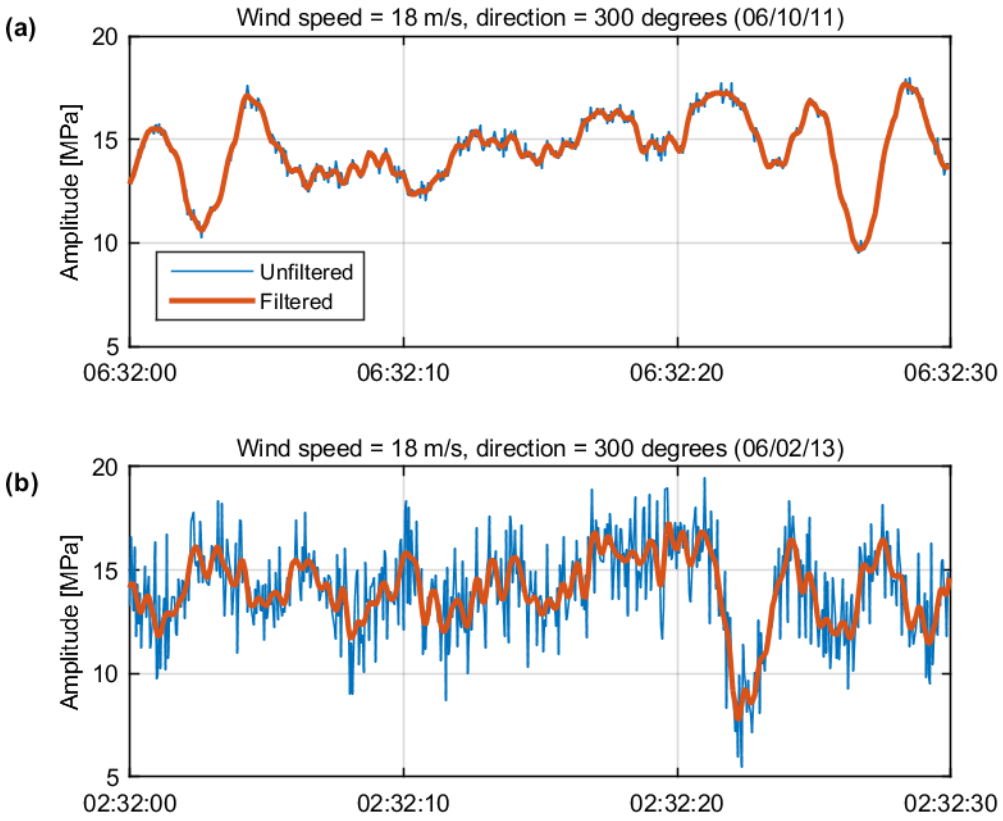

Figure 4-7. Time series plots from gauge K1-S4-SGA with low pass filtering, showing data periods prior to additional noise (a), and later with additional white noise (b). The effect of the low pass filter on the additional noise is particularly noticeable in Figure (b).

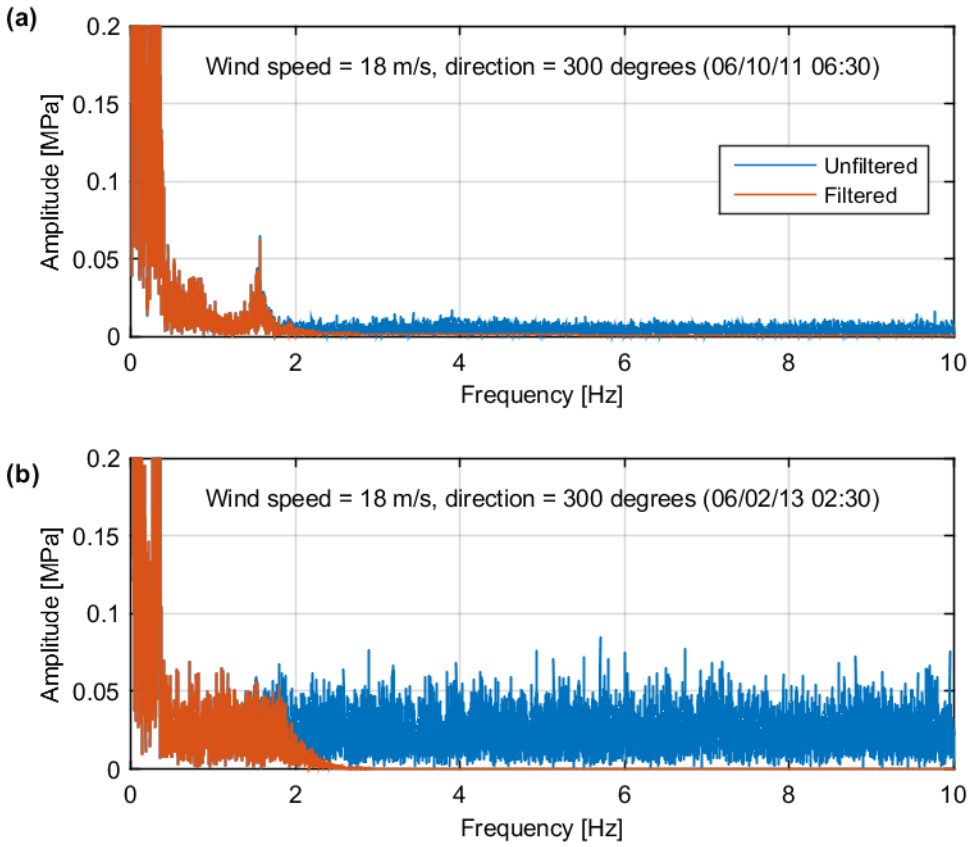

Figure 4-8. Amplitude spectrum from gauge K1-S4-SGA with low pass filtering, showing time periods prior to additional noise (a), and later with additional white noise (b). The effect of the low pass filter is seen at the 2 Hz cut-off frequency.

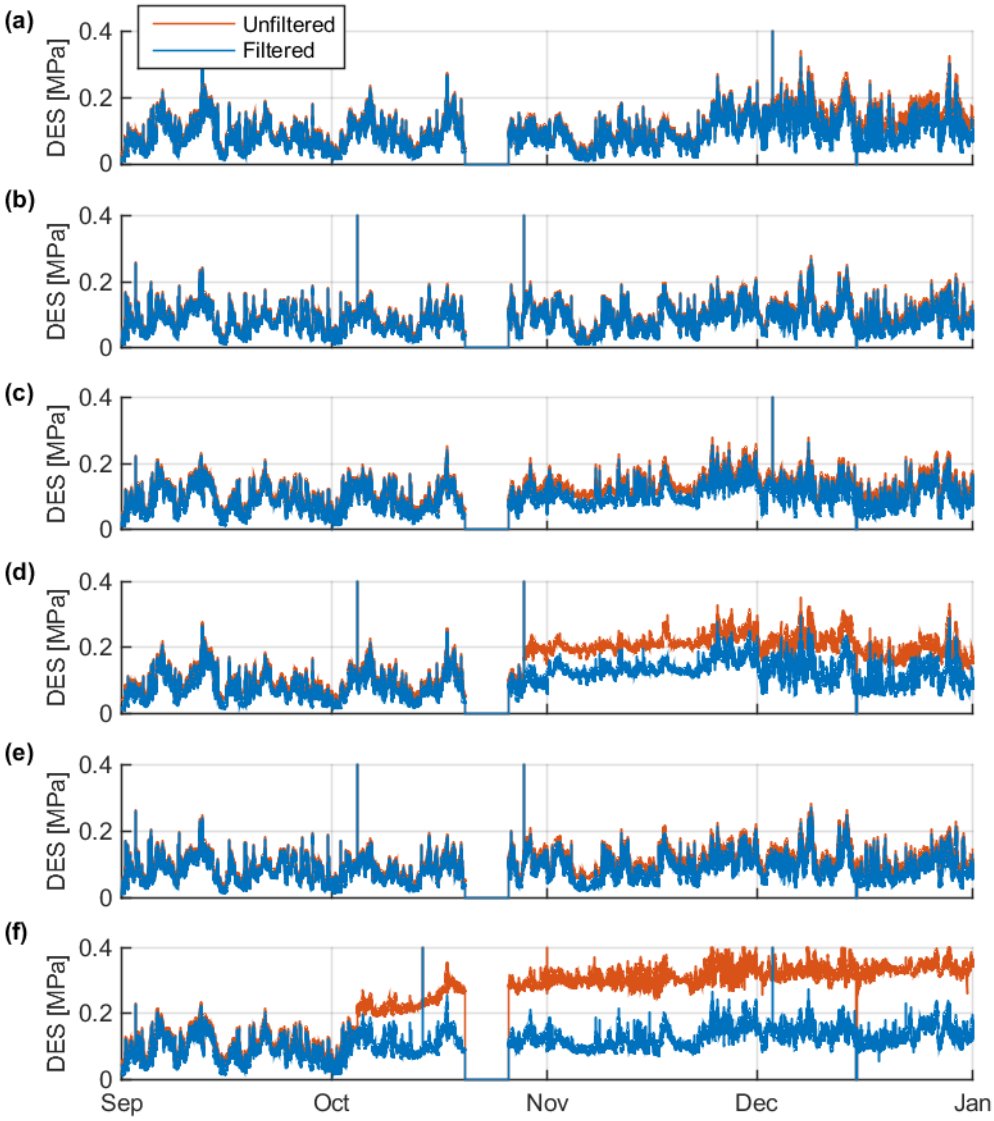

Figure 4-9. Impact of the 2 Hz low pass filter on Damage Equivalent Stress, calculated using *m* = 3 for each ten minute period of data for the beginning of the measurement period. Subplots (a) to (f) show data from Turbine K1 gauges S1-SGAV to S6-SGAV (top to bottom).

4.3 Datum Drift Correction

The initial datum values for each of the Turbine K1 global gauges, and their drift over the total measurement period, are shown in Figure 4-10 below. Figure 4-10a shows the datum offset for each ten minute period for gauge S1-SGAV along with the 1,000 point moving

average value. The maximum drift over the total measurement period of approximately 25 MPa can be expected to have a significant impact on the gauge function fitting, and therefore also the estimation of the global responses.

Figure 4-11 shows the ten minute mean stress values prior to datum drift correction in relation to the ideal mean stress level resulting from the design simulations, from which the method of identifying the long term gauge drift using Equation (3-3) can be seen. Figure 4-12 shows the same data with datum drift corrected, and the effect of the correction is shown in Table 4-1, quantified by the root mean squared error (RMSE) between the design and measured mean stress values.

Ideally, datum drift would be corrected where necessary through periodic re-calibration of the measurement system. However, where re-calibration may be impracticable due to site logistics or timescales, for example, the methodology outlined in Section 3.1.2.6 allows datum drift to be corrected whilst accounting for large scale stress variations due to changes in rotor thrust loading. This is necessary prior to combination of the gauge signals via cosine function fitting, with results presented in the following section.

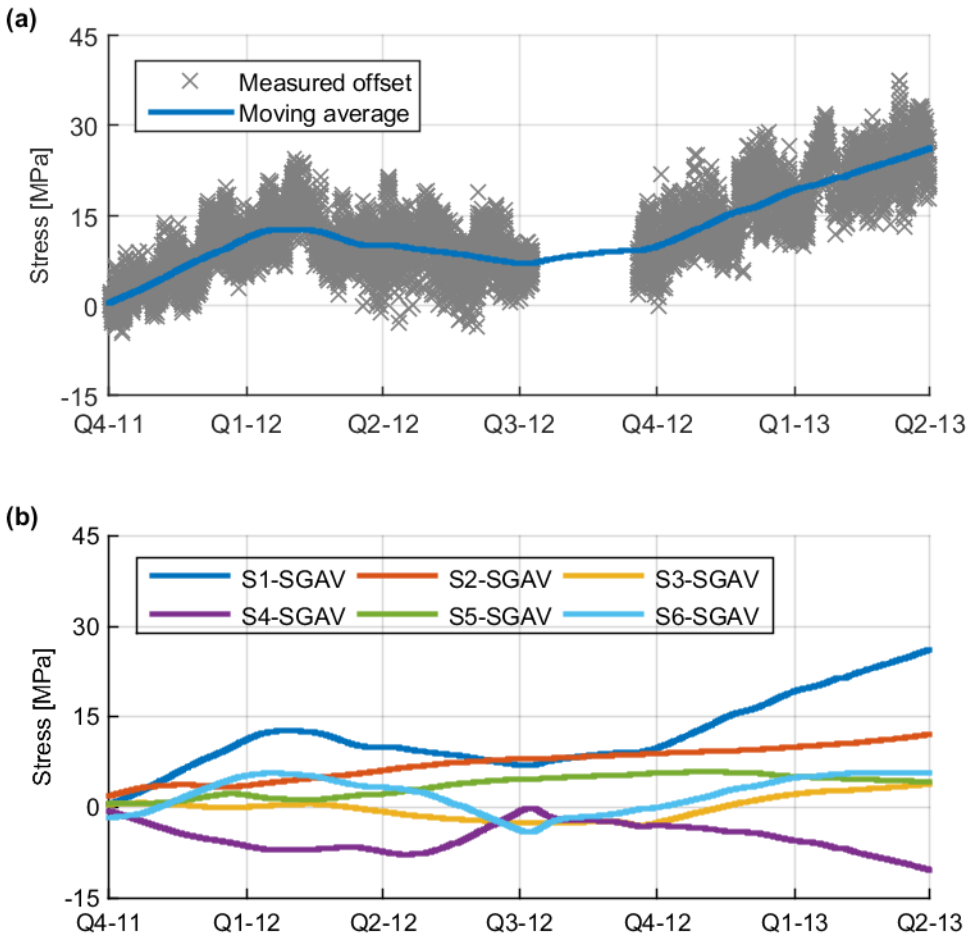

Figure 4-10. Datum drift in Turbine K1 global gauges. (a) Measured offset data points for S1-SGAV calculated using Equation (3-3), and the 1,000 point moving average value used to correct the data. (b) Moving averages calculated for each of the Turbine K1 global gauges.

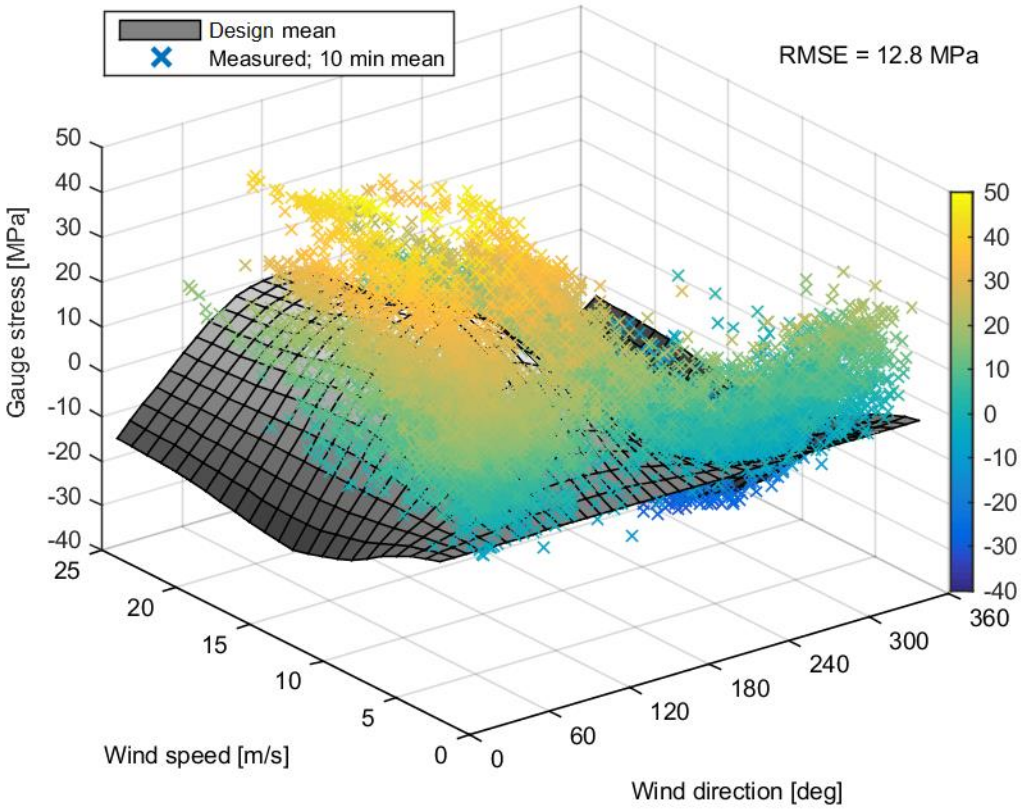

Figure 4-11. Design and measured mean stress from gauge K1-S1-SGA prior to datum drift correction. Design mean value calculated from power production DLC simulation results.

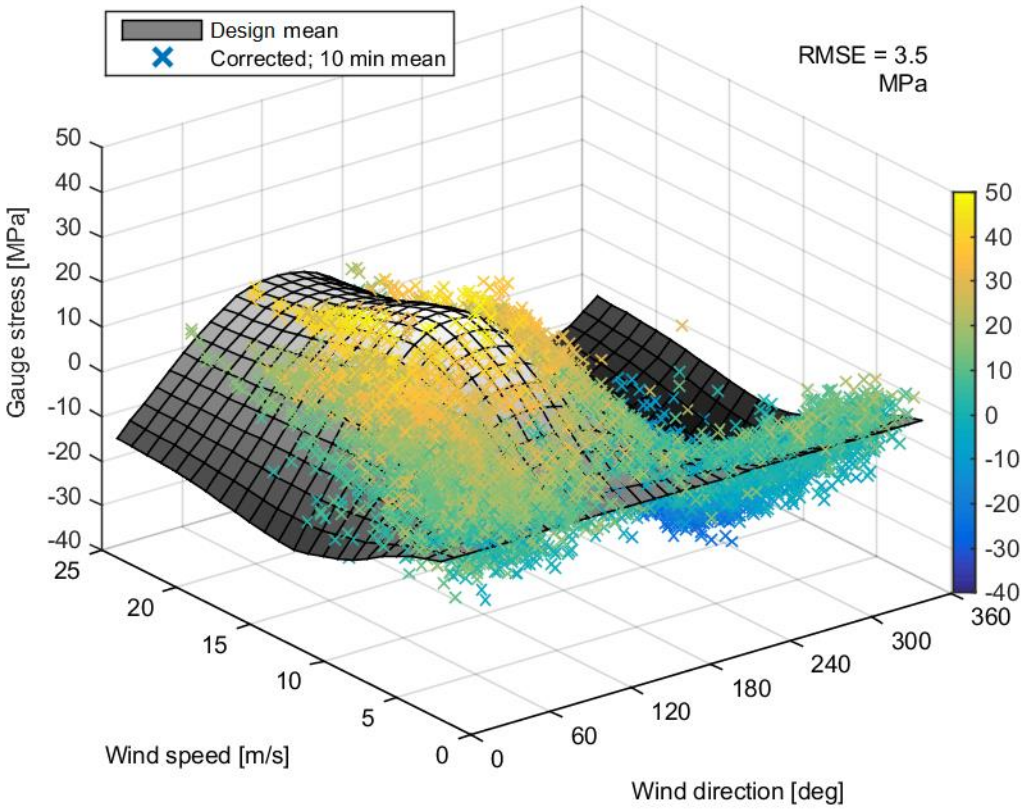

Figure 4-12. Design and measured mean stress from gauge K1-S1-SGA after datum drift correction. Design mean value calculated from power production DLC simulation results.

Table 4-1. Root Mean Squared Error values calculated with and without datum drift correction, for Turbine K1 global gauges.

	Non-corrected [MPa]	Corrected [MPa]
S1-SGA	12.78	3.52
S2-SGA	7.12	1.91
S3-SGA	2.49	1.88
S4-SGA	5.97	2.88
S5-SGA	4.14	2.23
S6-SGA	4.58	2.89

4.4 Cosine Fitting

Figure 4-13 below shows the impact of fitting the measured gauge stresses to a cosine function using Equation (3-9) on the DES calculated from filtered gauge data, calculated using Equation (2-18). It can be seen that the increased DES resulting from the additional white noise which occurs after approximately one to two months and which is still partially retained after application of the low pass filter (as displayed in Figure 4-9) is spread between the remaining gauges. Essentially, the increased DES values which are evident in S4-SGAV and S6-SGAV from November onwards are reduced by the cosine fitting, while the DES values for the remaining gauges result in a corresponding increase. This indicates that the additional white noise which cannot be removed from the data below the 2 Hz filter cut-off frequency can be partially reduced by function fitting with the remaining gauges. Therefore, the procedure is believed to be conservative as the impact of the additional noise, which is effectively distributed across all gauges by the function fitting, serves to artificially increase the calculated fatigue damage. This is additional to the main objective of the function fitting procedure, which is to allow measured strains to be related to global bending moments, Equation (3-12).

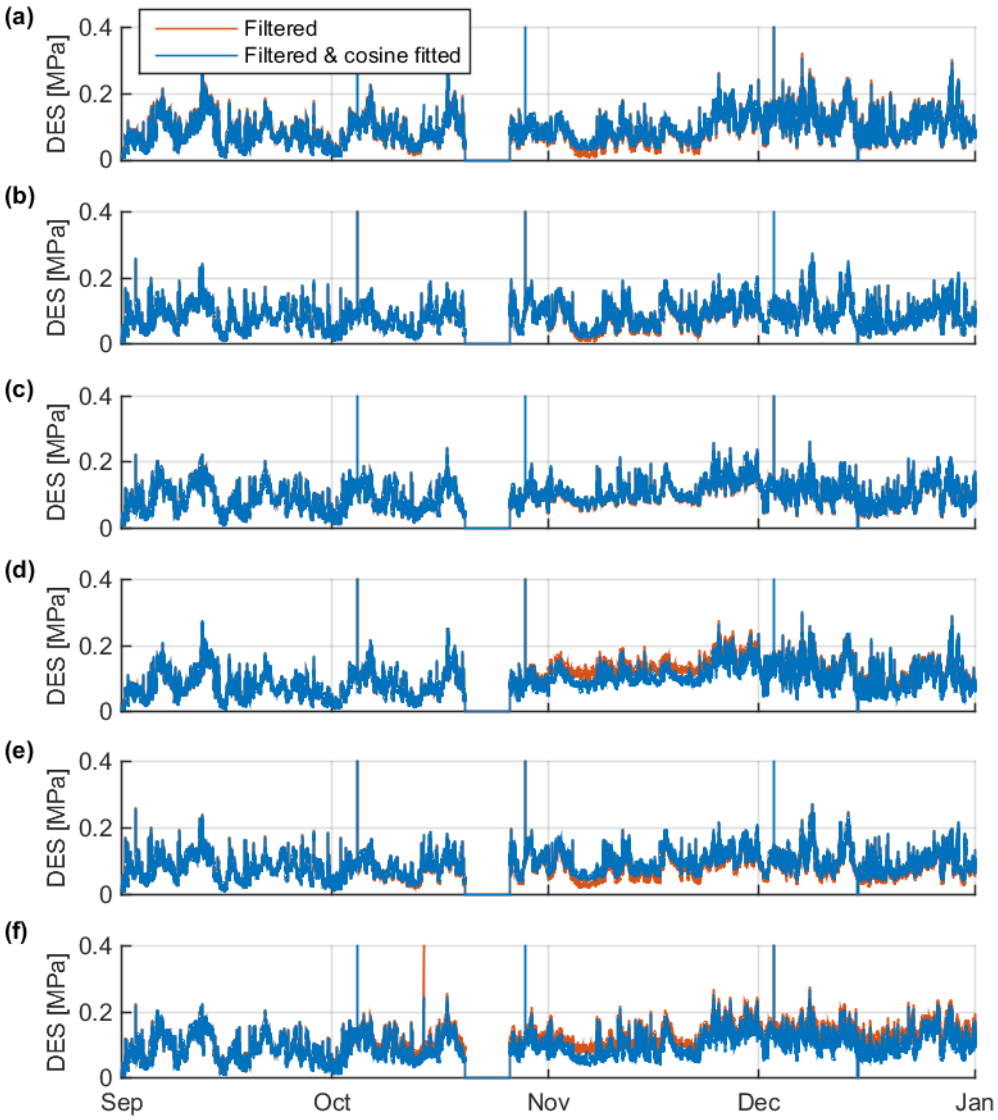

Figure 4-13. Impact of the cosine fitting function on Damage Equivalent Stress, calculated using $m = 3$ for each ten minute period of data for the beginning of the measurement period. Subplots (a) to (f) show data from Turbine K1 gauges S1-SGAV to S6-SGAV (top to bottom).

4.5 Sensitivity of Fatigue Calculations to Digital Sampling

The underlying peak cycle stresses, which may have been missed by the digital sampling of the data, were estimated by fitting a quadratic curve to three data points at each maxima and minima using the methodology outlined in [56]. The corresponding fatigue damage was

compared to the damage calculated from the as-measured time series using Equation (3-40), expressed at the ratio of normal fatigue damage to the damage calculated with extrapolation of the cycle turning points, using a total of 10^4 individual ten minute data periods. The distribution of the results is shown in Figure 4-14 below. The distributions are bounded by the reduced fatigue values estimated by Equation (3-16) at the first and second mode structural frequencies using $m = 3$; the first mode dominates the response of the structure, and this is reflected in the proximity of the distributions in Figure 4-14 to the value estimated for the first mode frequency. The same is true for the distribution calculated using $m = 5$, where the analytical reduced damage fraction from Equation (3-16) equals 0.998 at $f_s/f_n = 60$.

The mean of the distributions are 0.995 and 0.996, calculated with fatigue damage exponents of $m = 3$ and $m = 5$, respectively, and therefore the reduction in estimated fatigue due to digital sampling of the stress signal was deemed to be negligible, and no further peak extrapolation of the measured data was used for the fatigue analysis.

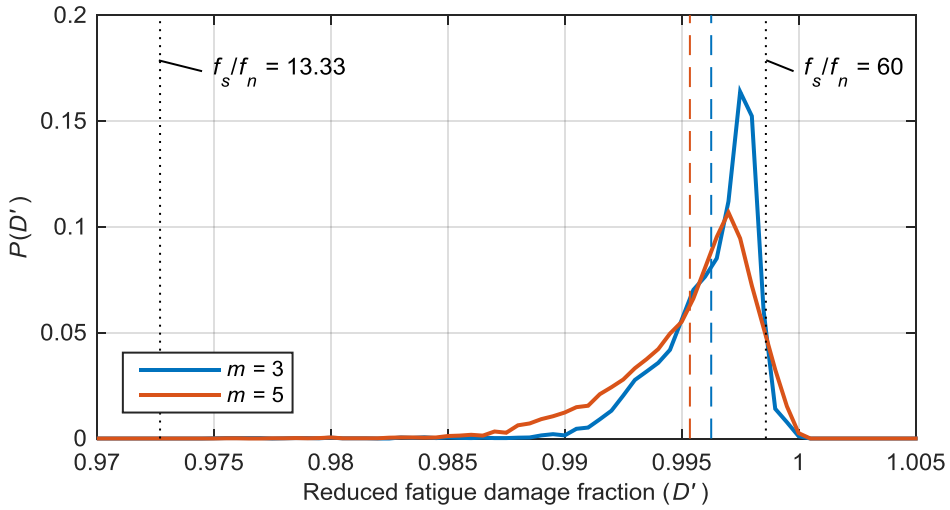

Figure 4-14. Distribution of the reduced fatigue damage resulting from digital sampling of the measured data, calculated using Equation (3-40). The mean values from each distribution are shown with a dashed line of the same colour. The reduced fatigue damage calculated from Equation (3-16) for normalised sample frequencies of 20/1.5 = 13.33 and 20/0.33 = 60 using *m* = 3, relating to the second and first modes of the support structures, are shown for comparison.

5 Discussion of Results: Environmental and Operational Data Processing

5.1 Measured Wind Distribution

The measured wind data taken from Turbine K1 SCADA over the period 2010-2013 were used to calculate the operational wind speed and direction distribution. Figure 5-1 compares the operational data with the directional distribution used for design. The design fatigue analysis was based on the wave distribution, as this was shown to produce a conservative assessment using combined wind and wave loading directions [87]. The operational wind speed measurements from Turbine K1 were fitted to a Weibull function from Equation (2-7), and the measured wind speed and direction distribution was then used as the frequency of occurrence to factor the design loads, to investigate the impact of the operational distribution on the total fatigue damage. The comparison of the fatigue damage produced by the design and measured distributions, expressed as a DEM using Equation (3-17), is shown in Table 5-1. The difference in through-life fatigue damage calculated using the two distributions is negligible, and therefore the design distribution was used for calculation of further results.

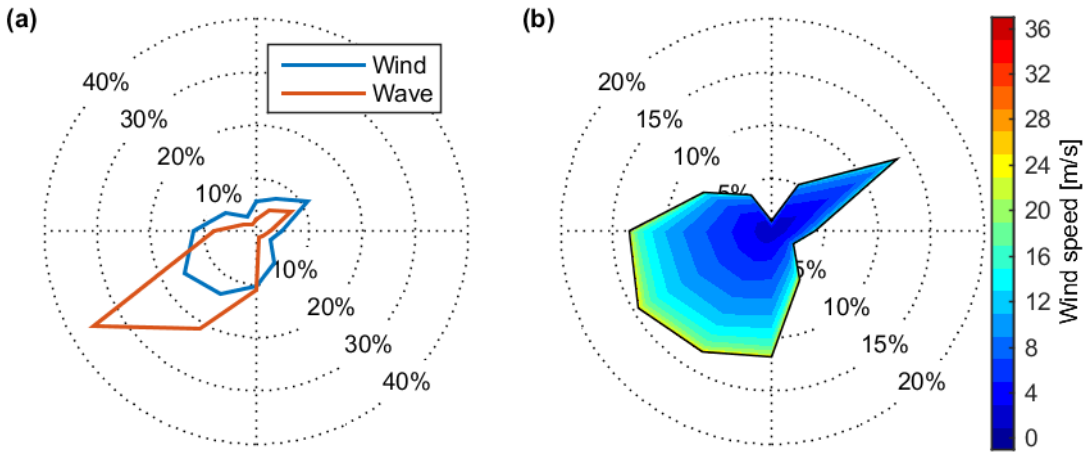

Figure 5-1. Comparison of design and measured wind distributions. (a) Design wind and wave direction distributions (from [87]). (b) Wind speed and direction distribution from Turbine K1 SCADA data, 2010-2013 (wind speeds fitted to a single Weibull function for all directions).

Table 5-1. Ratio of Damage Equivalent Moment resulting from the design and measured wind distributions. Results are normalised by the design DEM.

	Design	Measured
m = 3	1.00	0.96
m = 5	1.00	1.00

5.2 Measured Turbulence

5.2.1 Assessment of Meteorological Mast Turbulence

The MM data was found to contain distorted values of wind speed mean and standard deviation which was characteristic of the effect of rounding, as described in Section 3.1.3.1.2. The raw data is shown in Figure 5-2, and is compared to the minimum rounding error function given by Equation (3-26) with a fitted period indicating an anemometer correlation coefficient of P = 1.2505 m/s/Hz. Results from the 10^6 Monte Carlo simulations produced the distribution of mean and standard deviation rounding errors shown in Figure 5-3, which were used to correct the rounded data using Equations (3-22) and (3-23). The mean wind speed measurements were then extrapolated to turbine hub height using Equation (2-3), and the corrected data are plotted in Figure 5-4 along with an effective turbulence level calculated from Equation (3-18). The rounding correction produces a reduction in the estimation of σ_{eff} for low wind speed and turbulence values, while the increase in mean wind speed values due to extrapolation to hub height produces a reduction in σ_{eff} for the higher wind speeds. The corrected data provided the best assessment available of site turbulence conditions, as detailed in Section 5.2 below where the data are compared with other available measurements.

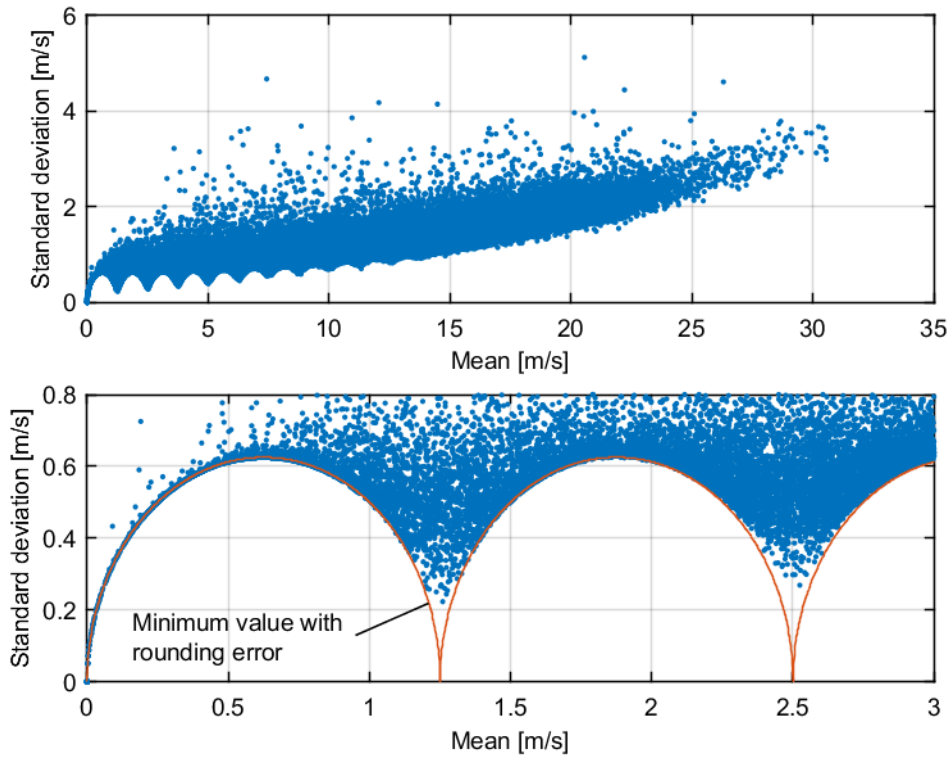

Figure 5-2. Wind speed mean and standard deviation measurements from the MM pre-construction measurement campaign. The bottom figure displays the minimum rounding error function (Equation (3-26)) with a fitted correlation coefficient of *P* = 1.2505.

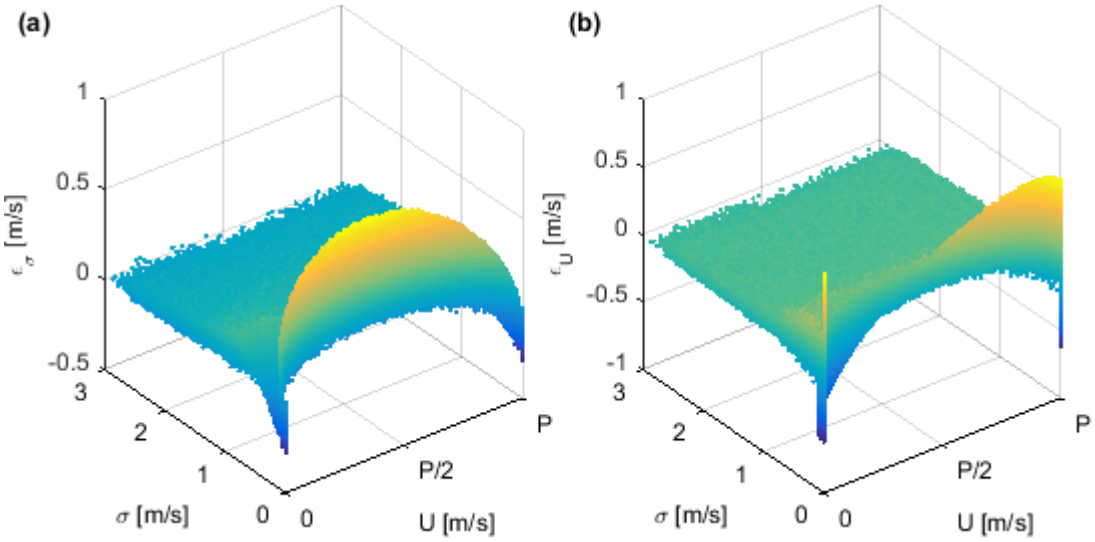

Figure 5-3. Distribution of MM data rounding errors calculated using Monte Carlo simulation, against standard deviation and mean wind speed for each ten minute period. (a) Standard deviation rounding error from Equation (3-23). (b) Mean wind speed rounding error from Equation (3-22).

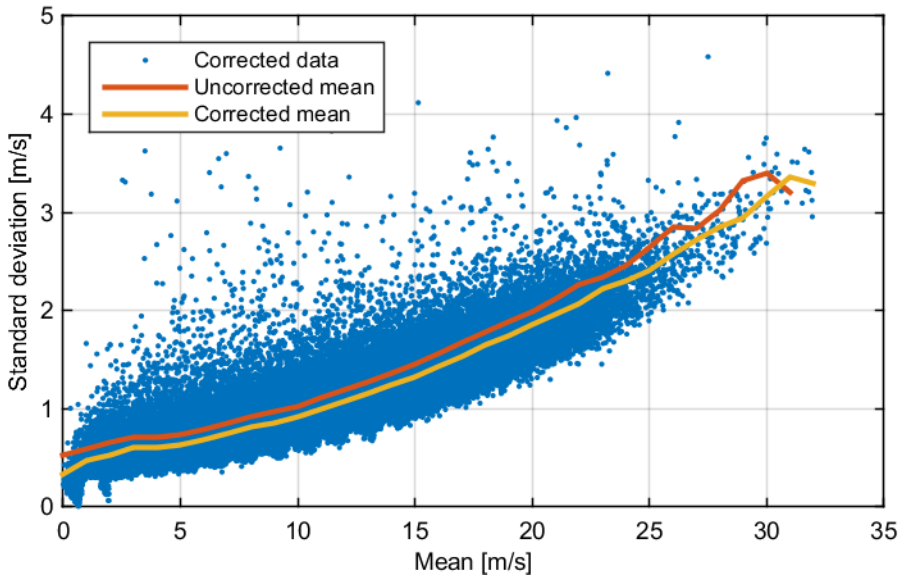

Figure 5-4. Meteorological Mast turbulence data, corrected for rounding errors with mean wind speed extrapolated to hub height. The red line shows the effective turbulence calculated for the uncorrected data shown in Figure 5-2.

5.2.2 Assessment of K1 SCADA turbulence

The nacelle mounted anemometer used by the SCADA system to record wind speeds is known to be affected by blockage effects of the rotor and nacelle [116]. The vortices shed by the blades periodically distort the flow measured by the anemometer such that the recorded mean and standard deviation of the wind speed may differ from the undisturbed flow. Turbine K1 TI measurements were therefore compared with measurements made by the MM and LIDAR systems to understand the effect of the presence of the turbines.

Unfortunately, a concurrent measurement period between the MM and the SCADA data sets was not available, as the MM had been decommissioned on completion of the design stage site assessment. However, the original location of the MM was in close proximity to Turbine K1, as shown in Figure 1-1, and should therefore provide a reliable comparison for undisturbed wind directions which are unaffected by the rest of the wind farm, based on the assumption that the site conditions are consistent for large sample sizes. The temporal coverage of the different datasets is shown in Figure 5-5.

Figure 5-6 shows the effective TI values calculated using Equation (2-6) for each of the datasets, using wind measurements from the 150° to 300° directional sector to ensure that the SCADA measurements at Turbine K1 were not affected by trailing wakes. The corrected MM TI can be seen to closely follow the K1 values above cut-in wind speed. The de-trended K1 TI values were calculated using Equation (2-4) in order to remove the effects of large

variations in mean wind speed, and show a slightly reduced TI value at all wind speeds. It should be noted that it was not possible to de-trend the MM or LIDAR data using Equation (2-4), as the data sets were only available in ten minute periods. The LIDAR data can be seen in Figure 5-6 to give the lowest assessment of turbulence at all wind speeds, and is likely to underestimate the wind variation due to the known volumetric averaging effect associated with this measurement system [39].

Finally, Figure 5-7 shows the de-trended TI_{eff} calculated using operational SCADA data from all wind directions for Turbines H4 and K1. The additional wake turbulence present at Turbine K1 for certain wind directions results in a higher TI_{eff} than the de-trended values shown in Figure 5-6, while the H4 measurements are seen to produce higher *TI* values for nearly all wind speeds. The combined TI levels are found to be approximately half the highest IEC TI values for nearly all wind speeds. This highlights the conservative turbulence levels that are required by the standards to be selected at the design stage. Therefore, the de-trended Turbine K1 TI values were deemed to give the best assessment of operational turbulence seen by the measured turbines, and were used to define the turbulence levels for use in the numerical simulations presented in Section 8.

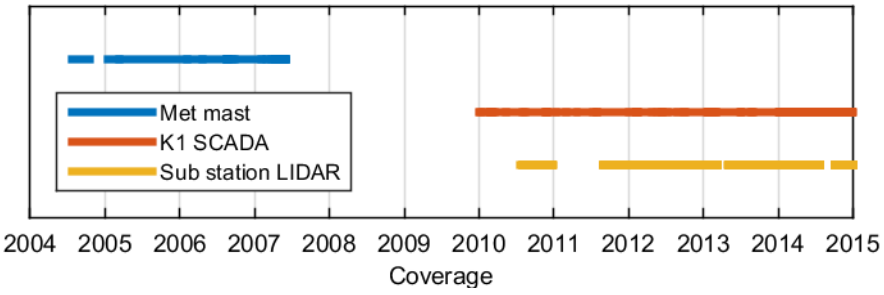

Figure 5-5. Measurement periods for different sources of wind data.

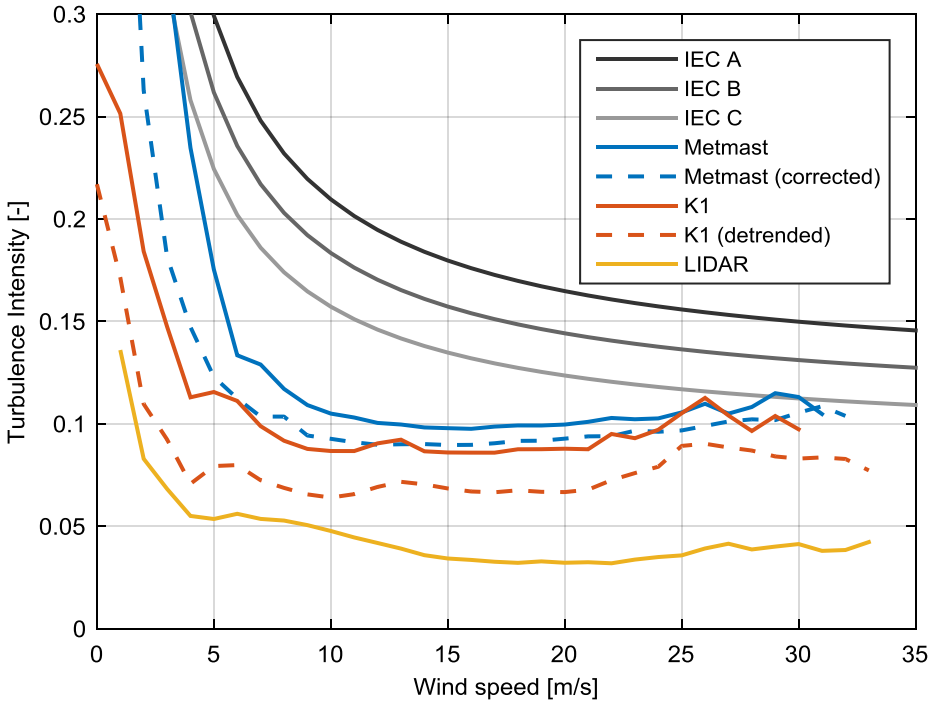

Figure 5-6. Comparison of TI_{eff} levels recorded for the directional sector 150° to 300°. TI_{eff} calculated using m = 3. The IEC turbulence categories are shown for comparison.

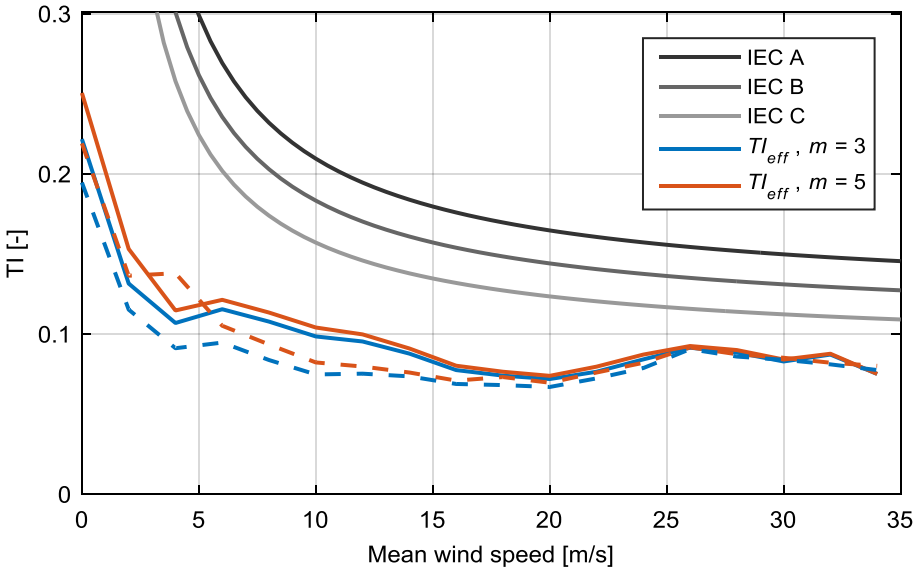

Figure 5-7. Effective turbulence intensity (TI_{eff}) measured at Turbines H4 and K1 (solid lines and dashed lines, respectively), calculated using Equation (2-6). The standard IEC turbulence classes as given in [21] are shown for comparison.

5.2.3 Site Turbulence Distribution

Standard deviation measurements using SCADA data from multiple turbine locations were used to evaluate the level of turbulence across the wind farm during the 18 month load measurement period. The selected turbines are shown in Figure 5-8, which highlights the directional transects used to investigate the number of turbine rows required for convergence of wake induced turbulence. Effective standard deviation values for the identified wind directions are shown in Figure 5-9 and Figure 5-10, and display the lowest level of turbulence at Turbine K1 (which experiences the ambient, undisturbed flow from these directional sectors).

No significant increase in turbulence measurements is found for successive turbine rows after Turbine H4 below rated wind speeds (U_{rated} = 13 m/s), but Figure 5-9 shows that increased turbulence levels were found further downstream at higher wind speeds with the closest turbine spacing of 5.1 rotor diameters. Figure 5-11 and Figure 5-12 show that this trend is consistent with other directions, as Turbine H4 displays close to maximum levels of σ_{eff} below U_{rated}, but lower levels at higher wind speeds except for wind directions aligning with multiple closely spaced rows of turbines (approximately 25° and 290°, Figure 5-12). Therefore the wind directional distribution needed to be taken into account in the analysis.

Accounting for the distribution of wind speeds and directions over the measurement period, the combined effective turbulence level for all wind directions was calculated using (from Equation (3-18)),

$$\sigma_{eff}(\bar{U}) = \left[\frac{1}{N}\sum_{i=1}^{N}\sigma_{eff}(\bar{U})_i^{\,m}\right]^{1/m} \tag{5-1}$$

where the directional distribution is accounted for by default. The calculated values are shown for each turbine in Figure 5-13. Turbine K1 exhibits low level turbulence at all wind speeds, while H4 is close to the maximum value in the wind farm up to U_{rated}. Turbines D3 and F3 display the highest turbulence at wind speeds above U_{rated}, indicating that the level of ambient turbulence continues to increase with successive rows after Turbine H4. Therefore, turbine location H4 does not constitute the location of highest turbulence throughout the wind farm for all wind speeds. However, to account for this the effect of screening the measurements to identify periods of high turbulence at Turbine H4 was investigated, and is described in Section 5.2.4 below.

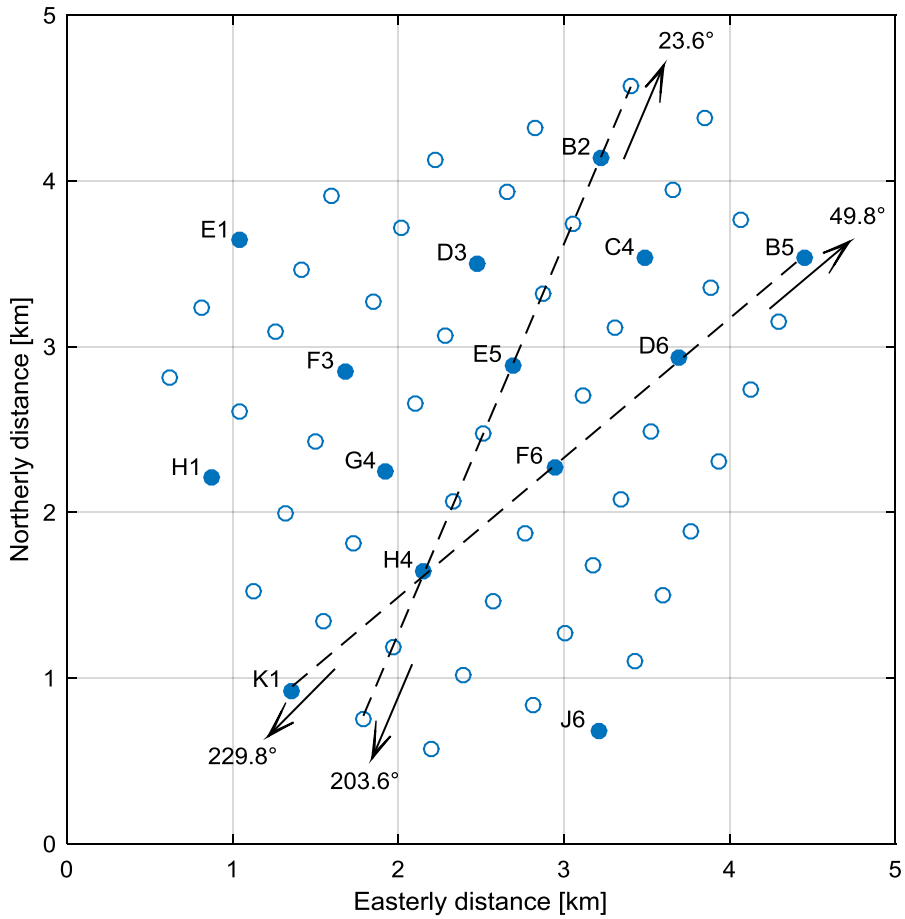

Figure 5-8. Turbine locations used to investigate the distribution of wind turbulence throughout the wind farm. Directional transects relate to data plotted in Figure 5-9 and Figure 5-10.

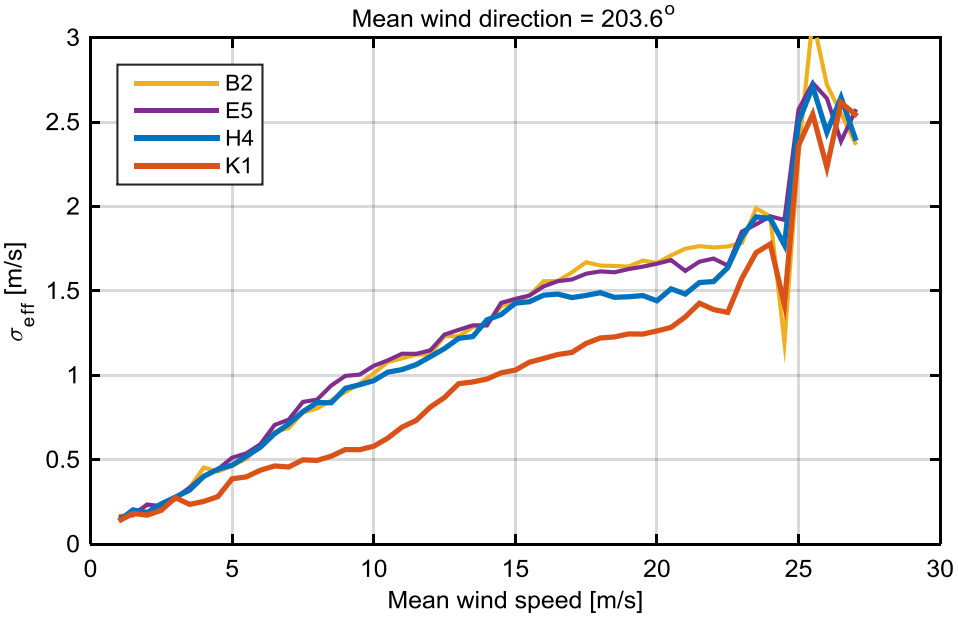

Figure 5-9. Effective standard deviation for turbine spacing of approximately 5.1 rotor diameters (turbines aligned in the mean wind direction of 203.6° +/- 5°).

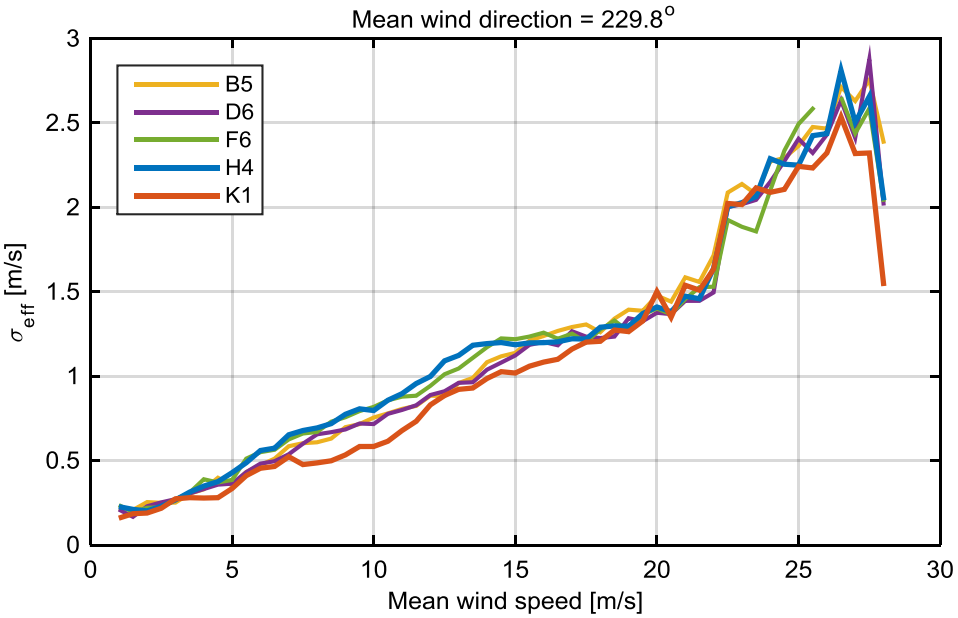

Figure 5-10. Effective standard deviation for turbine spacing of approximately 11.7 rotor diameters (turbines aligned in the mean wind direction of 229.8° +/- 5°).

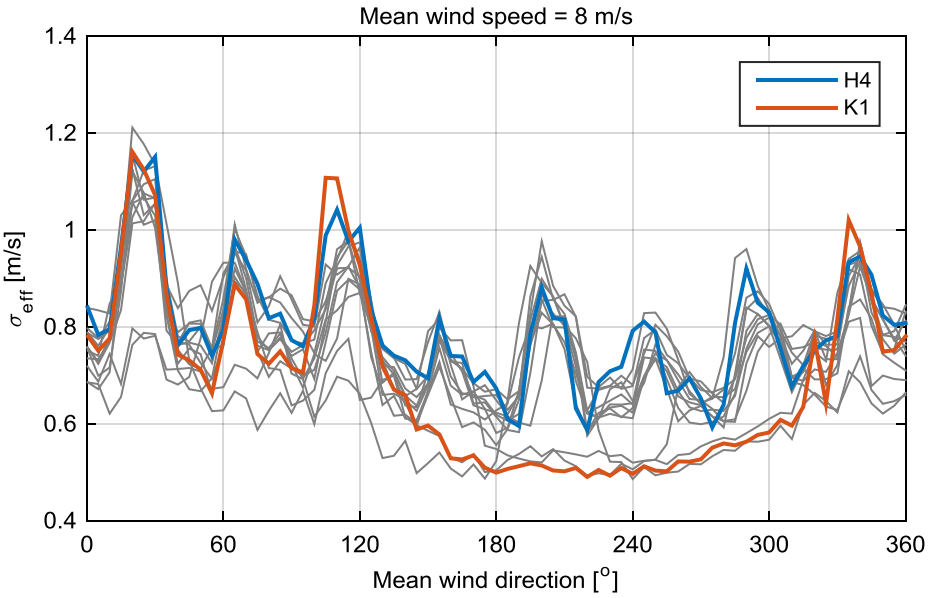

Figure 5-11. Effective standard deviation for all wind directions below rated wind speed (U = 8 m/s +/- 1 m/s). Turbines H4 and K1 are highlighted, with the grey lines showing the remaining turbines used, (identified in Figure 5-8).

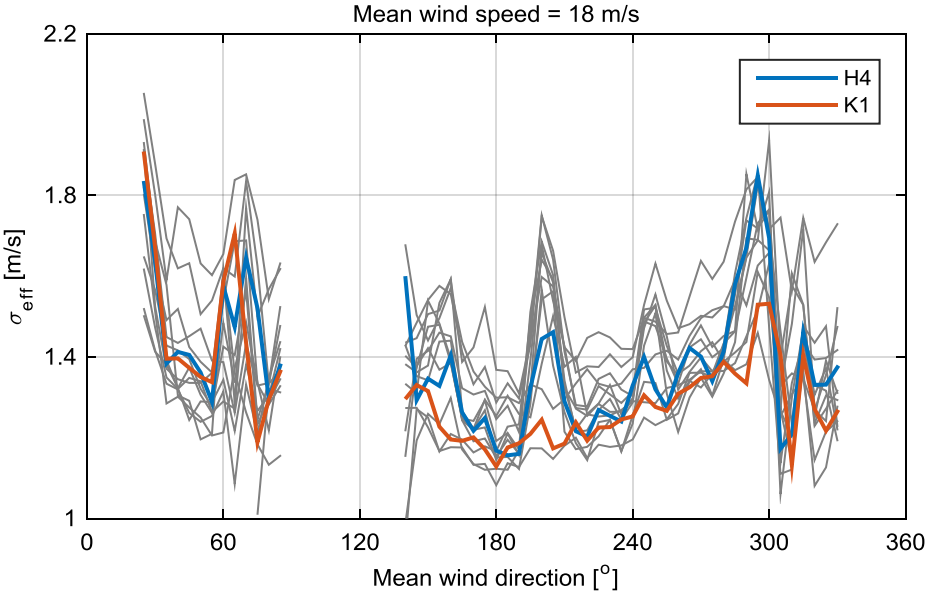

Figure 5-12. Effective standard deviation for all wind directions above rated wind speed (U = 16 m/s +/- 1 m/s). Turbines H4 and K1 are highlighted, with the grey lines showing the remaining turbines used, (identified in Figure 5-8). Sufficient data was not recorded at this wind speed for wind directions from the North and the South East.

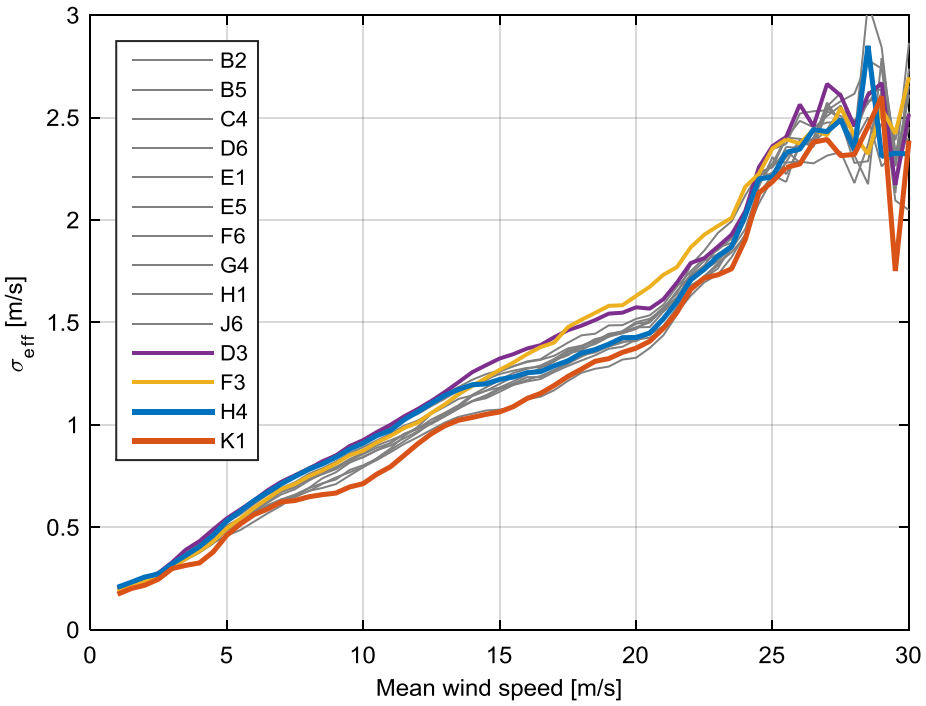

Figure 5-13. Effective standard deviation for the full two year dataset, 2011 to 2012 inclusive. Turbines D3 and F3 (highlighted) display the highest level of σ_{eff} above rated wind speed.

5.2.4 Selection of Maximum Turbulence Periods at Turbine H4

Due to the spread of turbulence values measured for each wind speed and direction bin, it was possible to use the Turbine H4 SCADA data to identify the periods which would match the maximum level of σ_{eff} in the wind farm. Using a measurement period corresponding to the 18 month load measurements, the maximum turbulence value in the wind farm was identified for each wind speed and direction bin, $\sigma_{eff}(\bar{U},\bar{\theta})$, this time using bin sizes of $d\bar{U}$ = 2 m/s and $d\bar{\theta}$ = 30° to match the LC bin sizes. The H4 data was then filtered to identify the turbulence measurements which would produce an equivalent turbulence value, $\sigma_{eff}{}^{*}(\bar{U},\bar{\theta})$, to match the highest value in the wind farm, effectively by selecting the highest turbulence values in the distribution at each wind speed and direction bin. An example of the methodology is shown in Figure 5-14. To obtain the combined $\sigma_{eff}{}^{*}$ for all directions as a function of wind speed, the $\sigma_{eff}{}^{*}(\bar{U},\bar{\theta})$ values were then factored by the number of occurrences of each mean direction sector in the measurement period and combined using,

$$\sigma_{eff}{}^{*}(\bar{U}) = \left[\frac{\sum_{i=1}^{n_\theta} P(\bar{U},\bar{\theta}_i) \times \sigma_{eff}{}^{*}(\bar{U},\bar{\theta}_i)^m}{P(\bar{U})}\right]^{1/m} \quad (5\text{-}2)$$

where n_θ is the number of mean wind direction bins used. The combined high turbulence $\sigma_{eff}{}^{*}$ values for H4 are compared to the normal turbulence values calculated for the rest of the wind farm in Figure 5-15 below, and show that the selected periods for Turbine H4 result in a combined turbulence level which matches the highest turbulence in the wind farm, for all power production wind speed bins.

In this way, although the load measurements were not taken from the highest turbulence location in the wind farm, the H4 measurements could be used to quantify the loading that would be produced by the most turbulent location. The loading results are presented in Section 6.3.1.1.

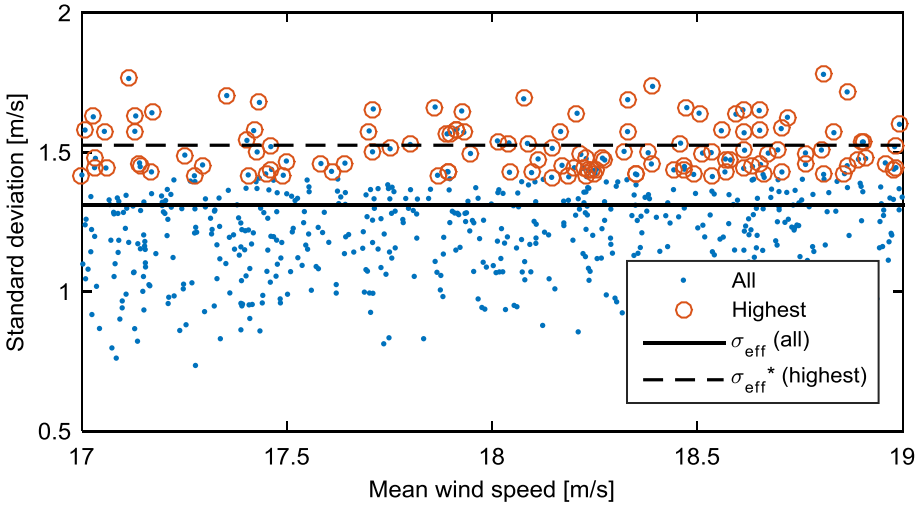

Figure 5-14. Turbulence values measured at Turbine H4 for the $\bar{U}$ = 18 m/s, $\bar{\theta}$ = 240° wind vector bin. The solid black line shows the σ_{eff} value for all the data, while the dashed line shows the σ_{eff} for the highest measurements (selected to match the highest σ_{eff} measured in the wind farm at each ($\bar{U}$, $\bar{\theta}$) bin).

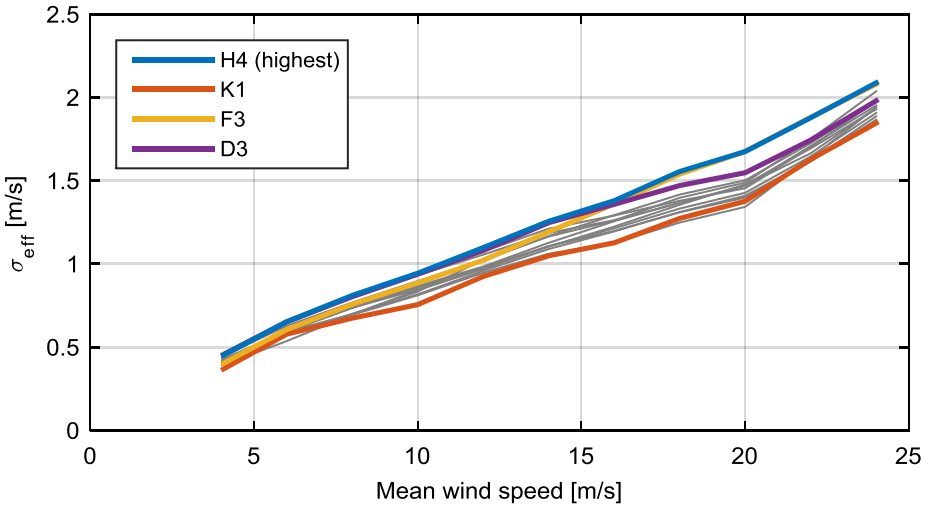

Figure 5-15. H4 effective turbulence intensity, produced by matching the highest σ_{eff} in the wind farm for each ($\bar{U}$,$\bar{\theta}$) bin. Grey lines show results from the remaining turbines used for the analysis (shown in Figure 5-8).

5.3 Wave Conditions

Wave elevations were measured at the offshore substation on the South East side of the wind farm. Although the measurements were not taken at Turbine K1, Figure 5-16 shows the correlations between significant wave heights and the wind speed and direction measurements from K1 SCADA. Directions which include the highest wind speeds also include the greatest values of significant wave height, and the correlations, quantified as the adjusted R-squared value from Equation (3-27), are strongest for the directions which are not fetch-limited.

From Figure 5-16, it can also be noticed that the quadratic fit to the data for the 90° and 120° directional sectors has produced a downwards curve, contrary to the fits to the remaining directional sectors. This is likely to be a result of a poor fit due to the few measurements available from these directions, with only low wind speeds recorded during the measurement period.

Figure 5-16 presents a simple non-parametric fit to the measured data, but demonstrates a strong correlation between the magnitudes of wind and wave loading, based on wind direction sectors alone. Although wave direction information is not included in the measured data, these results are considered to confirm the information provided in the design stage metocean study indicating a strong directional correlation between wind and waves [87].

However, although analysis conducted at the design stage found that modelling DLCs with fully aligned wind and waves would produce conservative results for the given turbine definition and site conditions [87], there is the potential for an assessment of measured fatigue loading to be non-conservative if the measurements used happen to coincide with a less onerous combination of loading directions. As the available data did not allow for further refinement of the MLC bins based on wave direction, a statistical approach was used to assess the conservatism of the measured loading used to define the full loading histogram, and is presented in Section 6.1.

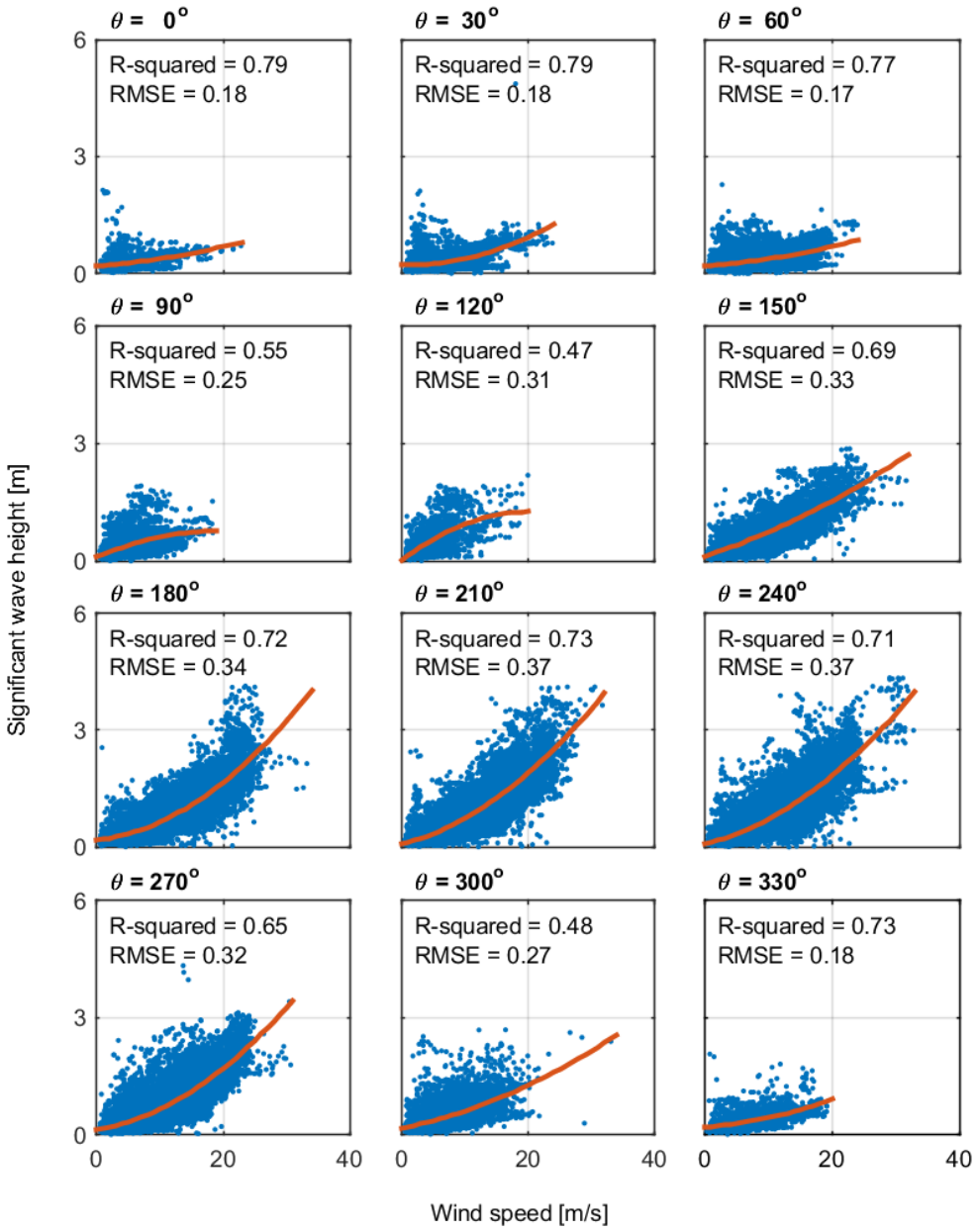

Figure 5-16. Correlations between mean wind speed and significant wave height for each 30° directional sector. The red lines show a second order polynomial function fitted to the data using least squares regression.

5.4 Tide Heights

Ten minute tide height data from the local measurement station is shown in Figure 5-17. The maximum and minimum tide levels found during the recorded period at 9.30 mCD and 0.05 mCD, respectively. Tide height data was used with the assessment of the distribution of fatigue damage presented in Section 6.1.

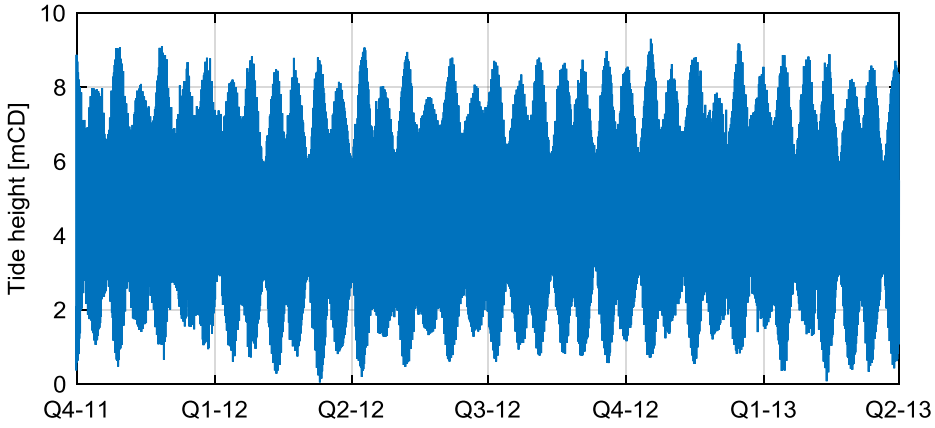

Figure 5-17. Tide measurements for the OWT site. Data extracted from [99].

5.5 Air Density

Using an average value of 80% humidity from a nearby weather station [103], the air density could be calculated using values of ambient temperature and pressure measured by the Turbine K1 SCADA system, from which an average value of 1.229 kg/m^3 was derived (Figure 5-18 below). It should be noted that with the assumption of dry air (0% humidity) an average density of 1.234 kg/m^3 was found, which is in the order of the value used by the turbine designer [93]. The average air density value was used with the wind turbine numerical simulations presented in Chapter 8.

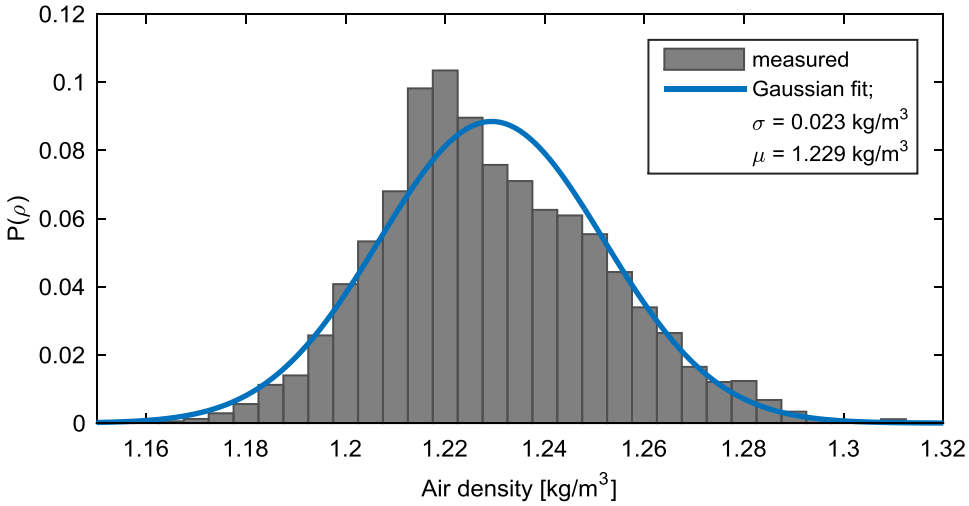

Figure 5-18. Air density distribution calculated from K1 SCADA data using Equation (3-28) and an assumed value of 80% relative humidity.

6 Discussion of Results: Load Case and Capture Matrix

6.1 Distribution of Measured Fatigue Damage

By dividing the fatigue LCs into wind speed and direction bins, the implicit assumption is that the variation in fatigue loading can be sufficiently described by this environmental loading variable alone. Figure 6-1 shows the correlation within each wind bin between DES and other environmental loading variables which are known to influence the level of fatigue loading: namely tide level, significant wave height, air density, and turbulence intensity. The strongest influence is found with the wave and turbulence loading, with a consistent range of R-squared values for most wind bins. There appears to be a slight correlation between DES and tide level for the higher wind speeds, which is likely to arise from coupling with the wave amplitude for the dominant wave loading direction. Air density is seen to produce minimal influence on the level of DES at the highest wind speeds, with slight correlations found for some of the least frequently occurring wind bins, possibly due to the small number of data points. Therefore, Figure 6-1 indicates that the distribution in fatigue loading found at each wind speed and direction bin is influenced by several variables, but most significantly by the level of wave and turbulence loading.

The full load measurement period of approximately 18 months can be argued to be representative of the variation in environmental and operational variables that would occur over the life of the turbine. Therefore, the fatigue damage produced by the entire measurement period was used as a bench mark against which to assess the load histogram produced using the methodology outlined in IEC-TS-61400-13 [29].

Using the periods in which the turbine was operating in power production mode, a Bootstrap approach was used to quantify the confidence limits that the full measurement dataset was sufficiently representative of the underlying distribution of fatigue damage. The Bootstrap distribution of the mean population fatigue damage, calculated from Equation (3-30), is given in Figure 6-2. Restating the notation presented in Section 3.2.1, D_p is the fatigue damage value produced by the entire population of measurements, and $P(D_p)$ is the distribution of values calculated using the Bootstrap resampling approach. The distributions presented in Figure 6-2 are normalised by the mean of the Bootstrap damage values, and show a coefficient of variation (standard deviation divided by the mean) of 0.55% using a Wöhler exponent of $m = 3$, and 1.80% using $m = 5$. This represents a high confidence that the full dataset will be sufficiently representative of the through-life fatigue damage distribution, or within +/- 1.1% and 3.6% tolerance, using m = *3* and m = *5* respectively, at

the 95% confidence level. Therefore the complete dataset of power production measurements were assumed to be sufficiently representative of the underlying distribution, and are referred to here as the population distribution. The results are normally distributed as predicted by the central limit theorem [105], which also states that the standard deviation of a measurement is proportional to the square root of the sample size. Therefore, the high confidence in the estimate of damage using the complete dataset is a direct result of the large 18 month measurement period.

The probability of a small, random sample of n measurements at each wind vector bin producing a full fatigue load histogram which is greater than a certain tolerance of the population value is shown in Figure 6-3. The probabilities were calculated using a single-sided test, and therefore the expected result of the sampled damage approximately equalling the full population value at 50% should be true for all sample sizes. Again, according to the central limit theorem, the standard deviation of the sampled estimates is proportional to the square root of the sample size, and therefore the larger sample sizes produce closer estimates of the underlying damage. Choosing an acceptable confidence level of 95% and a sample size of $n = 30$ (as used in the IEC-TS-61400-13 methodology), the potential under-estimation is $\beta = 97\%$ of the population damage level for $m = 3$, and $\beta = 83\%$ for $m = 5$. This suggests an unacceptable level of uncertainty for the higher damage exponent, using a sample size of 30 random measurements. Ultimately, however, a direct comparison is necessary between the full population damage values and the sampled histogram values using the IEC-TS-61400-13 methodology, and this is presented in Section 6.3.1.

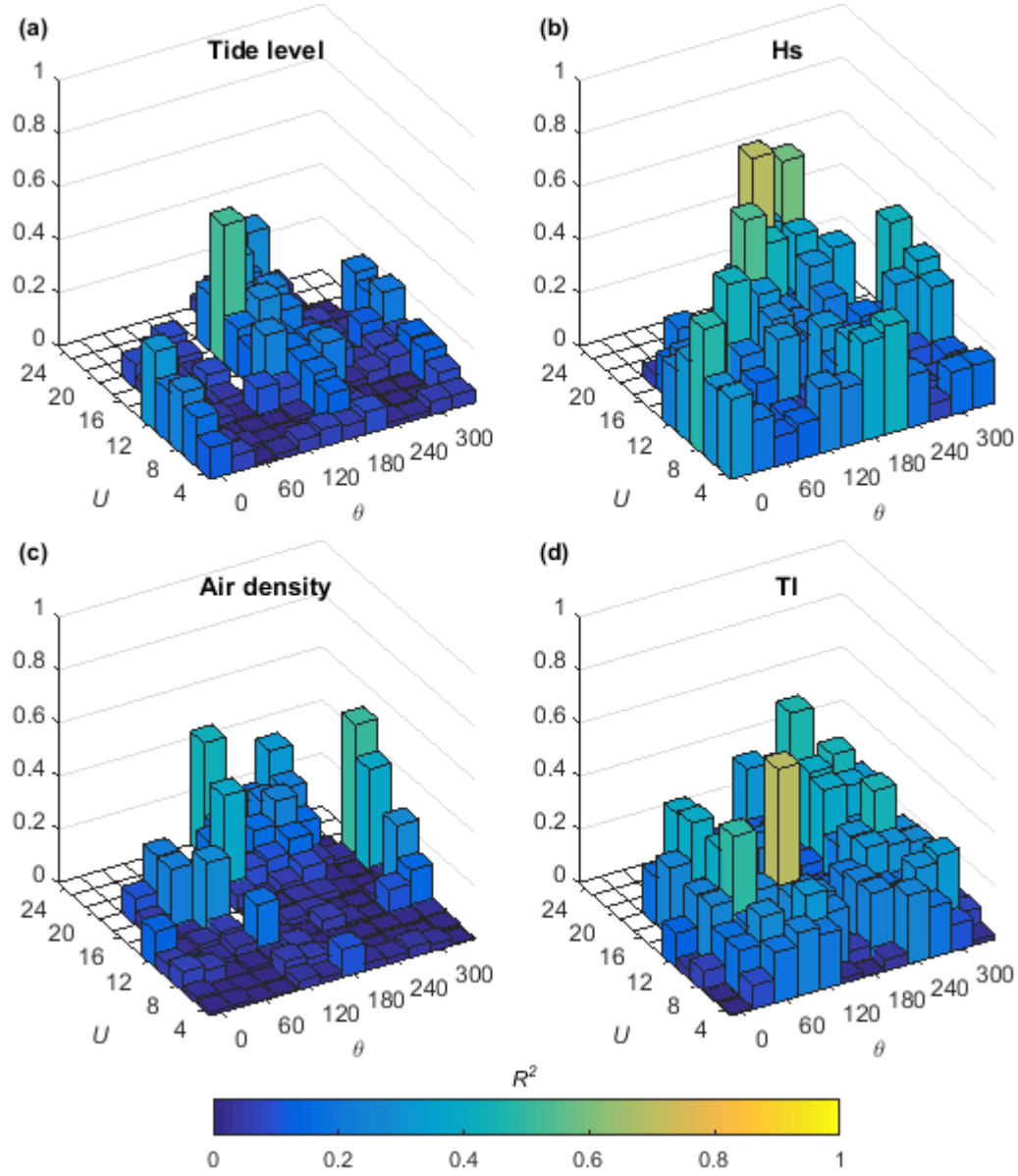

Figure 6-1. Correlation between environmental variables and measured DES values, within each wind speed [m/s] and direction [°] bin for the power production Load Cases. Correlation calculated as the adjusted R-squared value for a fitted second order polynomial to the data in each wind bin, for (a) tide level, (b) significant wave height, (c) air density, (d) turbulence intensity.

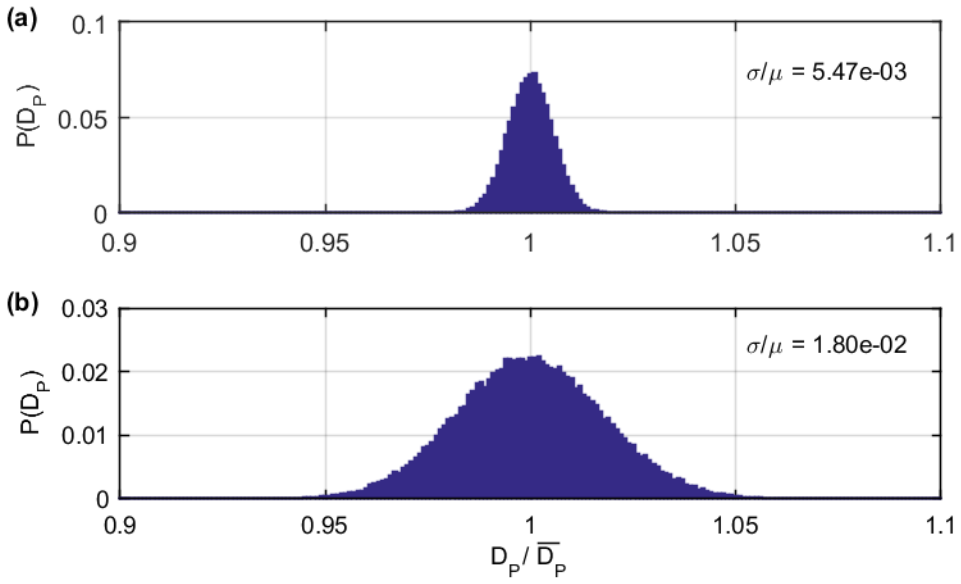

Figure 6-2. Bootstrap distribution of fatigue damage calculated from the full population of power production measurements, normalised by the mean value. (a) Fatigue damage calculated using *m* = 3. (b) Fatigue damage calculated using *m* = 5.

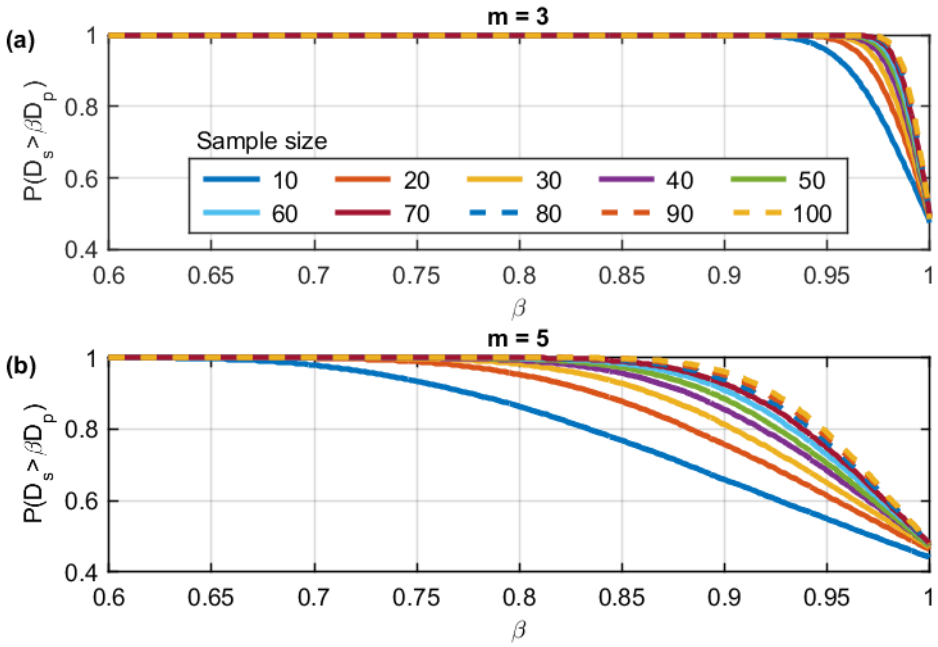

Figure 6-3. Probability of sampled Load Cases producing a total fatigue damage value greater than a certain fraction of the population value, from Equation (3-33). (a) Damage calculated using Wöhler exponent of *m* = 3. (b) Wöhler exponent *m* = 5.

6.2 Capture Matrices

Load Cases which were identified within the measured data to meet sufficiently the minimum criteria outlined in Table 3-5 are shown in the Capture Matrices (CM) below (Table 6-1 to Table 6-5, where blue highlights bins which were covered at Turbine H4 only, pink indicates Turbine K1 only, and green indicates sufficient measurements at both turbines). Where a LC was not sufficiently represented by the measured data, the simulated loads calculated by the turbine designer were reverted to in order to produce a full representation of the through life loading. This approach is believed to be conservative based on comparison of MLCs which were adequately classified, as outlined in Section 6.3 below.

Table 6-1. Coverage of the measured data for the power production LCs.

LC 1.1		$\bar{\theta}$ [°]											
H4 only	K1 only	0	30	60	90	120	150	180	210	240	270	300	330
$\bar{U}$ [m/s]	4	MLC	MLC	MLC	MLC	MLC	MLC	MLC	MLC	MLC	MLC	MLC	MLC
	6	MLC	MLC	MLC	MLC	MLC	MLC	MLC	MLC	MLC	MLC	MLC	MLC
	8	MLC	MLC	MLC	MLC	MLC	MLC	MLC	MLC	MLC	MLC	MLC	MLC
	10	MLC	MLC	MLC	MLC	MLC	MLC	MLC	MLC	MLC	MLC	MLC	MLC
	12	MLC	MLC	MLC	MLC	DLC	MLC	MLC	MLC	MLC	MLC	MLC	MLC
	14	DLC	MLC	MLC	MLC	DLC	MLC	MLC	MLC	MLC	MLC	MLC	MLC
	16	DLC	MLC	MLC	MLC	DLC	MLC	MLC	MLC	MLC	MLC	MLC	MLC
	18	DLC	MLC	MLC	MLC	DLC	MLC	MLC	MLC	MLC	MLC	MLC	MLC
	20	DLC	MLC	DLC	MLC	DLC	MLC	MLC	MLC	MLC	MLC	MLC	DLC
	22	DLC	DLC	DLC	DLC	DLC	DLC	MLC	MLC	MLC	MLC	DLC	DLC
	24	DLC	DLC	DLC	DLC	DLC	DLC	MLC	MLC	MLC	MLC	DLC	DLC

Table 6-2. Coverage of the measured data for the start-up LCs.

LC 3.1		$\bar{\theta}$ [°]											
H4 only	K1 only	0	30	60	90	120	150	180	210	240	270	300	330
$\bar{U}$ [m/s]	4	MLC	MLC	MLC	MLC	MLC	MLC	MLC	MLC	MLC	MLC	MLC	MLC
	13	DLC	DLC	DLC	DLC	DLC	DLC	MLC	DLC	DLC	MLC	DLC	DLC
	20	DLC	DLC	DLC	DLC	DLC	DLC	MLC	DLC	MLC	MLC	DLC	DLC

Table 6-3. Coverage of the measured data for the shut-down LCs.

LC 4.1		$\bar{\theta}$ [°]											
H4 only	K1 only	0	30	60	90	120	150	180	210	240	270	300	330
$\bar{U}$ [m/s]	4	MLC	MLC	MLC	MLC	MLC	MLC	MLC	MLC	MLC	MLC	MLC	MLC
	13	DLC	DLC	DLC	DLC	DLC	DLC	MLC	DLC	DLC	MLC	DLC	DLC
	20	DLC	DLC	DLC	DLC	DLC	DLC	MLC	MLC	MLC	DLC	DLC	DLC

Table 6-4. Coverage of the measured data for the emergency shutdown LCs.

LC 5.1		$\bar{\theta}$ [°]											
H4 only	K1 only	0	30	60	90	120	150	180	210	240	270	300	330
$\bar{U}$ [m/s]	13	DLC	DLC	DLC	DLC	DLC	DLC	DLC	DLC	DLC	DLC	DLC	DLC
	25	DLC	DLC	DLC	DLC	DLC	DLC	DLC	DLC	DLC	DLC	DLC	DLC

Table 6-5. Coverage of the measured data for the idling LCs.

LC 6.4		$\bar{\theta}$ [°]											
H4 only	K1 only	0	30	60	90	120	150	180	210	240	270	300	330
$\bar{U}$ [m/s]	3	MLC	MLC	MLC	MLC	MLC	MLC	MLC	MLC	MLC	MLC	MLC	MLC
	26	DLC	DLC	DLC	DLC	DLC	DLC	DLC	MLC	MLC	MLC	DLC	DLC
	28	DLC	DLC	DLC	DLC	DLC	DLC	DLC	MLC	MLC	MLC	DLC	DLC
	30	DLC	DLC	DLC	DLC	DLC	DLC	DLC	DLC	MLC	DLC	DLC	DLC
	32	DLC	DLC	DLC	DLC	DLC	DLC	DLC	DLC	DLC	DLC	DLC	DLC
	34	DLC	DLC	DLC	DLC	DLC	DLC	DLC	DLC	DLC	DLC	DLC	DLC

6.3 Load Case Comparison

Damage Equivalent Stress values were calculated using Equation (2-18) for each ten minute LC period at the 90° circumferential location, for both the measured and design data, and results are compared in the following sections.

6.3.1 LC 1.1 Power Production

The full population of DES values measured at Turbine K1 during power production operating conditions, for one wind directional sector, are shown in Figure 6-4 in comparison to the values produced by the simulated DLCs. The mean DES, and the scatter of results calculated with the Bootstrap resampling methodology, indicate that the measurements provide a good representation of the underlying fatigue loading, with a maximum coefficient of variation found at the 4 m/s wind speed bin (2.98% and 6.24% with $m = 3$ and $m = 5$, respectively). The mean DES measurement is around 60% of the design value at most wind speeds, relating to lower fatigue damage in the order of $0.6^3 = 21.6\%$ and $0.6^5 = 7.8\%$ of the design level using $m = 3$ and $m = 5$, respectively, at most of the wind speeds shown in Figure 6-4.

The mean DES values display noticeable changes in mean gradient around 8 m/s and 14 m/s, which correspond with changes in the operating state of the rotor speed and blade pitch angle, as shown in Figure 6-5. This effect is also apparent in the DES values calculated from the design data shown in Figure 6-4, indicating that the turbine operating state is well

represented in the design model simulations. However, the measured data display a number of high DES outliers in the range of 5 to 10 m/s which are distinct from the majority of data points measured in this region, and do not appear to be represented in the design values. The impact on the mean DES value is particularly strong with the use of $m = 5$, which attributes higher weighting to large amplitude stress cycles. The cause of the outliers is shown in Figure 6-6, which plots the stress time series relating to one of the outlying data points in Figure 6-4. As wind speed and turbine output power increase, the controller for this particular turbine model pitches the rotor blades out of the wind and de-powers to allow the generator to switch between low voltage and high voltage connection, known as a star-delta switch [117]. The time stamps in Figure 6-6 are seen to be imperfectly synchronised due to the fact that they come from different measurement systems, but the transient event is evident in each of the high DES outliers identified in Figure 6-4.

Figure 6-7 and Figure 6-8 show the frequency domain response of the structures in the fore-aft and side-side directions, respectively. The wind directions were chosen to align with the turbine rows, meaning that increased turbulence levels due to trailing wakes would occur during the measurement periods (see Figure 1-1 for the wind farm layout). The amplitude spectrums are calculated from FFT of a ten minute period of data during power production operation, and averaged over 30 measurements to provide a smoothed response spectrum. The rotor frequency produces a narrow band response during operation at 12 m/s and 18 m/s, where the turbines operate at fixed speed. Below approximately 10 m/s the turbines operate at variable speed, and the structural response is seen to be spread over a wider frequency band in the 8 m/s wind speed plot. The first mode responses of the structures are most clearly identified in the side-side direction (Figure 6-8), while the lower frequency response (<0.2 Hz) to turbulent wind loading is evident in the fore-aft direction, particularly for wind directions which produce increased turbulence due to trailing wakes, Figure 6-7). It can also be seen that the structural response at Turbine K1 is generally higher than at Turbine H4, except in the low frequency region for the 210° wind direction where Turbine K1 experiences the un-waked flow. A small part of the fore-aft response in Figure 6-7 is likely to be due to wave loading, in the region of 0.1 Hz for the higher wind speeds. However, the response to wave loading is likely to be small in comparison to the response to wind turbulence.

The difference between mean DES values calculated from the population measurements from turbines K1 and H4 at each wind vector bin is shown in Figure 6-9. The colour scale shows that the loading at Turbine K1 is higher at nearly all wind vector bins, apart from the

240° to 300° sector for lower wind speeds; from these directional sectors Turbine H4 is aligned downwind of trailing wakes from several turbines, while K1 receives only the ambient turbulence level. Additionally, the wave loading from this directional sector is low, as the fetch is limited. Notably, for high wind speeds from the South West and North East directions, corresponding with the dominant sectors from the wave distribution, the fatigue loading at Turbine K1 is appreciably higher than at H4.

Mean DES values from each wind bin for the power production cases were factored by the design through-life frequency of occurrence to produce a total value, and results are presented in Table 6-6 in comparison with the results produced from the simulated design loads. Only wind vector bins which were measured at both turbine locations were included in the analysis. The DES values produced from the entire population of power production measurements are found to have a lower value of fatigue damage than design by a factor of $(9.72/17.35)^3 = 17.6\%$ at Turbine H4, and $(10.04/17.35)^3 = 19.4\%$ at Turbine K1, using $m = 3$. The relative percentage differences are even more pronounced using $m = 5$. These results show that, where a direct comparison between design and measured LCs are available, the measured fatigue loading is demonstrably lower than design, by an amount which is significantly greater than the estimated confidence limits presented in Figure 6-2 and Figure 6-3. The assessment of methods used to account for the LC bins which were not adequately covered by measurement are presented in the following sections.

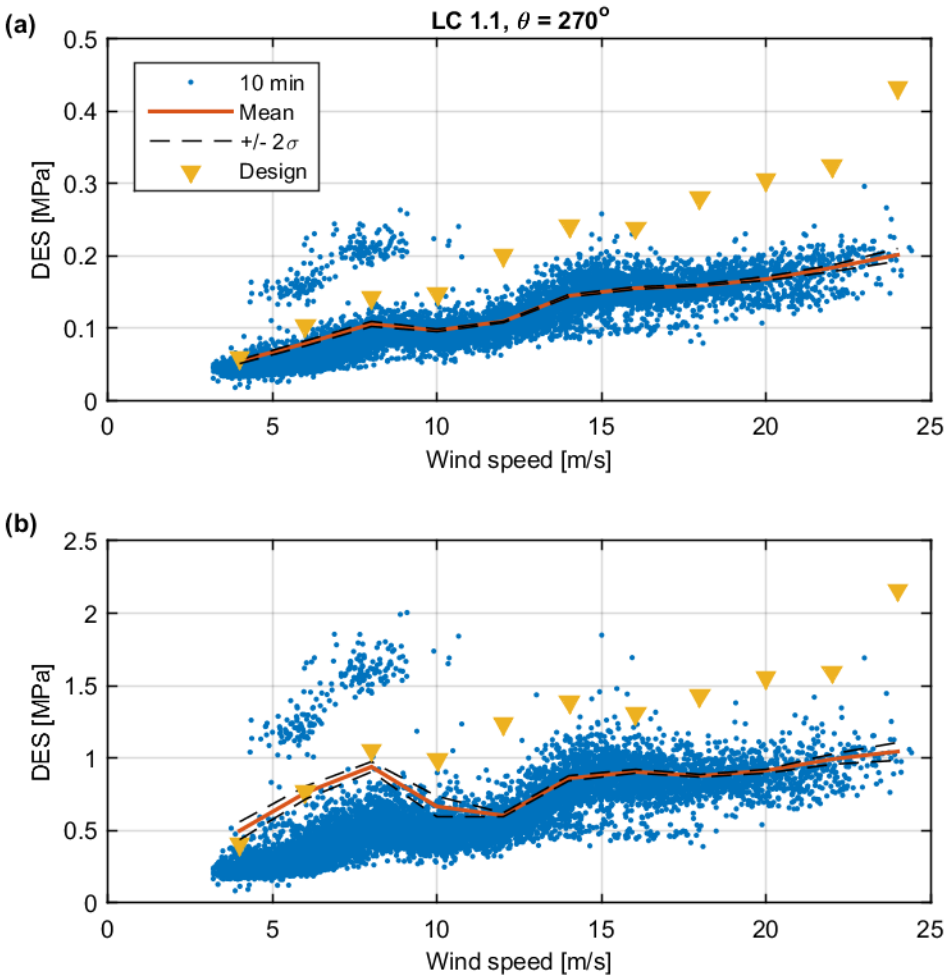

Figure 6-4. DES measured during power production operating conditions, for the 270° wind direction (Turbine K1). Blue dots show single measurements calculated from ten minute periods, red line and black lines show the Bootstrap mean and two standard deviations, respectively, for each 2 m/s wind speed bin, and yellow triangles show the mean DES value calculated from the DLC simulations. (a) DES calculated using *m* = 3. (b) DES calculated using *m* = 5.

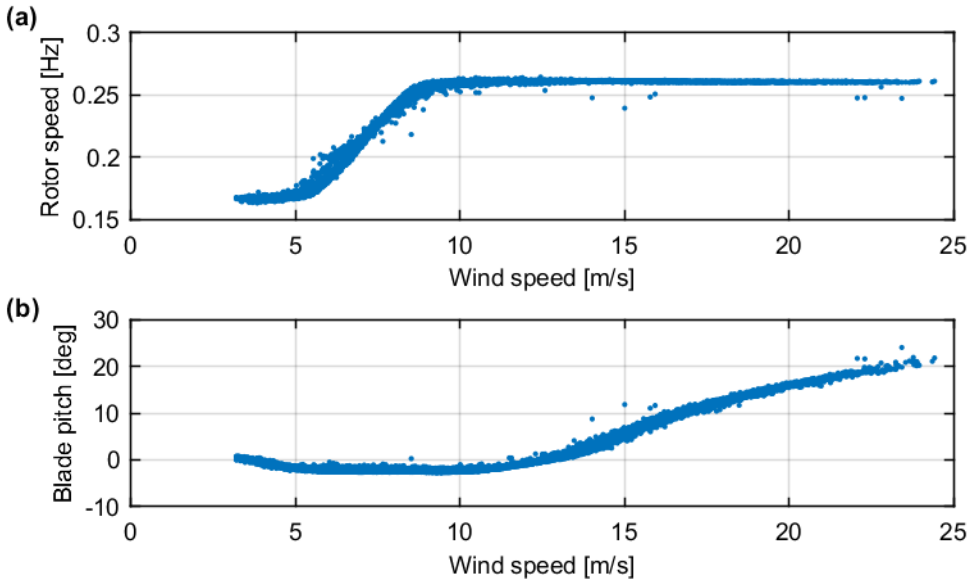

Figure 6-5. Rotor speed and blade pitch angle during power production wind speeds. (a) Rotor frequency during power production operating conditions. (b) Blade pitch angle during power production operating conditions.

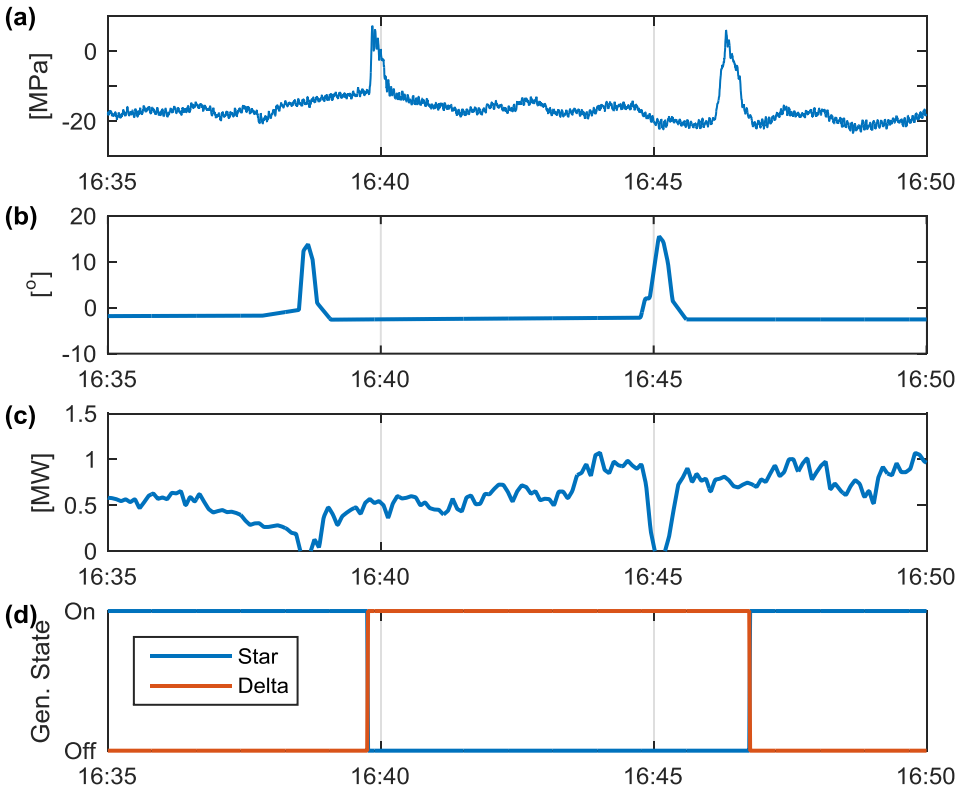

Figure 6-6. Time series data for one of the outlying data points shown in Figure 6-4 (mean wind speed = 7 m/s, direction = 270°). (a) Measured stress measured on the leeward side of the turbine. (b) Blade pitch angle. (c) Output power. (d) Generator grid connection state.

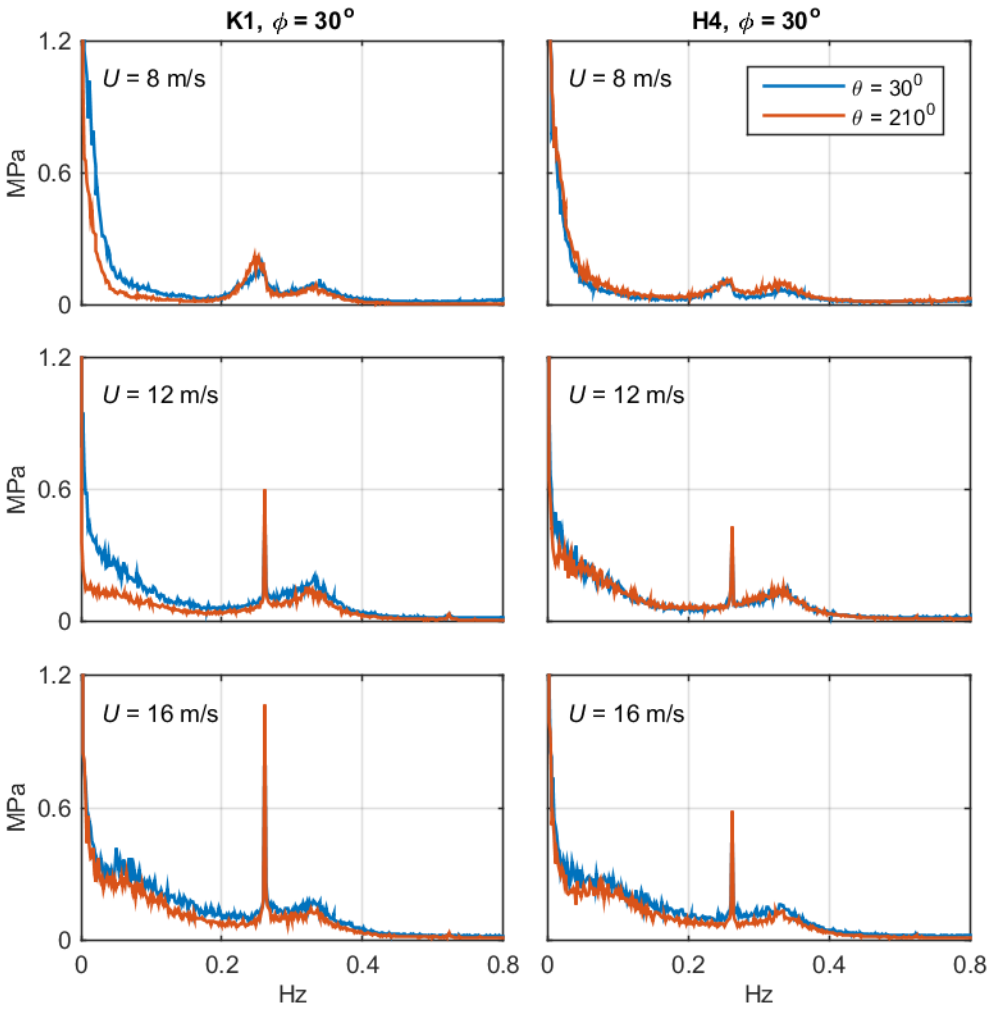

Figure 6-7. Comparison of amplitude spectrums for the fore-aft response (circumferential location ϕ aligned with wind direction), under different wind speeds. Blue lines show wind direction from the North East, while orange lines show wind direction from the South West. The 1P rotor frequency response is apparent at 0.2617 Hz, while the first Eigenfrequency of the structures occur at approximately 0.3283 Hz and 0.3300 Hz for Turbines K1 and H4, respectively. Spectrums calculated from FFT, and averaged over 30 measurements to give a smoothed response.

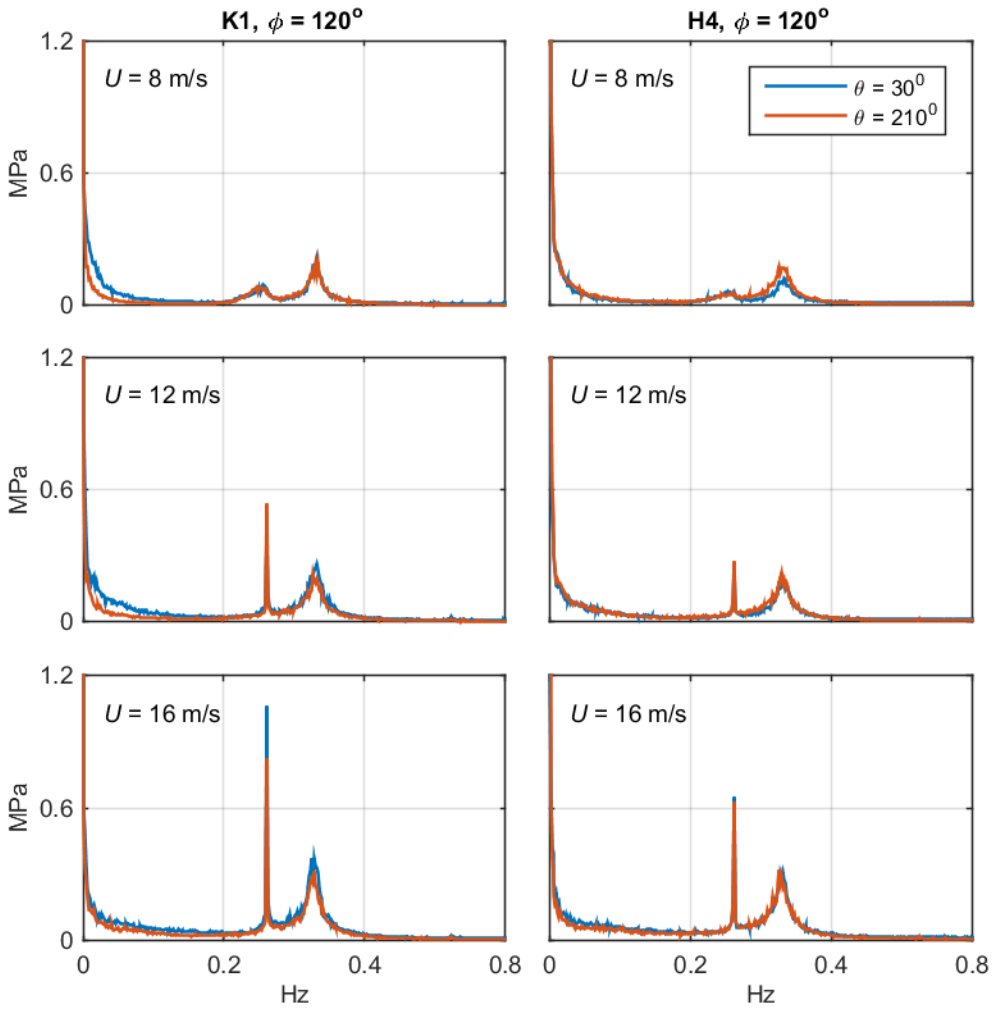

Figure 6-8. Comparison of amplitude spectrums for the side-side response (circumferential location ϕ perpendicular to the wind direction), under different wind speeds. Blue lines show wind direction from the North East, while red lines show wind direction from the South West. The 1P rotor frequency response is apparent at 0.2617 Hz, while the first Eigenfrequency of the structures occur at approximately 0.3283 Hz and 0.3300 Hz for Turbines K1 and H4, respectively. Spectrums calculated from FFT, and averaged over 30 measurements to give a smoothed response.

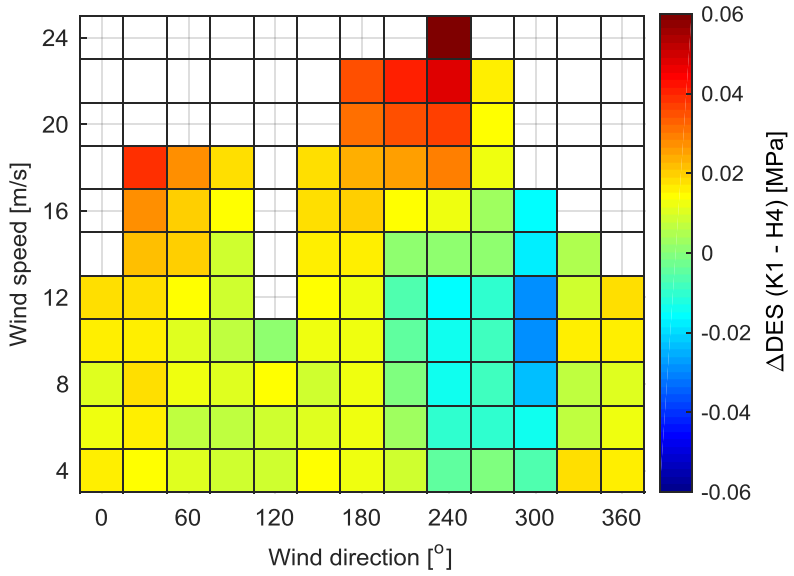

Figure 6-9. Difference between Turbine K1 and H4 mean DES for the full population measurements in MPa, calculated using *m* = 3. Power production cases only.

Table 6-6. Total DES values for the power production Load Cases, factored by the design life frequency of occurrence. Only wind vector bins which were covered by both turbines are included in the total DES values.

Calculation method	Design [MPa]		Measured H4 [MPa]		Measured K1 [MPa]	
	m = 3	*m* = 5	*m* = 3	*m* = 5	*m* = 3	*m* = 5
Population (6.3.1)	17.35	17.26	9.72	11.11	10.04	10.96
High turbulence (6.3.1.1)	17.35	17.26	10.09	11.43	-	-
Sample (6.3.1.2)	17.35	17.26	10.46	12.64	11.30	14.17
Directional extrapolation (6.3.1.3)	17.85	17.66	9.84	11.14	10.26	11.08

Note: Calculation method refers to the method used to identify measurements, with methodology and results described in the indicated sections. The directional extrapolation results represent a complete CM for the power production LC, whereas the rest are represented by incomplete coverage of all wind speed and direction combinations. Relevant section covering discussion of each calculation method included in brackets.

6.3.1.1 Comparison of Loading with the Highest Turbulence Conditions at Turbine H4

In Section 5.2.4, results are presented showing that high turbulence measurements at Turbine H4 could be identified to match the highest mean turbulence locations in the wind farm at each power production wind speed. The mean DES values corresponding to these high turbulence periods are shown in Figure 6-10, in comparison to the values produced by the full population of measurements found for Turbine K1. Comparing Figure 6-9 with Figure 6-10, a noticeable difference can be seen as the high turbulence data periods at Turbine H4 produce slightly higher fatigue damage in comparison to K1. The effect is most noticeable at higher wind speeds, where the high damage region at Turbine K1 for the 210° to 270° directional sector is comparatively lower.

By factoring the mean LC DES($\bar{U}$, $\bar{\theta}$) by the design frequency of occurrence, it was possible to identify the total through-life DES values and compare damage at the two locations. The results are presented in Table 6-6 above, and show that the high turbulence periods at H4 produce a higher level of fatigue damage in the order of $(10.09/9.72)^3$ = 111.8% using m = 3, and $(11.43/11.11)^5$ = 115.3% using m = 5. The high turbulence periods at H4 produce a higher total DES value than the population measurements at K1 using both Wöhler exponents.

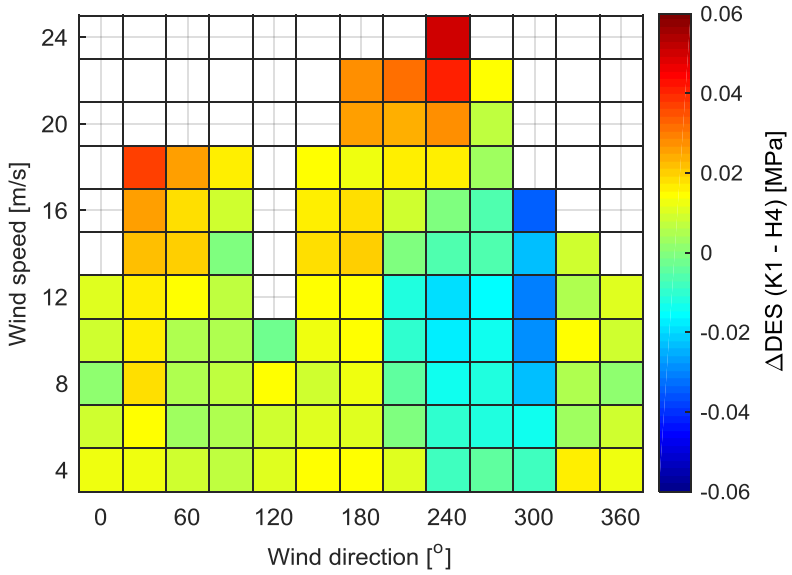

Figure 6-10. Difference between the high turbulence period DES at Turbine H4, and the full population mean DES at Turbine K1. DES calculated using m = 3, power production cases only.

6.3.1.2 Comparison of Population and Sampled Measurements

In Figure 6-11 and Figure 6-12 the full population of measurements for one directional sector are compared to the sampled measurements used to define the power production MLCs according to the criteria outlined in Section 3.2.3. From these figures, the sampling criteria is seen to introduce a conservative selection bias which results in a higher mean DES value for nearly all LC wind speed bins. The bias is particularly significant with Turbine K1 for the 6 m/s and 8 m/s wind speeds, where the measurements are significantly distorted by the high DES outliers described in Section 6.3.1 above. The effect is also evident for Turbine H4, but the sampled periods are more distributed about the main trend.

The significance of the selection bias is quantified in Table 6-6 above, which presents the total sampled DES calculated by factoring the mean value for each wind vector bin by the design frequency of occurrence, and summing the total. As the DES value effectively gives a linearised calculation of fatigue, the relative fatigue damage between the sampled MLCs and the full population measurements is in the order of $(10.46/9.72)^3 = 124.6\%$ for Turbine H4, and $(11.30/10.04)^3 = 142.6\%$ for K1, using $m = 3$.

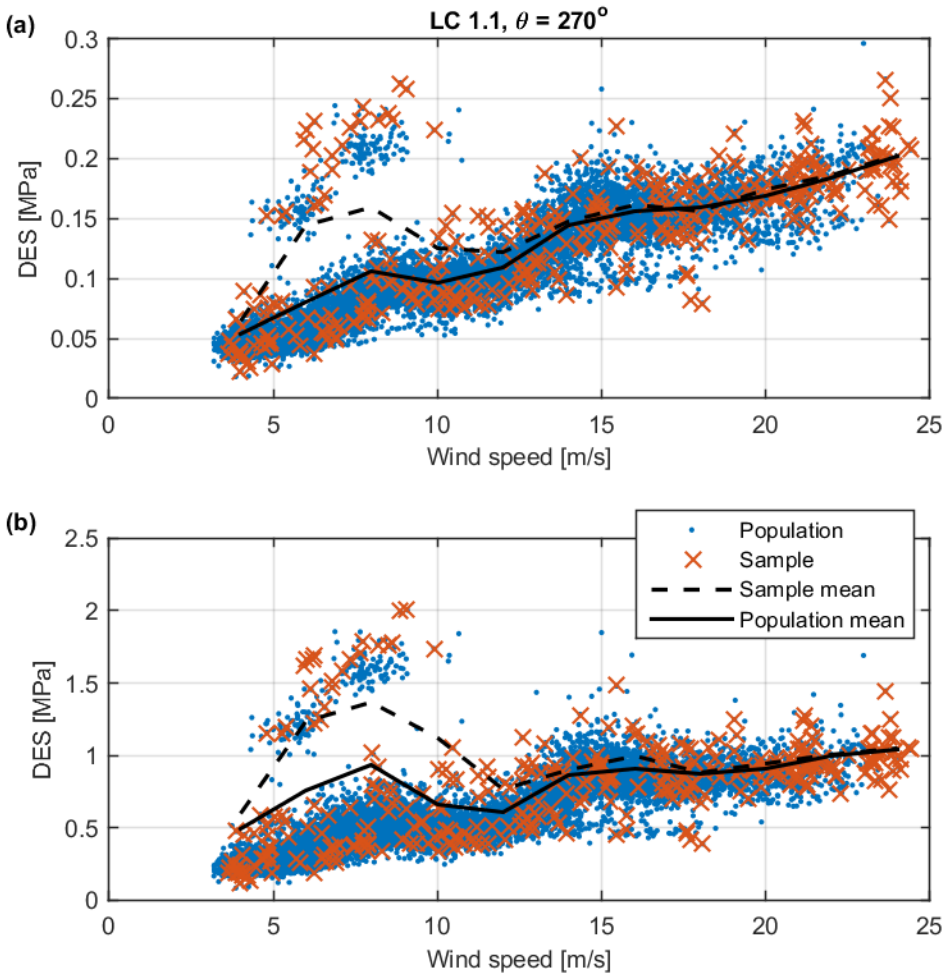

Figure 6-11. Population and sample DES values for Turbine K1, for the power production LCs. (a) DES calculated using *m* = 3. (b) DES calculated using *m* = 5.

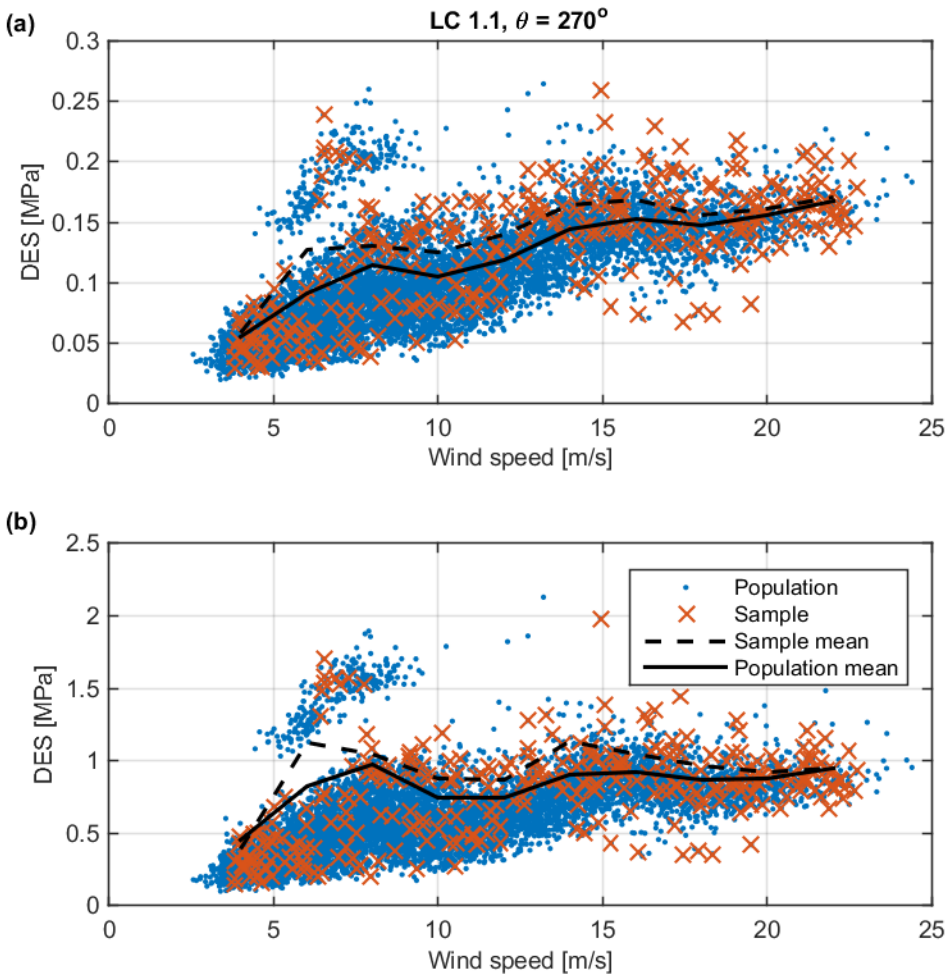

Figure 6-12. Population and sample DES values for Turbine H4, for the power production LCs. (a) DES calculated using *m* = 3. (b) DES calculated using *m* = 5.

6.3.1.3 Directional Extrapolation of Measurements

The directional extrapolation of the MLCs to directions which were not covered by the CM is based on the assumption that the environmental loading from a direction θ_1 can be represented by the loading from a second direction θ_2. Assuming that the wave loading from the most frequently occurring directions is more severe than the directions which were not covered by measurement, the methodology followed was therefore to prioritise the directional variation of turbulence loading. Figure 6-13 shows the directional distribution of turbulence measurements at turbines H4 and K1, and displays the impact of trailing wakes from upwind turbines. Only the power production LCs were used for this analysis due to the limited measurements available for the transient LCs.

For both turbines, measurements from the 240° directional bin were used to replace missing MLCs at the highest wind speeds as no other measurement directions were available, as shown in the CMs in Table 6-1. Figure 6-13 shows that Turbine H4 is aligned with the trailing wake from turbine J2 from this direction bin, and therefore the extrapolation of this MLC measurement should be conservative. For Turbine K1, however, the 240° sector produces only ambient turbulence loading, and therefore MLCs from the 330° directional bin were used to replace missing measurements below 20 m/s.

Measurements were then extrapolated for missing power production LCs using Equation (3-36), and the resulting mean DES was calculated from Equation (3-34). The results were then factored by the design frequency of occurrence, and totals are presented in Table 6-6. The total fatigue damage measured at the turbines for the power production LCs only is in the order of $(9.84/17.85)^3 = 16.8\%$ of the equivalent damage calculated from the design data for Turbine H4, and $(10.26/17.85)^3 = 19.0\%$ for Turbine K1, using $m = 3$.

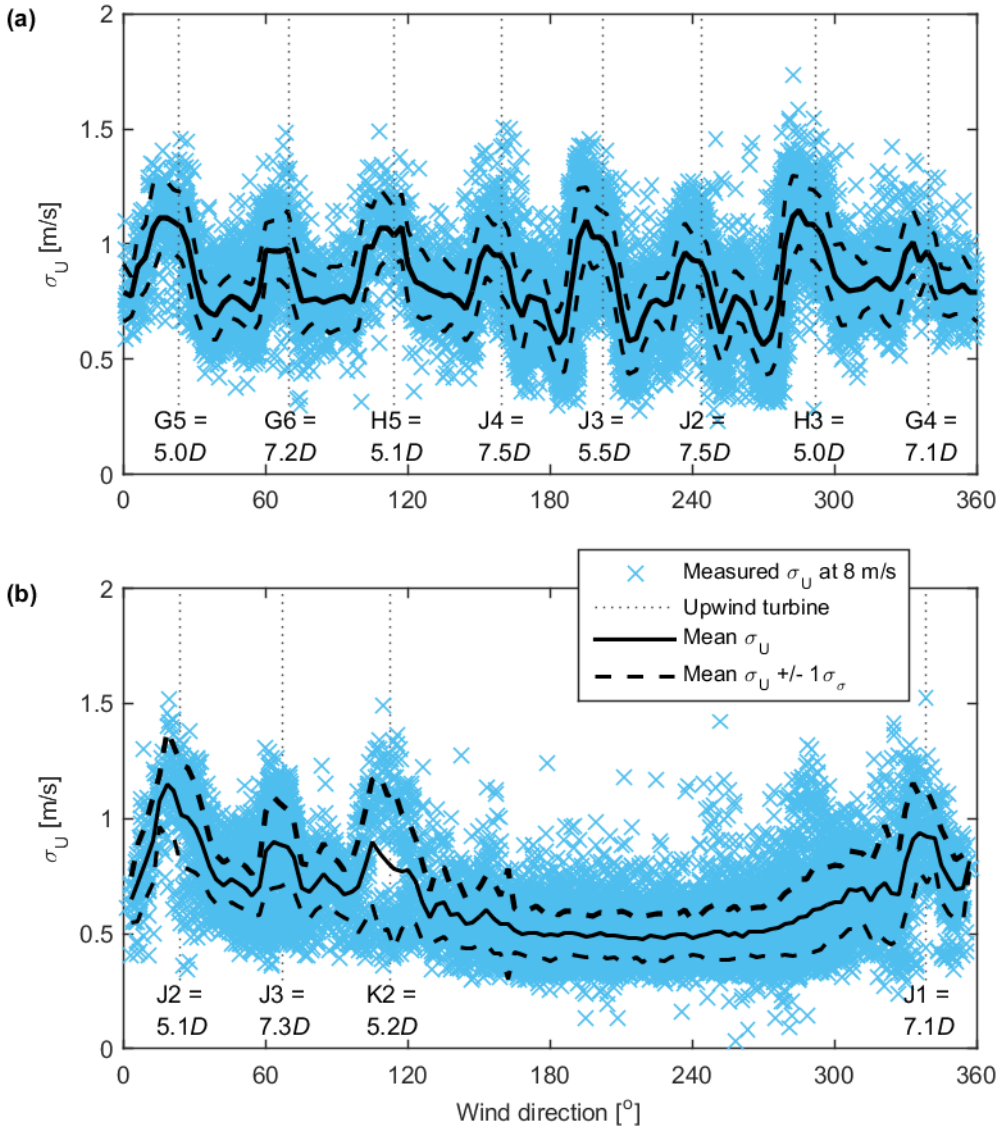

Figure 6-13. Ten minute turbulence measurements at 8 m/s mean wind speed at Turbines H4 (a) and K1 (b). The direction of the closest upwind turbines is identified by the dotted line, with the distance to each turbine given in number of rotor diameters.

6.3.2 LC 3.1 Normal Start-Up

The results for the normal start-up LCs are shown in Figure 6-14 below. The DES values calculated from the design data are seen to be of comparable magnitude to the measured values, apart from start-up at high wind speed where large conservatism is found with the

design data. Significant spread is found for start-up at intermediate wind speeds for Turbine H4, while comparably low scatter is found at high and low wind speeds.

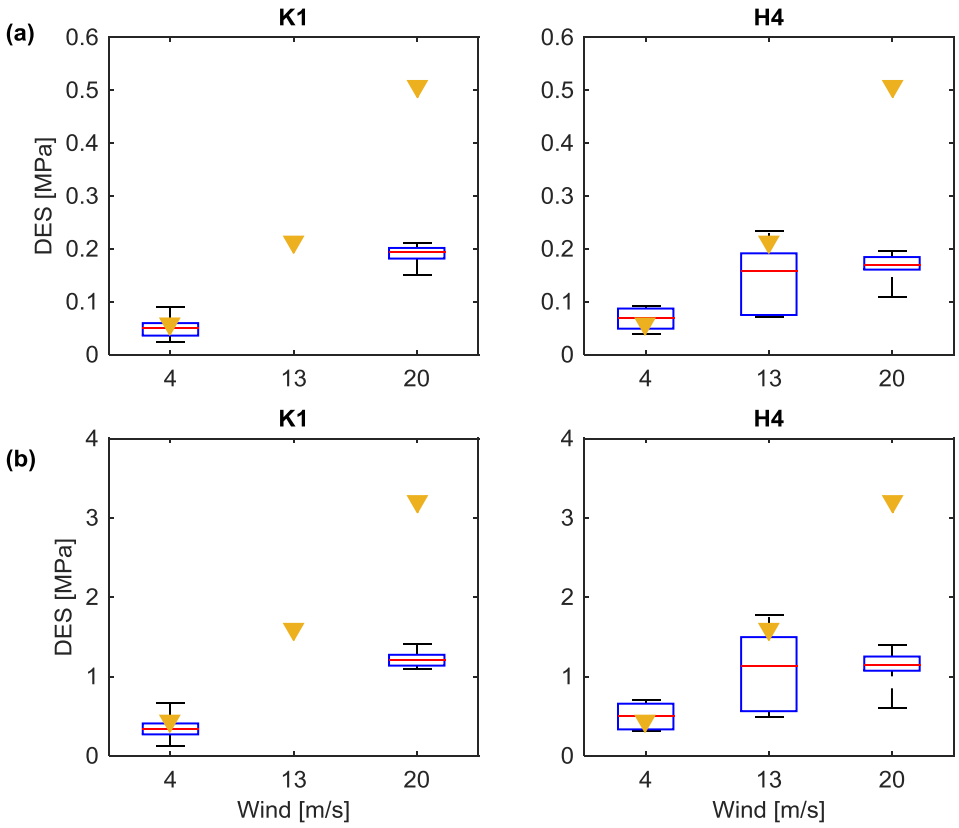

Figure 6-14. Sampled DES values for the normal start-up Load Cases ($\bar{\theta}$ = 270°). Red line shows the mean DES, boxes show 50% of the data points, and whiskers show the limits of the measured data. Yellow triangles show the design values. (a) DES calculated using *m* = 3. (b) DES calculated using *m* = 5.

6.3.3 LC 4.1 Normal Shut-Down

The results for the normal shut-down LCs are shown in Figure 6-15 below. The DES values calculated from the design data are seen to be of similar magnitude compared to the measured values at each wind speed. Significant spread is found for shut-down at intermediate wind speeds for Turbine H4.

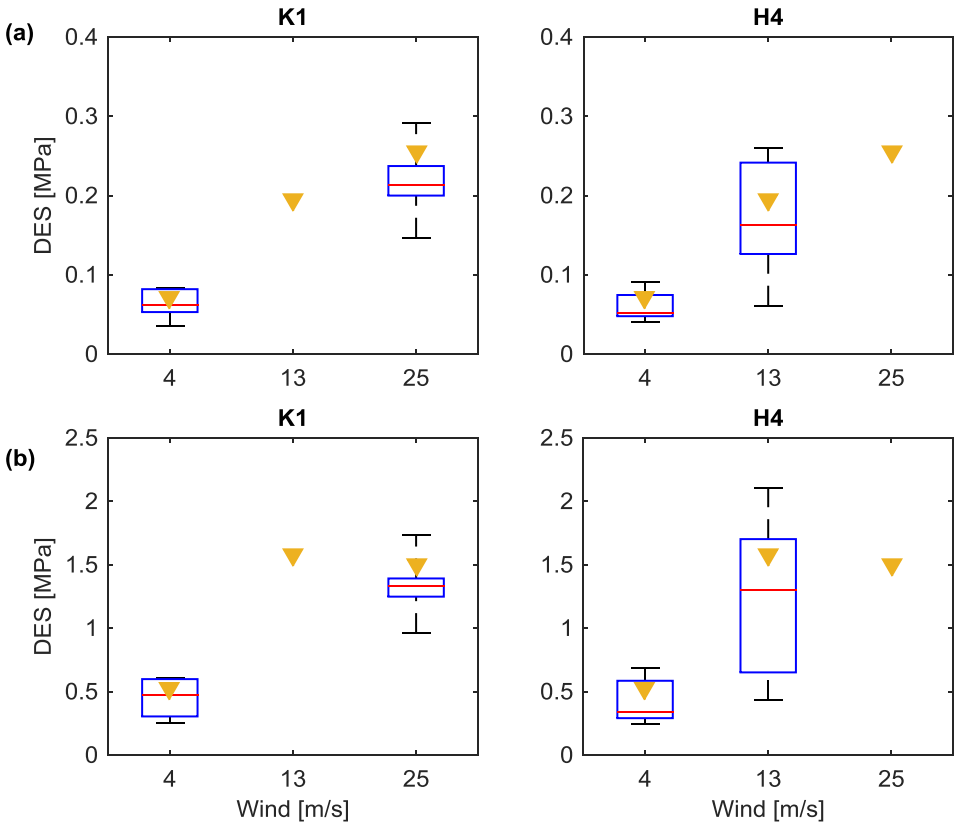

Figure 6-15. Sampled DES values for the normal shut-down Load Cases ($\bar{\theta}$ = 270°). Red lines show the mean DES, boxes show 50% of the data points, and whiskers show the limits of the measured data. Yellow triangles show the design values. (a) DES calculated using *m* = 3. (b) DES calculated using *m* = 5.

6.3.4 LC 5.1 Emergency Shutdown

Insufficient emergency stop events were identified from the measured data to meet the criteria specified in Table 3-5. Therefore, the DLC data was reverted to for all occurrences of this LC.

6.3.5 LC 6.4 Idling

The sampled MLC results for the idling LCs are shown in Figure 6-16 below. The DES values calculated from the design data are seen to be significantly larger than the measured values, while Turbine K1 DES values are found to be slightly higher than H4 under corresponding conditions.

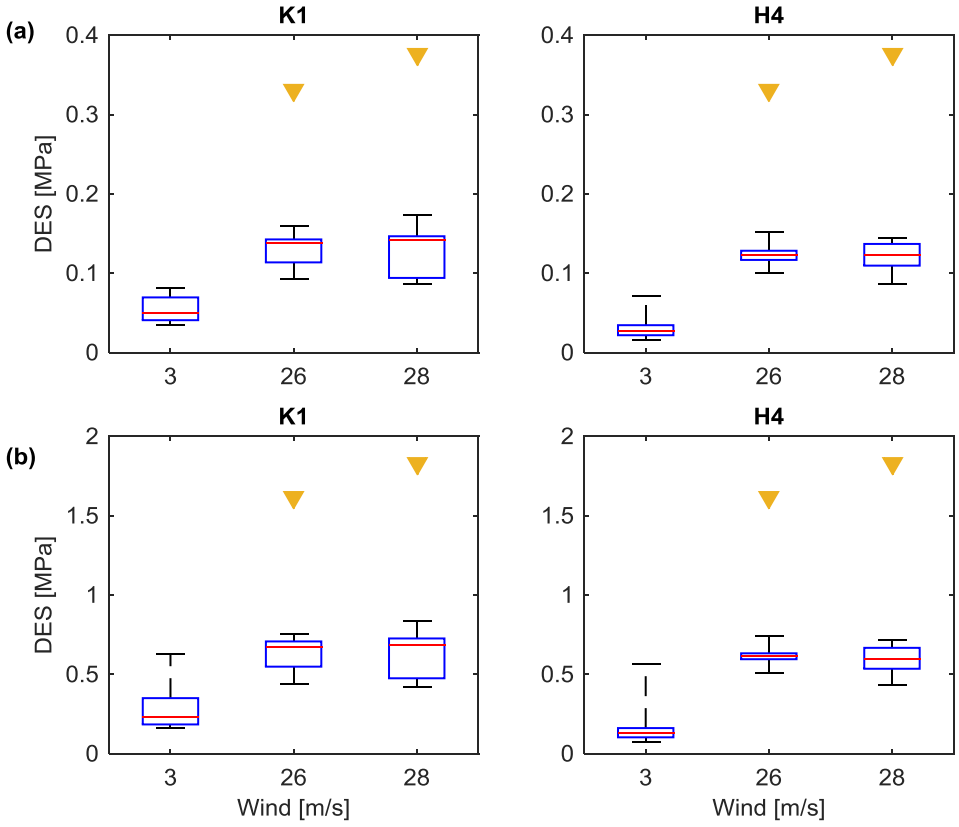

Figure 6-16. Sampled DES values for the idling Load Cases ($\bar{\theta}$ = 270°). Red line shows the mean DES, boxes show 50% of the data points, and whiskers show the limits of the measured data. Yellow triangles show the design values (note that design values were not provided for wind speeds below rated velocity). (a) DES calculated using *m* = 3. (b) DES calculated using *m* = 5.

6.4 Full Life Histogram Comparison

The Capture Matrices are presented in Section 6.2, and show the LCs and wind vector bins which were sufficiently represented by the MLCs. To ensure a comprehensive coverage of all possible loading directions, the DLCs were used where insufficient measurements were available; this approach was assumed to result in a conservative assessment based on the

comparison of measured and design data from Section 6.3. The LCs were factored by the through life frequency of occurrence taken from design (shown in Figure 6-17 for the power production LCs), and combined to give the total value according to Equation (3-35).

The results for the power production LCs measured at Turbine K1 are displayed in Figure 6-18, and show that the DLC cases which were used to replace insufficient measured data contribute a significant proportion of the total damage estimation, even when factored by the through life frequency of occurrence.

The complete results for all LCs are presented in Table 6-7, from which it can be seen that the measured loads produce lower DES values for all but LC 6.4 (idling conditions). This is due to the inclusion of the low wind speed LCs in the measured histogram, which were not included in the design approach, probably because they provide such a small contribution to the overall level of fatigue damage. This constitutes the main difference between design and measured loading for the idling LC, as very few measurements were recorded above rated wind speed (see the CM in Table 6-5). Additionally, no MLCs were recorded for the emergency stop LC (LC 5.1), and therefore the DES values for the measured histograms are equal to the design value. The largest reduction in DES value is found with the power production LCs, with the design level of fatigue damage in the order of $(17.85/11.58)^3 = 366\%$ greater than Turbine H4 using $m = 3$, or $(17.85/12.17)^3 = 316\%$ for Turbine K1.

Figure 6-19a compares the cycle histograms produced by the measured and design data. The measured histograms display a reduced number of cycles in the range of 5 to 30 MPa, and the corresponding reduction in fatigue in this region in shown in Figure 6-19b and c.

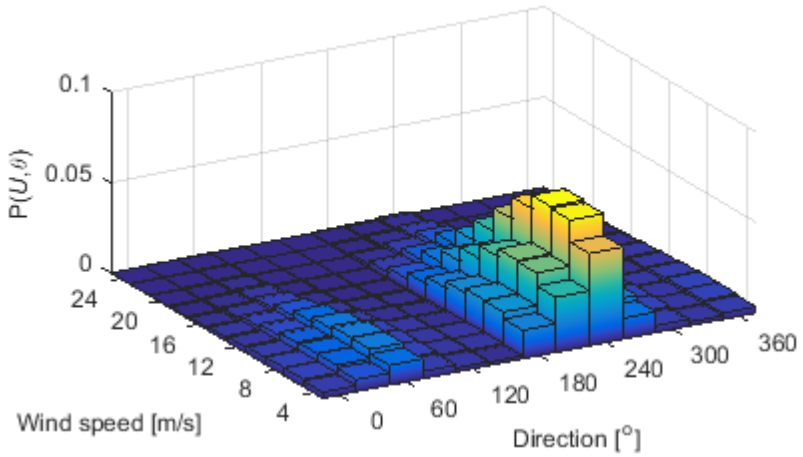

Figure 6-17. Design probability distribution for the power production Load Cases (LC 1.1).

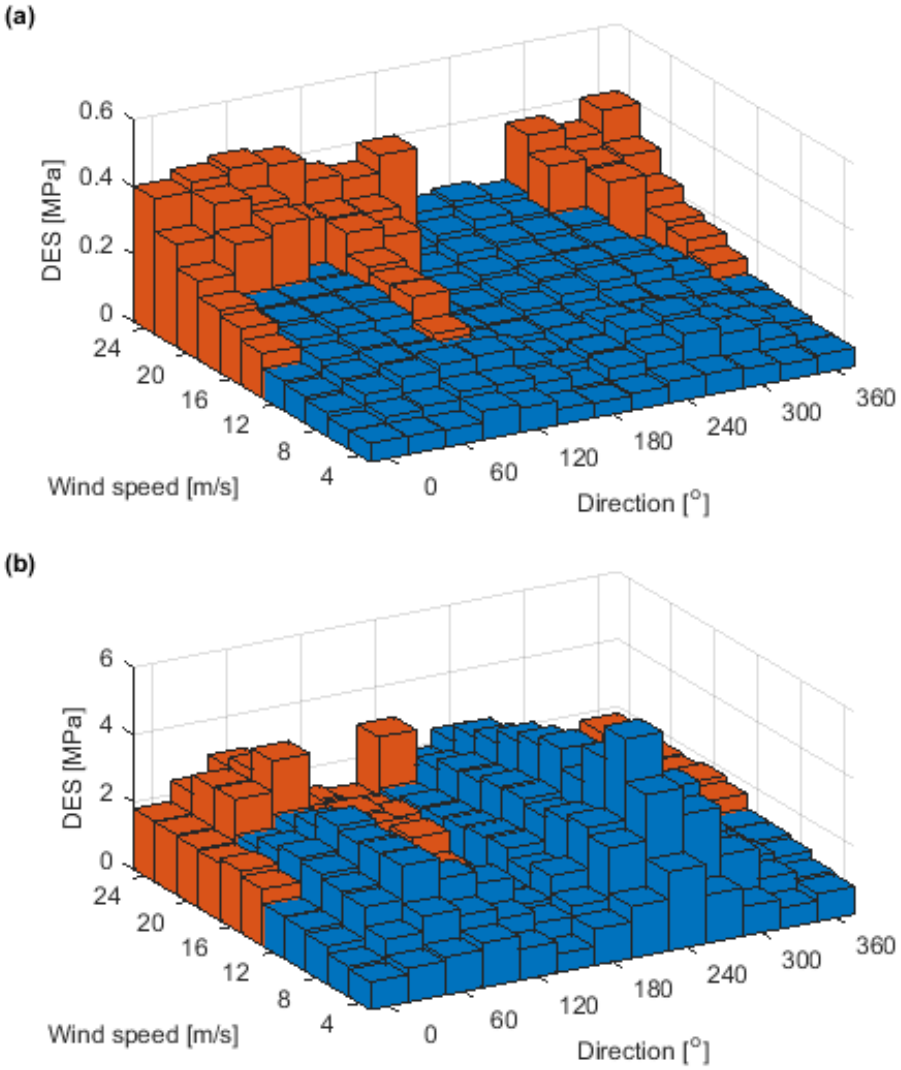

Figure 6-18. DES calculated for the power production MLCs (blue) and DLCs (orange) at Turbine K1. (a) DES for the power production Capture Matrix. (b) Power production DES, factored by the frequency of occurrence (shown in Figure 6-17).

Table 6-7. Comparison of DES produced by the design and measured load histograms, factored by the design life frequency of occurrence. The total value is calculated according to Equation (3-35).

LC	Design [MPa]		Measured H4 [MPa]		Measured K1 [MPa]	
	$m = 3$	$m = 5$	$m = 3$	$m = 5$	$m = 3$	$m = 5$
1.1	17.85	17.66	11.58	13.73	12.17	14.80
3.1	3.03	7.76	2.57	6.09	2.60	6.05
4.1	2.76	6.72	2.49	6.04	2.71	6.10
5.1	1.68	6.64	1.68	6.64	1.68	6.64
6.4	5.90	11.14	5.94	11.14	5.99	11.14
Total	18.11	18.11	12.17	14.71	12.72	15.55

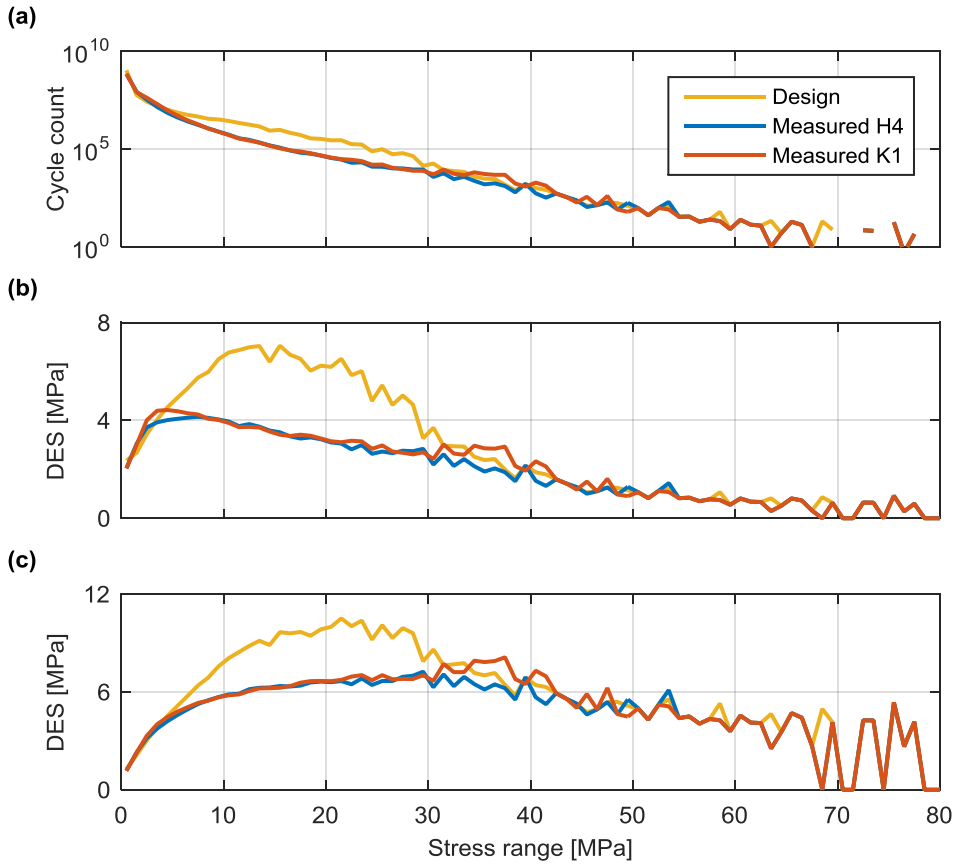

Figure 6-19. Comparison of fatigue load histograms. (a) Number of cycles corresponding to each stress range bin. (b) DES calculated for each stress range bin, using *m* = 3. (b) DES calculated for each stress range bin, using *m* = 5.

7 Discussion of Results: Transition Cycles

7.1 Definition of a Representative Wind History

The wind variability metric calculated using Equation (3-39) was used to quantify changes in wind speed and direction from a range of datasets. Changes in wind speed and direction are used here as a measure of the potential significance of transition cycles on the total fatigue load histogram for an OWT support structure. Results are shown in Figure 7-1, which displays comparatively large variability in the wind vector at the two onshore sites in the US (Panther Creek and Munnsville), with the lowest variation found at the OWEZ and Rødsand sites. However, as the datasets came from different measurement heights an adjustment based on knowledge of the site specific wind shear profile would be necessary to make an accurate comparison.

However, the aim of the study was to investigate whether a single year could be considered a representative period in order to quantify the wind variability at a given site. Therefore the standard deviation of the calculated variability values were taken, normalised by the mean to give a value which should be independent of measurement height, and results are presented in Table 7-1. The σ/μ values vary from 1.71% at Pulaski Shoals off the coast of Florida, US, to 8.58% at Munnsville in New York state, US, indicating that the duration required to define a representative period may be site-specific.

These results do not reveal specific information about transition cycles for any of the sites, as the significance of transition cycles depends on the proportion of fatigue damage resulting from the standard ten minute LC period, which is dependent upon the specific turbine and environmental loading conditions. Therefore, to ensure that annual variability can be accounted for at a given site, it is recommended that, where available, measured wind data spanning multiple years is utilised when assessing the significance of transition cycles on the total fatigue load histogram for an OWT support structure.

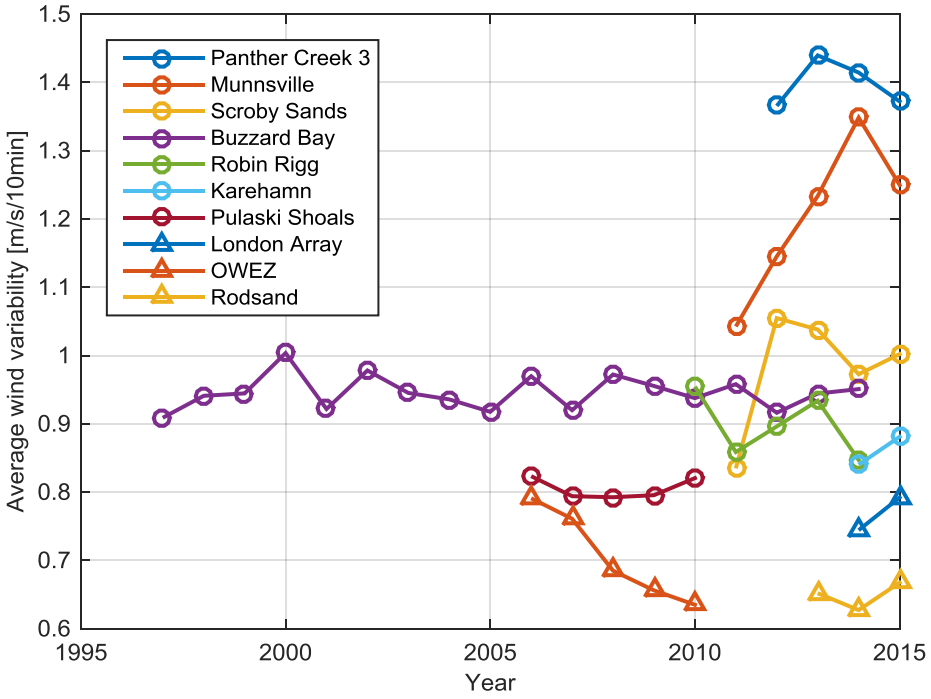

Figure 7-1. Average wind variability measured per calendar year, calculated using Equation (3-39).

Table 7-1. Average annual wind speed variability coefficient of variation.

Site Name	σ/μ
Buzzard Bay	2.54%
Karehamn	2.37%
London Array	3.11%
Munnsville	8.58%
OWEZ	8.55%
Panther Creek III	2.18%
Pulaski Shoals	1.71%
Robin Rigg	4.62%
Rodsand II	2.55%
Scroby Sands	7.98%

7.2 Continuous Measurement Period

Results from RF processing of a continuous one year period of measured data are presented below. Figure 7-2 shows the ratio of fatigue damages produced by RF processing the data in independent ten minute periods (using the simple and half cycle counting methodologies outlined in Section 2.2.3.4), to the damage produced by RF counting the data as a continuous sequence. The fatigue damage ratios can be seen to converge on a steady value after approximately two to three months, which is indicative of the time scale required to account for transition cycles accurately based on the analysed data set. The final damage ratios for the one year period are given in Table 7-2, which show that not accounting for transitions between each ten minute period results in 37% to 52% of the fatigue damage produced by RF counting the data as a continuous period, using $m = 5$. Using $m = 3$, however, the level of fatigue damage using the half cycle and simple RF counting methodologies is only 93% to 97% of the true value; this can be seen from Figure 7-3b to be due to the lower damage exponent attributing a greater proportion of the fatigue damage to the high frequency/low amplitude fatigue cycles. Therefore, transition cycles can be found to contribute a significant proportion of fatigue damage using the higher Wöhler exponent, for the measured dataset.

Figure 7-2 also shows the effect of accounting for transition cycles which occur between each ten minute period by using the maximum and minimum stress points in each ten minute period, similar to the methodology presented by Larsen and Thomsen [72]. However, it is noted that the method presented by Larsen and Thomsen was based on variations in ten minute mean wind speeds only, whereas the current study utilised the maximum and minimum stress points in each ten minute period as a function of both mean wind speed and direction. The results show that the Larsen and Thomsen method is found to overestimate the level of fatigue loading by a factor of 114% to 129% for the Turbine H4 data with $m = 3$ and $m = 5$, respectively, and by 112% to 123% for Turbine K1, compared to the damage calculated by RF counting the data correctly as a continuous series. The over estimation can be seen from Figure 7-3 to arise from a greater number of stress ranges identified in the 15 MPa to 40 MPa region, compared to the cycles identified by RF counting the data as continuous series. This overestimation results from the effective double-counting of the RF residue from the ten minute periods as both half cycles and as partial transition cycles from the synthetic time series of concatenated maximum and minimum stresses. Therefore, accounting for the transition cycles using the continuous RF residue concatenation methodology presented in Table 3-7 is recommended in order to identify all stress cycles accurately according to the RF algorithm, and to avoid unnecessary conservatism.

It is noted that the results presented here are calculated using Equation (3-40), and are therefore representative of fatigue damage calculation using constant gradient S-N curves. Again, this equation has been used to compare RF methodologies as any linear factor on stress ranges, which could result from a geometric hot spot and resulting stress concentration, or from the use of a material partial factor (safety factor), for example, would cancel out by taking the ratio of fatigue damages. In practice, S-N curves with a double gradient may be employed depending on the corrosive effects of the operating environment, such as the 'in air' and 'sea water with cathodic protection' curves shown in Figure 2-7. In this case the shape of the load histogram in relation to the two sections of the S-N curve would become significant in determining the level of fatigue damage produced by each RF processing method. However, it was found that, for the load histograms analysed with the current results, fatigue damage ratios calculated using these S-N curves produced very similar or identical results to those presented in Figure 7-2 and Table 7-2. The total damage ratios for the one year data periods analysed are presented in Table 7-3 and show that the damage ratios for the 'sea water with cathodic protection' S-N curve are practically identical to the constant gradient results using $m = 5$ from Table 7-2, while the impact of transition cycles is slightly less using the 'in-air' S-N curve (results using a 'sea water with free corrosion' S-N curve have not been included, but produce the same results as shown in Table 7-2 for the Wöhler exponent of $m = 3$ due the constant S-N gradient). This is due to the position of the 'knee' in the double gradient curves (which are shown in Figure 2-7), and the proportion of cycle fatigue damage which is calculated with each part of the S-N curve. These results confirm the finding that transition cycles contribute a significant percentage of fatigue damage, for the measured dataset.

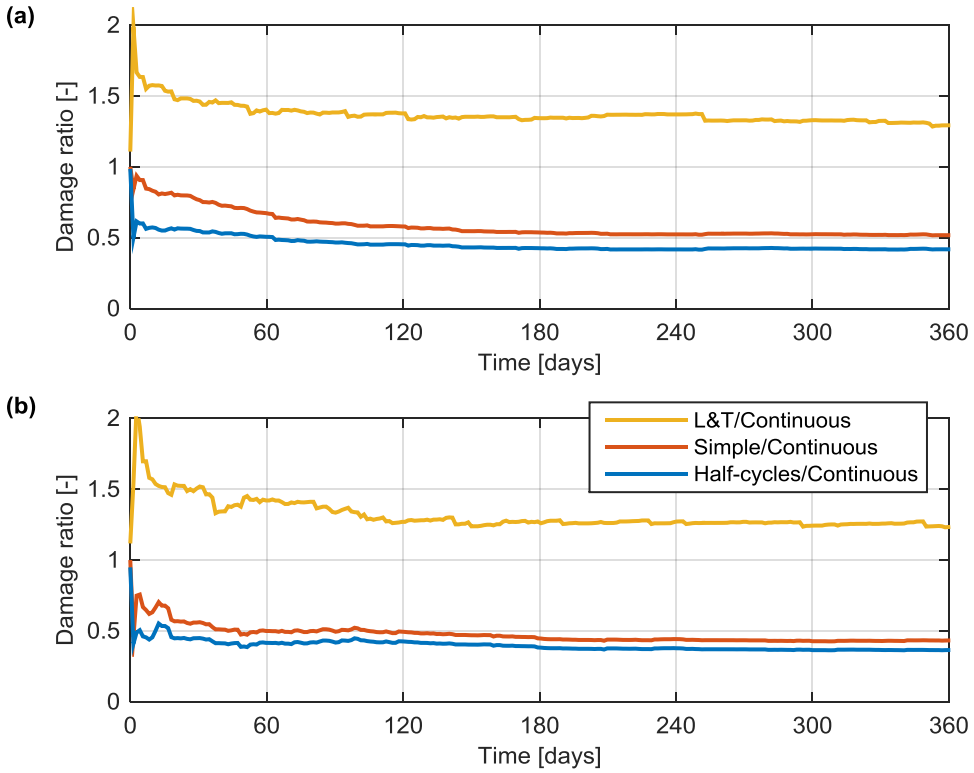

Figure 7-2. Ratio of accumulated fatigue damages calculated using Equation (3-40), with $m = 5$; expressed as damage produced using different counting methods described in Table 3-7, divided by the damage produced by RF counting the data as a continuous series. (a) Damage ratio calculated from H4 data. (b) Damage ratio from Turbine K1.

Table 7-2. Ratio of fatigue damage for a one year measurement period. Simplified damage ratio calculated with Equation (3-40), with constant S-N gradient. Damage ratio expressed as the indicated method divided by the result from the continuous dataset.

	Turbine H4		Turbine K1	
	$m = 3$	$m = 5$	$m = 3$	$m = 5$
One-pass	0.925	0.418	0.925	0.365
Simple RF	0.965	0.518	0.957	0.433
Larsen & Thomsen	1.136	1.293	1.116	1.233

Table 7-3. Ratio of S-N curve fatigue damage for a one year measurement period. Damage ratio calculated as the indicated method divided by the result from the continuous dataset, using D class S-N curves from [55].

	Turbine H4		Turbine K1	
	In-air	Cathodic protection	In-air	Cathodic protection
One-pass	0.495	0.419	0.447	0.365
Simple RF	0.610	0.519	0.529	0.433
Larsen & Thomsen	1.303	1.293	1.245	1.230

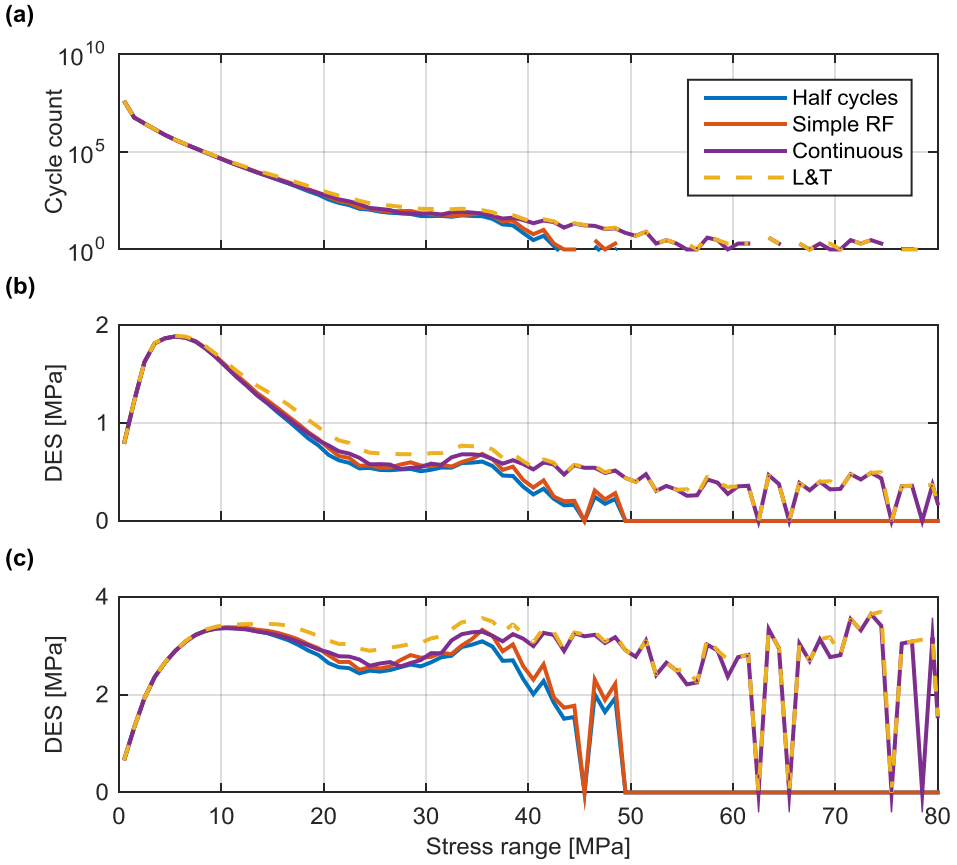

Figure 7-3. Cycle histogram and fatigue damage spectrums calculated from a one year continuous data period. (a) Cycle histograms from Turbine K1. (b) Corresponding DES value calculated using *m* = 3. (c) DES calculated using *m* = 5.

7.3 Transition Cycles from a Representative Wind History

The four year wind history from operational SCADA measurements presented in Section 5.1 was used to identify a sequence of LCs which should be representative of the wind farm site, accounting for the variability of the wind speed and direction vector. The LC sequence is shown in Figure 7-4, broken down into the operational states used for the fatigue analysis. Note that the variation in mean wind direction, and the variation in mean wind speed for LC 1.1 and LC 6.4, are not shown in Figure 7-4, but are accounted for the in the DLC/MLCs used for the analysis. The representative LC sequence was then used to investigate the impact of transition cycles on the full design life histogram using the methodologies outlined in Table 3-8.

The ratio of full life damage values are shown in Table 7-4, which compares the fatigue damage produced with the inclusion of transition cycles identified from the representative LC history, to the fatigue damage produced without accounting for transition cycles (calculated from Equation (3-35), and presented in Table 6-7). The Larsen and Thomsen' [72] method of accounting for transition cycles produces an increased level of fatigue damage using the data from Turbine K1, in the order of 121% using $m = 3$, or 161% using $m = 5$. The 'continuous' method, however, does not include the double counting of cycles which result from the Larsen and Thomsen method, and the fatigue load histogram should therefore be representative of the true loading. The resulting increase in fatigue damage calculated for Turbine K1 is in the order of 110% using $m = 3$, or 137% using $m = 5$. Similar results are found with data from both Turbine H4 and the design simulations, and therefore transition cycles are found to have a significant contribution under the loading conditions at the analysed site. However, the level of LC conservatism identified in the design data, as presented in Section 6.4, means that the design loads are still conservative. The main significance of transition cycles in this context is therefore identified in the main topic of interest for this thesis; in the construction of a fatigue load histogram from operational data, where a complete description of the loading is necessary in order to ensure the assessment is not non-conservative.

The stress cycles which contribute the additional fatigue damage identified by the synthetic stress histories are shown in Figure 7-5 to Figure 7-7. Additional fatigue damage can be identified in the high stress/low frequency region of the loading spectrums, relating to the stress cycles which arise from large changes in loading direction due to changes in mean wind speed and direction. Although the fatigue damage produced using the measured data

(Figure 7-6 to Figure 7-7) is lower than that produced by the design simulations (Figure 7-5), the additional fatigue damage appears in the same region of the loading spectrums.

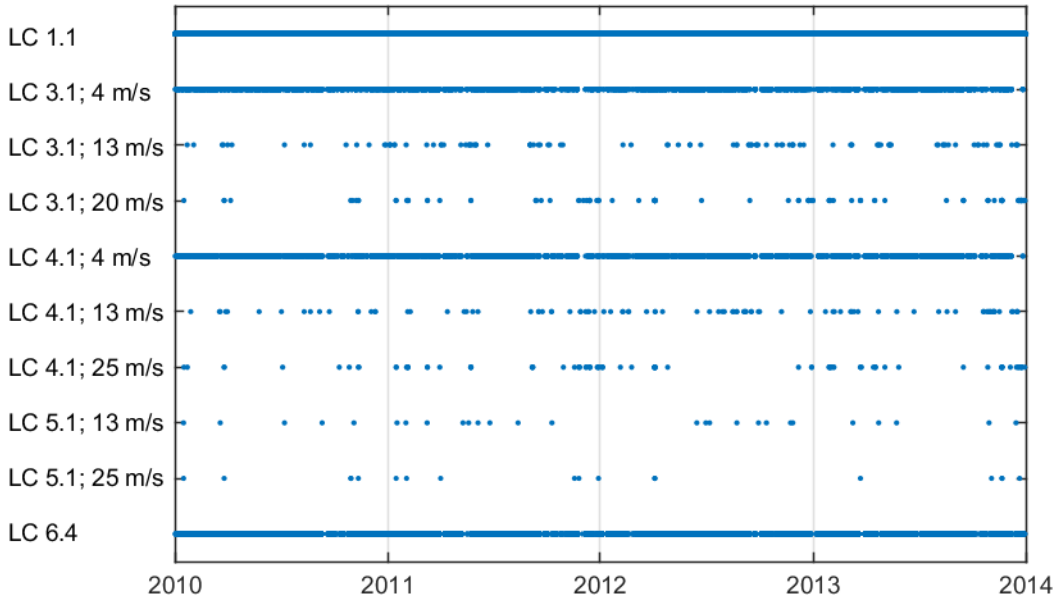

Figure 7-4. Four year representative Load Case sequence identified from the ten minute average wind history. LC 1.1 = normal power production, LC 3.1 = normal start-up, LC 4.1 = normal shut-down, LC 5.1 = emergency stop, LC 6.4 = idling conditions.

Table 7-4. Ratio of fatigue damage values produced by accounting for transition cycles using the representative LC history, to that produced without transition cycles.

Method	Design [MPa]		Measured H4 [MPa]		Measured K1 [MPa]	
	$m = 3$	$m = 5$	$m = 3$	$m = 5$	$m = 3$	$m = 5$
Continuous	1.06	1.37	1.08	1.37	1.10	1.37
Larsen & Thomsen	1.13	1.50	1.19	1.63	1.21	1.61

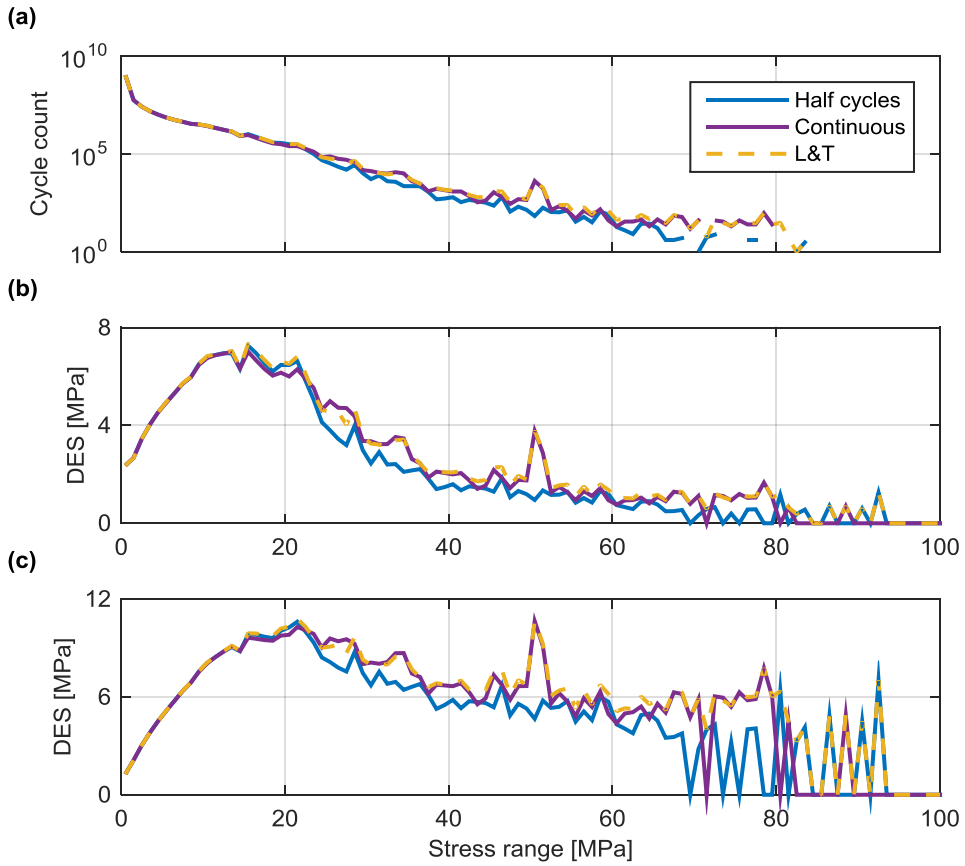

Figure 7-5. Impact of transition cycles on the total cycle and fatigue damage spectrums, from design data. (a) Cycle histograms. Blue line; calculated without accounting for transition cycles. Purple line; accounting for transition cycles using residue concatenation corresponding to a four year representative wind history. Yellow line; accounting for transition cycles using the maximum and minimum stresses from each LC, corresponding to a four year representative wind history. (b) DES vector produced using *m* = 3. (c) DES vector produced using *m* = 5.

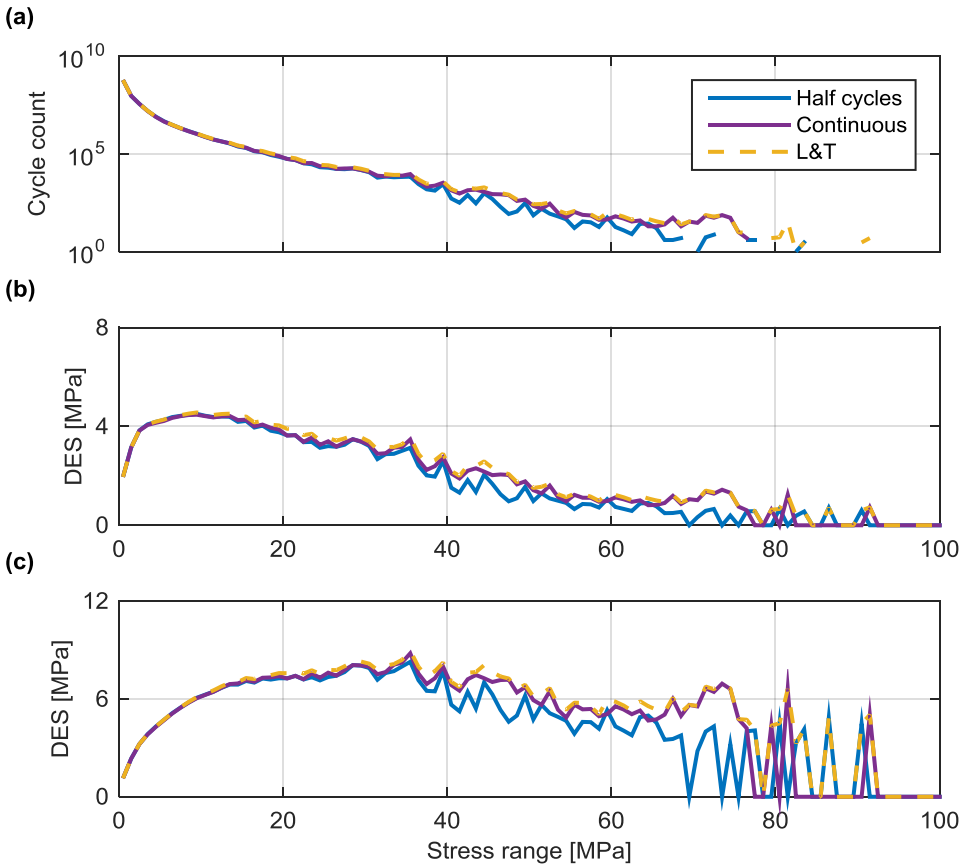

Figure 7-6. Impact of transition cycles on the total cycle and fatigue damage spectrums, from Turbine K1. (a) Cycle histograms. Blue line; calculated without accounting for transition cycles. Purple line; accounting for transition cycles using residue concatenation corresponding to a four year representative wind history. Yellow line; accounting for transition cycles using the maximum and minimum stresses from each LC, corresponding to a four year representative wind history. (b) DES vector produced using *m* = 3. (c) DES vector produced using *m* = 5.

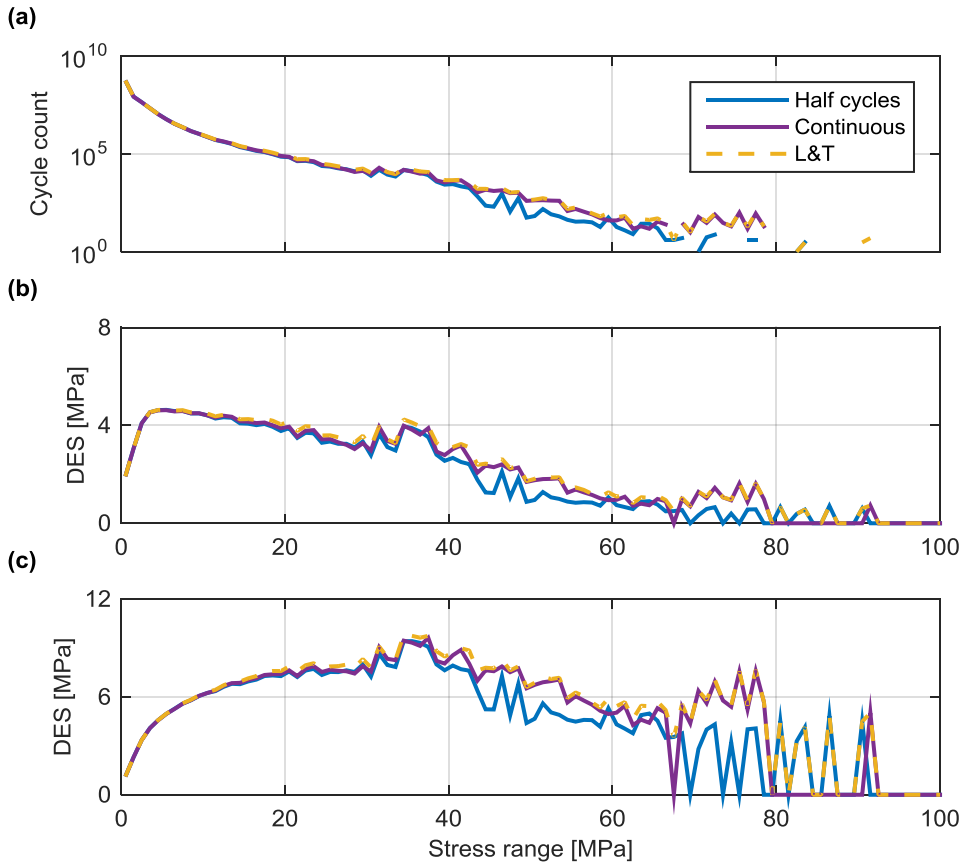

Figure 7-7. Impact of transition cycles on the total cycle and fatigue damage spectrums, from Turbine H4. (a) Cycle histograms. Blue line; calculated without accounting for transition cycles. Purple line; accounting for transition cycles using residue concatenation corresponding to a four year representative wind history. Yellow line; accounting for transition cycles using the maximum and minimum stresses from each LC, corresponding to a four year representative wind history. (b) DES vector produced using *m* = 3. (c) DES vector produced using *m* = 5.

8 Discussion of Results: Wind Turbine Simulation

Chapter 6 compared results of measured fatigue loading with design results, and identified how levels of design conservatism can be assessed through measurement. This chapter presents results from model simulations which were used to investigate the potential variation in levels of fatigue loading across the OWF site, and potential changes in structural frequency.

8.1 Comparison with Design

This section presents a comparison of results from the design simulations produced by the turbine designer, and the Bladed model defined with similar environmental loading (IEC Class B turbulence values, and the same wave spectral parameters) and structural definition (water depth and first natural frequency of the support structure). Under these conditions the response behaviour of the Bladed model can be compared directly to the design simulations to assess how effectively it represents the OWT dynamics.

Time series simulation results are presented in Figure 8-1 and Figure 8-2, and show the fore-aft bending moment output at the sea bed level of -10.6 mCD, under two mean wind speed loading conditions. Figure 8-1 presents an example time series for wind speeds below rated (at $\overline{U}$ = 8 m/s), from which it can be seen that the Bladed model produces a more dynamic fore-aft response than the design simulation. From Figure 8-1c, the rotor frequency response is not clearly apparent as the rotor operates at variable speed, and is blended with the structural response around the first natural frequency of 0.295 Hz. The Bladed model also produces greater response at higher frequencies (around 0.6 Hz and 1.1 Hz), which are likely to be produced by the blade frequencies and higher mode response of the structure. The low frequency response at the left of the spectrum (<0.1 Hz) is consistent with the design model results, and is due to the similar turbulence values used in both simulations. The peak wave period for this simulation of T_p = 3.93 s also appears to result in structural response which merges with the first natural frequency of the structure, although the wave heights are small at this wind speed bin.

Figure 8-2 compares the model results above rated wind speed at $\overline{U}$ = 16 m/s, and shows greater similarity between the Bladed model and the design simulations. The Bladed model produced a more dynamic response than the design model around the structural first mode frequency, but notably the wave loading frequencies (where T_p = 6.13 s at this LC bin) produce a greater response at 0.14-0.19 Hz which is distinct from the first mode response

frequency range. Additionally, higher frequency responses around $0.8 - 1$ Hz are again apparent in the Bladed model. The low frequency response below 0.1 Hz is again consistent with both models due to the wind turbulence levels used.

The level of fatigue damage produced by the time series can be related to a DEM from Equation (3-17) at the sea bed level in either the x or y direction, as shown in Figure 8-3. Figure 8-4 shows the M_y bending moment DEM, under wind loading directions from 0° and 270°, representing the side-side and fore-aft directions, respectively. It can be seen that, although the side-side DEM is of small magnitude and is reasonably well represented by the Bladed model, the fore-aft DEM is an approximate factor of two times higher than the design simulation results, relating to an increased fatigue damage level of approximately $2^3 = 8$, or $2^5 = 32$ times the design value, using $m = 3$ or $m = 5$ respectively.

Figure 8-5 presents the M_y DEM comparison for all power production LC bins, and shows that the trend displayed in Figure 8-4 is consistent over all directions. However, an increased DEM is apparent in the Bladed model for loading from the Easterly direction, from which the peak wave period, at $T_p = 3.88$ s for the maximum wind speed bin, presumably interacts with the rotor and first structural frequency. As this elevated DEM is not present in the design simulation results, it appears that the Bladed model does not represent well the model used by the turbine designer. The total, combined DEM values, factored by the design life frequency of occurrence, are given in Table 8-1, and show an equivalent increased level of fatigue damage for the Bladed model compared to the design simulation in the order of $(28.7/20.0)^3 = 293\%$ using $m = 3$, or $(24.2/19.5)^5 = 294\%$ using $m = 5$. Therefore, the model is found to significantly over-predict the dynamic response of the structure and the corresponding level of fatigue damage, and cannot be expected to provide realistic results. However, in the absence of a more realistic representation of the turbine behaviour, the impact on fatigue loading of varied environmental loads and structural responses were investigated using the Bladed model, as the sensitivity of the level of fatigue loading to different variables can still be investigated, and these results are presented in Section 8.2 below.

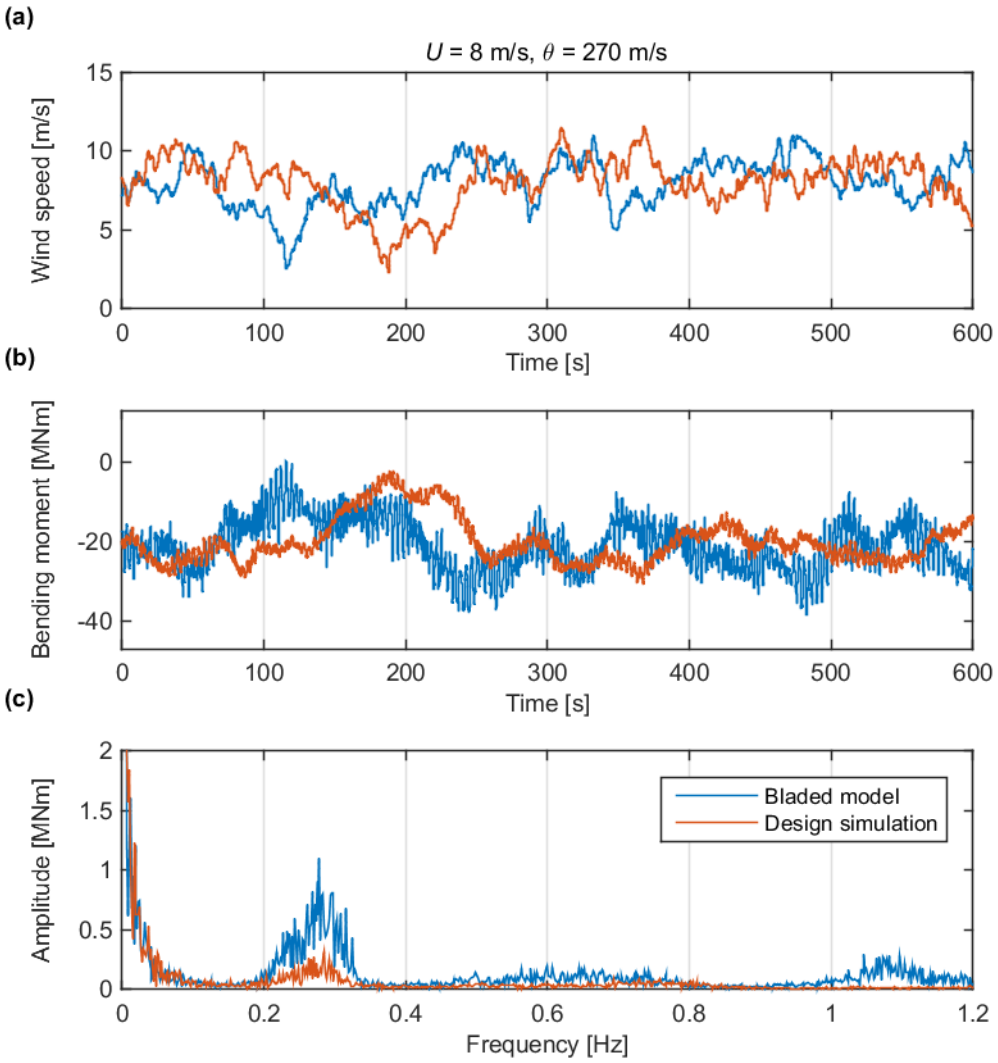

Figure 8-1. Comparison of bending moment results from the Bladed model and the original design simulation data, below rated wind speed. (a) Wind time series at hub height. (b) Bending moment time series at -10.6 mCD. (c) Amplitude spectrum calculated from FFT of the ten minute time series (average value from two simulations).

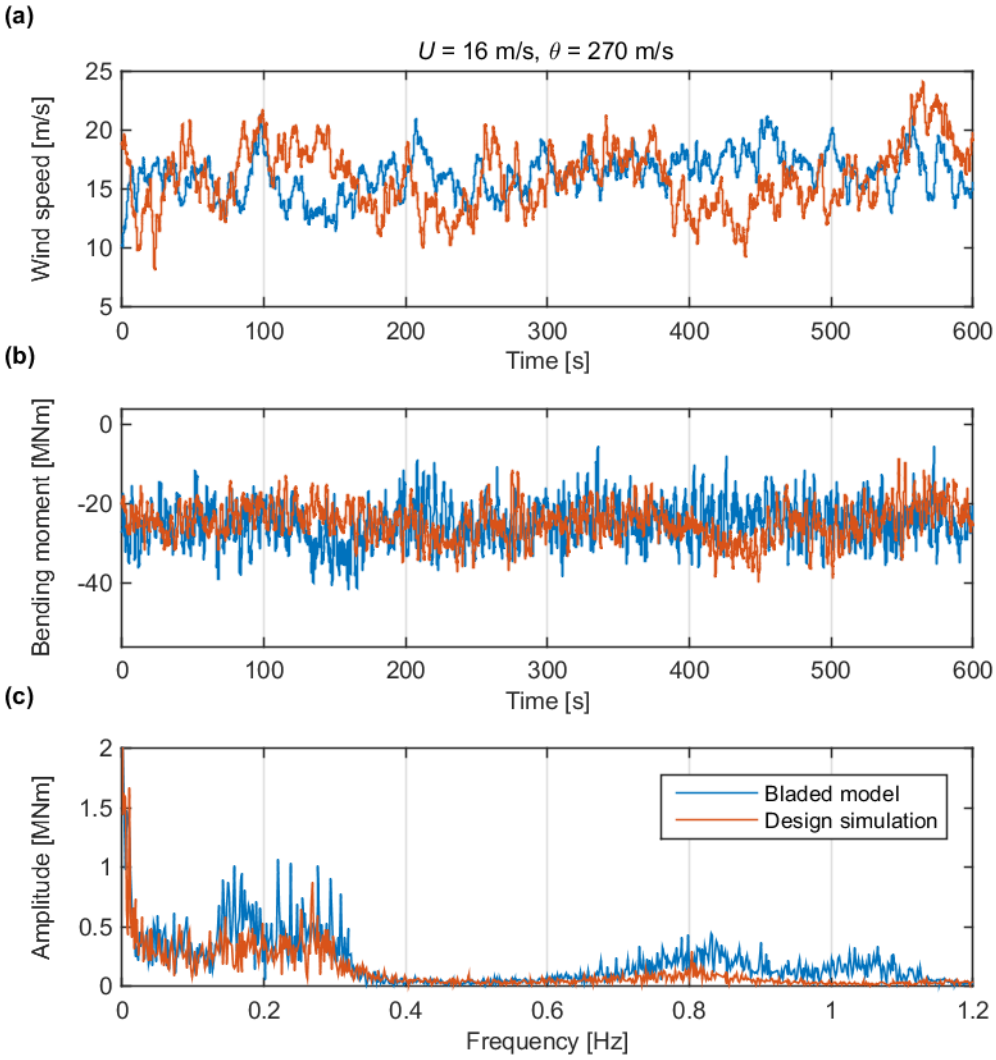

Figure 8-2. Comparison of bending moment results from the Bladed model and the original design simulation data, above rated wind speed. (a) Wind time series at hub height. (b) Bending moment time series at -10.6 mCD. (c) Amplitude spectrum calculated from FFT of the ten minute time series (average value from two simulations).

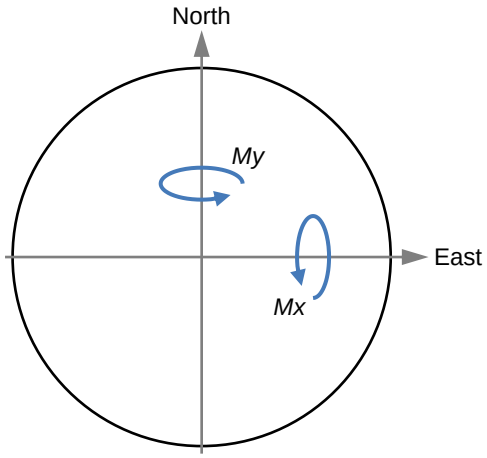

Figure 8-3. Orientation of support structure bending moment outputs.

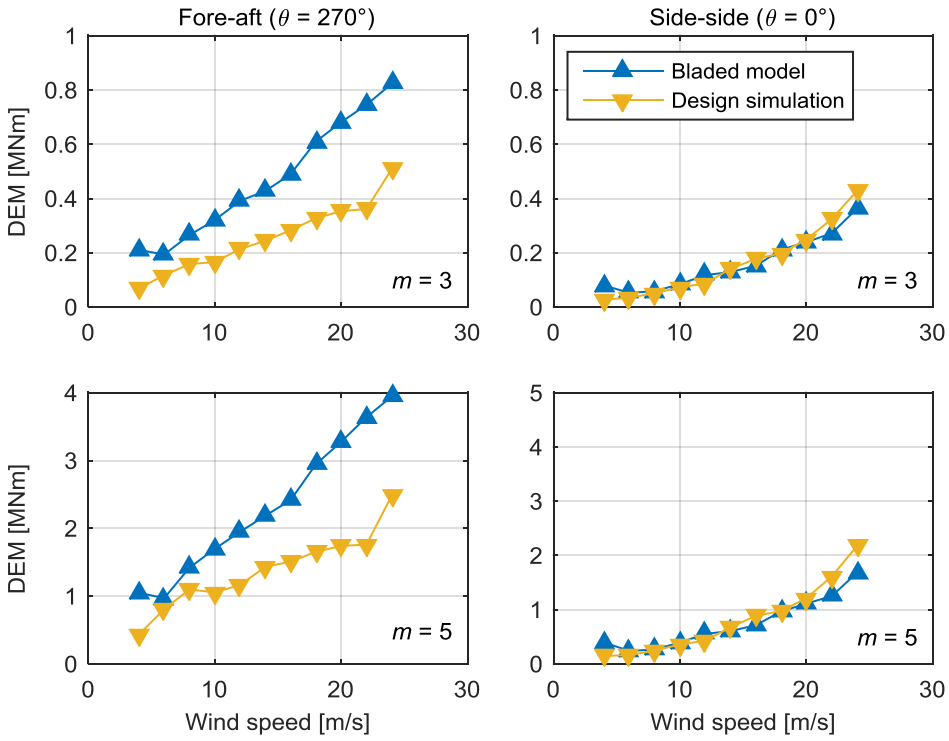

Figure 8-4. Comparison of M_y DEM results for loading direction in the fore-aft and side-side directions. Results relate to the 0° and 270° loading directions in Figure 8-5.

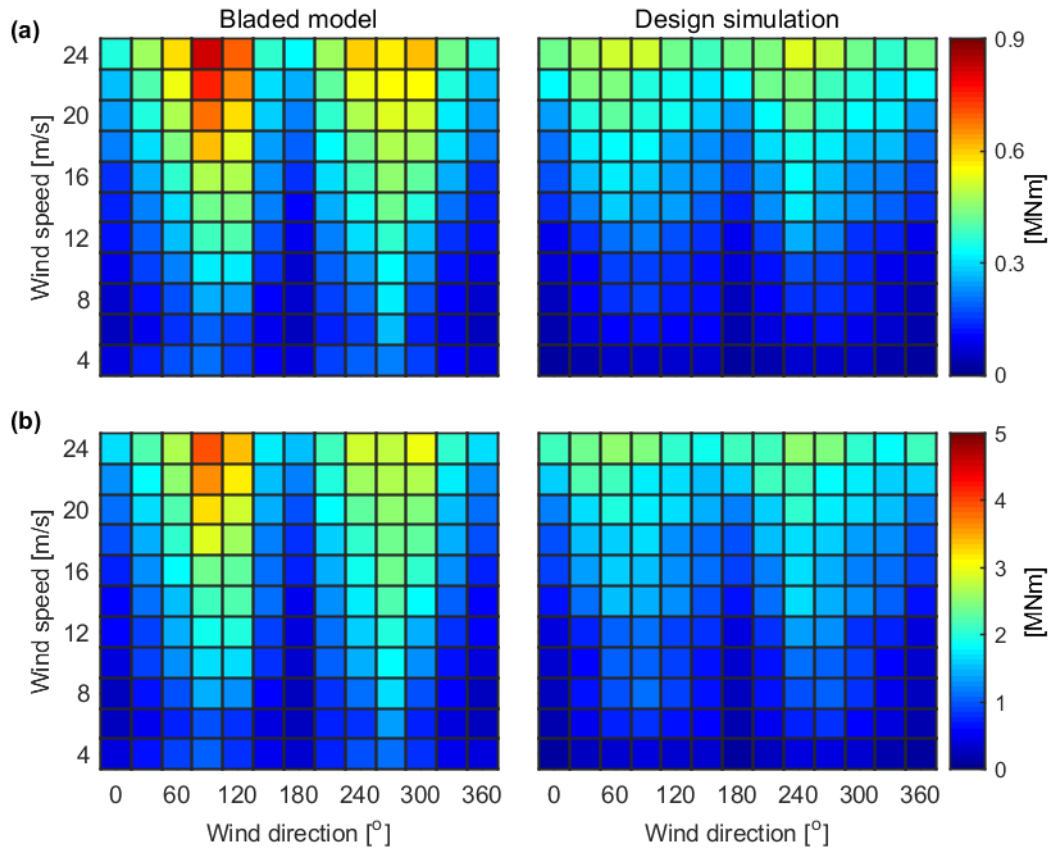

Figure 8-5. Comparison of M_y DEM results for each power production LC bin. (a) DEM calculated using m = 3. (b) DEM calculated using m = 5.

Table 8-1. Comparison of combined power production M_y DEM values at -10.6 mCD, factored by the design life frequency of occurrence.

	Design simulation [MNm]	Bladed model [MNm]
m = 3	20.04	28.69
m = 5	19.47	24.16

8.2 Site Variation

8.2.1 Variation of Structural Frequency

The model was varied to investigate the range of sea bed depths expected to occur across the wind farm, based on site analysis conducted by the turbine substructure designers which provided an upper, intermediate, and lower bound sea bed level (0 mCD, -5 mCD, and -10.6 mCD, respectively) [95]. The structural natural frequencies provided at these three

levels, and a number of natural frequency values in between, were matched via trial and error to an EF depth as described in Section 3.4.1.1, and results are shown in Figure 8-6. The results indicate an EF depth of 4.36 to 4.54 MP diameters, which is consistent with the range of results indicated in the literature [118], [119]. The sea bed level used as the boundary of the water column defined for the hydrodynamic wave loading was matched to each natural frequency using linear interpolation and extrapolation from the three levels provided by the designers, and these results are also shown in Figure 8-6 below.

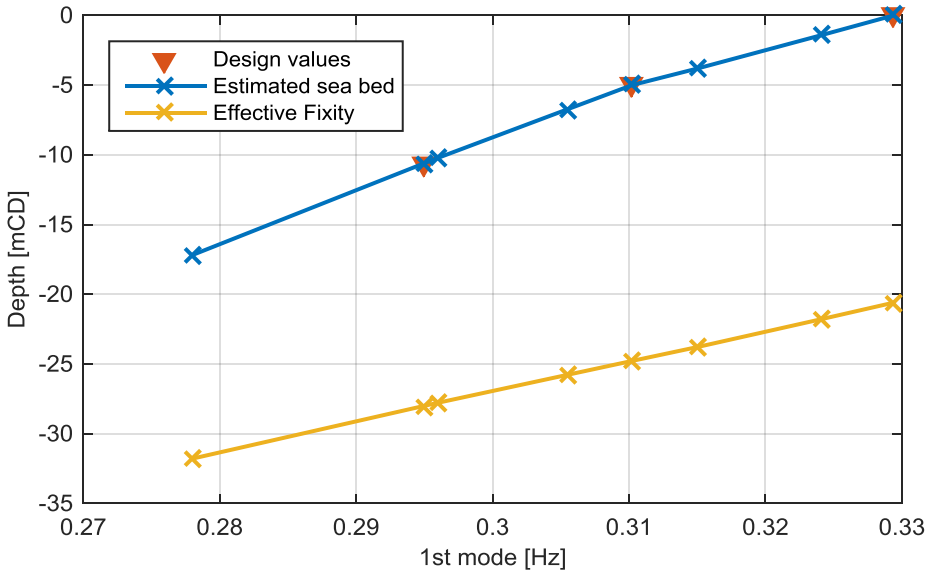

Figure 8-6. Effective Fixity depths used for the Bladed model simulations, chosen to match the range of first mode natural frequencies given in the design documentation [95]. The estimated sea bed depths were linearly interpolated and extrapolated from the design sea bed values. Crosses indicate the different natural frequency definitions used for the Bladed model simulations.

8.2.2 Turbulence Levels

The range of support structure definitions was simulated under different turbulence levels, in order to investigate the discrepancy between design and measured loading. Turbulence levels produced by the normal turbulence model [21] with IEC turbulence Classes B and C were used to represent the values used by the turbine designers, as displayed in Figure 8-7. Additionally, the TI_{eff} values derived from operational data at Turbine K1 were used, and are shown in Figure 8-7 for comparison.

Examples of the Bladed model results under low and high turbulence levels are shown in Figure 8-8 and Figure 8-9 for one support structure definition, and show similar response levels around the wave and structural first mode frequencies. The low turbulence results show a decreased response below approximately 0.1 Hz, as would be expected, and also a decrease in the higher frequency response above 0.6 Hz.

The power production LC M_y bending moment results produced by the Bladed simulations were RF counted and converted into a DEM value according to Equation (3-17). DEM values for each LC were then factored by the design life frequency of occurrence and combined into a total value using Equation (3-35), using only the power production LCs. Results are presented in Figure 8-10, which includes results from the design simulations provided by the turbine designers. A large reduction in fatigue damage can be seen from the IEC B class turbulence results to the TI_{eff} results by an amount which is comparable to the discrepancy between the Bladed model and the design simulation results, or by $(20.61/28.69)^3 = 37\%$ using $m = 3$, and $(19.47/26.17)^5 = 23\%$ using $m = 5$. Although the Bladed model is known to give a poor representation of the structural dynamics and to over-estimate the level of fatigue loading, the simulation results display the conservatism which is present in the original design results due to the use of upper bound levels of environmental loading.

Additionally, the range of structural natural frequencies modelled has produced a large variation in fatigue damage. Although the variation is not linear with structural frequency, over the range of design frequencies provided in [95] of 0.295 Hz to 0.33 Hz, the reduced level of fatigue damage is in the order of $(13.24/20.61)^3 = 27\%$ using $m = 3$, or $(12.04/19.61)^5 = 9\%$ using $m = 5$. The fatigue damage level is seen to increase with a further reduction in structural frequency down to the minimum value modelled of 0.278 Hz, and this increase would be expected to continue as the structural frequencies approach and interact with the rotor and wave loading frequencies. Again, although the Bladed model is known to over-estimate the level of fatigue loading in the structure, these results display the conservatism present in the design simulation results due to a worst-case (lower bound) estimation of the structural first mode frequency, and the variation in dynamic response and levels of fatigue loading that may be expected if the dynamics of the operational structures change over their operational life.

An improved model of the operational wind turbine structural dynamics, including detailed definition of the turbine controller and blade properties, and knowledge of the operational wave loading conditions, would require additional measurement and analysis which is

outside of the scope of this thesis. However, a similar approach may be useful to validate an improved model of the wind turbine, which could then be used to quantify more accurately the variation of fatigue loading of structures across an OWF site and therefore aid in selection of monitored turbines, and may be a valuable tool to allow the impact of temporal changes to be accounted for in the analysis of through-life fatigue loading.

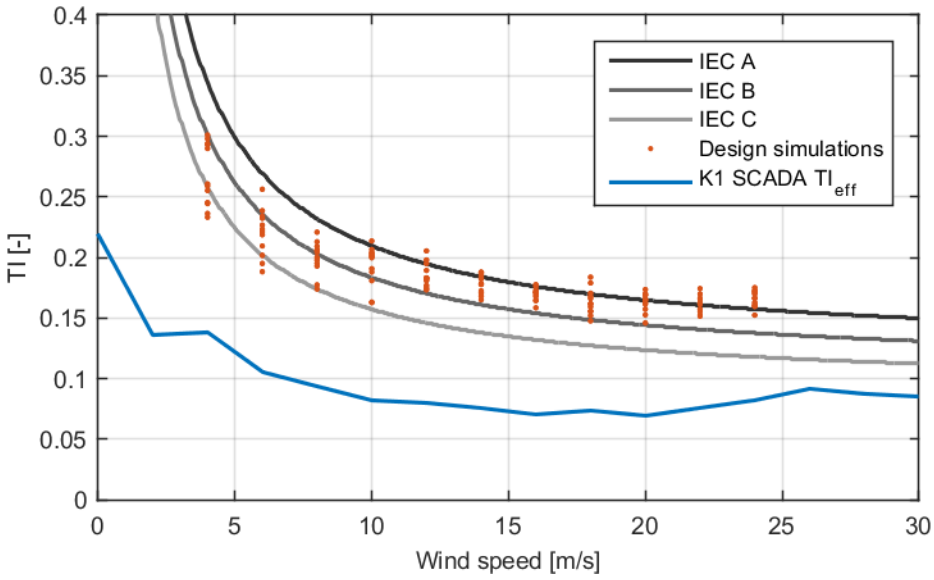

Figure 8-7. Turbulence Intensity values used to investigate the impact on structural fatigue loading. IEC B, IEC C, and the measured TI_{eff} values from Turbine K1 were used with the Bladed model.

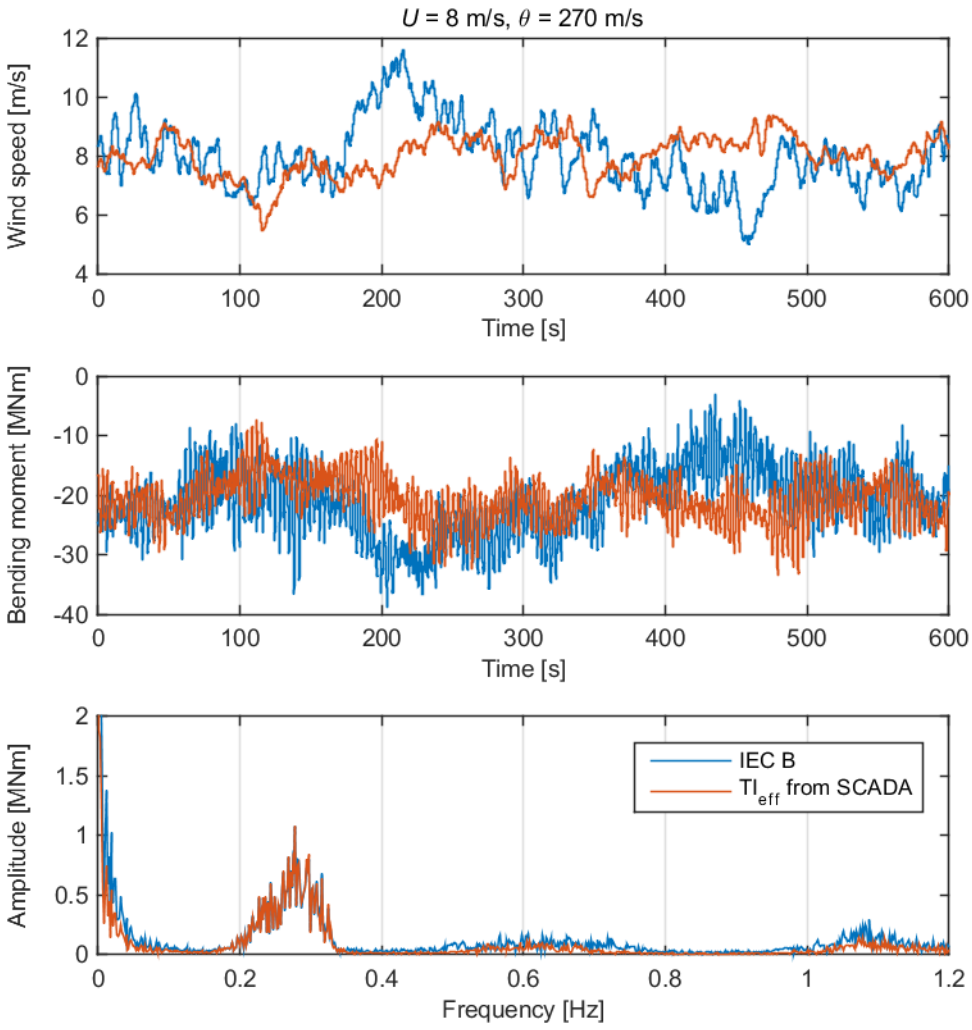

Figure 8-8. M_y bending moment results from the Bladed model under measured TI_{eff}, compared with IEC B class turbulence, below rated wind speed. (a) Wind time series at hub height. (b) Bending moment time series at -10.6 mCD. (c) Amplitude spectrum calculated from FFT of the ten minute time series (average value from two simulations).

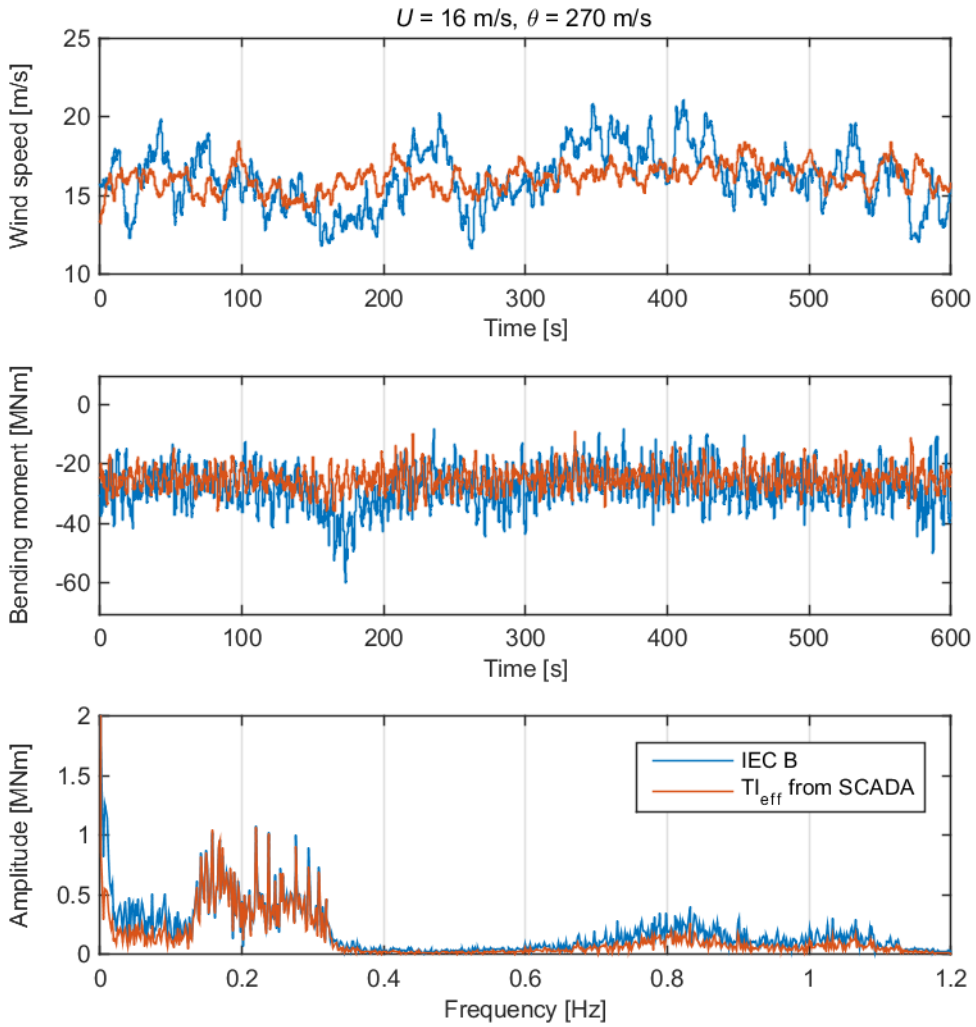

Figure 8-9. M_y bending moment results from the Bladed model under measured TI_{eff}, compared with IEC B class turbulence, above rated wind speed. (a) Wind time series at hub height. (b) Bending moment time series at -10.6 mCD. (c) Amplitude spectrum calculated from FFT of the ten minute time series (average value from two simulations).

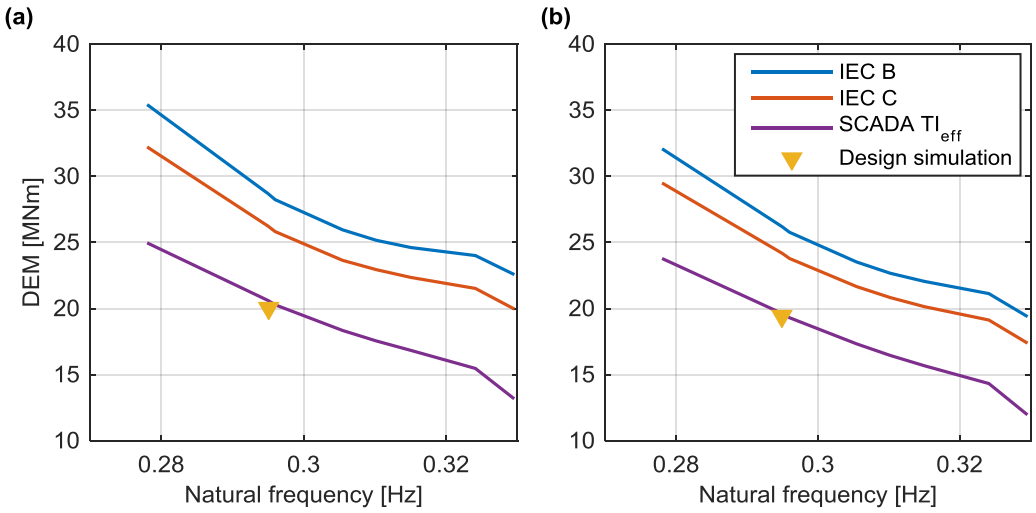

Figure 8-10. Damage Equivalent Moments produced by the range of different structural definitions and turbulence levels. (a) DEM calculated using $m = 3$. (b) DEM calculated using $m = 5$. The design value comes from a model with a first mode structural frequency of 0.295 Hz and a level of turbulence loading which is comparable to IEC B.

9 Conclusions and Recommendations for Future Work

9.1 Measured Load Data

Results presented in Chapter 4 detail the analysis of the measured load data, the effect of the processing that was used to screen the data and to reduce noise, and the influence of stress raising features at the location of measurement resulting from the stopper brackets and the grouted connection.

The FE analysis suggests that the gauge location will pick up a slight influence from the presence of the brackets, by a factor of approximately 7% under the most compressive loading direction, compared to results from simple BBT. As a symmetrical FE model was used with a constrained displacement boundary condition on the cut surface, it was only possible to analyse the stresses at the gauge location under four loading directions (aligned at 0, 60, 120, 180 degrees to the TP circumferential position), but the methodology developed in Section 4.1.2 enabled the results to be related to any direction. Using the FE results as a transfer function to convert the time series design loads provided by the turbine designer to stresses at the gauge location, it was found that the through-life calculated fatigue damage would be increased compared to results calculated from simple BBT. However, as the accuracy of the FE model is reliant on a number of assumptions, such as the friction coefficient used at the grout/steel interface, or the even distribution of loading shared by each of the six stopper brackets (which is affected by manufacturing tolerances), it was decided to use simple BBT to calculate the design stresses. Therefore, the FE analysis was used to demonstrate that this would produce a conservative comparison between measured and design loading.

The measured data displayed a significant reduction in the SNR for some of the gauges after a period of approximately two months, such that the variation in fatigue damage with the level of environmental loading became swamped. The distortion has the characteristics of white noise and does not appear to be a physical response of the structure, and therefore a low pass filter with a cut-off frequency of 2 Hz was used to improve the underlying signal. The cut-off frequency was designed to retain frequencies at which structural responses have a non-negligible impact on calculated fatigue life, with minimal attenuation of the second structural mode response (Figure 3-8), and therefore the filtering is believed to be conservative.

A methodology has been developed to allow long term gauge datum drift to be distinguished from the mean stress levels which vary according to the underlying response of the turbines to changes in wind speed and direction. Over the 18 month measurement period the largest datum drift was found with gauge S1-SGAV at a range of approximately 28 MPa, with a large improvement achieved with datum correction methodology, quantified by calculation of the RMSE value. The correction methodology is effective for gauge locations which should include minimal uncertainty in the underlying stress level, such as the shell of cylindrical towers. Locations closer to more complex geometries, such as the top of the welded stopper brackets themselves, may include considerable uncertainty in the measured stress levels due to uneven loading resulting from manufacturing tolerances. Therefore the drift correction methodology requires detailed understanding of the local stress distribution.

The sensitivity of fatigue damage calculations to the potential for digital sampling to miss the underlying peaks and valleys of the stress cycles was investigated using an approximation based on a simple sinusoid. The reduction in the level of calculated fatigue damage was shown to be negligible when the sample frequency is sufficiently high, and 20 Hz was confirmed to be acceptable for the measured data.

9.2 Environmental and Operational Data Processing

Chapter 5 presents results from the analysis of environmental data measured at the wind farm, and compared distributions of wind speed and turbulence levels with values used for the design analysis.

The measured wind data from the Turbine K1 SCADA system was used to factor the fatigue damage from the design simulation results over the life of the wind farm. Compared to the design frequency of occurrence, which was based on the design wind speed and the wave direction distributions, the measured distribution was found to produce a slightly lower level of fatigue damage by a factor of $0.96^3 = 88\%$ using $m = 3$, or $1.00^5 = 100\%$ using $m = 5$. The measured and design wind distributions may differ due to the use of the shorter four year measurement period, or the presence of the operational wind farm altering the local wind conditions due to blockage effects, for example. However, as the design distribution was found to produce a slightly higher level of fatigue loading, it was used for the construction of the measured load histogram.

The site turbulence assessment relied on three sources of measured data; from the design stage MM, the Turbine SCADA systems, and the LIDAR system mounted on the offshore substation. The MM data was found to include a slight distortion due to rounding which

resulted in an increased value of standard deviation at lower turbulence levels, and a methodology was developed to enable the mean turbulence level to be corrected. Unfortunately, the measurement periods for the MM and operational data do not overlap, but using the wind direction sector from which Turbine K1 is unaffected by trailing wakes, very good agreement was found between the MM and SCADA datasets. The LIDAR data, however, was found to provide a comparatively low value of wind standard deviation due to the effect of volumetric averaging. Therefore, the turbine SCADA data was identified as the most practical source of turbulence measurements for the operational turbines, and was used for the average operational turbulence level in the wind turbine simulations presented in Chapter 8.

The distribution of turbulence across the wind farm, presented in Section 5.2.3, shows that although Turbine H4 is located in the third row of turbines with respect to the dominant wind direction, the level of turbulence, resulting from combined ambient environmental turbulence and turbulent trailing wakes, continues to increase with successive turbine rows for wind speeds above U_{rated} = 13 m/s. These findings are in agreement with results presented in [120], where the authors also identified that wake loading above rated wind speeds can increase the level of fatigue loading significantly when multiple wakes are aligned. It has therefore been identified that, when all wind directions are taken into consideration, Turbine H4 experiences the approximate maximum turbulence level within the wind farm for wind speeds up to U_{rated}, but not for higher wind speeds. For this reason, a methodology was developed to screen the turbulence measurements at Turbine H4 to identify the periods which produce the maximum level within the wind farm. Results presented in Table 6-6 and Section 6.3.1.1 show that this increases the mean DES at Turbine H4 by approximately 3% to 4%, with the turbine in normal power production operation.

The wave radar measurements were compared to wind speed and direction measurements at Turbine K1 in order to investigate the assumption of directional alignment used during the design stage. By fitting a second order polynomial to these data, it was possible to identify a strong correlation with a maximum R^2 value of around 0.7 for directions which include the highest level of loading. Although there exists a significant amount of scatter which is not explained by the correlation, and which may be better explained by a further refinement of the LCs by wave height and tide level (which has been measured to have a range of over 9 m), the design assumption of aligned wind and wave directions has been used for the construction of the measured load histogram due to:

- The quality and coverage of the available wave data.

- The lack of directional measurement recorded with the wave radar data meaning that wind/wave misalignment could not be determined.
- The probabilistic analysis presented in Section 6.1, which showed that the sampled load measurements for each wind speed and direction bin are expected to produce a high confidence in the damage value produced by the measured load histogram.

9.3 Load Case and Capture Matrix

Chapter 6 presents the measured fatigue load histogram results, and compares operational damage values with results from the original design simulations.

As the LC analysis was based on environmental conditions characterised by the mean wind speed and direction values only, a degree of variation would still be expected in the level of fatigue loading due to other environmental variables, the dominant variables being found to be the level of wave and turbulence loading (Figure 6-1). Based on the assumption that a long enough measurement period will be sufficiently representative of the underlying distribution of fatigue damage measurements, the full 18 month data period was used as the basis to compare fatigue damage from the two measured turbines. Section 6.1 presents the Bootstrap analysis used to quantify this assumption, and shows the normal distribution of calculated fatigue damage values which is defined by the central limit theorem [105]. The standard deviation of the damage results produced by the Bootstrap analysis is low (approximately 0.55% using $m = 3$) due to the large sample size, as also defined by the central limit theorem.

The spread of results produced by taking a small sample of measurements at each wind vector bin is perhaps more complicated to compute than that for the entire population, as the small number of samples in each bin must be weighted accurately by the through-life frequency of occurrence. Additionally, a single sided test has been used to compare the sampled values with the population mean, as a conservative estimate of fatigue damage is assumed to be acceptable. The results provide a 95% confidence level that the sampled fatigue damage will fall above a 3% acceptable tolerance of the population value of fatigue damage, using 30 randomly selected periods in each LC bin. However, the values that were actually selected for the Measured Load Histograms were found to produce a significantly higher level of fatigue damage, as presented in Table 6-6 for the power production LCs. The source of this sample bias is due to the fact that the selection of sampled periods applied an additional constraint on the minimum number of turbulence intensity (TI) bins required to define each MLC, as specified by the methodology outlined in IEC-TS-61400-13 [29].

However, no guidance is given in [29] as to how to ensure that the samples used to characterise the MLC are representative of the underlying distribution of TI, which is typically lognormal (skewed towards low-TI values) [35]. As attempting to ensure that the selected periods reflect the underlying turbulence distribution would add significant complexity to the selection criteria, a flat turbulence distribution was used, using all TI bins identified in the mean wind vector bin, and based on the assumption that this would result in a conservative assessment of the turbulence loading. An example of the sampled distribution is shown in Figure 9-1 below. Additionally, as the star-delta switch described in Section 6.3.1 occurs in response to increasing or decreasing wind speeds they are likely to be associated with a high TI, and hence the high DES outliers in Figure 6-11 and Figure 6-12 tend to be over-sampled. As Turbine H4 in general experiences higher turbulence than K1 due to trailing wake effects, there are more TI bins available during normal operation and therefore the selection criteria provides less bias towards the star-delta switch events. The source of this selection bias may be addressed by including all available measurements in the definition of each MLC, thus ensuring by default that the underlying TI distribution is more accurately represented.

The Capture Matrices presented in Section 6.2 highlight that fact that it is unrealistic to expect a short term measurement campaign to fully define the conditions which may be expected to occur over the life of an OWT. The approach taken in this analysis has been to replace missing load case measurements with the corresponding design data, and by comparing with design the measurements which were recorded it was demonstrated that the approach was conservative. Replacing missing measurements via directional extrapolation to give a complete representation of the loading, as presented in Section 6.3.1.3, has produced a lower level of fatigue damage than reverting to the design data, by a factor of $(9.84/11.58)^3 = 61.4\%$ for Turbine H4, and $(10.26/12.17)^3 = 42.6\%$ for Turbine K1, using $m = 3$ (from Table 6-6 and Table 6-7, for the power production cases only). However, as the level of environmental loading is not accurately represented using the directional extrapolation methodology due to uncertainties in the representation of environmental loading, a conservative assessment is not assured and therefore the relative damage values should only be used to estimate the level of conservatism that results from the combined MLC/DLC methodology.

Other sources of conservatism are of course more difficult to quantify, such as the influence of the stress raising effects of the stopper brackets which are picked up by at the gauge locations, or the effect of the presence of white noise below the filter cut-off frequency, as

discussed in Section 9.1 above. However, by ensuring that a conservative approach is taken wherever uncertainty does exist, it is believed that the measured load histogram should provide a robust comparison with the design loading. By comparing the measured load histograms from the two locations used for this analysis, Turbine K1 is found to produce the highest level of fatigue damage, and therefore can be considered to be the dominant fatigue location.

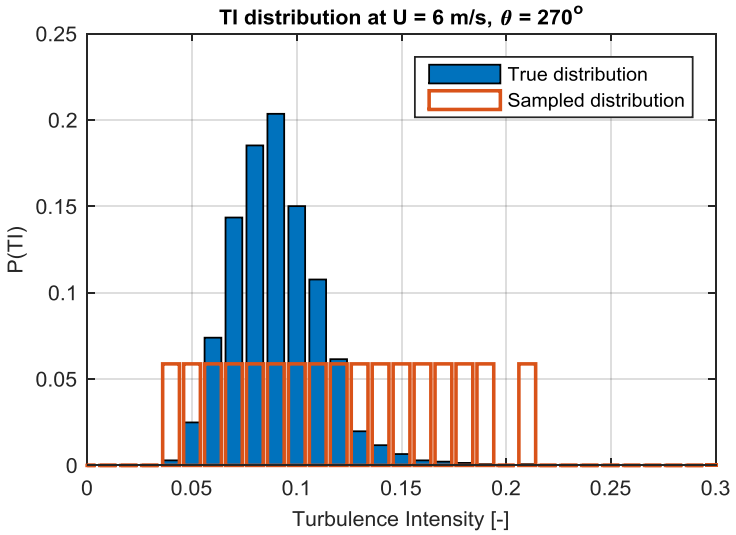

Figure 9-1. Distribution of Turbulence Intensity measurements for the 6 m/s, 270° wind bin, and an example of the flat distribution that was used to sample from it.

9.4 Transition Cycles

Results presented in Chapter 7 detail the analysis of transition cycles and compare the impact that they have on the total level of fatigue in the measured structures.

By RF counting a continuous period of measured data it has been possible to accurately quantify the impact of transition cycles, and to compare with conventional RF methods. The contribution to overall fatigue damage in the support structure has been found to be significant for Wöhler exponents of $m = 5$, relating to S-N curves for steel in an air environment or with cathodic protection [55], but is effectively negligible for lower values. Comparing the results to values found in the literature (presented in Table 9-1 below) it seems that the fatigue contribution of transition cycles is higher than found in previous studies. An important point to note is that the significance of transition cycles is dependent upon the level of fatigue damage that can be calculated from each independent ten minute period; i.e. the more dynamic the structure, the less the contribution to overall fatigue that

will arise from changes in ten minute mean wind speed and direction. As turbine technology and design methods improve, such as the general trend from stall regulated turbines towards variable speed, pitch regulated machines, turbine dynamic response has reduced, meaning that the effect of transitions cycles may have become proportionally more significant.

The wind variability metric results which are calculated from Equation (3-39) show that the degree of wind speed and direction variation at a given site may be expected to change from year to year, by an amount which will vary from site to site depending upon the local wind climate. As transition cycles are characterised by changes in mean stress level, which will in turn be a function of the rotor thrust which actually decreases above rated wind speeds for pitch regulated turbines, Equation (3-39) may not give an accurate representation of the impact of the wind variability on these stress cycles. A more representative approach may be to define a transfer function between wind speed and rotor thrust and then to quantify the arc length mapped out by the thrust vector as a function of wind speed and direction. However, as higher wind speeds result in a more dynamic turbine response, the RF residue cycles can be expected to be of larger amplitude, and therefore using linear wind speed instead of the rotor thrust profile goes some way to compensate for this effect. Ultimately, however, it is preferable to use multiple years to define the wind time history used to quantify the impact of transition cycles, and the results presented in Section 7.1 indicate that a specific assessment is required to determine the length of a representative history for a given site.

From the synthetic stress time series produced from the four year period of operational SCADA data from Turbine K1, transition cycles were found to contribute slightly less to the overall level of fatigue damage than from the continuous period of measured data. The cause of this discrepancy is likely to be due to the inclusion of DLC data in the measured load histogram to replace the measurements which were missing from the Capture Matrix. The design data was found to be more damaging than the measurements for a direct ten minute comparison, and importantly, the design data was used to represent all emergency stop load case periods, none of which were sufficiently identified in the measured data.

Although the contribution to overall fatigue damage from the measured load histogram was reasonably small, and indeed, discrepancies by a factor of two can be expected as normal in fatigue calculations for wind turbine structures [56], the reality is that transition cycles can be found to have an impact for wind turbine support structures and as it is possible to account for them correctly according to the RF algorithm. Therefore, it is suggested that they be included in the load histogram to ensure a conservative assessment is made of the total fatigue loading.

Table 9-1. Comparison of impact of transition cycles provided by the literature. Damage ratio calculated from RF processing data in independent ten minute periods divided by the value produced by including transition cycles.

Source	Damage ratio		
	$m = 3$	$m = 4$	$m = 5$
Current work	0.925	-	0.365
Larsen & Thomsen [72]	0.970	-	-
Mouzakis & Morfiadakis [73]	-	0.893	0.877

Note: Results taken from Larson & Thomsen [72] are calculated using a methodology which has been found to overestimate the value of fatigue damage contributed by transition cycles, and are based on a synthetic stress history. Results taken from Mouzakis & Morfiadakis [73] are comparable to the methodology presented in the current work, but come from a seven day period of measurement.

9.5 Wind Turbine Simulation

Chapter 8 presents results of the wind turbine simulation work that was conducted to investigate the possible variation in fatigue loading across the wind farm. Comparing the Bladed simulation results to the design data under the same level of environmental loading conditions and structural frequency, it is clear that the Bladed model produces a much more dynamic response. The increased dynamic response results in a higher level of DEM calculated for the fore-aft direction by a factor of approximately two, but a comparable value in the side-side direction, suggesting that the dominant cause of the difference is found in the interaction of the rotor with the aerodynamic loading. This could arise from the definition of the aerofoil coefficients, the rotor shape, the controller definition, or a combination of effects. Therefore, the model definition does not appear to closely represent the structural dynamics of the turbines, and significantly over predicts the level of fatigue damage.

The range of natural frequencies used for the analysis was based on the range of design values provided by the foundation designer. Where sea bed levels may change due to scour or accretion of sand around the turbine structure, it is possible that the Eigen frequencies of the structure may also be affected. Although the results produced by the model are not representative of the structural response, the effect of the natural frequency changes on the calculated DEM may be indicative of the change in fatigue loading that may result. With such large variation in the level of fatigue loading over the range of support structure definitions, the difference between the measured structural frequencies and the worst case value used for design is likely to be a large source of the design conservatism identified.

The reduced turbulence levels that were used for the analysis resulted in a reduced DEM and corresponding fatigue damage by the order of 37% using $m = 3$, and 23% using $m = 5$.

Although the model aerodynamics are clearly not representative, it is likely that a major component of the conservatism in the design which has been identified by the measurements is due to the less severe environmental loading found during operation.

9.6 Implications and Further Work

The results of the analysis presented in this thesis suggest that significant reductions in fatigue loading can be identified through measurement of operational loads. Uncertainty in the severity of environmental loading, in particular the level of turbulence and wave loading for OWTs, which are basically random, stochastic processes, means that a probabilistic approach needs to be taken at the design stage to ensure a safe design is achieved with an acceptable level of risk of failure. Simplistically, if turbines were designed to achieve the 20 year design life based on the mean level of loading identified for a site, then 50% of the structures could be expected to fail in operation. However, by monitoring the level of environmental loading and the structural response of turbines gathered from operational experience, the degree of fatigue loading becomes a matter of record and the amount of 'damage consumed' can be identified. Quantifying confidence levels in sampled estimates of measured loading has been shown to be useful where incomplete knowledge exists of the variation in environmental loading, which is likely to be the case for most OWT structures). This may be necessary to allow a conservative assessment of the loading to be demonstrated for certification, as the methodology is not currently explicitly defined in standards. Load measurement may therefore be a useful strategy when wind farms approach the end of their design life and operators need to decide whether life extension of their assets is worthwhile, as other approaches such as full inspections and non-destructive testing of welds are not likely to be financially practicable for OWT support structures.

The analysis presented in this work is based on measurements taken on two turbines over a finite time period. It is important to stress that changes to the structural dynamics within the wind farm, which may result from changing bathymetry over time, can be expected to have an effect on the level of fatigue loading experienced by the structures. Therefore it may be deemed necessary to revisit the load analysis if notable changes are identified, such that changes to the mean rate of fatigue damage can be identified and accounted for. An alternative approach may be to revisit the model simulations with either more detailed reverse engineering of the blade structural and aerodynamic properties and turbine controller definition, which may be difficult to obtain directly from the original equipment manufacturer (OEM) due to intellectual property issues, or through direct collaboration with

the OEM themselves. The ability to revisit and validate design assumptions through the use of operational data may be attractive for both OEMs and wind farm operators.

References

[1] RenewableUK, "UK Wind Energy Database," [Online]. Available: http://www.renewableuk.com/en/renewable-energy/wind-energy/uk-wind-energy-database/. [Accessed 25 04 2016].

[2] European Wind Energy Association, "The European Offshore Wind Industry - Key Trends and Statistics 2015," 2016.

[3] UK Energy Research Centre, "Great Expectations: The Cost of Offshore Wind in UK Waters - Understanding the Past and Projecting the Future," 2010.

[4] The Crown Estate, "Offshore Wind Cost Reduction Pathways Study," 2012.

[5] DNV-GL, "DNVGL-ST-0262: Lifetime Extension of Wind Turbines," 2016.

[6] I. Lotsberg, "Structural Mechanics for Design of Grouted Connections in Monopile Wind Turbine Structure," *Marine Structures,* vol. 32, pp. 113-135, 2013.

[7] P. Dallyn, A. El-Hamalawi and A. Palmeri, "Wear in Large Diameter Grouted Connections for Offshore Wind Energy Converters," in *Proceedings of the 10th International Conference on Advances in Steel Concrete Composite and Hybrid Structures*, Singapore, 2012.

[8] Det Norske Veritas, "DNV-OS-J101: Design of Offshore Wind Turbine Structures," 2013.

[9] A. R. Black, T. Mathiesen and L. R. Hilbert, "Corrosion Protection of Offshore Wind Foundations," in *NACE International*, Housten, 2015.

[10] M. M. Luengo and A. Kolios, "Failure Mode Identification and End of Life Scenarios of Offshore Wind Turbines: A Review," *Energies,* vol. 8, pp. 8339-8354, 2015.

[11] Department of Energy & Climate Change, "International domestic energy prices," [Online]. Available: https://www.gov.uk/government/statistical-data-sets/international-domestic-energy-prices. [Accessed 18 06 2015].

[12] S. Tegen, M. Hand, B. Maples, E. Lantz, P. Schwabe and A. Smith, "2010 Cost of Wind Energy Review," 2012.

[13] Department for Business, Energy & Industrial Strategy, "Digest of United Kingdom Energy Statistics," 2016.

[14] R. Green and N. Vasilakos, "The Economics of Offshore Wind," *Energy Policy,* vol. 39, pp. 496-502, 2011.

[15] S. Bhattacharya, "Challenges in Design of Foundations for Offshore Wind Turbines," *Engineering and Technology Reference,* pp. 1-9, 2014.

[16] South Baltic Offshore Wind Energy Regions, "Wind Energy Regions: Denmark," [Online]. Available: http://www.southbaltic-offshore.eu/regions-denmark.html. [Accessed 04 04 2016].

[17] 4Coffshore, "East Anglia One Offshore Wind Farm," [Online]. Available: http://www.4coffshore.com/windfarms/east-anglia-one-united-kingdom-uk64.html.

[Accessed 15 06 2016].

[18] 4Coffshore, “Fukushima Floating Offshore Wind Farm Demonstration Project: Phase 2,” [Online]. Available: http://www.4coffshore.com/windfarms/fukushima-floating-offshore-wind-farm-demonstration-project-%28forward%29-phase-2-japan-jp13.html. [Accessed 04 04 2016].

[19] M. Zaaijer, “Comparison of Monopile, Tripod, Suction Bucket and Gravity Base Design for a 6 MW Turbine,” in *Offshore Windenergy in Mediteranean and Other European Seas*, 2003.

[20] International Electrotechnical Commission, “IEC 61400 - Online Collection: Wind Turbines,” [Online]. Available: https://collections.iec.ch/iec61400?ref=gspromo. [Accessed 27 06 2016].

[21] International Electrotechnical Commission, “IEC 61400-1 Wind turbines Part1: Design Requirements,” 2005.

[22] Det Norske Veritas, “DNV-OS-J101: Design of Offshore Wind Turbine Structures,” 2004.

[23] Germanischer Lloyd, “Guideline for the Certification of Offshore Wind Turbines,” 2005.

[24] J. V. D. Tempel, “Doctoral thesis on: Design of Support Structures for Offshore Wind Turbines,” 2006.

[25] CORDIS, “Recommendations for design of offshore wind turbines (RECOFF),” 31 08 2004. [Online]. Available: http://cordis.europa.eu/project/rcn/54147_en.html. [Accessed 04 04 2016].

[26] International Electrotechnical Commission, “IEC 61400-3: Wind Turbines Part 3: Design Requirements for Offshore Wind turbines,” 2009.

[27] DNV-GL, “DNVGL-ST-0126: Support Structures for Wind Turbines,” DNV-GL AS, 2016.

[28] P. H. Madsen, J. Dekker, S. Thor, K. McAnulty, H. Matties and R. Thresher, “Recommended Practices for Wind Turbine Testing and Evaluation: 3. Fatigue Loads (edition 2),” International Energy Association, 1990.

[29] International Electrotechnical Commission, “IEC-TS-61400-13. Wind Turbine Generator Systems Part 13: Measurement of Mechanical Loads,” 2001.

[30] International Electrotechnical Commission, “IEC-61400-13. Wind Turbines Part 13: Measurement of Mechanical Loads,” 2015.

[31] Germanischer Lloyd, “Guideline for the Continuous Operation of Wind Turbines,” 2009.

[32] J. Jia, “Wind and Structural Modelling for an Accurate Fatigue Life Assessment of Tubular Structures,” *Engineering Structures*, vol. 33, pp. 477-491, 2011.

[33] DNV-GL, *Bladed Software; Theory Manual*, 2014.

[34] W. Popko, F. Vorpahl, A. Zuga, M. Kohlmeier, J. Jonkman, A. Robertson, T. J. Larsen, A. Yde, K. Sætertrø, K. M. Okstad, J. Nichols, T. A. Nygaard, Z. Gao, D.

Manolas, K. Kim, Q. Yu, W. Shi, H. Park, A. Vásquez-Rojas, J. Dubois, D. Kaufer, P. Thomassen, M. J. d. Ruiter, T. v. d. Zee, J. M. Peeringa, H. Zhiwen and H. v. Waaden, "Offshore Code Comparison Collaboration Continuation (OC4), Phase I—Results of," *Journal of Ocean and Wind Energy,* vol. 1, pp. 1-11, 2014.

[35] Det Norsk Veritas, "DNV-RP-C205: Environmental Conditions and Environmental Loads," 2010.

[36] DNV/Risø, "Guidelines for Design of Wind Turbines: 2nd Ed.," 2002.

[37] T. Hald, C. Mørch, L. Jensen, L. C. Bakmar and K. Ahle, "Revisiting Monopile Design Using P-Y Curves: Results From Full Scale Measurements on Horns Rev," in *European Offshore Wind,* Stockholm, 2009.

[38] Germanischer Lloyd WindEnergie GmbH, "Recommendations for Design of Offshore Wind Turbines (RECOFF); Deliverable D1 - External Conditions, state of the art," 2003.

[39] R. Wagner, T. Mikkelsen and C. Michael, "Investigation of Turbulence Measurements with a Continuous Wave, Conically Scanning LiDAR; Risø-R-1682(EN)," 2009.

[40] J. Medley, W. Barker, M. Harris, M. Pitter, C. Slinger, T. Mikkelsen and M. Sjöholm, "Evaluation of Wind Flow With a Nacelle-Mounted, Continuous Wave Wind LIDAR," in *European Wind Energy Association*, Barcelona, 2014.

[41] A. Sathe, J. Mann, N. Vasiljevic and G. Lea, "A Six-Beam Method to Measure Turbulence Statistics Using Ground-Based Wind Lidars," *Atmospheric Measurement Techniques,* vol. 8, pp. 729-740, 2015.

[42] G. Larsen and K. Hansen, "De-Trending of Wind Speed Variance Based on First-Order and Second-Order Statistical Moments Only," *Wind Energy,* vol. 17, no. 12, pp. 1905-1924, 2013.

[43] Thies Clima, "Wind Sensor; First Class Advanced," [Online]. Available: http://www.thiesclima.com/windsensor_first_class_e.html. [Accessed 09 02 2016].

[44] Zephir LiDAR, [Online]. Available: http://www.zephirlidar.com/wp-content/uploads/2014/09/ZephIR-300-met-mast-alternative.jpg. [Accessed 09 02 2016].

[45] W. Weibull, "A Statistical Function of Wide Applicability," *Journal of Applied Mechanics - Transactions of the American Society of Mechanical Engineers,* vol. 18, pp. 293-297, 1951.

[46] "NY University public documents," [Online]. Available: https://files.nyu.edu/mrg217/public/mle_introduction1.pdf.

[47] Measuring Network of Wind Energy Institutes (Measnet), "Evaluation of Site-Specific Wind Conditions: Version 1," 2009.

[48] J. Kaimal, "Spectral Characteristics of Surface-Layer Turbulence," *Quarterly Journal of the Royal Meteorological Society,* vol. 98, pp. 563-589, 1972.

[49] T. Burton, D. Sharpe, N. Jenkins and E. Bossanyi, Wind Energy Handbook, Chichester: Wiley, 2001.

[50] K. Hasselmann, T. Barnett, E. Bouws, H. Carlson, D. Cartwright, K. Enke, J. Ewing, H. Gienapp, D. Hasselmann, P. Krusemann, A. Meerburg, P. Müller, D. Olbers, K. Richter, W. Sell and H. Walden, "Measurements of Wind-Wave Growth and Swell Decay During the Joint North Sea Wave Project (JONSWAP)," Deutschen Hydrographischen Institut, Hamburg, Germany, 1973.

[51] Y. Goda, "A Review on Statistical Interpretation of Wave Data," Port and Harbour Research Institute, 1979.

[52] W. J. Pierson and L. Moskowitz, "A Proposed Spectral Form for Fully Developed Wind Seas Based on the Similarity Theory of S. A. Kitaigorodskii," *Journal of Geophysical Research,* vol. 69, no. 24, pp. 5181-5190, 1964.

[53] J. R. Morison, M. P. O'Brien, J. W. Johnson and S. A. Schaaf, "The Force Exerted by Surface Waves on Piles," *Petroleum Transactions, AIME,* vol. 189, pp. 149-154, 1950.

[54] S. Suresh, Fatigue of materials, Cambridge: Cambridge University Press, 1994.

[55] Det Norsk Veritas, "DNV-RP-C203: Fatigue Design of Offshore Steel Structures," 2010.

[56] H. J. Sutherland, "On the Fatigue Analysis of Wind Turbines," Sandia National Laboritories, 1999.

[57] A. Z. Palmgren, "Die Lebensdauer von Kugellagern [The life of ball bearings]," *Verein Deutscher Ingenieure,* vol. 68, pp. 339-341, 1924.

[58] M. A. Miner, "Cumulative Damage in Fatigue," *Journal of Applied Mechanics,* vol. 13, pp. A159-A164, 1945.

[59] F. Brennan and I. Tavares, "Fatigue Design of Offshore Steel Mono-pile Wind Substructures," *Proceedings of the Institution of Civil Engineers,* vol. 167, no. EN4, pp. 196-202, 2014.

[60] S. J. Maddox, "International Effforts on Fatigue of Welded Constructions. A Review of Commission XIII Activities," *Welding in the World,* vol. 31, pp. 86-92, 1993.

[61] ASTM E1049-85, "Standard Practices for Cycle Counting in Fatigue Analysis," (Reapproved 2011).

[62] D. Socie, "Rainflow Cycle Counting: A Historical Perspective," in *The International Symposium on Fatigue Damage Measurement and Evaluation Under Complex Loadings,* Fukuoka, 1991.

[63] M. Matsuishi and T. Endo, "Fatigue of Metals Subjected to Varying Stress," in *Jpn Soc. Mech. Eng.*, Fukuoka, 1968.

[64] H. Okamura, S. Sakai and I. Susuki, "Cumulative Fatigue Damage Under Random Loads," *Fatigue Eng. Mater. Struct.,* vol. 1, pp. 409-419, 1979.

[65] S. Downing and D. Socie, "Simple Rainflow Counting Algorithms," *Int. J. Fatigue,* vol. 4, no. 1, pp. 31-40, January 1982.

[66] C. Amzallag, J. Gerey, J. Robert and J. Bahuaud, "Standardization of the Rainflow Counting Method for Fatigue Analaysis," *Int. J. Fatigue,* vol. 16, no. 4, pp. 287-293, 1994.

[67] C. McInnes and P. Meehan, "Equivalence of Four-Point and Three-Point Rainflow Cycle Counting Algorithms," *Int. J. Fatigue,* vol. 30, no. 3, pp. 547-559, 2008.

[68] P. Johannesson, "Doctoral thesis on: Rainflow Analysis of Switching Markov Loads," Lund Institute of Technology, 1999.

[69] G. Glinka and J. Kam, "Rainflow Counting Algorithm for Very Long Stress Histories," *Int. J. Fatigue,* vol. 9, no. 3, pp. 223-228, 1987.

[70] G. Marsh, C. Wignall, P. R. Thies, N. Barltrop, A. Incecik, V. Venugopal and L. Johanning, "Review and Application of Rainflow Residue Processing Techniques for Accurate Fatigue Damage Estimation," *International Journal of Fatigue,* vol. 82, pp. 757-765, 2016.

[71] G. Marsh and A. Incecik, "Fatigue Load Monitoring of Offshore Wind Turbine Support Structures," in *Eur. Wind Energy Assoc. Offshore*, Frankfurt, 2013.

[72] C. Larsen and K. Thomsen, "Low Cycle Fatigue Loads; Risø-R-913(EN)," 1996.

[73] F. Mouzakis and E. Morfiadakis, "Identification of Low-Cycle Effects on Wind Turbine Compaonent Lifetime Estimation," in *Proceedings of The 19th British Wind Energy Association Conference*, Edinburgh, 1997.

[74] R. W. Hyers, J. G. McGowan, K. L. Sullivan, J. F. Manwell and B. C. Syrett, "Condition Monitoring and Prognosis of Utility Scale Wind Turbines," *Energy Materials,* vol. 1, pp. 187-203, 2006.

[75] M. Ozbek, D. J. Rixen, O. Erne and G. Sanow, "Feasibility of Monitoring Large Wind Turbines Using Photogrammetry," *Energy,* vol. 35, pp. 4802-4811, 2010.

[76] W. Weijtjens, A. Iliopoulos, J. Helsen and C. Devriendt, "Monitoring the Consumed Fatigue Life of Wind Turbines on Monopile Foundations," in *European Wind Energy Association: Offshore*, Copenhagen, 2015.

[77] P. S. Maybeck, Stochastic Models, Estimation, and Control, vol. 1, London: Academic Press Inc., 1979.

[78] J. P. Bentley, Principles of Measurement Systems, 4th ed., Harlow: Pearson Education Ltd., 2005.

[79] S. Butterworth, "On the Theory of Filter Amplifiers," *Wireless Engineer,* vol. 7, pp. 536-541, 1930.

[80] W. E. Thomson, "Delay Networks Having Maximally Flat Frequency Characteristics," *Proceedings of hte Institution of Electrical Engineers,* vol. 96, pp. 487-490, 1949.

[81] National Instruments, "How Is Temperature Affecting Your Strain Measurement Accuracy?," 22 June 2011. [Online]. Available: http://www.ni.com/white-paper/3432/en/#toc2. [Accessed 12 12 14].

[82] Omega, "The Strain Gauge," [Online]. Available: http://www.omega.co.uk/literature/transactions/volume3/strain3.html. [Accessed 12 12 2014].

[83] E.ON, "Technical Specification for Wind Turbine Foundation Monitoring," 2010.

[84] T. S. Obdam, L. Rademakers and H. Braam, “Flight Leader Concept for Wind Farm Load Counting: First Offshore Implementation,” in *Offshore Wind and Other Marine Renewable Energies in Mediterranean and European Seas*, Brindisi, 2009.

[85] RPS Consulting Engineers, “Supplementary Metocean Study; Report Number IBE0025/AKB/RW1/Apr06,” 2006.

[86] Foundation Designer, “Design Report: Scour Design (Revision 1): 221186 – 4.2.20,” 2009.

[87] Foundation Designer, “Design Report: Time Domain Fatigue Analysis; 221186 – 4.2.4,” 2007.

[88] M. B. Christiansen and B. C. Hasager, “Wake Effects of Large Offshore Wind Farms Identified from Satellite SAR,” *Remote Sensing of Environment*, vol. 98, pp. 251-268, 2005.

[89] Foundation Designer, *Drawing no. RR-SS-06-0009*, 2007.

[90] Strainstall, “Structural Monitoring System Installation Report; Report Number J4226_K1,” 2012.

[91] Dassault Systémes, *ABAQUS version 13.3*, 10 rue Marcel Dassault, CS 40501, 78946 Vélizy-Villacoublay Cedex, France.

[92] Densit, “Ducorit Data Sheet,” [Online]. Available: http://www.densit.com/Files/Billeder/Densit_v2/Pdf%20files/renewable/pro_ducorit_itw-uk.pdf. [Accessed 21 07 2015].

[93] Turbine Designer, “Supplementary Information: 8.1.1 Tower Loads; HH 79.975 IEC1s,” 2007.

[94] Foundation Designer, “Design Report: Computer Model; 221186 – 4.2.12,” 2007.

[95] Foundation Designer, “Design Report: Natural Frequency Analysis; 221186 – 4.2.3,” 2007.

[96] J. D. Sørensen, S. Frandsen and N. J. Tarp-Johansen, “Fatigue Reliability and Effective Turbulence Models in Wind Farms,” in *ICASP10 : Applications of Statistics and Probability in Civil Engineering: Proceedings of the 10th International Conference*, Tokyo, 2007.

[97] N. Metropolis and S. Ulam, “The Mointe Carlo Method,” *Journal of the American Statistical Association*, vol. 44, pp. 335-341, 1949.

[98] Garrad Hassan Ltd, “Assessment of the Energy Production of the Proposed Wind Farm; 4253/BR/01,” 2004.

[99] Natural Environment Research Council, “British Oceanographic Data Centre,” [Online]. Available: http://www.bodc.ac.uk/. [Accessed 07 09 2015].

[100] A. Grinsted, “Tidal fitting toolbox,” 07 03 2008. [Online]. Available: http://uk.mathworks.com/matlabcentral/fileexchange/19099-tidal-fitting-toolbox. [Accessed 07 09 2015].

[101] International Organization for Standardization, “Standard Atmosphere; ISO 2533:1975,” 1975.

[102] T. W. Schlatter and D. V. Baker, "NOAA Thermodynamic Subroutines," 12 06 1991. [Online]. Available: http://icoads.noaa.gov/software/other/profs. [Accessed 08 02 2016].

[103] WeatherSpark, "Average Weather For Isle of Man, United Kingdom," [Online]. Available: https://weatherspark.com/averages/28738/Isle-of-Man-United-Kingdom. [Accessed 08 02 2016].

[104] B. Efron, "Bootstrap Methods: Another Look at the Jackknife," *The Annals of Statistics,* vol. 1, pp. 1-26, 1979.

[105] C. Chatfield, Statistics for Technology, 3rd ed., Chapman & Hall, 1983.

[106] National Oceanic and Atmospheric Administration, "Station BUZM3 - Buzzards Bay," [Online]. Available: http://www.ndbc.noaa.gov/station_page.php?station=buzm3. [Accessed 26 10 2015].

[107] NoordzeeWind, "Reports & Data," [Online]. Available: http://www.noordzeewind.nl/en/knowledge/reportsdata/. [Accessed 23 10 2015].

[108] National Oceanic and Atmospheric Administration, "Station PLSF1 - Pulaski Shoals," [Online]. Available: http://www.ndbc.noaa.gov/station_page.php?station=plsf1. [Accessed 27 10 2015].

[109] DNV-GL, *Bladed, version 4.6.*

[110] C. Devriendt, P. J. Jordaens, G. De Sitter and P. Guillaume, "Damping Estimation of an Offshore Wind Turbine on a Monopile Foundation," in *European Wind Energy Association*, Copenhagen, 2012.

[111] Turbine Designer, "General Specification: 3.0 MW - 50 Hz," 2009.

[112] J. Jonkman, S. Butterfield and W. Musial, "Definition of a 5 MW Reference Wind Turbine for Offshore System Development," National Renewable Energy Laboratory, 2009.

[113] DNV-GL, "Bladed User Manual," 2014.

[114] J. Mann, "The Spectial Structure of Neutral Atmospheric Surface-Layer Turbulence," *Journal of Fluid Mechanics,* vol. 273, pp. 141-168, 1994.

[115] E.ON UK, "Part 1 - Technical requirements; Section 3 - Design Basis (Wind Turbine Foundations); RR/MC/019".

[116] F. Ormel, *EWEA Workshop Presentation; Advanced Nacelle Anemometry and SCADA-Data, Analysis Techniques and Limitations,* Lyon, 2012.

[117] P. Fokianou, M. Samarakou, D. Kandris and E. D. Fylladitakis, "Star-Delta Switches Evaluation for Use in Grid-Connected Wind Farm Installations," *Advances in Mechanical Engineering,* 2014.

[118] N. Barltrop and A. Adams, Dynamics of Fixed Marine Structures, Oxford: Butterworth-Heinemann, 1991.

[119] M. B. Zaaijer, "Sensitivity Analysis for Foundations of Offshore Wind Turbines: OWTES Task 4.1," Delft University of Technology, 2002.

[120] T. J. Larsen, G. Larsen, H. A. Madsen and S. M. Peterson, “Wake Effects Above Rated Wind Speed: An Overlooked Contributor to High Loads in Wind Farms,” in *European Wind Energy Association*, Paris, 2015.

Appendix

The following publication is included in this appendix;

G. Marsh, C. Wignall, P. R. Thies, N. Barltrop, A. Incecik, V. Venugopal and L. Johanning, "Review and Application of Rainflow Residue Processing Techniques for Accurate Fatigue Damage Estimation," *International Journal of Fatigue*, vol. 82, pp. 757-765, 2016.

Review and Application of Rainflow Residue Processing Techniques for Accurate Fatigue Damage Estimation

Gabriel Marsh [a,b], Colin Wignall [b], Philipp R. Thies [a,c], Nigel Barltrop [a,d], Atilla Incecik [a,d], Vengatesan Venugopal [a,e], Lars Johanning [a,c]

a Industrial Doctoral Centre for Offshore Renewable Energy, The University of Edinburgh, King's Buildings, Edinburgh EH9 3JL, UK

b E.ON Technologies Limited, Technology Centre, Ratcliffe on Soar, Nottingham NG11 0EE, UK

c College of Engineering, Mathematics and Physical Science, Renewable Energy Research Group, University of Exeter, Penryn Campus, Penryn TR10 9EZ, UK

d Department of Naval Architecture, Ocean and Marine Engineering, University of Strathclyde, Glasgow G4 0LZ, UK

e Institute for Energy Systems, School of Engineering, The University of Edinburgh, King's Buildings, Edinburgh EH9 3JL, UK

Corresponding author:

Mr Gabriel Marsh

E.ON Technologies (Ratcliffe) Limited

Technology Centre, Ratcliffe on Soar

Nottingham

NG11 OEE, UK

g.marsh@ed.ac.uk

Highlights

- The residue which remains from the Rainflow algorithm is identified and discussed
- Damaging transition cycles are missed by conventional Rainflow methods
- An analytical proof is presented to allow extended periods to be processed accurately
- The significance of the new approach is demonstrated with case study examples

Abstract

Most fatigue loaded structural components are subjected to variable amplitude loads which must be processed into a form that is compatible with design life calculations. Rainflow counting allows individual stress cycles to be identified where they form a closed stress-strain hysteresis loop within a random signal, but inevitably leaves a residue of open data points which must be post-processed. Comparison is made between conventional methods of processing the residue data points, which may be non-conservative, and a more versatile method, presented by Amzallag et al [Amzallag C, Gerey JP, Robert JL, Bahuaud J. Standardization of the rainflow counting method for fatigue analysis. Int. J. Fatigue 1994; 16:287–293], which allows transition cycles to be processed accurately.

This paper presents an analytical proof of the method presented by Amzallag et al. The impact of residue processing on fatigue calculations is demonstrated through the application and comparison of the different techniques in two case studies using long term, high resolution data sets. The most significance is found when the load process results in a slowly varying mean stress which is not fully accounted for by traditional Rainflow counting methods.

Keywords: Cyclic counting methods, Load histories, Rainflow residue, Random loading, Variable amplitude fatigue

1. Introduction

The calculation of conservative load cycle spectra is a fundamental aspect of fatigue design, requiring an estimate to be made of expected operational loading conditions. Complex lifecycle loading may be simplified by dividing the process into discrete load cases, such as take-off and steady flight conditions for the analysis of aircraft components. Fatigue life can then be quantified in terms of time to crack initiation through the concept of linear damage accumulation, or by the application of crack growth models. Both approaches utilise information about the range, mean and number of stress cycles that will occur [1].

The identification of individual fatigue loading cycles within a random stress amplitude time series is achieved through the use of a suitable cycle counting algorithm. Typical methods include level-crossing counting, range-pair counting, reservoir counting, and Rainflow counting. Variations of these algorithms are included in the ASTM cycle counting standard [2].

1.1. *Background to the Rainflow counting algorithm*

Rainflow (RF) counting has become the most widely accepted method for the processing of random signals for fatigue analysis, and testing has demonstrated good agreement with measured fatigue lives when compared to other counting algorithms [3]. The concept was first developed by Matsuishi and Endo [4], where the identification of cycles was likened to the path taken by rain running down a

pagoda roof. In the paper, the authors defined a full RF cycle as a stress range formed by two points which are bounded within adjacent points of higher and lower magnitude; as the stress path returns past the first turning point it can be seen to form a cycle as described by a closed stress-strain hysteresis loop (Figure 1a). For the case where successive stress points are either converging or diverging, the hysteresis curves do not form a closed loop (Figure 1b). For this case the authors assumed that fatigue damage could be attributed to each successive range as half-cycles.

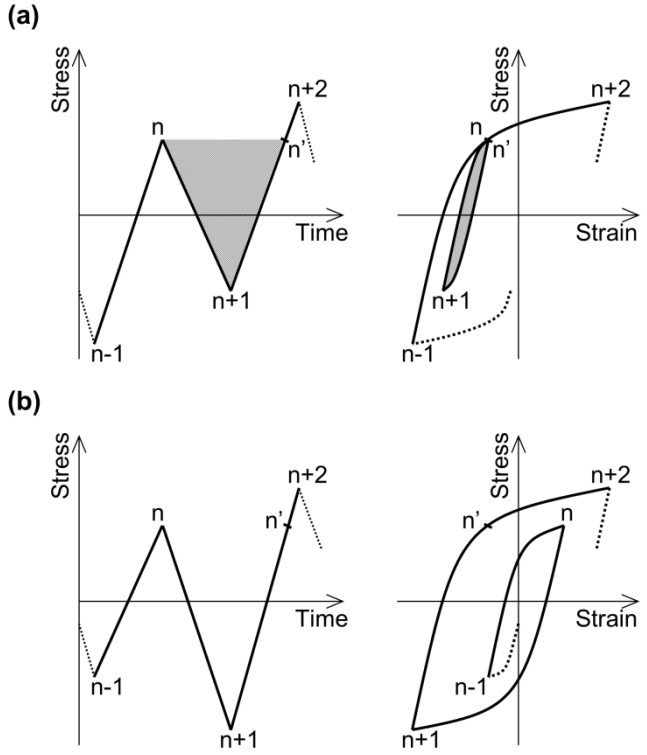

Figure 1. (a) Stress time series of turning points and the corresponding closed stress-strain hysteresis loop formed by points n, n+1 and n'. (b) Diverging stress time series and the corresponding open stress-strain hysteresis curves.

The method was further developed by Okamura et al. [5] and Downing & Socie [6] as a vector based algorithm which identified full RF cycles and half-cycles based on a three-point criteria without the need to rearrange the data series, and enabled efficient utilisation in computer software. This greatly reduced the data storage requirements as the stress signal could be read into the algorithm in real-time and processed directly into RF cycle spectra. This definition of the algorithm has been refined and included in the ASTM cycle counting standard [2]. Amzallag et al. [7] conducted a wide ranging industry consultation and defined a standardised algorithm which identified RF cycles based on a four-point criterion. The three and four point versions of the algorithm were shown to identify the same cycles by McInnes & Meehan [8], who presented a series of fundamental properties of RF counting to demonstrate the equivalence of the two methods. Although various forms of the RF algorithm exist,

the four-point algorithm presents the most unambiguous criterion for the identification of closed hysteresis loops, and is defined below.

1.2. *Four-point Rainflow counting criterion*

RF counting requires the time history to be first processed into a Peak-Valley (PV) series consisting of local maxima and minima which define the turning points, or load reversals, of a time series. Point x_m is identified as a local maxima or minima within a time series of length *M* if,

$$x_{m-1} < x_m > x_{m+1} \; or \; x_{m-1} > x_m < x_{m+1} \qquad (1)$$

$$m = 2, 3, 4, \dots, M-1$$

Once the data have been filtered according to the PV criteria, full RF cycles are identified in the range formed by points x_n to x_{n+1} if they meet the four-point criterion,

$$|x_{n-1} - x_n| \geq |x_n - x_{n+1}| \leq |x_{n+1} - x_{n+2}| \qquad (2)$$

$$n = 2, 3, 4, \dots, N-2$$

Where *N* signifies the length of the PV filtered series. If the range formed by points x_n to x_{n+1} meets the four-point criterion then the points are recorded before deleting them from the PV series, thus enabling further ranges to be formed between the adjacent points x_{n-1} and x_{n+2}. The process is repeated until all ranges which meet the four-point criterion are recorded and deleted from the PV series.

Storage of the counted ranges is achieved with a two dimensional histogram to record the cycle stresses. The form of the histogram may be chosen to preserve detailed cycle hysteresis information which may be significant in further statistical analysis, for example with the min-max or max-min matrices where cycles are binned according to the loading sequence [9]. As a minimum, the histogram should record the cycle range and mean stress levels as inputs to final damage calculations.

1.3. *Rainflow residue*

Once all full RF cycles which meet the four-point criterion have been identified and deleted from the PV series, a 'residue' of data points will typically remain. The residue consists of a series of diverging data points from the start to the maximum and minimum points, followed by a converging section of points to the end of the PV data series. Referring to Figure 2, no remaining closed hysteresis cycles can be identified within a diverging or converging series as no further ranges are bounded by adjacent points of higher and lower value. However, as the stress path formed by the residue constitutes some of the largest ranges in the original series, they should be accounted for if a conservative estimate of

fatigue damage is to be made. Two dominant methods exist in the literature to process the RF residue and are outlined in Sections 2.1 and 2.2.

Whenever a subset of a longer time history is RF counted, cycle ranges which are formed between points which span beyond the subset have the potential to be cropped. If there is a large variation in the mean stress level, which is not fully contained within the subset period, then some of the largest cycles will not be accounted for. These cycles are termed 'transition cycles' or 'ground cycles' [10], and a degree of artificiality will be introduced if the residue data points are processed as an isolated set, as closed hysteresis cycles cannot be formed. The only way to accurately identify all RF cycles within a data set according to the four-point criterion is to process the entire time history consecutively. However, the application of RF counting algorithms must always utilise a finite length of data, as chosen by the analyst and by limitations on computational capacity.

Glinka & Kam [11] presented an approach which allowed extended time periods to be read and processed incrementally, thus limiting the required computational capacity by minimising the amount of data required to be handled by the RF algorithm at any one time. A more versatile method is included in Amzallag et al. [7, pp. 292-293] which addresses the same issue by concatenating consecutive residue periods which remain after RF processing. However, although the method allows transition cycles to be accounted for accurately according the four-point criterion, it has not found widespread acknowledgement and no generalised proof of the methodology has been presented.

The three methods of processing the RF residue periods are presented in Section 2 below. An analytical proof is presented in Section 3 which demonstrates the equivalence of cycles which are identified from the residue concatenation methodology outlined in [7] with those which would be identified by RF processing a continuous series. In Section 4, the different approaches are applied to two case studies in order to illustrate the potential impact of the choice of residue processing method on calculated fatigue damage. Finally, Section 5 outlines the suitability of each of the three methods for practical applications.

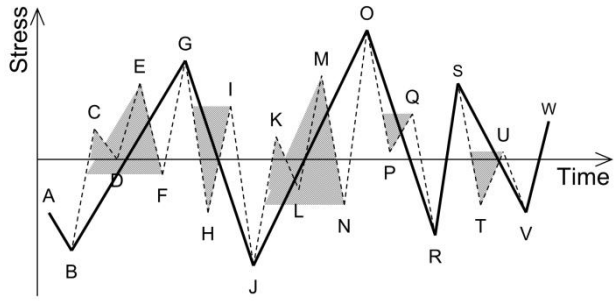

Figure 2. Residue remaining after application of the four-point criterion (points connected by solid line). Full RF cycles would be identified between points *C-D*, *E-F*, *H-I*, *K-L*, *M-N*, *P-Q*, *T-U*.

2. RF residue processing methodologies

The three distinct methods available for processing the residue data points are described below and presented in the process diagram in Figure 3.

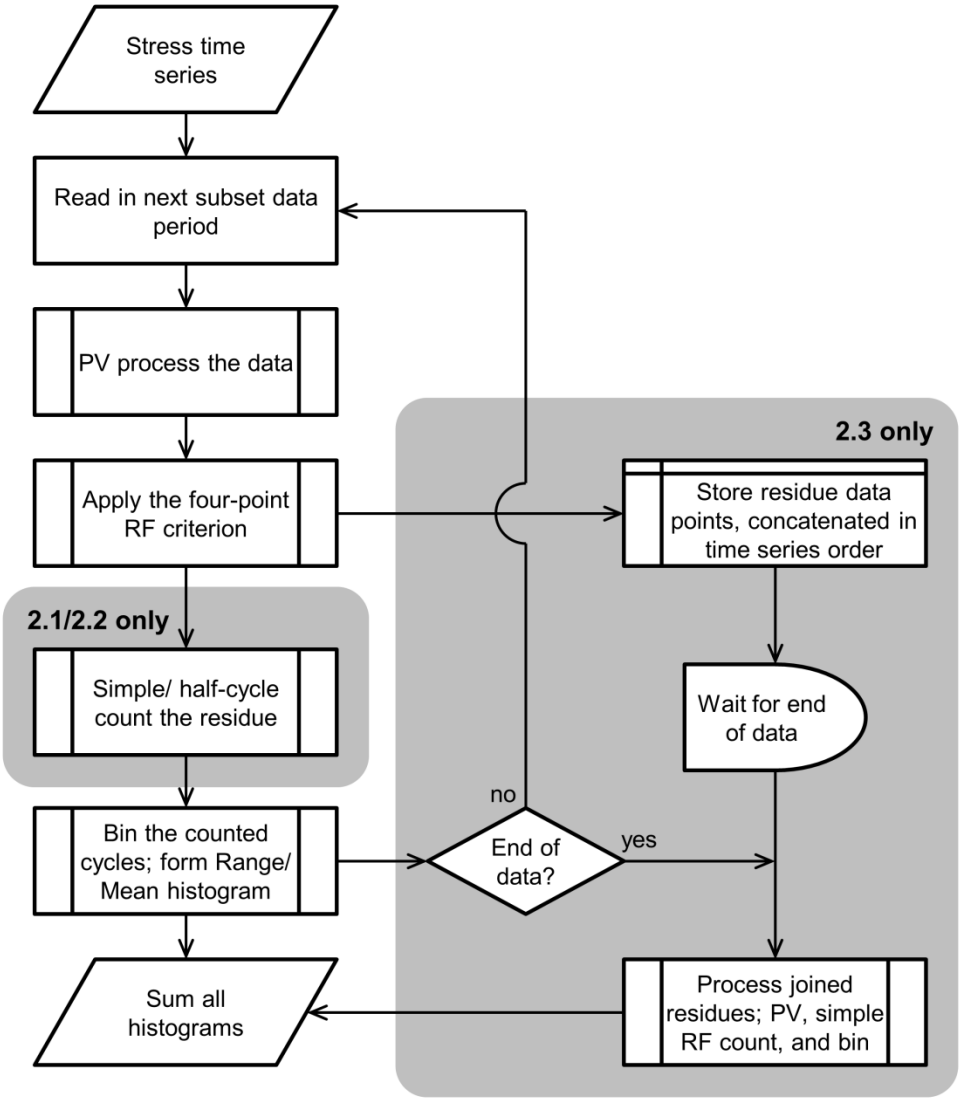

Figure 3. RF counting process diagram for long time periods (modified from [12]). Grey boxes identify steps which relate to the residue processing methods outlined in Sections 2.1, 2.2, 2.3 below.

2.1. *Half-cycle counting methodology*

This approach is identified in the original definition of RF counting given by Matsuishi & Endo [4], where the authors assumed that each successive range will attribute half a cycle of fatigue damage in the material. From Figure 2, subsequent half-cycle ranges are identified between points *A-B*, *B-G*, *G-J*, *J-O*, *O-R*, *R-S*, *S-V*, *V-W*. At least twice as many ranges will be identified from the residue data points as would be identified as fully closed cycles. Therefore, when the counted residue cycles are stored in the RF histogram the number of cycles added to each bin is reduced by a factor of 0.5. The ASTM RF

counting definition of the three-point algorithm [2, pp. 5-6] is capable of identifying half-cycles which occur up to the maximum data point in the series; after completion of the algorithm, the residue data points following the maximum still remain and must be accounted for as half cycles. Half-cycle counting may be applied directly to the residue which remains from application of the four-point RF criterion, and the resulting cycles can be shown to be identical to those produced by the three-point algorithm.

2.2. *Simple Rainflow counting methodology*

If the stress time history is representative of a repeated loading sequence then all residue data points will ultimately form fully closed cycles as they will fall between repeated extremes. With the four-point algorithm this can be achieved by joining two repeated residues and then reapplying the four-point criterion (Equation 2). Closed cycles can then be identified between the repeated maximums, leaving the residue points outside of the maximums which can then be discarded. This is expressed as [*residue*] + [*residue*] → [*residue*] + {*cycles*} [7].

From Figure 2, the residue series is repeated to give a sequence *A-B-G-J-O-R-S-V-W-A-B-G-J-O-R-S-V-W*. Equation (1) is then reapplied and the repeated point *A* must be deleted to ensure that the PV sequence is maintained. Equation (2) is then reapplied to identify closed cycles from all points that fall between *J* and repeated point *O*; ranges are formed by points *V-W*, *R-S*, *B-G*, *J-O*. The remaining points account for the repeated residue, and are therefore discarded.

The simple RF counting methodology is implemented in the three-point algorithm by rearranging the stress time series to start and end with the maximum data point prior to PV processing and RF counting, and will identify identical cycles [8]. Therefore, the approaches implemented in [2, pp. 6-7], [6, p. 32], [7] and [8] are equivalent.

2.3. *Residue concatenation methodology*

The following steps apply the residue concatenation procedure outlined in [7, pp. 292-293] to the simple case of two PV periods, with reference to Figure 4 and Figure 5:

1. Define two series of PV processed data points A_1, B_1, C_1,…, H_1 and A_2, B_2, C_2,…, H_2.
2. Apply the four-point criterion (Equation 2) to both series to identify all full RF cycles. Full cycles are identified between points D_1-E_1, and E_2-F_2 (Figure 4a).
3. Store the cycles and delete the identified data points D_1, E_1 and E_2, F_2 from the respective PV series (Figure 4b). No more full RF cycles can be identified according to Equation (2). The remaining points form the two RF residues.

4. Concatenate the two residues in their original chronological order. Apply the PV criteria to the concatenated points H_1 and A_2 to ensure the PV series is maintained. Delete point H_1 (Figure 4c).
5. Repeatedly apply the four-point criterion to the concatenated series until all fully closed RF cycles have been stored and removed from the concatenated series. (Figure 5a to Figure 5c). Full RF cycles are identified between points A_2-B_2, F_1-G_1, C_2-D_2 sequentially.
6. The remaining residue points are shown in Figure 5d, and must be processed by either half-cycle or simple RF counting. In practice, successive residue periods may be concatenated to allow additional close hysteresis cycles to be unlocked.

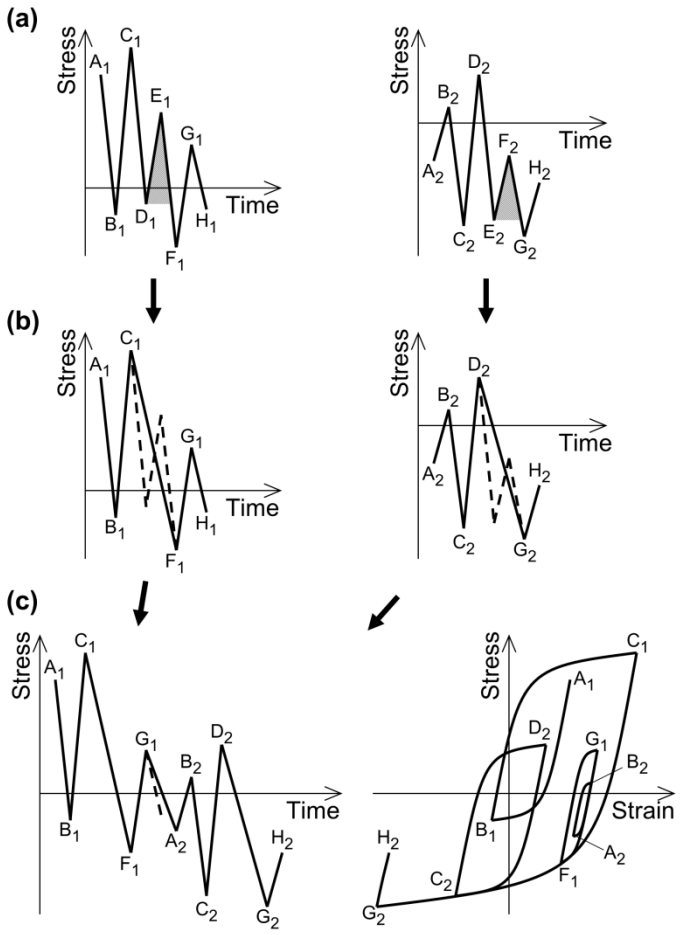

Figure 4. (a); two separate PV series. (b); the residue series from which no further fully closed RF cycles can be identified. (c); concatenation of the two RF residue series in stress-time and stress-strain space.

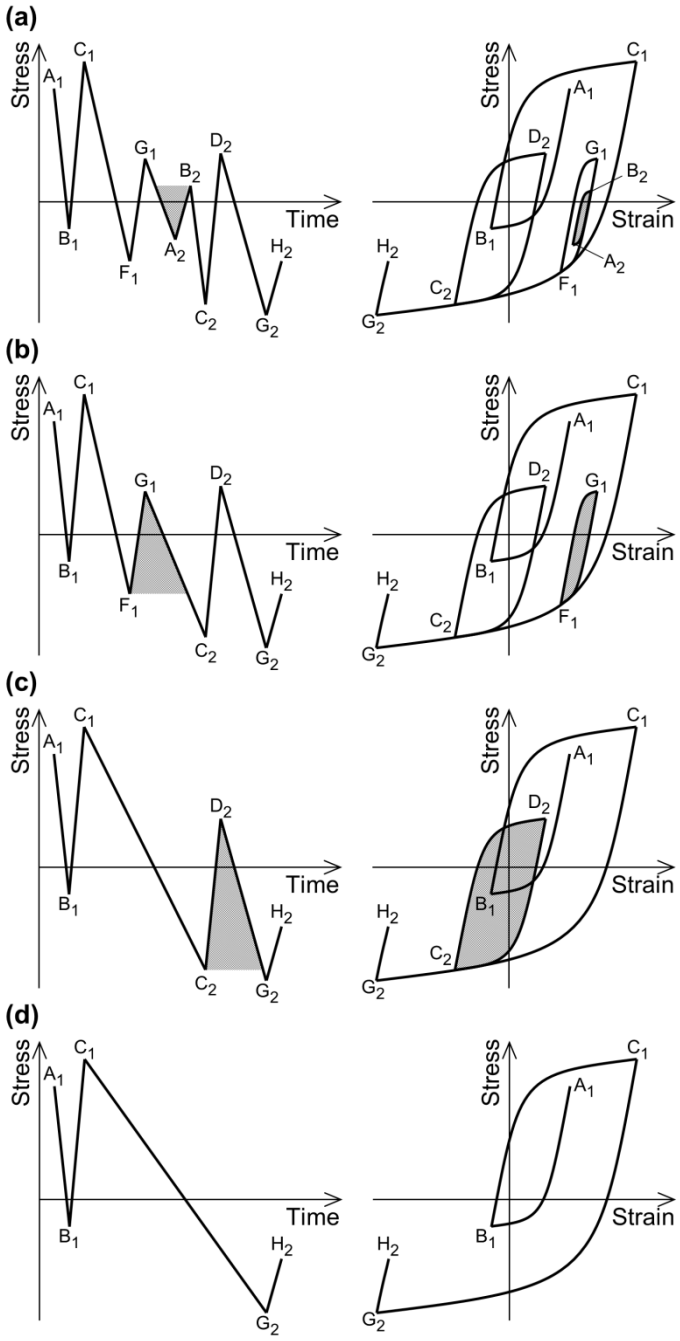

Figure 5. Identification of fully closed RF cycles within the concatenated residue series (from Figure 4).

3. Equivalence of concatenated series

The residue concatenation method outlined in section 2.3 can be shown to account accurately for transition cycles between consecutive periods by following the fundamental properties of the four-point criterion presented by McInnes & Meehan [8].

3.1. *Identical RF cycles are identified using residue concatenation as would be identified from a continuous series*

McInnes & Meehan defined an 'end-point bounded sequence' (EPBS) as any series of data points in which the maximum and minimum values lie at the start and end of the series. As all points are bounded between these local extremes, all the ranges contained between the end points will form fully closed cycles according to the four-point criterion. The authors show that the full cycles contained within an EPBS are independent and unaffected by the data points which lie outside of the sequence (Property 3.5, [8, p. 552]). Furthermore, as the residue remaining from the four-point algorithm consists of a set of EPBSs from the PV series (Property 3.8, [8, p. 554]), all the ranges which meet the four-point criterion will do so independently of the data points which occur before or after the PV series. Therefore, according to these two properties, the specific RF cycles which can be identified from separate periods must also form valid cycles within a continuous series.

McInnes & Meehan also showed that the RF cycles which meet the four-point criterion will do so regardless of the order in which the criterion is applied (Property 3.3, [8, p. 551]). Therefore, the EPBSs which may be formed between residue periods when they are concatenated can release additional RF cycles which would otherwise have been identified from a continuous series.

Referring to Figure 4a, the data point subsets C_1, D_1, E_1, F_1 and D_2, E_2, F_2, G_2 both form EPBSs and therefore, according to Property 3.5 [8, p. 552], the full cycles formed by the ranges D_1 to E_1 and E_2 to F_2 are independent and unaffected by the concatenation of the two residues. Points C_1 to G_2 then produce an EPBS within the concatenated residues which allows additional full cycles to be formed by the ranges A_2-B_2, F_1-G_1, and C_2-D_2 (Figure 5). According to Property 3.3 [8, p. 551], the same cycles would be identified from a continuous series, although they would have been extracted in a different order.

3.2. *Deleted residue end points do not affect the correct identification of RF cycles*

RF cycles which fall within an EPBS that includes the end point in a residue series are not affected if the point must be deleted after concatenation in order to maintain the PV sequence. This is true because, although the first or last point in an EPBS might be deleted, the sequence would always be extended to a bounding point which is of greater range. Figure 6 demonstrates the three basic configurations for the connected ends of two concatenated residues (additional permutations exist which are essentially mirror images in the horizontal and vertical planes). Figure 6a shows the configuration where the PV sequence is maintained and no points are required to be deleted. Figure 6b shows the case where one point must be deleted to fulfil the PV criteria and the EPBS formed by B_1 to C_1 is extended to B_1 to A_2 as point C_1 is removed. Figure 6c shows the case where both the concatenated end points must be deleted and the EPBSs formed by B_1 to C_1 and A_2 to B_2 are both

extended to the range formed by B_1 to B_2. Therefore, Property 3.5 [8, p. 552] holds true when RF residues are concatenated and the PV criteria is reapplied.

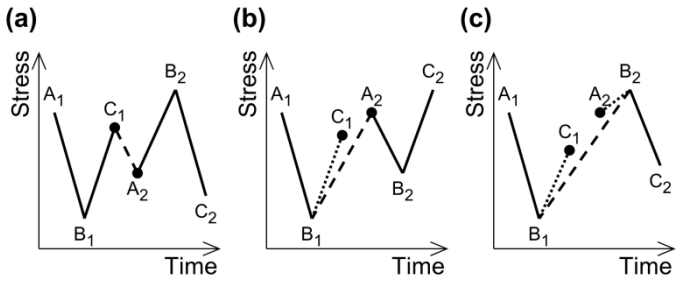

Figure 6. Detail of the connected ends of two concatenated residues. Residue end points are shown with a dot, deleted points (which do not meet the PV criteria) are indicated by a dotted line, and joined points are indicated by a dashed line.

4. Residue processing comparison using experimental data

The significance of the different residue processing methods can be compared by investigating their impact on calculated fatigue damage.

4.1. *Fatigue damage comparison methods*

The Palmgren-Miner linear damage hypothesis assumes that the fatigue damage in a loaded component can be expressed as the sum of damages contributed by each stress cycle,

$$D = \sum_{i=1}^{k} \frac{n_i}{N_i} \tag{3}$$

where D is fatigue damage fraction, and n_i/N_i is the ratio of operational cycles to the maximum allowable number of cycles at each stress range. Although fatigue crack propagation can be found to be influenced by the load sequence, the linear damage sum is commonly used in design cases which require a statistical representation of the loading, such as environmental loading where the load sequence is rarely well defined at the design stage. Therefore, the linear damage sum has been used for this analysis, although a more detailed fracture mechanics approach may also benefit from the ability to correctly identify large amplitude hysteresis cycles.

The maximum allowable number of cycles N is taken from empirical S-N data, as generalised by the Basquin relation,

$$\log N = \log \bar{a} - m \log \Delta\sigma \tag{4}$$

where $\Delta\sigma$ is either stress range or amplitude (stress range will be used here in accordance with the RF cycle definition), m is the Wöhler exponent, and $\log \bar{a}$ is the intercept of the curve on the $\log N$ axis. Combining Equations (3) and (4), the ratio of fatigue damages can be expressed as,

$$\frac{D_A}{D_B} = \frac{\sum_{i=1}^{k} n_{A_i} \Delta\sigma_i{}^m}{\sum_{i=1}^{k} n_{B_i} \Delta\sigma_i{}^m} \quad (5)$$

where n_A and n_B are the cycle spectra produced by different RF counting methods. It can be seen that, by taking the damage ratio, the $\log \bar{a}$ intercept term cancels and the impact of the different counting methods is affected only by the Wöhler exponent from the S-N curve. It can also be seen that a hypothetical linear increase in stress ranges such as may arise from a stress concentration factor, for example, would also cancel with the damage ratio, indicating that the difference between the RF counting methods would be affected by the underlying load process, but not by the stress magnitude. As a fatigue endurance limit could be exceeded by such a linear increase in stresses any results calculated in this analysis would be trivial; i.e. the use of a constant gradient S-N curve means that the form of Equation (5) enables the general case to be examined.

S-N data is typically derived from component testing with a zero mean cycle stress. However, stress cycles in the tensile range may produce greater levels of fatigue damage, and S-N test results are known to be strongly dependent on the mean stress level. Mean stress correction models may therefore be used to adjust the stress range prior to damage calculation from S-N curves using,

$$\Delta\sigma_{\bar{\sigma}} = \Delta\sigma_0 \left(1 - \left[\frac{\bar{\sigma}}{\sigma_{UTS}}\right]^Z\right) \quad (6)$$

where $\Delta\sigma_{\bar{\sigma}}$ is the stress range or amplitude at non-zero mean stress $\bar{\sigma}$, $\Delta\sigma_0$ is the equivalent stress range or amplitude at zero mean stress, and σ_{UTS} is the ultimate tensile strength of the material. Values of Z=1 and Z=2 give the Goodman and Gerber relations, respectively, while the Soderberg relation is given with Z=1 and σ_{UTS} replaced by the yield stress [1]. Mean stress correction models are applicable in the tensile range only, therefore $\Delta\sigma_{\bar{\sigma}} = \Delta\sigma_0$ is used in compression.

The impacts of the residue processing methodologies were then assessed against the following variables:

- The underlying load processes
- The Wöhler exponent used to calculate fatigue damage
- The length of the subset period used for the half-cycle and simple RF methods outlined in Sections 2.1 and 2.2

4.2. *Measured datasets*

Two datasets representing different load processes were used to investigate the residue processing methodologies. The offshore measurement buoy shown in Figure 7a is governed by dynamic wave loading, but the mooring system is also effected by a semi-diurnal tidal cycle. The offshore wind turbine shown in Figure 7b also experiences hydrodynamic loading, but the structural response is dominated by the aerodynamic and operational loads.

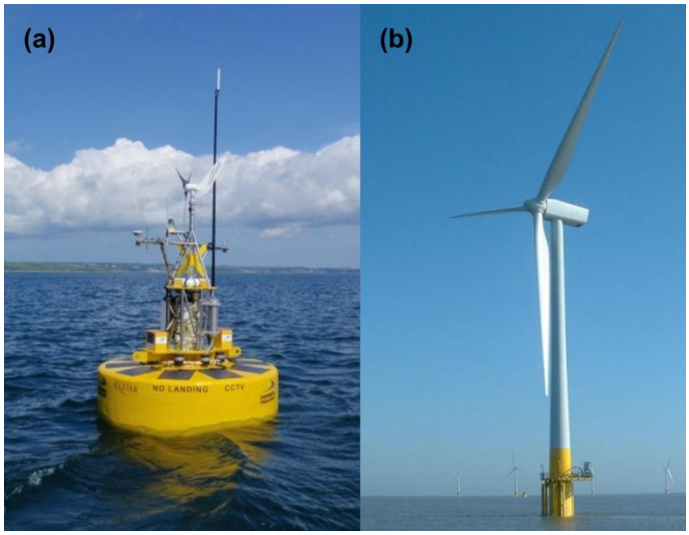

Figure 7. (a) Offshore measurement buoy. (b) A multi-megawatt offshore wind turbine.

For the offshore measurement buoy, a load cell was used to measure forces located at the connection between the buoy and a catenary mooring line, recorded with a sample rate of 20 Hz. The force time series was then converted to stresses using the geometry of the attachment shackle. Details of the mooring system are outlined in [13].

For the offshore wind turbine support structure, strain gauge measurements were also recorded at 20 Hz sample rate and converted to time series stresses using the Elastic Modulus of the base material. The gauge was located away from any stress raising features at the base of the wind turbine near the mean water level, axially aligned with the cylindrical tower to measure the nominal bending stresses. Material constants for the measured components are shown in Table 1.

Table 1, Material constants for the analysed steel components

	Wind turbine	Buoy
Yield stress	335 MPa	270.7 MPa
Ultimate tensile stress	490 MPa	505.8 MPa
Elastic modulus	210 GPa	-

4.3. *Results*

Figure 8a shows a six month stress history from the offshore measurement buoy. The accumulated fatigue damages were calculated according to Equation (5), expressed as the ratio of damages produced by RF counting the time series in subsets (using the half-cycle and simple residue processing methods outlined in Sections 2.1 and 2.2) to the damages produced by RF counting a continuous period (using the residue concatenation method outlined in Section 2.3). Figure 8b shows the damage ratios produced using ten minute subsets; a typical simulation length for a wind turbine load case due to the level of statistical stationarity of the wind loading process found over this time scale [14]. Figure 8c shows the damage ratios that result using three hour subsets, a length of time which is typically used to characterise wave loading due to assumed sea-state stationarity over this period [15]. Wöhler exponents of $m = 3$ and $m = 5$ were used, relating to typical S-N curves for steel components [16]. The data were processed using a verified in-house RF counting code which was developed in MATLAB [17].

Figure 9 displays a one year period of stress data collected from the multi-megawatt offshore wind turbine support structure and the corresponding accumulated fatigue damage ratios, calculated in the same way. The shapes of the RF cycle spectrums produced by both datasets are shown in Figure 10.

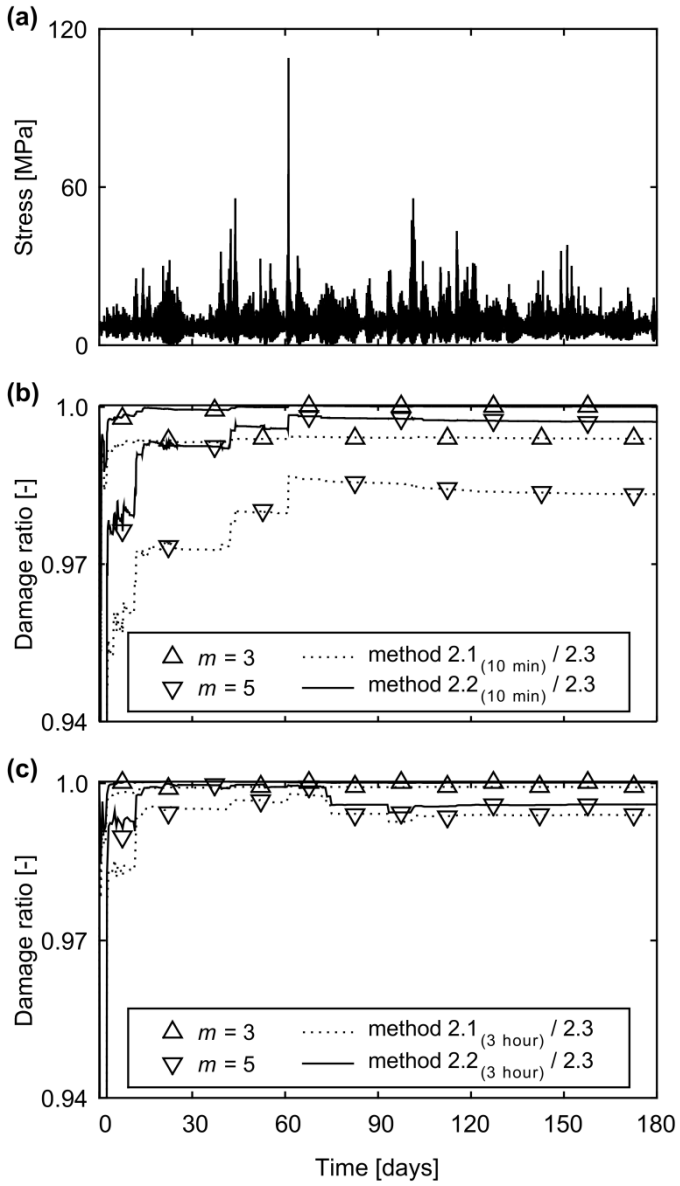

Figure 8. (a) Stress time history from a catenary mooring attachment point. (b) Ratio of accumulated fatigue damages calculated using Equation (5); damage produced by half-cycle and simple RF counting ten minute subsets, divided by the damage produced by RF counting the data continuously. (c) Ratio of accumulated damages using three hour subsets.

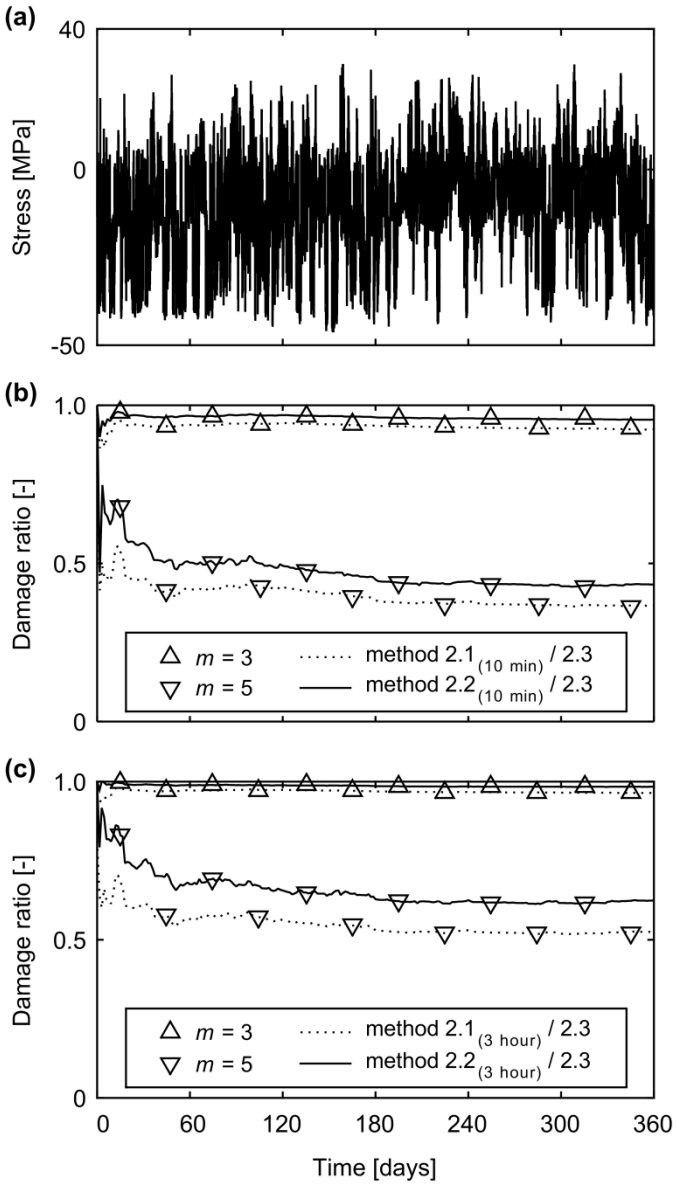

Figure 9. (a) Stress time history from a multi-megawatt wind turbine support structure. (b) Ratio of accumulated fatigue damages calculated using Equation (5); damage produced by half-cycle and simple RF counting ten minute subsets, divided by the damage produced by RF counting the data continuously. (c) Ratio of accumulated damages using three hour subsets.

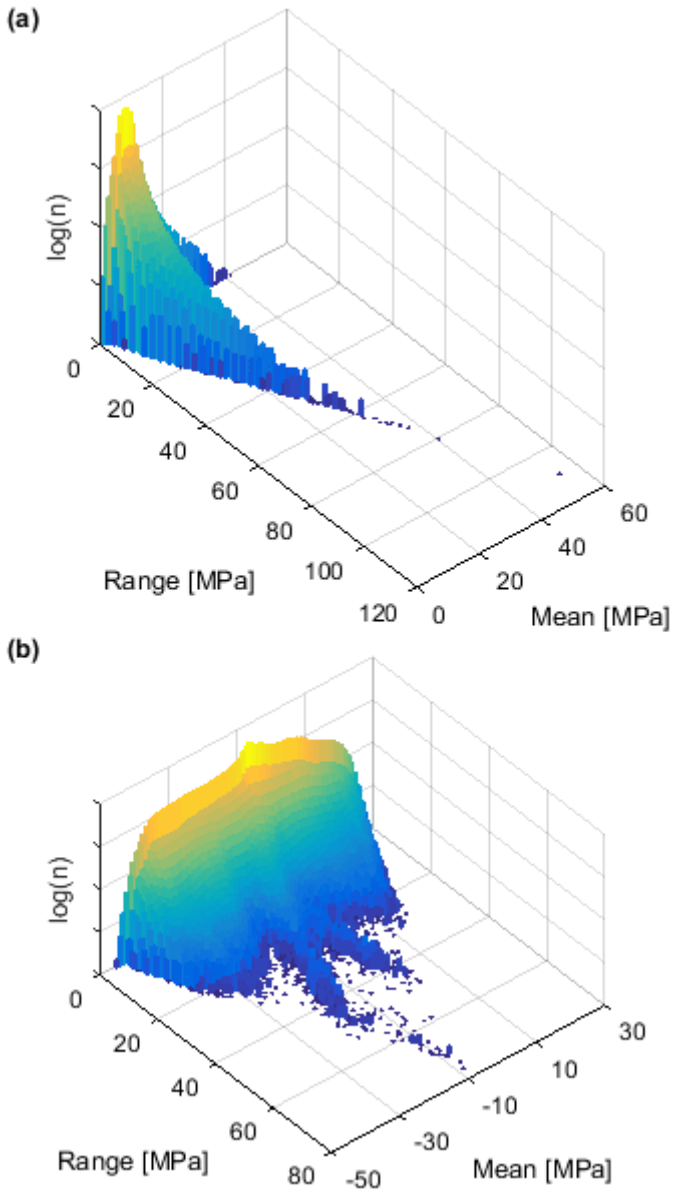

Figure 10. Range-Mean cycle histograms for the full (a) measurement buoy and (b) wind turbine datasets, RF counted using the continuous algorithm from Section 2.3. The cycle counts are shown on a logarithmic scale with the values omitted due to confidentiality requirements.

The final values of the damage fraction ratios, together with the impact of the mean stress compensation models (Equation 6), are shown in Table 2.

Table 2, Mean stress compensated damage ratios for the complete datasets. The uncompensated values relate to the final damage ratios from Figure 8 and Figure 9.

	Measurement Buoy								Wind Turbine							
method:	$2.1_{(10\ min)}$ / 2.3		$2.2_{(10\ min)}$ / 2.3		$2.1_{(3\ hour)}$ / 2.3		$2.2_{(3\ hour)}$ / 2.3		$2.1_{(10\ min)}$ / 2.3		$2.2_{(10\ min)}$ / 2.3		$2.2_{(3\ hour)}$ / 2.3		$2.2_{(3\ hour)}$ / 2.3	
m =	3	5	3	5	3	5	3	5	3	5	3	5	3	5	3	5
Uncompensated	0.99	0.98	1.00	1.00	1.00	0.99	1.00	1.00	0.92	0.37	0.95	0.43	0.96	0.53	0.98	0.62
Goodman	0.99	0.98	1.00	1.00	1.00	1.00	1.00	1.00	0.93	0.38	0.96	0.44	0.96	0.54	0.98	0.64
Gerber	0.99	0.98	1.00	1.00	1.00	0.99	1.00	1.00	0.92	0.37	0.95	0.43	0.96	0.53	0.98	0.63
Soderberg	0.99	0.98	1.00	1.00	1.00	1.00	1.00	1.00	0.93	0.38	0.96	0.45	0.97	0.54	0.99	0.65

5. Discussion

The results presented in Section 4 show that the significance of transition cycles on calculated fatigue damage is dependent upon the underlying load process, the slope of the S-N curve, and the subset length chosen to RF process the data.

The catenary mooring system shown in Figure 8a is representative of the typical scenario where the maximum and minimum stresses in the load process occur well within the time frame which can be processed by conventional RF methods. Longer term variations in mean stress levels do occur over the 12 hour tidal cycle, but are of small amplitude in comparison to the stress response from dynamic wave loading. The effect of the varying mean stress is noticeable at the start of the dataset when the transition cycles are more significant in comparison to the low dynamic wave loading. Larger loading events at 2.5 days and 61 days result in closer correlation, with convergence of the calculated damage levels within 97% for each of the RF methods. The longer subset length of 3 hours produces a closer correlation between the methods, as more of the tidal cycle is included in the subset period.

The wind turbine data shown in Figure 9, however, includes a large change in the tower mean stress level as a result of the quasi-static rotor thrust loading which changes with variations in wind speed and direction. The dynamic structural response, which is overlaid on the varying mean stress, is of comparatively low amplitude. The result is that RF counting of the data in subsets using the methodologies outlined in Sections 2.1 and 2.2 accounts for only 37% to 62% of the fatigue damage which results when the data is processed as a continuous series, using a Wöhler exponent of $m = 5$. The difference in damage levels are seen to converge after approximately 2 to 6 months, which is indicative of the length scale of the stress cycles which arise from changes in the quasi-static wind loading. With a Wöhler exponent of $m = 3$, however, the difference in fatigue damage produced by

each of the residue processing methods is negligible, due to the fact that a shallower S-N curve gradient will attribute less weight to the high amplitude/low frequency stress ranges which characterise transition cycles. It should be noted that use of an S-N curve which incorporates a 'knee', or a minimum fatigue endurance limit (which may justify the use of a filter incorporated into the RF analysis to remove stress cycles which are small enough not to effect fatigue life), would increase the impact of the transition cycles because greater significance would be attributed to the high amplitude cycles.

The inclusion of mean stress compensation models in the damage fraction ratio results presented in Table 2 is seen to have minimal impact on the significance of transition cycles, with between 2% and 4% less impact with the Goodman and Soderberg relations for the offshore wind turbine dataset with a Wöhler exponent of m = 5. Although the impact is relatively low (the damage from the wind turbine maximum tensile stress range of approximately 30 MPa would be impacted by the Soderberg relation by a factor of $(1 - 30/335)^{-5} = 1.6$), this is understandable as cycles from both RF residue processing methods would be effected, and the majority of cycles in the dataset are in compression. The effect of the mean stress compensation models is less than 0.5% in all other cases.

The fatigue damage levels calculated by the half-cycle and simple RF residue processing methods are of comparable magnitudes due to the fact that the bounding maximum cycle range is consistent. Both methods are applicable when the range of stresses produced by the load process is included within the RF counting subset. A typical example is the identification of load cycles experienced by a power station boiler where the load sequence, including maximum and minimum stresses, can be related to long term operational states. The EN standard for Water-tube boilers and auxiliary installations [18] specifies a range of methods for the processing of RF residue points which are comparable to the half-cycle counting and simple processing methods outlined in Sections 2.1 and 2.2.

Concatenation of residue periods, as outlined in Section 2.3, is capable of addressing two main shortfalls of the conventional methods. Firstly, large volumes of data, which may prohibit RF processing of the continuous series due to computational limitations, can be dealt with correctly. This may be particularly applicable to long term load measurement programmes which typically generate large quantities of data. Secondly, transition cycles which span RF counted periods can be correctly accounted for according to the four-point criterion. Although a factor of two scatter can be expected in S-N test results [19], the identification of RF cycles in a long time history can, and therefore should, be performed accurately.

Additionally, the residue processing method outlined in Section 2.3 could be incorporated into fatigue design by the load case approach through the utilisation of information regarding the long term load history. The design of support structures for multi-megawatt wind turbines, for instance, is facilitated by the time domain simulation of structural dynamics under a discretised set of environmental and

operational loading conditions [20]. An approach to account for transition cycles with operational wind turbine measurement programmes is outlined in [21], whereby a synthetic time history of maximum and minimum stresses from each load case is constructed corresponding to a long term history of wind speed and direction measurements. However, the approach can be found to be overly conservative as it involves the double counting of data points as both half-cycles within the ten minute load case period and as successive full RF ranges within the synthesised long term stress series. Residue concatenation can avoid this double counting as it accounts for transition cycles correctly according to the four-point criterion.

6. Conclusions

The three main variations of RF counting described above are distinguished by the way in which the residue is accounted for, and the most suitable method should be selected according to the application. Specific findings include:

- The concatenation of successive RF residue periods has been shown to enable the same closed hysteresis cycles to be identified as would be produced by RF counting the data as a continuous series.
- The conventional methods of half-cycle and simple RF counting the residue periods are suitable when the entire stress range seen by a component is contained within the analysed period of data.
- Concatenation of residue periods is suitable when the data to be processed contains a slowly varying mean stress which results in transition cycles which would otherwise be cropped by half-cycle or simple RF processing the data in subsets. Using this method, transition cycles can be accounted for correctly according to the four-point criterion.
- The impact of transition cycles is most significant with the use of higher Wöhler exponents.

Acknowledgements

The authors would like to thank E.ON Climate & Renewables for provision of the wind turbine structural measurements used in this work. The English translation of [4] provided by Professor Seiji Shimizu of Oshima College, Japan is also gratefully acknowledged. IDCORE is funded by the Energy Technologies Institute and the RCUK Energy programme; grant number EP/J500847/1.

References

[1] S. Suresh, Fatigue of materials, Cambridge: Cambridge University Press, 1994.

[2] ASTM E1049-85, "Standard practices for cycle counting in fatigue analysis," (Reapproved 2011).

[3] D. Socie, "Rainflow cycle counting: A historical perspective," in The International Symposium on Fatigue Damage Measurement and Evaluation Under Complex Loadings, Fukuoka, 1991.

[4] M. Matsuishi and T. Endo, "Fatigue of metals subjected to varying stress," in *Jpn Soc. Mech. Eng.*, Fukuoka, 1968.

[5] H. Okamura, S. Sakai and I. Susuki, "Cumulative fatigue damage under random loads," *Fatigue Eng. Mater. Struct.*, vol. 1, pp. 409-419, 1979.

[6] S. Downing and D. Socie, "Simple Rainflow counting algorithms," *Int. J. Fatigue,* vol. 4, no. 1, pp. 31-40, January 1982.

[7] C. Amzallag, J. Gerey, J. Robert and J. Bahuaud, "Standardization of the Rainflow counting method for fatigue analaysis," *Int. J. Fatigue,* vol. 16, no. 4, pp. 287-293, 1994.

[8] C. McInnes and P. Meehan, "Equivalence of four-point and three-point rainflow cycle counting algorithms," *Int. J. Fatigue,* vol. 30, no. 3, pp. 547-559, 2008.

[9] P. Johannesson, "Doctoral thesis on: Rainflow analysis of switching Markov loads," Lund Institute of Technology, 1999.

[10] H. J. Sutherland, "On the fatigue analysis of wind turbines," Sandia National Laboritories, 1999.

[11] G. Glinka and J. Kam, "Rainflow counting algorithm for very long stress histories," *Int. J. Fatigue,* vol. 9, no. 3, pp. 223-228, 1987.

[12] G. Marsh and A. Incecik, "Fatigue load monitoring of offshore wind turbine support structures," in *Eur. Wind Energy Assoc. Offshore,* Frankfurt, 2013.

[13] P. R. Thies, L. Johanning, V. Harnois, H. C. Smith and D. N. Parish, "Mooring line fatigue damage evaluation for floating marine energy converters: Field measurements and prediction," *Renew. Energy,* vol. 63, pp. 133-144, March 2014.

[14] Germanischer Lloyd WindEnergie GmbH, “Recommendations for Design of Offshore Wind Turbines (RECOFF); Deliverable D1 - External Conditions, state of the art,” 2003.

[15] Det Norsk Veritas, “DNV-RP-C205: Environmental Conditions and Environmental Loads,” 2010.

[16] Det Norsk Veritas, “DNV-RP-C203: Fatigue design of offshore steel structures,” 2010.

[17] MATLAB, release R2015a, Natick, Massachusetts: The MathWorks, Inc., 2015.

[18] BS EN 12952, “Water-tube boilers and auxiliary installations - Part 4: In-service life expectancy calculations,” European Committee for Standardisation, 2011.

[19] C. Boller and M. Buderath, “Fatigue in aerostructures - where structural health monitoring can contribute to a complex subject,” *Philos. Transact. Royal Soc. A*, vol. 365, no. 1851, pp. 561-587, 2007.

[20] International Electrotechnical Commission, “IEC 61400-1 Wind turbines Part1: Design Requirements,” 2005.

[21] C. Larsen and K. Thomsen, “Low cycle fatigue loads; Risø-R-913(EN),” 1996.